



Experimental studies of Fluid-Structure Interaction on Downwind sails

Julien Deparday

► To cite this version:

Julien Deparday. Experimental studies of Fluid-Structure Interaction on Downwind sails. Fluid mechanics [physics.class-ph]. Université Bretagne Occidentale, 2016. English. NNT : . tel-01368071v1

HAL Id: tel-01368071

<https://theses.hal.science/tel-01368071v1>

Submitted on 19 Sep 2016 (v1), last revised 20 Dec 2016 (v2)

HAL is a multi-disciplinary open access archive for the deposit and dissemination of scientific research documents, whether they are published or not. The documents may come from teaching and research institutions in France or abroad, or from public or private research centers.

L'archive ouverte pluridisciplinaire **HAL**, est destinée au dépôt et à la diffusion de documents scientifiques de niveau recherche, publiés ou non, émanant des établissements d'enseignement et de recherche français ou étrangers, des laboratoires publics ou privés.

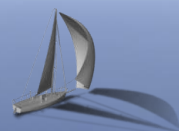


Distributed under a Creative Commons Attribution - NonCommercial - NoDerivatives 4.0 International License



université de bretagne
occidentale

UNIVERSITE
BRETAGNE
LOIRE



THÈSE / UNIVERSITÉ DE BRETAGNE OCCIDENTALE

sous le sceau de l'Université Bretagne Loire

pour obtenir le titre de

DOCTEUR DE L'UNIVERSITÉ DE BRETAGNE OCCIDENTALE

Mention : Génie Mécanique, Mécanique des Fluides et Energétique
École Doctorale EDSM

présentée par

Julien Deparday

Préparée à l'Institut de Recherche de l'Ecole
Navale, département Mécanique et
Energétique en Environnement Naval

Experimental studies of Fluid-Structure Interaction on Downwind sails

Thèse soutenue le 06 juillet 2016

devant le jury composé de :

Marco Belloli

Associate Professor, Politecnico di Milano / *Rapporteur*

Patrick Bot

Maître de Conférences, IRENAV / *Encadrant*

Frédéric Hauville

Maître de Conférences, IRENAV / *Encadrant - Membre invité du jury*

Pascal Hémon

Ingénieur de Recherche CNRS HDR, LadHyX / *Rapporteur*

Marc Rabaud

Professeur des Universités, Université Paris-Sud FAST / *Directeur de thèse*

Lionel Schouveiler

Professeur des Universités, IRPHE / *Président du Jury*

Bernard Simon

Professeur des Universités, UBO / *Examineur*

Résumé: Cette thèse présente une étude expérimentale sur un voilier instrumenté, menée pour décrire le comportement aéro-élastique des voiles et du gréement pour des navigations au portant. Les formes des voiles utilisées sont des surfaces non développables avec de fortes courbures provoquant une séparation massive de l'écoulement. De plus, les spinnakers sont des voiles fines et souples rendant l'interaction fluide-structure fortement couplée. A cause du non-respect de certaines règles de similitude, le comportement dynamique d'un spinnaker se prête mal à l'étude en soufflerie et nécessite une comparaison avec des mesures *in-situ*. Les simulations numériques instationnaires modélisant le comportement aéro-élastique des voiles et du gréement doivent être qualifiées et demandent également des validations. C'est pourquoi un système d'instrumentation embarquée est mis en place sur un J/80, un voilier de huit mètres de long. Il s'agit de mesurer dynamiquement la forme en navigation du spinnaker, les efforts dans les gréements dormant et courant, la répartition de pression sur la voile ainsi que le vent et les attitudes du bateau. La forme du spinnaker en navigation est obtenue grâce à un système de mesure photogrammétrique développé pendant la thèse. La précision de ce système, meilleure que 1,5%, permet de mesurer la forme générale de la voile ainsi que les déformations importantes telles que celles liées au fasyement du guindant. L'effort aérodynamique produit par le spinnaker est obtenu grâce à la mesure de l'intensité des efforts et de leurs directions aux trois extrémités (drisse, amure, écoute) ainsi que par la mesure des pressions sur la voile. Le comportement général du spinnaker est analysé en fonction de l'angle du vent apparent. Une nouvelle représentation utilisant les surfaces de Bézier triangulaires est développée pour décrire la forme tridimensionnelle du spinnaker. Quelques points de contrôles suffisent pour représenter la voile et caractériser le type de voile. Un comportement dynamique propre au spinnaker est également étudié. Le réglage supposé optimal d'un spinnaker est à la limite du fasyement, en laissant le guindant se replier légèrement. Cependant ce réglage n'a jamais été scientifiquement étudié auparavant. Nous avons montré qu'il s'agit d'une forte interaction fluide-structure tridimensionnelle où une importante dépression apparaît au bord d'attaque, qui augmente temporairement les efforts, ce qui n'est pas observé avec un réglage plus bordé.

Mots-clés: Interaction fluide structure, aérodynamique, instationnaire, expérience in situ, voilier instrumenté, voile de portant, spinnaker, mesure photogrammétrique, surface de Bézier, décomposition en modes propres

Abstract: A full-scale experimental study on an instrumented sailing yacht is conducted to better assess the aero-elastic behaviour of the sails and rigging in downwind navigations. The downwind sail shape is a non-developable surface with high curvature leading to massive flow separation. In addition, spinnakers are thin and flexible sails leading to a strongly coupled Fluid-Structure Interaction. Due to the non-respect of some rules of similitude, the unsteady behaviour of downwind sails cannot be easily investigated with wind tunnel tests that would need comparison with full-scale experiments. Moreover unsteady numerical simulations modelling the aero-elastic behaviour of the sails and rigging require validations. An inboard instrumentation system has been developed on a 8 meter J/80 sailboat to simultaneously and dynamically measure the flying shape of the spinnaker, the aerodynamic loads transmitted to the rigging, the pressure distribution on the sail as well as the boat and wind data. The shape of the spinnaker while sailing is acquired by a photogrammetric system developed during this PhD. The accuracy of this new system, better than 1.5%, is used to measure the global shape and the main dynamic deformations, such as the flapping of the luff. The aerodynamic load produced by the spinnaker is assessed by the measurements of the load magnitudes and directions on the three corners of the sail (head, tack and clew), and also by the pressure distribution on the spinnaker. The global behaviour of the spinnaker is analysed according to the apparent wind angle. A new representation using Bézier triangular surfaces defines the spinnaker 3D shape. A few control points enable to represent the sail and can easily characterise the type of sail. A typical unsteady behaviour of the spinnaker is also analysed. Letting the luff of the sail flap is known by sailors as the optimal trim but has never been scientifically studied before. It is found that it is a complex three dimensional fluid-structure interaction problem where a high suction near the leading edge occurs, producing a temporary increase of the force coefficient that would not be possible otherwise.

Keywords: Fluid structure interaction, aerodynamics, unsteady, full scale experiment, instrumented boat, downwind sail, spinnaker, photogrammetric measurement, Bézier surface, proper orthogonal decomposition

THÈSE

présentée à

L'UNIVERSITÉ DE BRETAGNE OCCIDENTALE

pour obtenir le titre de

DOCTEUR DE L'UNIVERSITÉ DE BRETAGNE OCCIDENTALE

Mention *Génie Mécanique: Mécanique des Fluides et Energétique*

par

Julien Deparday

Experimental studies of Fluid-Structure Interaction
on Downwind sails

soutenue le 06 Juillet 2016 devant la commission d'examen :

M. Belloli	Rapporteur
P. Bot	Encadrant
F. Hauville	Encadrant - Membre invité du jury
P. Hémon	Rapporteur
M. Rabaud	Directeur de thèse
L. Schouveiler	Président du jury
B. Simon	Examineur

Allow me to express now, once and for all, my deep respect for the work of the experimenter and for his fight to bring significant facts from an inflexible Nature who says so indistinctly "No" and so distinctly "Yes" to our theories.

Hermann Weyl (1885-1955)

Le hasard ne favorise l'invention que pour des esprits préparés aux découvertes par de patientes études et de persévérants efforts.

Louis Pasteur (1822-1895)

[...] pas même des heures plus tard, lorsque l'aurore rouge enflamma le mont Damavand pour envahir ma chambre et éclairer, au milieu des draps sillonnées de chair, son visage pâli par la fatigue, son dos infiniment nu où paressait, bercé par les vagues de son souffle, le long dragon des vertèbres et les traces de son feu, ces taches de rousseur qui remontaient jusque sur la nuque, autant d'astres de brûlures éteintes, la galaxie que je parcourais du doigt en dessinant des voyages imaginaires [...]

Boussole, Mathias Enard, (1972-)

Baaagaaa aapoouu!

Emilie Deparday (2015-)

Remerciements

Et me voilà à écrire cette page de remerciements...

Au premier jour de ma thèse, mon premier travail a été de lire la thèse de Benoît. Pour commencer doucement, j'ai d'abord lu ses remerciements. Et j'ai alors compris l'importance d'une thèse, et ce dans quoi je m'étais engagé. Je me suis alors demandé si à la fin de la mienne, quand ça serait à mon tour de remercier, j'aurais aussi ce plaisir de l'avoir fait et de dire merci à tout ceux qui ont été là pour moi...

Et je crois que c'est le cas!

Tout d'abord commençons par mes encadrants qui m'ont guidé, fait confiance, suivi dans la douleur avec certaines rédactions à courtes échéances. Donc merci à Patrick Bot pour toutes ces discussions dans le transrade où 30 minutes c'est court pour refaire toute la Physique. Merci à Frédéric Hauville, pour sa disponibilité, pour son aide dans le montage des manips et pour faire des trous dans le bateau.

Merci à Marc Rabaud, car même si Brest est loin de tout et notamment de Paris, il a su m'aider à poser les grandes lignes de ma thèse ainsi que relire et corriger efficacement mon manuscrit.

Merci aussi à mes rapporteurs Pascal Hémon et Marco Belloli d'avoir lu attentivement ma thèse pour ensuite avoir des discussions intéressantes et constructives. Je tenais également à remercier les autres membres de mon jury, Lionel Schouweiler et Bernard Simon d'avoir accepté de juger mon travail. Merci également à Alban Leroyer et Vincent Chapin d'être venus à l'Ecole Navale pour le comité de thèse et d'avoir posé leurs regards critiques sur mes travaux.

J'aimerais aussi remercier Benoît qui est resté quelques semaines de plus dans l'humidité finistérienne pour un passage de flambeau utile avant de partir en Californie. Merci aussi de continuer de m'aider après ton retour parmi nous.

Lorsque l'on fait une thèse expérimentale, il y a toujours des travailleurs de l'ombre, des gens qui sont là pour t'aider, voire préparer toute une partie de l'instru. Et bien sûr, on n'est jamais satisfait et on a toujours besoin de faire des modifs pour il y a 5 minutes. Donc merci à Alain Boulch et Didier Munck pour leur patience, leur investissement et pour leur aide si précieuse.

Merci au reste de l'équipe SCEFER et notamment Jean-Mich' pour faire le Père Noël (on a eu du beau matos!) et Jean-Charles et Raymond pour ces jolies pièces usinées rien que pour nous.

Concernant les essais, j'aimerais aussi remercier le CHSCT, sans qui les essais se seraient passés beaucoup trop facilement...

Merci aussi à tout l'IRENav pour la joie et la bonne humeur ambiante qui y règne. Que ce soit

l'administration, les enseignants-chercheurs, et les doctorants. Ah! Les doctorants... Quelle belle faune! Ce microcosme avec qui refaire le monde est si simple. Merci à vous tous. Et non, je ne vais pas vous lister car je suis sûr d'en oublier.

Mais j'aimerais remercier plus particulièrement Alex' pour avoir été ma co-bureau et avoir pu supporter tous mes goûts musicaux, et surtout ceux du vendredi aprem' (Vive les Spice Girls!). Merci à mon précédent co-bureau PiEl dont la patience n'a d'égale mesure que sa taille (On l'aura jamais fait cet apéro au jardin des Explorateurs au final). Et aussi un merci tout particulier à Christophe, Lamia et Georges. Je n'oublie pas non plus tout le reste de la Voil'ENav crew pas encore cité: Nico (t'es le prochain!) et Matt' pour les discussions si enrichissantes et les quelques repas/apéros fort sympatoches.

Petite pensée à mes amis kiwis: Youssef, Dario, Stephano, David et Alex pour ces 3 beaux mois au pays du long nuage blanc.

Une autre petite pensée beaucoup plus proche pour mes potes d'escalade et de kung-fu avec qui j'ai pu bien me vider l'esprit le soir.

Merci également à Dave d'avoir relu mon anglais si efficacement.

Voilà maintenant le paragraphe pour la famille. Et elle a compté! A Flo et Léna, à mes beaux-parents, et surtout à mes parents qui ont toujours cru en moi quoique je fasse.

Et j'ai gardé les 2 meilleures pour la fin. Merci ma petite chérie Gaëlle, d'avoir accepté que je retourne faire des études à Brest et de m'avoir tout le temps supporté et soutenu. Merci aussi pour cette magnifique fille. Et merci à toi aussi Emilie. Même si tu n'as pas toujours facilité la rédaction de ma thèse cet hiver avec toutes tes otites, je te pardonne car tu m'apportes suffisamment de bonheur tous les jours.

Je dédie cette thèse à ma Mimoune.

Contents

Abbreviations and Notations	v
Introduction	1
1 State of the art	5
1.1 Physics of sailing	6
1.2 Sail design	11
1.3 Apparent Wind	14
1.4 Aerodynamics of sails	16
1.5 Fluid-Structure Interaction	27
1.6 Research in sailing aerodynamics	35
1.7 Conclusions and motivations	43
2 Instrumented sailing yacht	45
2.1 Set up of the experiments	46
2.2 The J/80 class sailing yacht	49
2.3 Flying shape acquisition	51
2.4 Load measurement	64
2.5 Pressure acquisition system on spinnaker	73
2.6 Wind measurement	77
2.7 Boat data acquisition	80
2.8 Acquisition systems	85
2.9 Procedure and Post-processing	87
2.10 Conclusions	88
3 General behaviour of the spinnaker	91

3.1	Flying shapes	92
3.2	Loads on the spinnaker	114
3.3	Evolution of pressures	124
3.4	Conclusions	128
4	Flapping of the luff: an unsteady behaviour of the spinnaker	131
4.1	Observation of measured flapping	132
4.2	Modal analysis on pressure fluctuations	137
4.3	Physical interpretation of flapping and discussions	147
4.4	Conclusions	156
	Conclusion	159
	Appendices	165
A	Photogrammetry measurements, calibration and precision	167
A.1	Photogrammetry principles	167
A.2	Calibration	170
A.3	Precision of photogrammetric measurements	172
B	Calibration of all load sensors	175
C	Quaternions and projection of loads onto boat frame	179
C.1	Main principles of quaternion representation	179
C.2	Conversion of quaternions to other representations	181
C.3	Use of quaternions to represent the load vector onto the boat frame	182
D	Resampling for dynamic studies	185
D.1	Context and reasons for resampling	185
D.2	Study on a simple case	185
E	Résumé étendu en français	191
E.1	Introduction	191
E.2	État de l'art	193
E.3	Voilier instrumenté	200
E.4	Évolution du comportement du spinnaker	205

E.5 Le faseyement du guindant: un comportement instationnaire propre au spinnaker	211
E.6 Conclusion	218
Bibliography	225

Abbreviations and Notations

AoA	°	Angle of Attack
AW		Apparent Wind
AWA	°	Apparent Wind Angle
AWS	m/s	Apparent Wind Speed
BS	kn	Boat Speed
CFD		Computational Fluid Dynamics
COG	°	Course Over Ground
COW	°	Course Over Water
DoF		Degrees of Freedom
DES		Detached Eddy Simulation
DLC		Directionnal Load Cell
FPGA		Field-Programmable Gate Array
FSI		Fluid-Structure Interaction
fps	Hz	frame per second
GPS		Global Positioning System
HTC		Head-Tack-Clew plane
IMU		Inertial Measurement Unit
LES		Large Eddy Simulation
LEV		Leading Edge Vortex
NI Crio		National Instruments Compact Rio
NMEA		National Marine Electronics Association (norm)
NURBS		Non Uniform Rational B-Splines
POD		Proper Orthogonal Decomposition
SOG	kn	Speed Over Ground
SOW	kn	Speed Over Water
TW		True Wind
TWA	°	True Wind Angle
TWS	m/s	True Wind Speed
URANS		Unsteady Reynolds Averaged Navier-Stokes
VPP		Velocity Prediction Program
VSPARS		Visual Sail Position And Rig Shape

$a(t)$		Mode time coefficient (also called expansion coefficient) of POD mode
$B_{i,j}$		Bernstein basis function (also called blending function)
c		Curvilinear abscissa of a section of the sail
$C_{xy}(\tau)$		Normalised inter-correlation function of temporal signals $x(t)$ and $y(t)$
C_Y	$\frac{\rho_f U_0}{E}$	Cauchy number
D	$\frac{\xi_0}{L}$	Displacement number
E	N/m ²	Elastic modulus
F_{aero}	N	Aerodynamic force
f_r	$\frac{f_s \sqrt{S}}{AWS}$	Reduced frequency
f_s	Hz	Pseudo frequency of mode time coefficient
L	$\sqrt{S} = 8 \text{ m}$	Characteristic length of spinnaker
M	$\frac{\rho_f}{\rho_s}$	Mass number
P_i		Control points for Bézier curve
$R_{i,j}$		Control points for rectangular Bézier patch
Re	$\frac{\rho_f U_0 L}{\nu}$	Reynolds number
S	68 m ²	Spinnaker area
T	N	Tension
th	$5.0 \times 10^{-5} \text{ m}$	Average thickness of the spinnaker
$T_{i,j}$		Control points for triangular Bézier patch
U_0	m/s	Characteristic fluid velocity
U_R	$\frac{U_{fluid}}{U_{solid}}$	Reduced velocity
U_{fluid}	m/s	Velocity of the fluid
U_{solid}	m/s	Velocity of the solid
w	m	Normal displacement from plane ($\underline{u}, \underline{v}$)
β_{AW}	°	Apparent wind angle relative to the boat centreline
β_{TW}	°	True wind angle relative to the boat centreline
Δ	kg	Displacement of the boat
ΔC_P	$\frac{P_{leeward} - P_{windward}}{\frac{1}{2} \rho_f AWS^2}$	Differential pressure coefficient
Δp	Pa	Differential pressure
θ	°	Trim angle
$\dot{\theta}$	°/s	Pitching angular velocity
$\underline{\kappa}$	m^{-1}	Curvature tensor
κ_u	m^{-1}	Curvature in u direction
κ_v	m^{-1}	Curvature in v direction
λ	°	Leeway angle
μ	$1.80 \times 10^{-5} \text{ Pas}$	Dynamic viscosity of the fluid
ξ_0	1 m	Characteristic length of displacement during flapping
ρ_f	1.23 kg/m ³	Density of air
ρ_s	kg/m ³	Density of the solid
$\underline{\underline{\sigma}}$	N/m ²	Stress tensor in the fluid
$\varphi(x)$		Spatial mode of POD
φ	°	Heel angle
$\dot{\varphi}$	°/s	Rolling angular velocity
$\underline{\chi}$	N/m	Surface tension tensor
ψ	°	Heading
$\dot{\psi}$	°/s	Yawing angular velocity

$\ ...\ $	L^2 norm
$\langle...\rangle$	time average
$\nabla(...)$	gradient
$\nabla^2(...)$	divergence
$\underline{(...)}$	vector
$\underline{\underline{(...)}}$	tensor
$(\overline{\cdot})$	Dimensionless variables for the structure
(\sim)	Dimensionless variables for the fluid

Introduction

Performances achieved by recent racing yachts demonstrate the massive improvements made in yacht design, materials and fabrication. From experience and empirical evidence, yacht and sail designers now use more and more high technology materials and advanced research and development tools. To achieve competitive racing yachts, detailed studies are conducted with thinner safety margins. Reliability is therefore the key issue. Knowledge of dynamic loadings is now one of the limiting factors to design more powerful and lighter boats.

Offshore racing yachts like IMOCA Open 60, Mini 6.50 class or Class40 race very often in downwind and reaching conditions where maximum boat speeds are reached. Therefore efficient reaching or downwind sails make it possible to rapidly increase a speed differential, leading to a substantial gain over the other competitors. For solo racers, this importance is even more pronounced as they need stable downwind sails that do not need to be permanently trimmed.

While already many research studies have been conducted for upwind navigation, much less is known about downwind sails. The actual dynamic forces on a sailing yacht and full-scale real shapes of downwind sails are barely known.

To assess the overall performance of downwind sails, wind tunnel tests are generally conducted. However due to the non-respect of some rules of similitude, dynamic behaviour of downwind sails cannot be easily analysed with wind tunnel tests. They would need comparison with full-scale experiments.

For upwind sailing conditions, the sails' incidence angle and curvature are low. The wind flow on upwind sails is mostly attached and can be numerically modelled by an inviscid-flow model. For finer results on upwind sails, RANS models are now more and more efficient and therefore being used by sail designers and racing teams during development programmes.

Reaching and downwind sails are more complex to study. The sail shape is a non-developable surface with highly cambered sections. The wind flow is strongly detached. Inviscid-flow models are therefore irrelevant. The flow around a gennaker or spinnaker is hardly correctly modelled with RANS simulations. Large Eddy Simulations (LES) are starting to be used but are very time-consuming. They are thus not common in industrial applications.

Moreover gennakers and spinnakers are thin and very flexible sails. A light membrane with a massive

separation of the turbulent flow causes a strong unsteady fluid-structure interaction system.

Unsteady numerical models are developed for example by the company K-Epsilon -a firm offering numerical aero and hydrodynamics simulations- and Ecole Centrale de Nantes. To analyse the unsteady aerodynamical performance, these numerical tools model the aero-elasticity of the sails and rigging in dynamic sailing situations. A numerical tool, dedicated to upwind sails, called ARAVANTI using an inviscid-flow model is now integrated in a sail design software called SailPack developed by BSG Developments. However for downwind sails, there is still a need for validation of ARA-ISIS, a Fluid-Structure Interaction simulation tool coupling a finite element code ARA with a URANS solver ISIS-CFD.

The French Naval Academy Research Institute (IRENav), with the *Voil'ENav* project has competence in Fluid-Structure Interaction on soft membranes, and in particular on sails. Previous studies, mainly with the PhD project of [Augier, 2012], have made it possible to develop dedicated instrumentation on a sailing yacht in order to measure the unsteady aerodynamic loads, motion of the boat, flying shape of sails and navigation parameters during upwind navigation in regatta conditions. With the *Voil'ENav* project, IRENav has one of the most advanced full-scale instrumented sailing yachts to study unsteady physical phenomena on sails.

The first objective of this PhD is to develop from this instrumented sailing yacht, a full scale experimental setup for downwind navigations. We want to acquire in real conditions the time-resolved shape of the spinnaker, the aerodynamic loads of the sails and rigging, the motion of the yacht and the navigation parameters. This inboard instrumentation system has been improved partly thanks to the SAILING FLUIDS project, a UK-France-NZ collaboration project funded by the European Union's Seventh Programme for research, technological development and demonstration and from the Royal Society of New Zealand. Specific spinnaker load sensors and a dedicated pressure acquisition system developed by the Yacht Research Unit at the University of Auckland have been added. Full-scale experiments are also being jointly conducted at Ecole Navale in the Bay of Brest and at the University of Auckland in the Hauraki Gulf.

The second objective is the acquisition of several in-situ measurements for upwind and downwind navigations. These time-resolved data would enable us to better understand the physical behaviour of sails and to build a database for numerical-experimental comparisons.

The third objective is to acquire and analyse the evolution of the real spinnaker shape while sailing -called *flying shape*- for different downwind navigations in order to compare them with the shape created during the design stage -called *design shape*- and to be capable of giving feedback to sail designers.

The fourth objective is to analyse more precisely any unsteady behaviour of downwind sails and especially the flapping of the luff. It is said the most efficient trim for a spinnaker is on "the verge of luffing", when the leading edge of the sail starts flapping. It is a complex dynamic instability commonly aimed at by sailors but not well understood and never analysed before.

The first chapter introduces the specific sailing terms used in this thesis and the basics of the physics of sailing. Aerodynamics on sails is explained and highlights the complexity of the 3D fluid-mechanical phenomena present on downwind sails. The strongly coupled fluid-structure interaction on downwind sails is also highlighted. Finally the state of the art of experiments in the science of sailing is described.

The second chapter describes the instrumented sailing yacht. After reporting the global inboard instrumentation setup, each acquisition system is set out in detail with a focus on the accuracy and the dynamics of the measurements. The acquisition, the post-processing and the selection of stable runs are described at the end of this chapter.

The third chapter presents the general behaviour of the spinnaker from full-scale measurements. The flying shape of the sail is analysed and new representations of sail shape are introduced like the use of Bézier surface and control points. The evolutions of loads and pressures are described mainly according to the apparent wind. The strong variations of loads and pressures even during stable runs are emphasised.

The last chapter describes in detail a typical dynamic behaviour of downwind sails. From full-scale measurements, the "flapping" phenomenon is analysed with the use of a modal analysis. Finally an interpretation of this phenomenon is proposed.

Contents

1.1 Physics of sailing	6
1.1.1 Sailing terminology	6
1.1.2 Equilibrium of forces on a sailing yacht	8
1.2 Sail design	11
1.2.1 Sail cloth	11
1.2.1.1 Characteristics of sail cloth	11
1.2.1.2 Nylon	11
1.2.1.3 Polyester, Dacron	12
1.2.1.4 "Exotic" fibres	12
1.2.2 Sail manufacturing	12
1.2.2.1 Different designs	12
1.2.2.2 High technology manufacturing	12
1.2.2.3 Design shape	13
1.3 Apparent Wind	14
1.3.1 Wind Triangle	14
1.3.2 Twist	15
1.3.3 Upwash	15
1.4 Aerodynamics of sails	16
1.4.1 Aerodynamics on thin profiles	16
1.4.1.1 Definition of a thin profile	16
1.4.1.2 How is the lift generated?	17
1.4.2 General knowledge of sail aerodynamics	18
1.4.2.1 Typical pressure distribution around a sail for attached flow	18
1.4.2.2 Stability of sails	19
1.4.3 Upwind vs downwind	20
1.4.3.1 Projection of aerodynamic force onto boat frame	20
1.4.3.2 Shape differences	22
1.4.3.3 Detached flow	23

1.4.3.4	Dynamic instabilities	26
1.4.4	Conclusion	26
1.5	Fluid-Structure Interaction	27
1.5.1	Definition of Fluid-Structure Interaction	27
1.5.2	Classify Fluid-Structure Interaction (FSI) problems	28
1.5.2.1	Reduced velocity U_R and Displacement number D	28
1.5.2.2	Cauchy number C_Y and mass number M	29
1.5.2.3	Different types of numerical FSI couplings	30
1.5.3	Our case of study: downwind sails	30
1.5.4	Membrane	32
1.5.5	Summary of fluid-structure interaction of downwind sails	34
1.6	Research in sailing aerodynamics	35
1.6.1	Upwind aerodynamics	36
1.6.2	Downwind aerodynamics	36
1.6.3	Full-scale testing	39
1.6.3.1	Full-scale testing as a complement to wind tunnel testing and numerical computations	39
1.6.3.2	Different types of full-scale experiments	39
	Sailboat dynamometer	39
	Rigging load measurement	40
	Pressure measurement	40
1.6.4	Flying shape acquisition	40
1.6.4.1	Surface shape acquisition	40
1.6.4.2	Sail shape acquisition	41
1.7	Conclusions and motivations	43

1.1 Physics of sailing

During this research project, I focused on the aerodynamic part of the sailing yacht. However a sailing boat is at the interface of two fluids: air and water. Thanks to the sail, the sailing boat collects energy from the wind which is transferred to the hull and hydrodynamic appendices to make the boat move. To comprehend some reasons behind this research project and facilitate some further discussion, the main principles of the physics of sailing is described in this section.

1.1.1 Sailing terminology

In sailing, specific jargon is used and some conversations can be gobbledygook for the non-initiated. Therefore the main vocabulary used in this thesis is presented in figure 1.1.

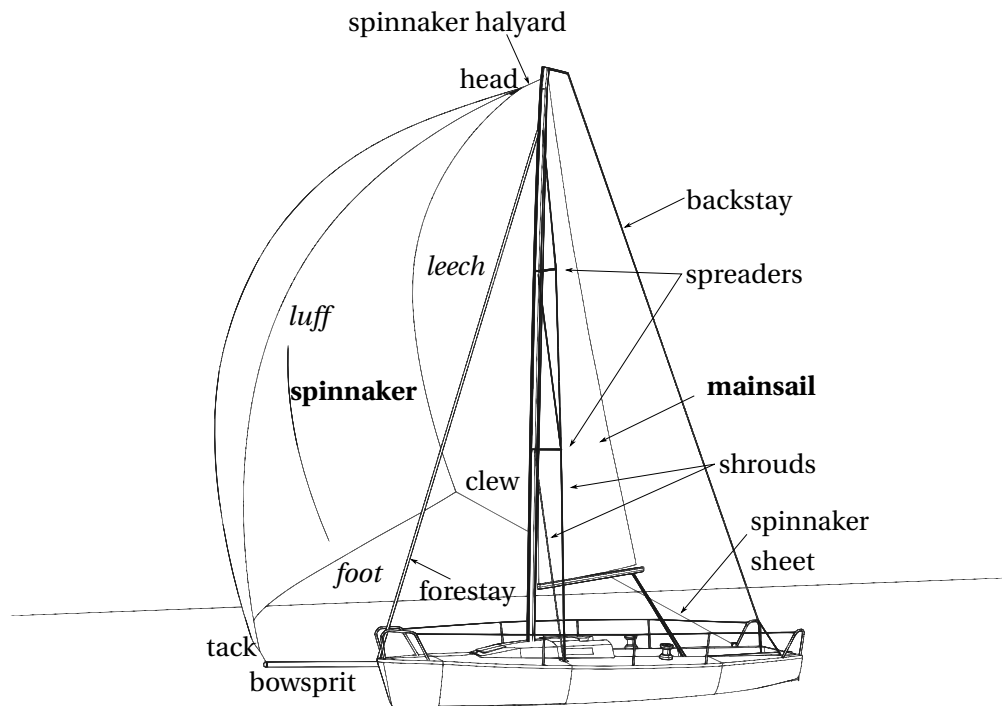


Figure 1.1 – Sail vocabulary used in this thesis with a J/80 sailing on port tack.

The edges of a sail are called *luff* (leading edge), *leech* (trailing edge) and *foot* (bottom). The corners of a sail are the *head*, *tack* and *clew*. At these corners, ropes are knotted to keep the sail hoisted. In general, only the sheet tied at the clew can be easily trimmed to control the shape of the sail. There are many more controls to adjust the sails and in particular the mainsail. For further and well described explanations, the reader is referred to [Chéret, 1997, Bethwaite, 2010].

Specific vocabulary is also set for the relative position of the sailing yacht with the wind. *Starboard* and *port* are respectively the right and the left side of the boat when facing forward (to the bow). A yacht sails on starboard tack when the wind comes over the starboard side of the boat, and respectively a yacht sails on port tack when the wind comes from this side. The side of the boat (and of the sails) on which the wind is blowing is called windward, and the other side leeward. When tacking, the heading of the sailing vessel is changed to the opposite tack by passing the wind through the bow. A gybe (or jibe) is similar but with the wind passing through the stern.

Figure 1.2 is a polar representation of the true wind angle. It illustrates the points of sail describing a sailing boat's orientation in relation to the wind direction. From close hauled to beam reaching, a boat is said to sail upwind. Generally the mainsail and a jib or a genoa are hoisted for those courses. Instead of a jib or genoa, a spinnaker or gennaker is used when sailing downwind¹. Symmetric spinnakers using a spinnaker boom are generally used for running courses. A J/80 class sailing yacht flies an asymmetric spinnaker tacked to a fixed bowsprit. It is important to note that an asymmetric spinnaker has always the same edge of the sail as the luff.

¹In some literature, the term *offwind* is used for running and reaching courses.

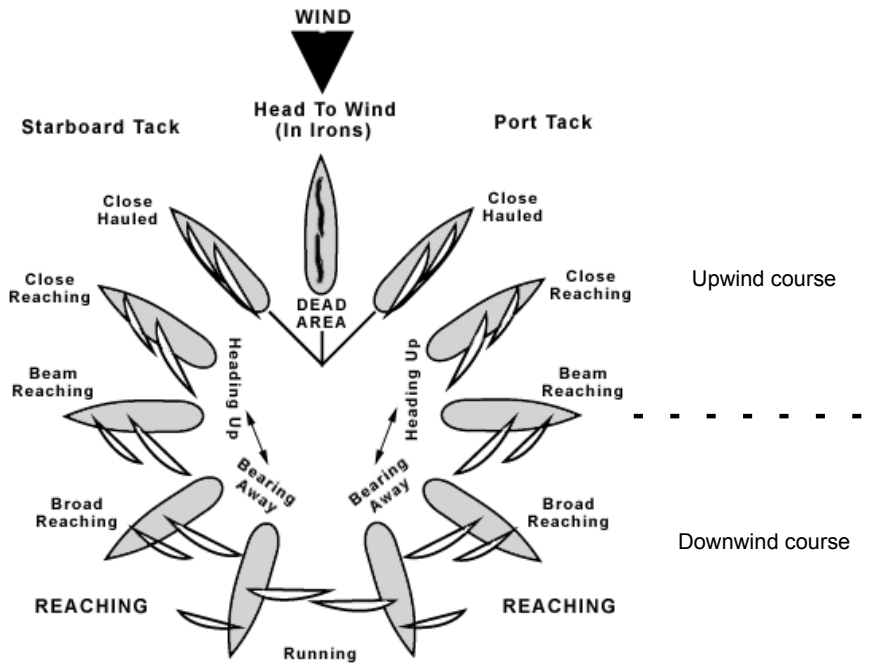


Figure 1.2 – Points of sail depending on the true wind angle. From sites.google.com/site/princetonsailing.

Other specific vocabulary used in this thesis is the attitude of the boat. It is similar to aircraft terminology. However in literature, these terms are not always strictly defined for the same motion. Figure 1.3 defines the terminology used in this thesis. The orthogonal reference frame used in this thesis -unless specified otherwise- has its origin at the aft base of the mast, with the x-axis pointing forward to the bow along the boat centreline, the y-axis positive to port and z-axis positive upwards. As an example, in figure 1.3 the yacht sails on port tack and the spinnaker hoisted creates an aerodynamic load with a negative y-component.

The Euler angles are used to orient the boat. As is common with the Euler angles, to orient correctly the boat in the earth frame, the first angle to be applied is the *heading* angle (around z), then the *trim* angle (around y) and finally the *heel* angle (around x). In this thesis the three terms defining the angular velocities are the *roll* (around x), *pitch* (around y) and *yaw* (around z).

1.1.2 Equilibrium of forces on a sailing yacht

Sails create aerodynamic forces transmitted to the sailboat. But how do these aerodynamic forces give a certain speed to the boat? In other words, what forces are opposed to them and balance the sailboat up to an equilibrium state? This section quickly explains the balance between hydrodynamic and aerodynamic forces. For further details, the reader is referred to several books: [Marchaj, 1962, Garrett, 1987, Larsson et al., 1994, Fossati, 2009].

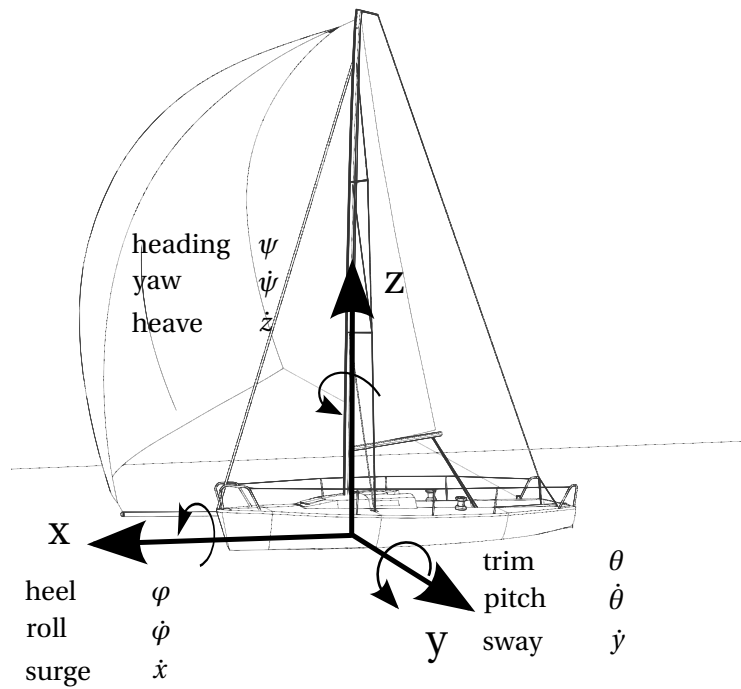


Figure 1.3 – Yacht reference frame and relative yacht motions.

A sailing yacht can be considered as a rigid body in an equilibrium state between the aerodynamic and hydrodynamic forces. A sail produces an aerodynamic force (explained in section 1.4) applied to the aerodynamic centre of effort, which is projected onto the boat frame in propulsive and side forces. According to Newton's law, in a symmetric way, hydrodynamic forces are opposed to them thanks to immersed lifting profiles (the appendages and the hull) producing side and resistance forces. These lifting profiles are mainly the keel, the rudder but also the hull². Since the boat should have the same performance on both tacks, these lifting profiles are symmetric unlike sails. Therefore to create a lifting force, the flow must encounter the symmetrical hydrodynamic profiles with a certain angle of attack: the sailing yacht sails slightly sideways with a certain angle called *leeway* λ ³. In other words, the boat speed vector is not along the boat centreline.

Figure 1.4 illustrates the aerodynamic force F_A applied on the centre of effort CE , balanced by the hydrodynamic force F_T applied on the centre of lateral resistance CLR . If the yacht is well balanced, the aero and hydrodynamic forces are on the same axis without the contribution of the rudder which is here only used to steer the yacht. Note the driving force is opposed to the hydrodynamic resistance which is made up the induced and viscous drag of the hydrodynamic parts and also the wave drag, due to the waves generated by the motion of the boat even on flat sea.

²Daggerboards and foils can also be used on certain racing monohulls with canted keel and multihulls.

³When measuring the Apparent Wind Angle (AWA), it is quite common to neglect the leeway when the aerodynamic part only is addressed as it is done in this thesis. The leeway angle is generally lower than 5° and is in the order of uncertainty of the AWA measurement -the AWA varies mainly between 20° and 160° -. Moreover the leeway angle is usually lower for downwind navigation. Furthermore at full scale, measuring the leeway is not an easy task. Some research has been carried out to better estimate the leeway [Douguet et al., 2013].

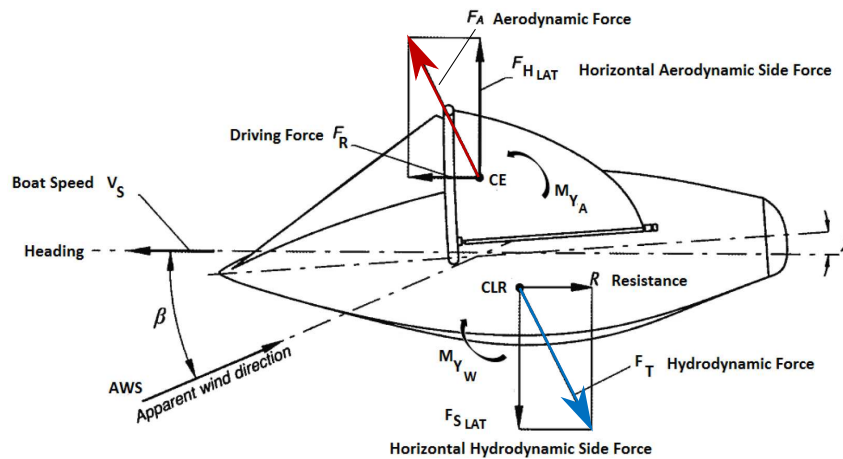


Figure 1.4 – Balance of aerodynamic and hydrodynamic forces in the x-y plane. From [Fossati, 2009].

Figure 1.5 illustrates that the aero and hydrodynamic forces are opposed. Due to their different application points they create a heeling moment restored by the stability of the yacht. When the boat is heeled, the centre of buoyancy is shifted to the leeward side and is no longer vertically aligned with the centre of gravity (circled in green dashed line in figure 1.5). It creates a righting moment which tends to

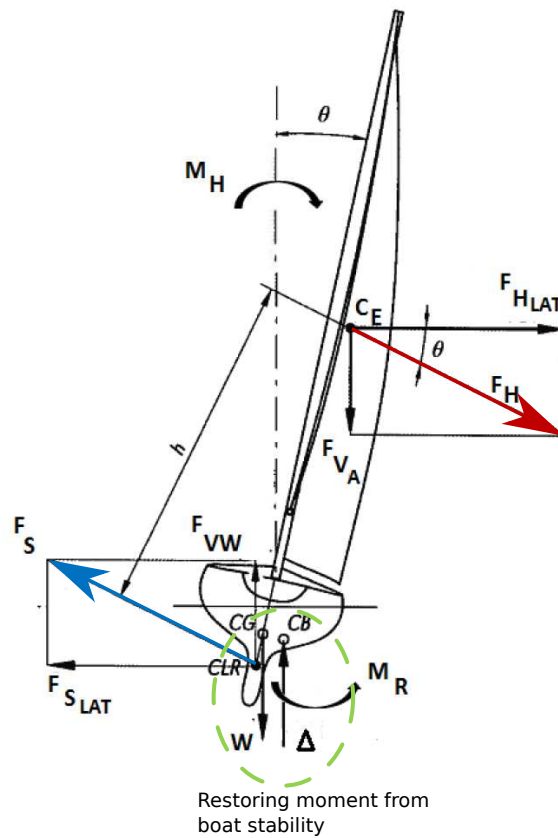


Figure 1.5 – Balance of aerodynamic and hydrodynamic forces in the y-z plane. From [Fossati, 2009].

upright the boat and is opposed to the heeling moment. During the design phase of a racing yacht, this righting moment is often used as the limit for the maximum aerodynamic force permitted, hence the maximum allowable rig height and sail area.

1.2 Sail design

This section briefly describes how a sail is manufactured. It will help the reader to understand what a design shape is and why measuring the flying shape, pressures and loads could improve sail design.

1.2.1 Sail cloth

1.2.1.1 Characteristics of sail cloth

The materials used for sail construction are now almost only synthetic fibres. Many different materials are used with advantages and drawbacks. There are 5 main specificities of sail cloth:

Elastic modulus (stretching)	A high elastic modulus means the sail cloth stretches only a little under stress. Therefore the sail is almost not deformed and can keep its shape.
Tenacity (breaking strength)	A high tensile strength means a high load is required to break sail fibres. Tenacity and stretching are not always correlated.
Weather resistant	Some sail cloth is more sensible to UV radiations or moisture or abrasion that can reduce its life time.
Flex loss	This corresponds to the strength lost due to bending or folding of the sail cloth.
Material cost	

1.2.1.2 Nylon

Nylon is mainly used for downwind sails. In the next section 1.3, we will explain that for downwind course, the Apparent Wind Speed (AWS) is lighter. Therefore to reach the maximum aerodynamic load permitted (often limited by the righting moment of the hull as explained in section 1.1.2), more sail area is required for downwind sails than for upwind sails. Moreover, downwind sails need to be easily hoisted and lowered, and must take little space when stored. Furthermore, downwind sails are often used at various AWA and their shapes should adapt to the flow.

Nylon cloth can easily be folded without damage, to store the sail in a limited space. Moreover its lightweight (hence more sail area is possible), its high tenacity and its good abrasion resistance make this sailcloth a good choice for downwind sails. However its low elastic modulus allows too much stretch to be

suitable for upwind sails. Nylon is also more sensitive to UV and moisture than polyesters. The spinnaker used on the J/80 sailing yacht is made of Nylon.

1.2.1.3 Polyester, Dacron

Polyester is also commonly referred to by the brand name Dacron. Due to its overall good characteristics, this sailcloth is widely used and popular for sails. The mainsail of the J/80 sailing yacht is made of Dacron.

1.2.1.4 "Exotic" fibres

For high-performance racing sails, "exotic" fibres such as aramids (Kevlar) or polyethylenes (Spectra or Dyneema) replace Polyester cloth. Their modulus is higher. However due to their high stiffness, the fibres cannot be woven tightly. A film (most of the time in Mylar) is used to reduce stretch in all directions and protect exotic fibres from abrasion. They are therefore called laminated sailcloth.

1.2.2 Sail manufacturing

1.2.2.1 Different designs

Sails are not developable surfaces. A sail cannot be fully laid down on a planar surface. It has an inherent volume created by the broadseams. Broadseams are curved edges of the panels constituting the sails. When a panel is sewn to another with a different curved edge, the broadseam generates a camber and therefore the association of all the broadseams between panels creates the volume of the sail.

There are different orientations of panels (cf. figure 1.6). The cross-cut design uses only one direction of the panels. The warp of the sailcloth is parallel to the foot. This design has the advantage of being cost-efficient and to better control the foot shape. The tri-radial design is defined by three different orientations radiating from the three corners of the sail (head, tack and clew). This design is more expensive but respects more the stress directions in the sail, therefore a smaller deformation of the sail relative to a cross-cut design. The spinnaker used for the experiments carried out during this PhD project has a tri-radial design.

1.2.2.2 High technology manufacturing

There are two main disadvantages in the conventional designs presented previously. First there is a lack of continuity of fibres from one panel to another, resulting in stress concentrations at seams. Second a precise control of the distribution of the fibres is not possible. This is why some sailmakers have developed complex manufacturing allowing fibre distribution over the whole sail. It results in a weight saving by decreasing the fibre quantity where small stress is present and increasing the fibre quantity at hotspots. The sailmaker *NorthSails* developed the 3DL® and the 3Di® technologies. The different layers of yarns of a laminated sail are laid on a 3D mould, which is an articulating floor controlled by actuators. *Incidence*

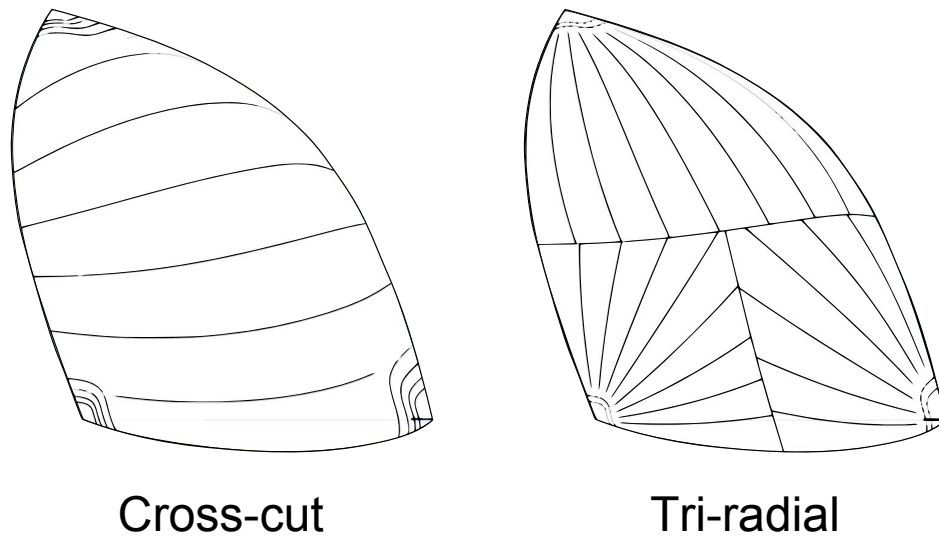


Figure 1.6 – Different sail designs for a J/80 spinnaker.

sail, a French sailmaker, has recently developed another technology called DFi® inspired from the D4 technology. Unlike *NorthSails*, a 3D mould is not used.

These high technology manufacturings create stiff sails with very small deformations and are not used to make spinnakers.

1.2.2.3 Design shape

The first stage, before choosing the correct sail cloth and manufacturing the sail, is the design stage. Using mostly his experience, and nowadays numerical simulations, the sail maker designs the shape with CAD tools. Whether it is to create design shapes for upwind or downwind sails, the sail designer commonly uses sections at different heights of the sail to create a design shape: leech and luff are divided into equidistant segments. Each division of the luff linked to a division at the leech defines a section. At each of these stripes, the sail designer controls aerodynamic parameters such as the cambers at different drafts, the entry and exit angles etc.

However for downwind sails, from an aerodynamic point of view, these stripes are not always contained in a plane parallel to the flow. They can be curved. Unlike upwind sails, spinnakers are far from 2D-extruded shapes but are 3D objects. Even though these geometric sections are widely used, it might not be the most appropriate way to define the 3D geometry of a spinnaker. During this research project, when measuring spinnaker flying shapes, I tried to quantify the geometry of a spinnaker in a different way, more consistent with its real flying shape.

A spinnaker is a highly cambered thin and flexible sail. Moreover the aerodynamics of a spinnaker is complex with a highly detached 3D flow. It produces a complex and strong fluid-structure interaction system where the shape easily varies with an unsteady wind, the trim of the sail and the yacht motion. For one spinnaker, there is one fixed design shape but there are several flying shapes depending on the course sailed, corresponding to different wind speeds and angles.

Nowadays, thanks to advanced numerical tools, one can estimate stress, strain and deformation in sails which is of great help for sail designers. Hence they know where and in which directions yarns should be applied. For upwind sails, the design shape is close to the real flying shape. But this is still not the case for downwind sails where displacements can be in the order of magnitude of the boat length. During this PhD project, I measured the flying shape of a spinnaker in order to be capable of giving feedback to sail designers and also to give data for validation of numerical tools that can be used by sail designers.

1.3 Apparent Wind

Because of a wide range of downwind courses (from beam reaching to running course), a wide range of wind angles and wind speeds can be experienced by the spinnaker, which modifies its shape and its aerodynamic loads. Moreover the wind is not the same along the span of the sail. These specificities are described in this section.

1.3.1 Wind Triangle

The flow seen by the sails is not exactly the wind as it could be measured at a fixed weather station for example. The yacht's velocity creates a wind, like the wind we can feel while cycling. The *apparent wind* encountered by the sails is the vectorial combination of both winds:

$$\vec{AW} = \vec{TW} - \vec{BS} \quad (1.1)$$

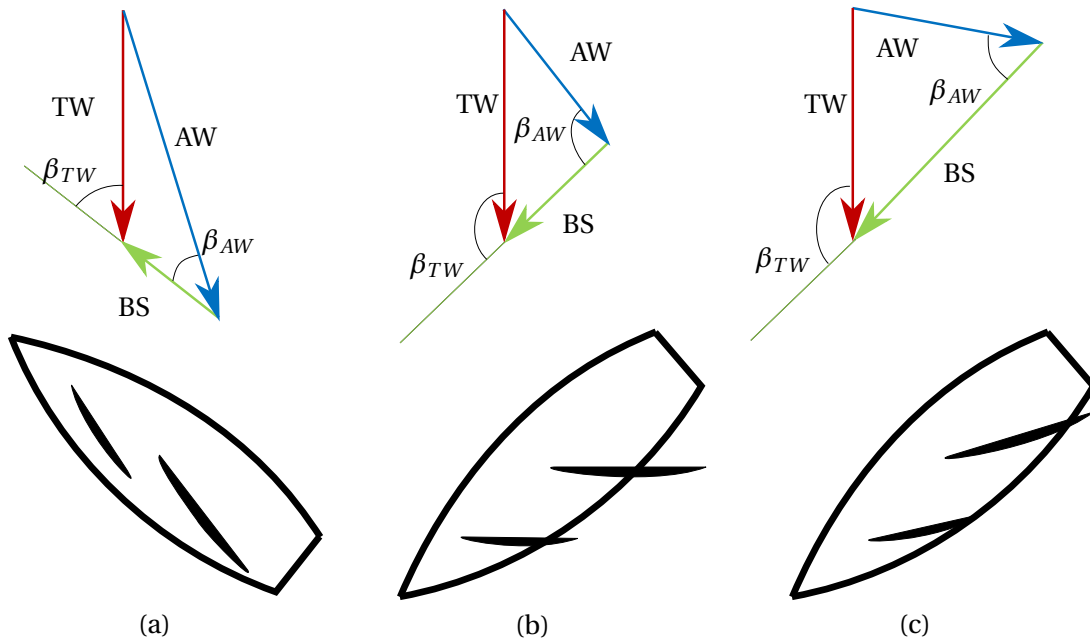


Figure 1.7 – Wind triangles in different configurations. (a) upwind course (b) reaching course (c) reaching course, fast boat. TW: True wind. AW: Apparent wind seen by sails. BS: Boat Speed.

Figure 1.7 shows different *wind triangles* according to different courses of the boat. In Figure 1.7-(a) the wind triangle for a yacht sailing upwind is represented. She goes "against" the true wind (TW). For this case the apparent wind is stronger and has a smaller angle relative to the boat centreline β_{AW} than the true wind. For case (b) and (c), the yachts sail at the same reaching course (same true wind angle) but at different speeds. For case (b), with a smaller Boat Speed, the apparent wind comes more from the aft. For Figure 1.7-(c) compared with (b), the yacht sails faster. The apparent wind is stronger and tighter than for case (b). In conclusion the sailing yacht makes its own wind which can create larger aerodynamic force thus going faster. Fast yachts like catamarans at the America's cup in 2013 have the "BS" vector preponderant to the "TW" vector. Therefore no matter where the wind comes from, the apparent wind angle is always tight and the speed high.

1.3.2 Twist

The wind encountered by a sail is not constant along its span, because the sailing boat is located in the *atmospheric boundary layer* which is about 1 km thick, and most of the variations happen in the first 100 m. Like any flow at an interface, a kinematic condition (see equation 1.7) is applied. Therefore a gradient of velocity exists. Moreover this interaction is not only mechanical but also thermal. Heat transfer between the lower and upper part of the boundary layer can exist and can create a variation of direction too. In the first 100 m where sailing yachts operate, the change in the average direction of the wind is generally ignored. And in absence of thermal process, the average wind speed profile can be described by a logarithmic profile [Hémon, 2006]:

$$U_{TW}(z) = U_{ref} k_t(z_0) \ln\left(\frac{z}{z_0}\right) \quad (1.2)$$

where z_0 is the surface roughness length, k_t the roughness coefficient depending on the variety of the terrain giving a certain roughness. On flat sea, the parameters are $z_0 = 0.005\text{ m}$ and $\kappa_t = 0.16$. The referential speed U_{ref} is generally the wind at 10 m height.

Due to the difference of true wind speed at different heights but the same boat speed, the apparent wind is twisted (cf. figure 1.8). This is the reason why sails, like the wings of a wind turbine, are designed with a twist in order to get a more uniform angle of attack along the height.

1.3.3 Upwash

The apparent wind measured at the top of the mast is also perturbed by the upwash effect of the sail. The sail acts like an airfoil and bends the incoming flow towards the leeward side. This effect is also present at the top of the sail and perturbs the wind above the mast where the anemometer measuring the apparent wind is placed. A measurement of the upwash is presented in the next chapter in subsection 2.6.2. The wind can be accelerated at the top of the mast by 15-20% and is deviated by the spinnaker by an angle of around 15° towards the aft. According to my knowledge, no results have been published on the upwash effect on the wind measurement at the top of the mast.

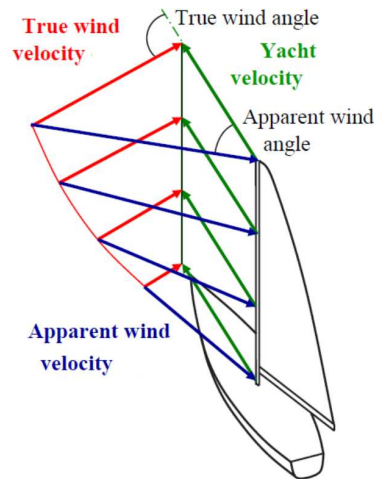


Figure 1.8 – Vertical speed gradient and twist of apparent wind for a sailing yacht. From [Hansen, 2006].

1.4 Aerodynamics of sails

The flow around a spinnaker causes complex fluid mechanics phenomena. Before explaining that the aerodynamics of spinnakers and gennakers are still not fully understood, I first explain how sails generate an aerodynamic force and highlight the difference between the aerodynamics of upwind sails -where the aerodynamics is better understood- and downwind sails.

1.4.1 Aerodynamics on thin profiles

1.4.1.1 Definition of a thin profile

A sail is a lifting body such as a foil or a wing, however it is considered as a thin profile. Unlike a wing, it has a negligible thickness compared to the other dimensions and also a higher camber and a higher angle of attack (AoA with respect to the Apparent Wind (AW) in figure 1.9). Figure 1.9 describes the terminology used to define a thin 2D profile which can represent a horizontal section of the sail. To design a sail, a sailmaker uses these parameters at different sections along the span of the sail. *Chord* is the segment from the leading edge to the trailing edge. *Camber* is the depth between the chord and the profile. *Maximum draft* is the position of the maximum camber along the sail, often expressed as a ratio of the chord. *Entry and exit angles* are the angles between the chord and the tangent lines drawn from the leading and trailing edges respectively. In sailing, it is also important to know the evolution of the angle of attack along the span. The *twist* is defined as the angle between the chord of the section and the chord of the foot (bottom of the sail) as a reference. The angle between the yacht and the sail is referred to as the *sheeting angle*.

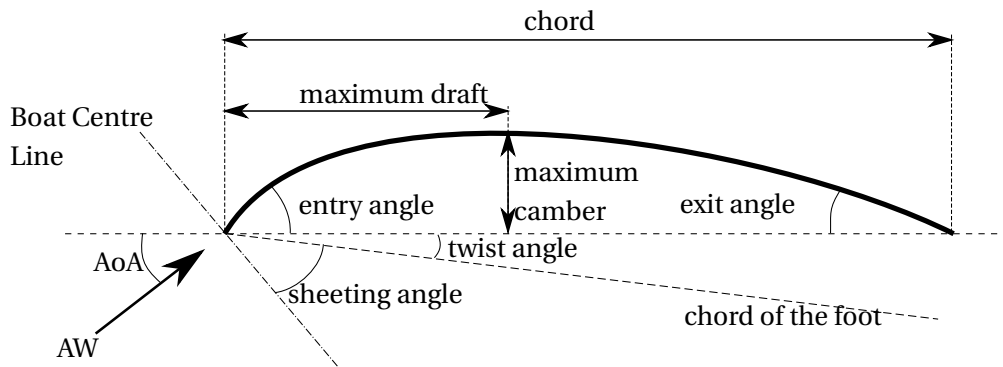


Figure 1.9 – Terminology for a 2D thin profile.

1.4.1.2 How is the lift generated?

A force is generated giving lift thanks to the difference of pressure between the suction side (convex side) and the pressure side (concave side). The profile deflects the flow and accelerates it at the suction (convex) side. The Bernoulli equation explains why the pressure is inversely proportional to the square of the velocity. Therefore a higher velocity means a lower pressure giving a suction, "aspirating" the profile resulting in a lift force. It is common to represent the pressure distribution around a thin profile non-dimensionalised by the dynamic pressure:

$$C_P = \frac{P - P_{ref}}{\frac{1}{2}\rho V^2} \quad (1.3)$$

Therefore a C_P representing a lifting force is negative. This is why it is common practice to display pressure distribution along the chord on the vertical axis, with the negative direction upwards (cf. figure 1.11). In this thesis, pressures on a sail are measured by measuring the difference of pressure between the suction side (leeward side in sailing terminology) and the pressure side (windward side in sailing terminology). The differential pressure coefficient ΔC_P is defined as follows:

$$\Delta C_P = \frac{P_{leeward} - P_{windward}}{\frac{1}{2}\rho AWS^2} \quad (1.4)$$

In the equation 1.4 instead of V , the Apparent Wind Speed (AWS) is used as the flow velocity seen by the sail. The definition of the AWS is described in greater detail in the section 1.3.

The aerodynamic force created by the pressure difference on the whole surface:

$$\underline{F}_{aero} = \int_A -(P \underline{n}) dA \quad (1.5)$$

The projection of \underline{F}_{aero} on the direction orthogonal to the free stream direction is the *Lift force*, and the direction parallel is the *Drag force*⁴. (cf. figure 1.10) Any force can be formulated dimensionlessly:

⁴Also called pressure drag, to differentiate from the friction drag often smaller at large Reynolds number. The total drag is the sum of those two forces.

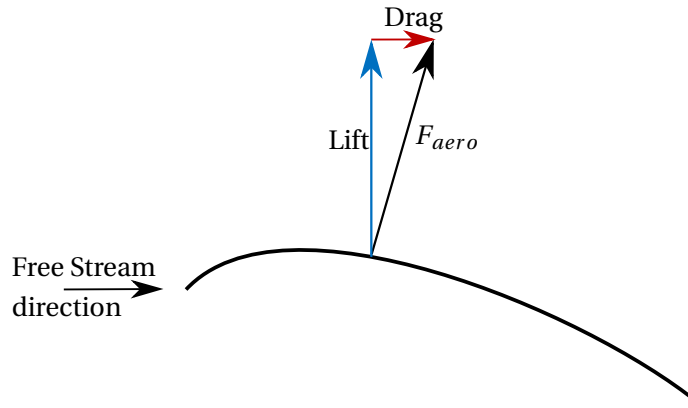


Figure 1.10 – Definition of lift and drag forces as components of the total aerodynamic force.

$$C_F = \frac{F}{\frac{1}{2} \rho S V^2} \quad (1.6)$$

with S the surface area of the profile on where the force is applied. In this thesis, S will often be the spinnaker area -and not the projected section- and V the Apparent Wind Speed (AWS) as measured at the top of the mast.

C_L and C_D are respectively the Lift coefficient and the Drag coefficient.

1.4.2 General knowledge of sail aerodynamics

In this section, the general knowledge of sail aerodynamics is explained based on attached flow around sails -thus more specifically on upwind sails- which is well known. Finally aerodynamics of downwind sails is compared with aerodynamics of upwind sails to highlight the complexity of the fluid mechanics phenomena in action.

1.4.2.1 Typical pressure distribution around a sail for attached flow

The pressure distribution along a sail is commonly divided into three parts (cf. figure 1.11). At the luff (leading edge), a peak of suction at about $C_P = -2$ occurs due to a bulb of recirculation in about the first 10% of the chord. This bulb appears when the Angle of Attack (AoA) is strictly positive (the flow is not tangent to the leading edge). Due to this vortex, the flow reattaches the sail and the absolute pressure coefficient at the suction side is reduced. In the second part, from 10% to 80% of the chord, another peak of suction is spotted due to the sail curvature. Near the trailing edge, the flow is detached from the sail and thus the absolute pressure distribution drops.

In section 1.4.3, the difference of flow and pressure distribution between upwind and downwind sails are explained.

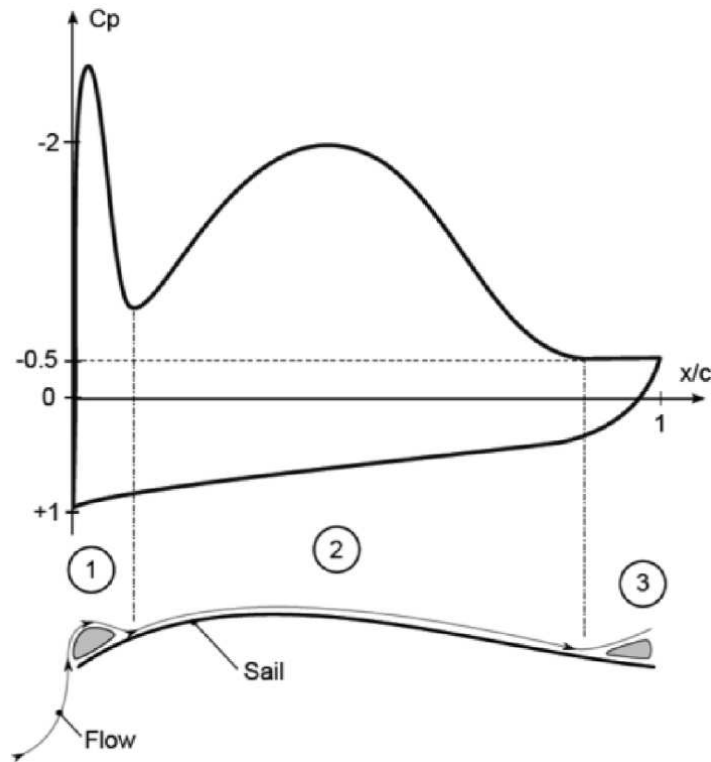


Figure 1.11 – Theoretical pressure distribution for a horizontal section of a sail along the chord. From [Viola and Flay, 2010].

1.4.2.2 Stability of sails

Sails are flexible thin profiles. The pressure modifies the shape which deflects the flow. Unlike thin undeformable profiles, the leading edge can collapse. This instability of the leading edge was first tackled by [Thwaites, 1961] and several others. [Newman, 1987] made a synthesis of these different results. Theoretically and experimentally the luff collapses at a certain ratio between the tension at the leading edge and the ratio between the angle of attack and the camber, due to static and dynamic instabilities:

$$\frac{\partial C_T}{\partial (\alpha \epsilon^{-1/2})} = 0.983$$

with C_T the tension coefficient at the leading edge, α the angle of attack, and $\epsilon = (l - c)/l$ where l is the length of the profile and c its chord length. The potential flow assumptions might be violated and therefore the experimental results usually do not correctly fit with these theoretical values.

Unlike upwind sails, downwind sails are not attached to the forestay on the whole luff, but only at the three corners of the sail: head, tack and clew. Thus this instability is even more pronounced and can be seen as the flapping of the luff. Furthermore, according to sailors, the optimum trim for spinnakers is when this instability is met, "on the verge of luffing". This subject is tackled in this thesis.

1.4.3 Upwind vs downwind

During this research project, an asymmetric spinnaker of a J/80 class sailing yacht was used for measurements. Previous subsections mostly described the theory based on potential flow or characteristics valid for upwind sails. Flow around downwind sails like a spinnaker is partly detached, hence more complex. This subsection defines the main differences from the fluid-mechanical point of view.

1.4.3.1 Projection of aerodynamic force onto boat frame

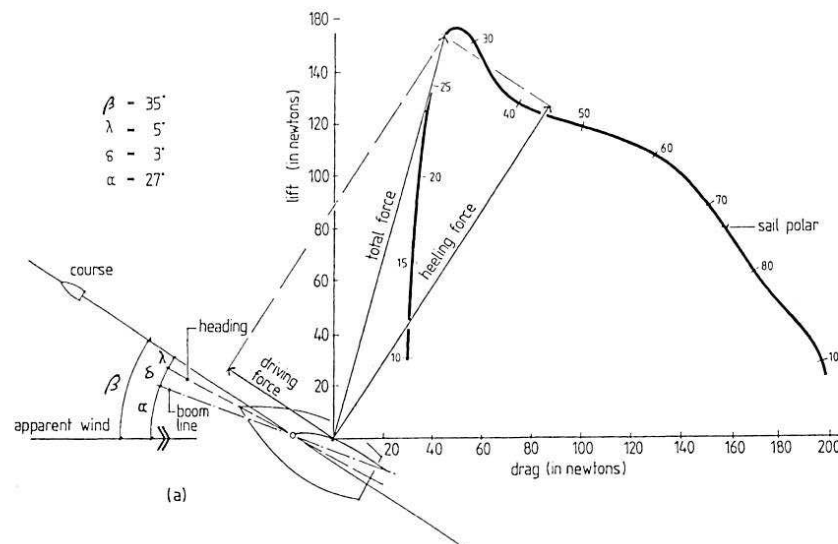
From a sailing point of view, the breakdown of the aerodynamic force of a sail as lift and drag components is not always the most appropriate. It is often more relevant to project the aerodynamic force onto the boat frame, the driving force (along the boat centreline) which needs to be maximised and the side force (perpendicular to the driving force) which needs to be minimised. Using these two latter forces, one can better quantify the performance of the sail.

To illustrate this, [Garrett, 1987] used a "polar diagram" representation with the drag in the horizontal axis, and the lift in the vertical axis. This polar diagram is placed at the centre of effort of the sail, and the projection along the course of the yacht is also drawn (cf. figure 1.12). Figures on the polar curve show the corresponding angle of attack of the profile to obtain this force.

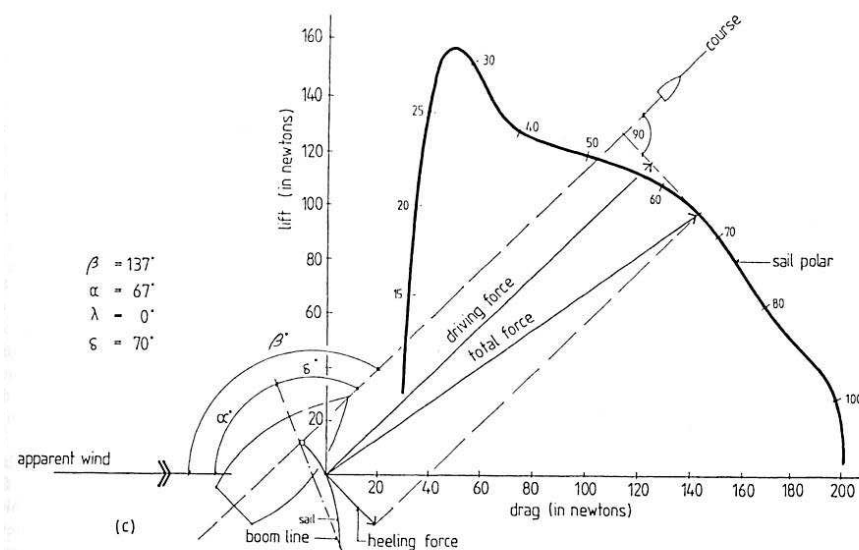
For upwind navigation, in the example of Figure 1.12a, the best driving force is obtained at an angle of attack of about 26° . The total force vector also represents the tangent to the curve from the origin. This point corresponds to the maximum value of lift-to-drag ratio. When sailing upwind, the heeling force is about three times higher than the driving force.

For downwind navigation, Figure 1.12b indicates that the lift-to-drag ratio is no longer relevant to reach the best performance. The optimum operating point is determined at an angle of attack of 67° . When sailing downwind, the heeling force is almost negligible and most of the total sail force goes into driving the boat forward. The drag component is comparable to the lift component.

The main difference between upwind and downwind navigation is the importance of the lift-to-drag ratio. For upwind sails, like in aeronautics, one seeks sails capable of producing high lift with little drag, whereas for downwind sails, one seeks sails operating in large angles of incidence, with high cambers to get high lift and drag forces. Downwind sails operate therefore in a more or less stalled condition. A separation of the flow on the leeward side occurs because the air flow has insufficient energy to overcome the adverse pressure gradient. A turbulent wake reduces the lift force but also increases the drag force. Moreover, downwind sails operate in a larger range of AWA than upwind sails. They can be used for example for beam reaching courses ($AWA \approx 90^\circ$), where the optimum operating point can still be the highest lift possible for certain boats. But unlike upwind navigation, the total force has a much greater driving force component than the heeling force. Since spinnakers can be used for a wide range of AWA, various types of flow are encountered. Furthermore flying shapes change accordingly. During this PhD project, pressure distributions, loads and flying shapes of the spinnaker were analysed according to the AWA.



(a) Boat sailing upwind.



(b) Boat sailing downwind.

Figure 1.12 – Polar diagram breaking down total aerodynamic force as drag and lift components as a function of the angle of attack (figures on sail polar), and also as driving and heeling force for upwind and downwind courses. From [Garrett, 1987].

1.4.3.2 Shape differences



(a) J/80s sailing upwind during the GPEN 2015. Credit Pierrick Contin.



(b) J/80s sailing downwind during the GPEN.

Figure 1.13 – J/80 sailing yachts sailing upwind with jibs, and downwind with asymmetric spinnakers during the *Grand Prix Ecole Navale*.

Figure 1.13 shows J/80 boats sailing upwind (cf. figure 1.13a) and downwind (cf. figure 1.13b) during a regatta. One can notice the difference of shape between a jib and a spinnaker. On one hand, a jib is mainly a 2D section extruded with a progressive reduced chord length going upwards. On the other hand, a spinnaker has a more complex 3 dimensional shape that can change during sailing. The luff is longer than the leech, and the horizontal sections more curved. The difference of shape highlights the difference of flow around the sail, therefore the pressure distribution and the aerodynamic load generated by the sail. The main differences of shape between upwind and downwind sails are:

Lower aspect ratio For spinnakers, the aspect ratio defined as the ratio of the mean chord to the span is lower than for upwind sails. [Fossati, 2009] presents polar curves⁵ for different aspect ratios (cf. figure 1.14). In this figure and in Figure 1.15, the lift coefficient is named C_P and the drag coefficient C_R . According to the description made in subsection 1.4.3.1 showing that a good lift-to-drag ratio is no longer necessary but rather a large aerodynamic force, we can conclude that a lower aspect ratio (like the spinnaker) gives better performance for downwind course.

More camber According to Figure 1.15 from [Fossati, 2009], for downwind sails, more camber (described in section 1.4.1.1) makes it possible to reach higher aerodynamic force producing higher driving force.

More twist Downwind sails have also more twist. If we scan the sections along the span of the sail, the angle between the boat centreline and the chord increases at a higher rate for downwind sails than for upwind sails. For downwind course, the Apparent Wind Angle (AWA) is more sensitive to the apparent wind gradient giving a twist to the wind. [Richards, 1997] has highlighted the importance of taking into account the twist for downwind sails. To illustrate this, Figure 1.16 shows the twist of

⁵These figures are also found in [Marchaj, 1962], and also found in one of the first books on yacht aerodynamics [Curry, 1928].

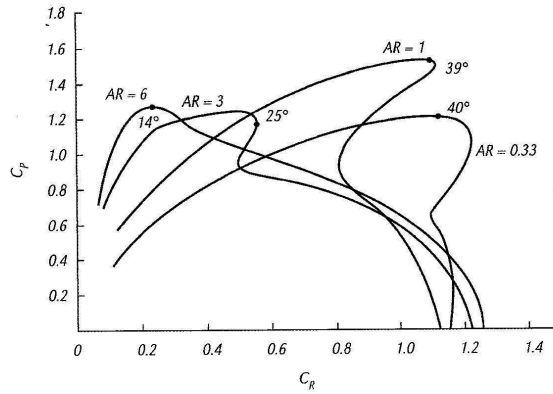


Figure 1.14 – Polar diagrams of three cambered plates with the same camber but different aspect ratios. From [Fossati, 2009].

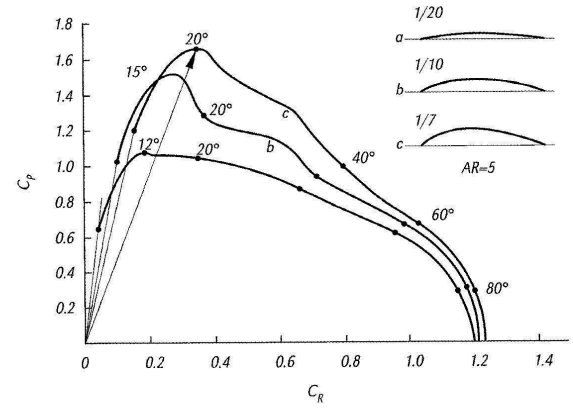


Figure 1.15 – Polar diagrams of three cambered plates with the same aspect ratio but different cambers. From [Fossati, 2009].

the apparent wind angle -in horizontal axis- according to the height -in vertical axis- for a J/80 class sailing boat. For the true wind, a logarithmic vertical wind profile is imposed using equation 1.2, with a roughness length of 0.2 mm described in [Flay, 1996], which is "*for flows over the sea in racing conditions*". The wind speed measured at the top of the mast is used as a reference. Thus from equation 1.2, we obtain:

$$U_{TW}(z) = U(H_0) \frac{\ln\left(\frac{z}{z_0}\right)}{\ln\left(\frac{H_0}{z_0}\right)}$$

where H_0 is the distance of the anemometer from the surface ($H_0 = 12 \text{ m} \cos(\text{heel})$).

Figure 1.16 shows that whereas the maximum twist found at the top of the mast is only 5° for this upwind course, for downwind course the maximum twist reaches 45°. Hence the upstream flow direction varies along the height, which produces a complex flow around the spinnaker.

1.4.3.3 Detached flow

Due to the highly 3D shape of a spinnaker, the flow is also 3 dimensional and can be strongly detached with vortex sheddings. [Viola et al., 2014] modelled with a Detached Eddy Simulation a rigid asymmetric spinnaker with a fixed flying shape as measured in a Wind Tunnel. Figure 1.17a extracted from this article schematically describes the pressure distribution expected around the spinnaker. It is close to what has been presented in figure 1.11. However the trailing edge separation appears more upstream, at 60% of the chord.

Figure 1.17b indicates that the flow separates on the suction side along all the leading edge and reattaches further downstream. Then the flow on the sail is deflected upwards. The flow remains attached until the trailing edge separation in the second half of the chord. The trailing edge separation starts sooner near the foot of the sail. Figure 1.17c presents the second invariant of the velocity gradient, Q , "*which is a measure of the difference between the rotation rate and the shear rate of the flow*". A tip vortex from the head of the spinnaker can be noticed and rolls with the tip vortex of the mainsail's head. At the spinnaker's

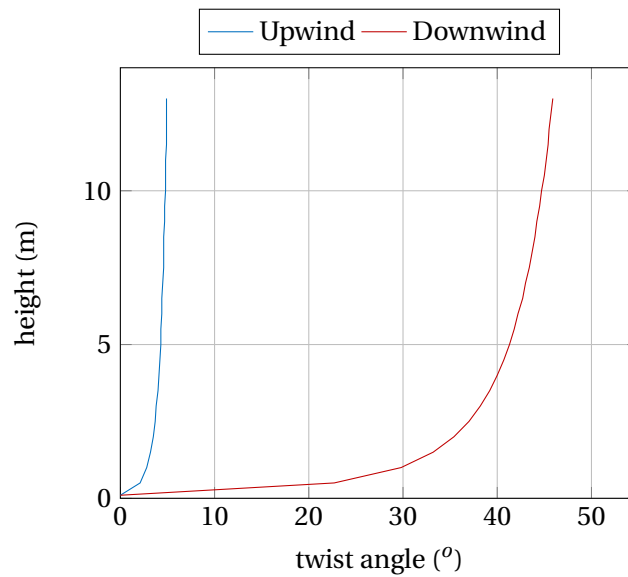
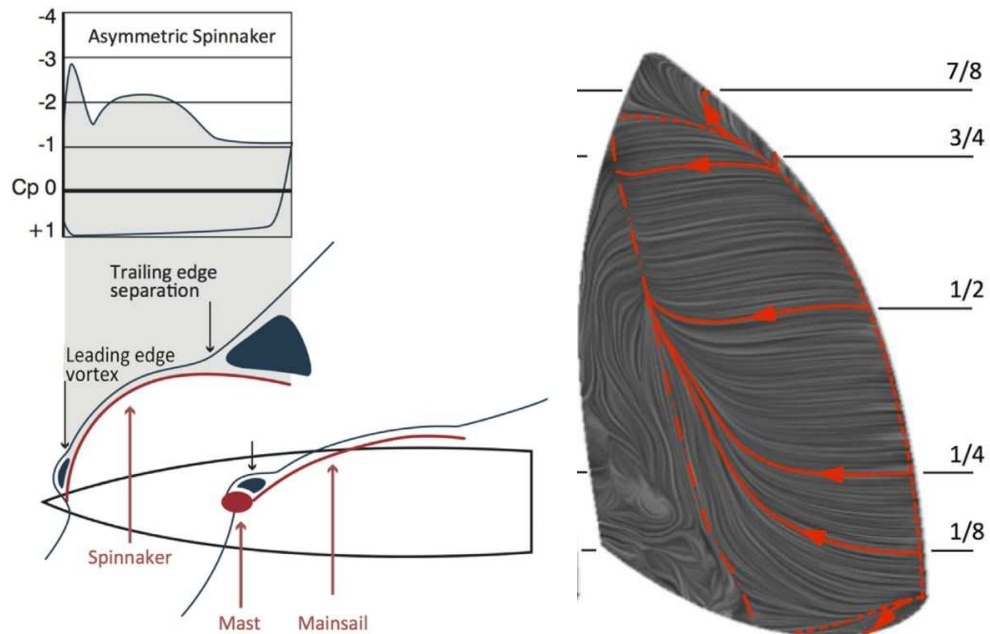


Figure 1.16 – Theoretical evolution of the twist angle of the apparent wind encountered by the spinnaker depending on the height above water using measured data on the instrumented J/80. Conditions TWS=15 kn at the height of the anemometer. For upwind: True Wind Angle (TWA)=40°, AWA=30°, heel angle=25°, Boat Speed (BS)=2.5 m/s. For downwind: TWA=150°, AWA=120°, heel angle=0°, BS=4 m/s. These data are averaged data from experiments.

foot, there are "*chordwise-stretched vortices convected downstream intermittently*". Mid-span intermittent vortices also appear at a lower frequency.

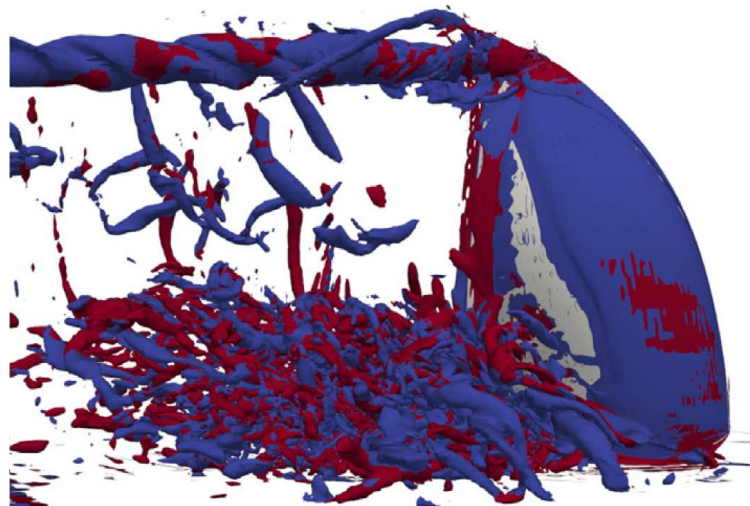
At the leading edge, according to [Viola et al., 2014]: "*the leading edge separation and reattachment form a coherent and steady leading edge vortex, which increases in diameter from the foot to the head, where it becomes the tip vortex and convects downstream in the direction of the far field velocity*". This Leading-Edge Vortex (LEV) is also commonly found in insects' and birds' flights during the downstroke of a flapping of wing [Van den Berg and Ellington, 1997, Birch and Dickinson, 2001], and during gliding of birds [Videler, 2004] which is similar to LEV found on Delta Wings [Polhamus, 1966]. However the LEV during flapping of wings is found for low Reynolds number (maximum around 10^3) and is found stable due to a spiral vortex in the span direction. At a higher Reynolds number, this LEV is less stable. For gliding and delta wings, typical Reynolds numbers are more in the order of magnitude of those for downwind sails. Nevertheless this LEV could be also assimilated to a tip vortex. Knowing that the simulation run by [Viola et al., 2014] was without any twisted wind and on a rigid sail, it is debatable whether this LEV is really present and stable at the leading edge of a full-scaled spinnaker on water. During this PhD project, pressures are measured on the sail to analyse the flow structure.

Anyhow, [Viola et al., 2014] showed the flow around a spinnaker is highly 3 dimensional and complex with many possible vortices. Therefore assuming a spinnaker sail as an extruded 2D section would be a rough approximation.



(a) Typical flow and pressure distributions in down-wind conditions.

(b) Flow field on the leeward side of the spinnaker with 32M-cell grid DES. Red lines show the time-averaged flow, red dashed-dotted lines show time-averaged separation line, and red dotted lines, reattachment lines.



(c) Iso-surfaces of Q-criterion $500s^{-2}$ coloured by helicity computed by DES with 32M-cell grid. Red means positive helicity and blue, negative.

Figure 1.17 – Results from [Viola et al., 2014] of a numerical simulation using Detached Eddy Simulation on a shape of an asymmetric spinnaker measured in a wind tunnel.

1.4.3.4 Dynamic instabilities

A spinnaker is only held at its three corners: head, tack and clew. The flying shape is set as an equilibrium between the pressure due to the wind and the tension in the sail. Therefore a small change of wind strength or direction, or a small change of trim highly affects the shape of the sail. Due to a strong coupling between the highly detached flow and the thin and flexible sail, dynamic instabilities can occur.

Unlike the jib, the luff is not maintained on the forestay and therefore it is more likely to fold. For sailors, it is commonly admitted that the best trim for a spinnaker is "on the verge of luffing". This means the spinnaker sheet is eased until the leading edge of the sail flaps a bit (cf. figure 1.18). The trimmer does not want to see a strong collapse of the luff but just a slight self-maintained flapping. In this thesis, I will tackle this dynamic behaviour of the spinnaker.

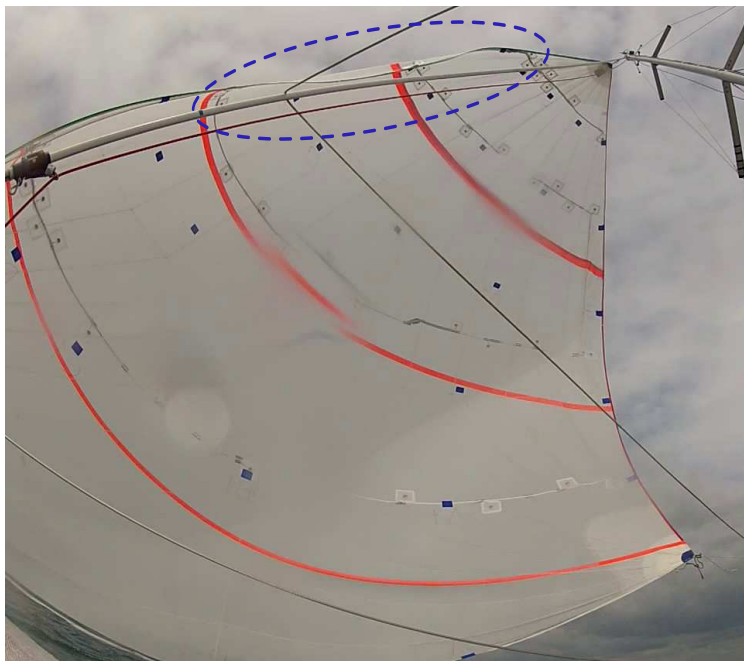


Figure 1.18 – Spinnaker at the optimum trim, slightly flapping at the luff -in the dashed blue ellipse-. View from the fore deck looking up towards the starboard side.

1.4.4 Conclusion

As a first approximation, a sail can be considered as a thin profile which already has a complex 2D flow (leading edge separation, trailing edge separation). However the flow around sails and especially downwind sails is a complex 3D flow: twisted apparent wind, and turbulent upstream flow, different vortices created, highly cambered profile. The shape is strongly affected by the aerodynamic pressure. Therefore measuring accurately the *flying shape*, loads and pressures of the spinnaker would allow us to better assess the fluid-mechanical phenomena present on a downwind sail.

1.5 Fluid-Structure Interaction

Not only is the flow around a spinnaker complex, but also an intricate and yet very interesting Fluid-Structure Interaction (FSI) problem is involved. This section briefly explains what Fluid-Structure Interaction (FSI) is and how different problems can be sorted out, before describing the spinnaker case.

1.5.1 Definition of Fluid-Structure Interaction

The interaction between a fluid and a structure happens when a fluid (liquid or gas) whether in movement or not encounters any deformable solid. The fluid can be inside the structure or outside. The fluid acts on the solid and vice versa (cf. figure 1.19). FSI problems are present in many fields. The first to cite should be the sadly famous Tacoma Narrows Bridge failure which highlights the importance of FSI problems [Billah, 1991, Green and Unruh, 2006]. But one can also find FSI problems in sound emitted by electric wire under strong wind, in ship manoeuvrability [Bertram, 2012], flexible hydrofoils [Lelong and Astolfi, 2015, Astolfi et al., 2015, Chae, 2015, Yan et al., 2015] or airfoils for wind turbine for example [Rafiee et al., 2016] and also in architecture with wind loading [Michalski et al., 2011, Belloli et al., 2014]. Famous physical problems have been investigated such as the flapping of the flag [Souilliez et al., 2006, Sawada and Hisada, 2007, Virost et al., 2013] or the instability of tubular cantilever conveying fluids (such as a garden hose) [Gregory and Paidoussis, 1966]. FSI field is also used in biomimetics such as insect or bird flight simulations [Song et al., 2008, Tregidgo et al., 2013, Nguyen et al., 2016] or aquatic animals propulsion reproduced with thin oscillating foils [Floch et al., 2012]. FSI simulations are also often used in biomedicine to simulate blood flow for example [Moireau et al., 2012]. There are many other application fields, anywhere a fluid is in interaction with a structure.

Studying the Fluid-Structure Interaction (FSI) makes it possible to determine for example loads on a solid, and therefore its structural integrity or its deformation. It is also often used to analyse possible unstable behaviours due to the coupling of the fluid and the structure resulting in large oscillations and therefore possible failure.

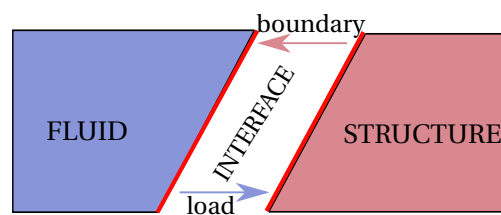


Figure 1.19 – Relation between the fluid and the structure in a Fluid-Structure Interaction (FSI) problem. Inspired from the MOOC *Fundamentals of Fluid-Solid Interactions* of LadHyX (www.coursera.org/course/fsi).

Both fluid and structure mechanics are branches of continuum mechanics. However they behave differently and therefore are modelled differently. While the solid behaviour is mainly driven by the displacement ξ , the fluid behaviour is mostly driven by the velocity ($\underline{U} = \frac{\partial \xi}{\partial t}$). For numerical models, this means that most of the time two different models are developed, one for the structure and another for the fluid. The algorithm coupling both models is therefore challenging and mostly defines the robustness of the numerical simulation.

1.5.2 Classify Fluid-Structure Interaction (FSI) problems

Non-dimensional parameters are necessary to characterise the importance of the different FSI effects as explained in [de Langre, 2002]. They are built with:

- the size of the FSI problem (generally the size of the structure): L
- the typical velocity of the fluid: U_0
- the dynamic viscosity of the fluid: μ
- the typical displacement of the solid: ξ_0
- the stiffness of the solid: E
- the density of the fluid: ρ_f and of the solid: ρ_s

At the interface, a *kinematic condition* relates the speed of the fluid to the velocity of the structure, and a *dynamic condition* describing the stress continuity:

$$U_R \tilde{U}(\tilde{x}) = D \frac{\partial \tilde{\xi}}{\partial \tilde{t}} \left(\tilde{X}, \tilde{t} \right) \quad \text{kinematic condition} \quad (1.7)$$

$$C_Y \left[-\tilde{p}(\tilde{x}) \underline{\underline{1}} + \frac{1}{Re} \left(\nabla^T \tilde{U}(\tilde{x}) + \nabla \tilde{U}(\tilde{x}) \right) \right] \cdot \underline{\underline{n}}(\tilde{x}) = \underline{\underline{\sigma}} \cdot \underline{\underline{n}}(\tilde{x}) \quad \text{dynamic condition} \quad (1.8)$$

with $\underline{\underline{\sigma}}$ the stress in the solid, $\underline{\underline{n}}$ the normal at the interface from the structure towards the fluid, and at the interface the position \tilde{x} for the fluid corresponds to a position \tilde{X} of the structure with a displacement $\tilde{\xi}$. As shown in Figure 1.19, for FSI problems, the structure deformation changes the boundary conditions of the fluid. The form of the solid determines the fluid boundary shape, and its deformation rate gives the velocity and acceleration as boundary conditions for the flow (equation 1.7); and the fluid transmits loads to the structure (equation 1.8).

The $(\tilde{\cdot})$ notation denotes the dimensionless variables for the fluid, and $(\tilde{\cdot})$ for the structure. The dimensionless time is used in both elements but can have different scales and therefore can differ:

$$\tilde{t} = \frac{t \sqrt{E/\rho_s}}{L} = \frac{\sqrt{E/\rho_s}}{U_0} \tilde{t}$$

Equations 1.7 and 1.8 are expressed with dimensionless parameters which make it possible to describe and therefore "classify" the FSI problems:

1.5.2.1 Reduced velocity U_R and Displacement number D

The *reduced velocity* means the velocity of the fluid and of the solid can be compared.

$$U_R = \frac{U_{fluid}}{U_{solid}} = \frac{T_{solid}}{T_{fluid}}$$

where T_{fluid} is the characteristic time for the fluid to travel over the structure, and T_{solid} is the characteristic time of the dynamic of the solid. The reduced velocity U_R can be used to make assumptions on the

time evolution but not necessarily on the amplitude of deformation of the structure.

The *displacement number* is defined as the ratio between the order of magnitude of displacement and the characteristic size of the FSI problem. It is used to see if the displacements are small or not compared to the size of the structure.

$$D = \frac{\xi_0}{L}$$

According to [de Langre, 2002], analysing the characteristic times of the fluid and of the solid, thus the reduced velocity, is an efficient way to sort out FSI problems. If U_R meets certain criteria with the displacement number, then a strong hypothesis can be applied:

$U_R \ll D$: For the structure, the fluid is motionless. Therefore $\bar{U} = 0$ and the loading of the fluid due to its convection velocity is neglected compared with the velocity of the structure.

$U_R \gg D$: The characteristic times of the structure and of the fluid are at different orders of magnitude. Thus for the fluid, the structure is motionless, and for the structure, the fluid loading is only static. When this criteria is met, the FSI problem can be called quasi-static aeroelasticity. A propeller or a wing of a plane are good examples.

$U_R^2 \gg D$: The velocity at the interface is not zero but acceleration of the structure is neglected. There is only a linear evolution of the motion of the structure. Foils in a pitch or heave motion are good examples of this case called pseudo-static aeroelasticity.

1.5.2.2 Cauchy number C_Y and mass number M

The Cauchy number is defined as the ratio between the fluid loading and the stiffness of the solid.

$$C_Y = \frac{\rho_f U_0}{E}$$

The Cauchy number evaluates the order of magnitude of the deformation due to the fluid loading. It is particularly important for numerical computations. If the Cauchy number is high, it means the structure can have strong deformation, therefore the numerical mesh needs to be remeshed or deformed.

The mass number $M = \frac{\rho_f}{\rho_s}$ is also valuable for convergence of numerical computations. If the mass number is around 1, the loading due to the added mass of the fluid in non stationary problems should be taken into account. The added mass can be described in various ways [Sarpkaya, 2004]. The fluid loading can be interpreted as a mass, meaning the loads are in phase with the accelerations of the structure. In the case for downwind sails, the added mass can be several orders of magnitude higher than the mass of the structure itself. It is therefore paramount to consider the fluid added mass.

In section 1.5.3, the values of these dimensionless data are defined and commented for our case: downwind sails.

1.5.2.3 Different types of numerical FSI couplings

As explained previously, structure and fluid have different approaches, usually an Eulerian approach for the Fluid and a Lagrangian approach for the structure. Moreover they do not necessarily have the same time-scale. Therefore the space and time discretisations are generally different. This raises numerical issues for FSI numerical simulations, that are:

The interface. At the interface, the stress in the fluid must equal the stress in the structure, while the meshing and the type of resolutions are different. Thus the stress field is not continuous between the fluid and the structure. The energy transfer might be inaccurate. This can lead to numerical instabilities.

Mesh deformation. The mesh of the fluid must follow the interface of the structure. Therefore for large displacements, the mesh should be automatically deformed or remeshed. The deformation of the mesh is often as computationally demanding as the resolution of the fluid or structure equations.

Coupling. When structure and fluid equations are solved with two different solvers, this is called a *partitioned approach*. The most efficient techniques can be used to solve the flow equations and the displacement of the structure. However stable and accurate coupling algorithms must be developed. If the both time scales (fluid and structure) are separated in each solver, and the coupling is only made at the interface, this is called an *explicit partitioned approach*. It is the least robust method and can resolve only weak couplings. When the two solvers have a similar time-scale and the coupling at the interface is made in an iterative loop, this method is called an *implicit partitioned approach* and can resolve weak and simple strong couplings. The last method is called *monolithic approach*. The equations governing the flow and the displacement of the structure are solved simultaneously, with a single solver. It is the most precise method and can resolve all types of coupling. However specific solver needs to be developed and it costs substantial CPU time. The spinnaker problem requires an implicit partitioned approach or a monolithic approach.

1.5.3 Our case of study: downwind sails

In Table 1.1, typical values of our air/spinnaker interaction are displayed.

The wind speed encountered by the sail (taking into account the boat speed) is around 5 m/s, the outside temperature is around 15°.

The spinnaker is a complex 3-dimensional shape, with the surrounding flow 3 dimensional as well. It has been decided to choose the characteristic length of the spinnaker as the square root of its surface. During this research project, I was mainly focused in large displacements of the sail due to the change of the angle of attack of the wind, or the flapping behaviour of the leading edge which has a time scale of about 1 s and a length scale of about 1 m.

During the PhD projects of [Augier, 2012, Durand, 2012], traction tests were carried out to quantify the material characteristics of the spinnaker cloth. The fabric is Nylon 32CHS, which was tested in the main

Fluid		
Velocity data	U_0	5 m/s
Density of air	ρ_f	1.23 kg/m ³
Dynamic viscosity of air	μ	1.80×10^{-5} Pa s
Char. Time of fluid	$T_f = \frac{L}{U_0}$	1.60 s
Structure		
Surface of spi	S_0	68 m ²
Char. Length of spi	$L = \sqrt{S_0}$	8 m
Order of mag. of displacement	ξ_0	1 m
Order of mag. of time	T_s	1 s
Surface density	ρ_{surfS}	0.05 kg/m ²
Surface elastic modulus	C	8×10^4 N/m
	Warp	83 400 N/m
	Fill	57 400 N/m
	Bias	10 600 N/m
Thickness	th	5.0×10^{-5} m
Elastic modulus	$E = \frac{C}{th}$	1.6×10^9 N/m ²
Volumic density	ρ_s	1000 kg/m ³

Table 1.1 – Main characteristics of our Fluid-Structure Interaction (FSI) study on the asymmetric spinnaker of a J/80 sailing yacht.

directions of the woven cloth and at 45°. The results in the 3 directions (warp, fill and bias) are shown in Table 1.1. With the thickness of the sail measured, we deduced the elastic modulus and the density of the structure to be used for non-dimensional parameters.

Reduced velocity	$U_R = \frac{T_s}{T_f}$	0.6
Displacement number	$D = \frac{\xi_0}{L}$	0.125
Mass number	$M = \frac{\rho_f}{\rho_s}$	1.2×10^{-3}
Cauchy number	$C_Y = \frac{\rho_f U_0^2}{E}$	1.9×10^{-8}
Reynolds number	$Re = \frac{\rho_f U_0 L}{\mu}$	2.7×10^6

Table 1.2 – Main non-dimensional numbers describing our FSI study on the asymmetric spinnaker of a J/80 sailing yacht.

Table 1.2 shows the main non-dimensional numbers that define and classify our FSI problem. First one can notice the reduced velocity U_R and the displacement number D have the same order of magnitude and therefore no strong assumptions presented in the subsection 1.5.2.1 can be used. There is strong dynamic coupling between the fluid and the structure due to the large displacements of the sail. However the low Cauchy number C_Y shows that the fluid loading implies only small deformation. Like a

membrane, the structure is subjected to large displacements but small deformations. Specificities of membranes are explained in greater detail in the next subsection 1.5.4.

The high Reynolds number Re indicates the viscous forces are not dominant and that the flow is mostly turbulent. Due to the high camber of the spinnaker, a massive flow separation can occur as explained in subsection 1.4.3 which largely differs from inviscid flow.

The mass number for the case of a surface with small thickness is not appropriate to describe the effect of the coupling due to the added mass. According to [Durand, 2012, chapter 3], a good parameter is the maximum ratio between the added mass per surface unit due to the fluid ma_f over the surface mass of the membrane ms_s . For a global estimation, this ratio becomes the ratio between the added mass due to the fluid Ma_f with the mass of the structure M_s , by integrating over the entire surface Γ .

$$r_{fs} = \frac{Ma_f}{M_s} = \int_{\Gamma} \frac{ma_f}{ms_s} d\Gamma = \frac{k_{ma} \rho_f S^{\frac{3}{2}}}{M_s} \quad (1.9)$$

To estimate the added mass due to the fluid on a structure with a vanishing thickness, [Durand, 2012, chapter 3] proposes this equation 1.9 which is based on inviscid fluid theory and on [Blevins, 1995, Brennen, 1982] to determine the coefficient k_{ma} -which is between 0 and 1-.

For the J/80 spinnaker, with $k_{ma} = 0.74$ and the estimated mass of the sail at $M_s \simeq 5 \text{ kg}$, we obtain:

$$r_{fs} \simeq \frac{500}{5} = 100 \quad (1.10)$$

The ratio is much larger than 1, therefore the loads due to added mass of the fluid are dominant. It also necessitates strong coupling schemes for numerical models.

1.5.4 Membrane

In Fluid Structure Interaction, sails are commonly modelled by membranes [Thwaites, 1961, Newman, 1987, Renzsch and Graf, 2010, Chapin et al., 2011, Lombardi et al., 2012, Durand et al., 2014]. [Trimarchi et al., 2013] used shell elements (which takes into account the bending stiffness) to model downwind sails, because shell elements can overcome some non-linearities -like the wrinkles- in numerical models. However, to apprehend the behaviour of the sail, it is easier and more common to represent the sail as a membrane. A membrane is a 3-dimensional structure with one dimension -the thickness- negligible compared to the two others. The normal stress in the transverse direction (perpendicular to the surface) is neglected and the membrane cannot support compression stresses. As a consequence, the membrane changes its shape to balance the external loads with the internal loads.

For the sake of simplicity, the equilibrium of a 2 dimensional membrane is first explained as in [Newman, 1987]:

In static conditions, Figure 1.20 explains that for a small curved arc ds of a membrane the outward normal force created by $\Delta p ds$ is balanced by the two tension components $T d\theta/2$ and $T d\theta/2$. We neglect

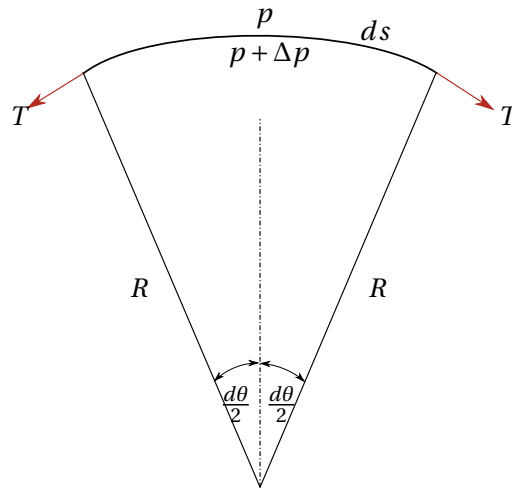


Figure 1.20 – Equilibrium of a two-dimensional membrane.

change of tension dT brought about by forces tangential to the membrane.

$$\begin{aligned}\Delta p ds &= T d\theta \\ \Rightarrow \Delta p &= \frac{T}{R}\end{aligned}\tag{1.11}$$

where R is the curvature radius. Note that this calculus is very similar to the Young-Laplace law due to surface tension at a fluid interface [Lautrup, 2010].

For a general 3 dimensional membrane with 2 orthogonal curvilinear coordinates u and v (cf. figure E.5), the generalisation of equation 1.11 is:

$$\Delta p = \frac{T_u}{R_u} + \frac{T_v}{R_v}\tag{1.12}$$

Equation 1.12 can only be applied in static conditions, and if the axes u and v are chosen so that the tensions T_u and T_v are principal. In other words, if R_u and R_v are the local maximum and minimum curvature radii.

[Durand, 2012] gives the more general equation:

$$\rho_{S.th} \frac{\partial^2 w}{\partial t^2} = \Delta p + \underline{\underline{\chi \kappa}}\tag{1.13}$$

with:

w : normal displacement from plane ($\underline{u}, \underline{v}$) (cf. figure E.5)

$\rho_{S.th}$: surface density

Δp : difference of pressure

$\underline{\underline{\chi}}$: tension tensor

$\underline{\underline{\kappa}}$: curvature tensor $-\frac{\partial^2 w}{\partial u \partial v} = -\nabla^2 w$

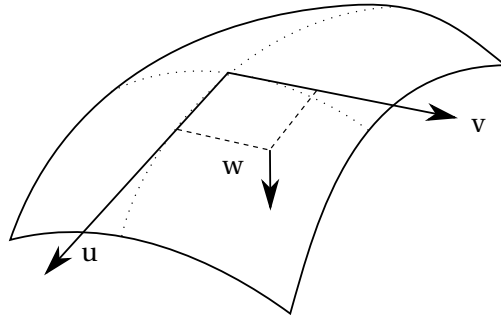


Figure 1.21 – Reference axes for a 3D membrane.

Note: The curvature tensor can be estimated by the mean curvature: $\nabla^2 w \approx \kappa_u + \kappa_v$

Due to its properties, the membrane has several nonlinearities that make analytical and numerical calculations more complex.

Geometrical nonlinearities: Membrane displacements can have large amplitudes. However they have small deformations. According to [Thomas, 2011], the displacement of a "fibre" of a membrane can be decomposed as a large amplitude rotation and a small deformation (cf. figure 1.22). The sail shape has rotations of large amplitudes (large displacements), but the sailcloth has only small elongation (small deformation). The large rotations are represented as cosine and sine forms which cannot be linearised. However, the assumptions of small deformation means we can say the stress-strain law is elastic and linear⁶. In equation 1.13, large rotations are taken into account by the curvature tensor and small deformations by the internal stress tensor.

Material nonlinearities: Sails are made by a superposition of different layers of different sizes with oriented fibres which make the material nonisotropic and hence a nonlinear evolution of the stress over the sail.

Wrinkles: The main feature of a membrane is its non-capability to support compression or shear stress. A compression in a membrane results in wrinkles and no stiffness. This is one of the main challenging nonlinearities for numerical simulations.

1.5.5 Summary of fluid-structure interaction of downwind sails

The case of downwind sail is a complex and yet a very interesting Fluid-Structure Interaction problem. This case is difficult to simulate with numerical tools due to the strong coupling between the highly detached and turbulent flow and the thin and flexible membrane. It involves large displacements of the

⁶For larger deformations, [Augier, 2012, Durand, 2012] showed the visco-elastic behaviour of Nylon (used for spinnaker sails) is not negligible. Moreover [Bles et al., 2009] observed a hysteresis in the visco-elasto-plastic behaviour of a polyamide fibre strap.

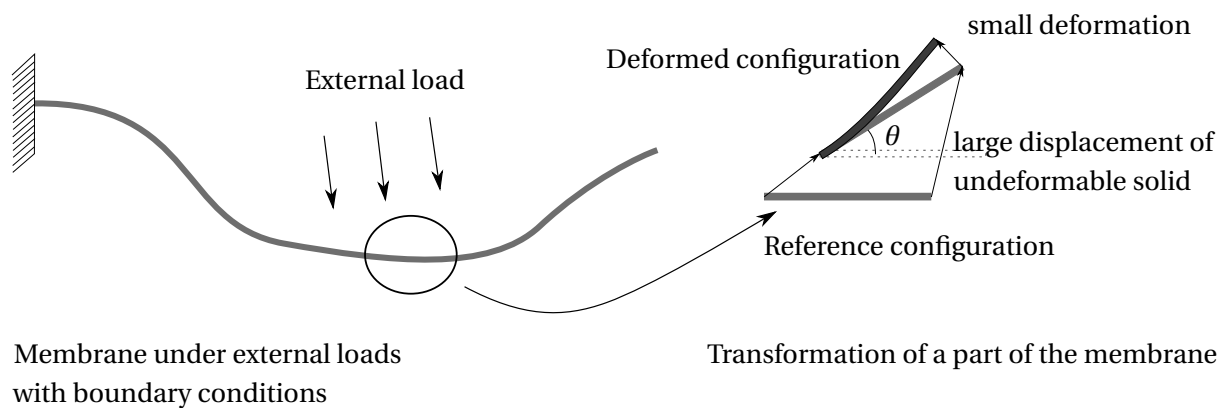


Figure 1.22 – Transformation of a fibre of a membrane in continuum mechanics. Inspired from [Thomas, 2011].

structure in a time-scale of the same order of magnitude than that of the fluid. Therefore the added mass effect is preponderant. For numerical tools, strong coupling schemes are required with automatic remesh. Some numerical simulations resolved in time have been achieved [Durand, 2012, Durand et al., 2014]. However validations are still needed. For unsteady numerical/experiments comparisons and also to better apprehend the interaction between the fluid and the structure, full-scale experiments with time-resolved measurements are carried out during this PhD research project.

1.6 Research in sailing aerodynamics

A lot of research topics in sailing have already been tackled, mainly thanks to the America's Cup where the latest technologies and innovative developments are used.

To assess the performance of sailing yachts, Velocity Prediction Programs (VPPs) are developed: [Roux et al., 2008, Le Pelley and Richards, 2011, Graf et al., 2016, Doyle et al., 2016] for the latest. They are now widely used by naval architects and racing teams. Combining the hydrodynamic and aerodynamic forces, a VPP predicts the performance of a yacht.

To estimate the hydrodynamic forces, there is the famous database of *Delft Systematic Yacht Hull Series* developed since 1975 to assess the residuary resistance of a sailing yacht ([Keuning and Katgert, 2008]). Nowadays research on planning hulls using numerical simulations are carried out ([Huetz and Guillermin, 2014, Prince and Claughton, 2016]), as well as on hydrofoils since the fastest boats can fly above water thanks to the lift generated by foils ([Astolfi et al., 2015, Heppel, 2015]). The aerodynamics of sailing yachts are explained in more detail in the next subsection. But readers should note it is not an exhaustive review and nor does it present all the subjects. For example research on rigid wings is not presented even though it is being explored more and more due to the high performance achieved with these "non-conventional" sails ([Viola et al., 2015, Chapin et al., 2015, Blakeley et al., 2015]).

Finally, sailing is not only a complex means of transportation from the point of view of physics but it is also an interesting tactical and strategic game, with important decisions to be made to win a regatta. Analysing the chance of winning by quantifying the risk is therefore another topic [Tagliaferri and Viola, 2016]. Sailing can also be modelled like a "chess game" using a *stochastic game approach* [Belouaer et al., 2015].

1.6.1 Upwind aerodynamics

Tables 1.3 and 1.4 classify main research projects already carried out by splitting them into 3 approaches: full-scale testing, wind tunnel testing and numerical simulation. These fields are again split in 2: Static and dynamic attitudes. In the "static" column, there are articles presenting time-averaged results with static input (no motion of the yacht nor variations of wind, and fixed trim) as opposed to articles presented in the "dynamic" column.

Historically, the first numerical simulations were run for upwind navigations with an attached flow around the sail using Vortex Lattice Methods. In these recent past years, higher precision numerical simulations have been validated by comparison of pressure distributions acquired in a wind tunnel [Viola et al., 2013, Nava et al., 2016] or at full-scale [Clauss and Heisen, 2005]. At the same time FSI numerical simulations are more commonly used even in sail design companies [Ranzenbach et al., 2013]. In parallel of numerical computations, some facilities have been specifically built for sailing research ([Claughton and Campbell, 1994, Flay, 1996, Fossati et al., 2006, Graf and Müller, 2009, Campbell, 2014a]). In a Wind Tunnel, aerodynamic loads are measured thanks to a yacht model linked to a balance projecting loads such as propulsive and side forces.

In articles presenting dynamic results, pitching motion creating variations of wind speed and angles is analysed by measuring the variations of flying shapes and loads either numerically: [Augier et al., 2014] or in wind tunnels: [Gerhardt et al., 2011, Fossati and Muggiasca, 2011] and also at full scale: [Augier et al., 2012] who compared full-scale data with numerical simulations. The dynamics of the tacking manoeuvre was studied as well at full scale and numerically [Masuyama and Fukasawa, 2011] and also in the wind tunnel [Gerhardt et al., 2009]. Recently, dynamic trimming [Aubin et al., 2016] and also dynamic body motions on dinghies [Schutt and Williamson, 2016] are starting to be studied.

If we analyze the research topics in sail aerodynamics presented in Table 1.3, all the "slots" have been filled and many typical dynamic motions encountered in upwind navigations are studied.

1.6.2 Downwind aerodynamics

For downwind situations: measuring pressures on a spinnaker (flexible [Viola and Flay, 2009] or rigid in a Wind Tunnel: [Richards et al., 2006]) is one of the main topic and results are often compared between the 3 types of testings [Viola and Flay, 2011] or between two: [Hansen et al., 2002, Viola et al., 2014]. As explained previously, measuring the flying shape is also of interest: ([Ranzenbach and Kleene, 2002, Graf and Müller, 2009, Mausolf et al., 2011, Renzsch and Graf, 2013]). Some numerical simulations used FSI numerical tools [Renzsch and Graf, 2010, Trimarchi et al., 2013, Lombardi et al., 2012, Durand et al., 2014] or Detached Eddy Simulations [Viola et al., 2014].

From a dynamic point of view, due to the high complexity of the spinnaker behaviour, very few studies have been carried out. Numerically, some impressive numerical tools have been developed with the possibility of studying the unsteady behaviour of the sail such as a dynamic trimming of the spinnaker clew sheet making the luff flapping [Durand et al., 2014]. In a wind tunnel, the forces during a gybe [Banks et al., 2010] or the pressure fluctuations on a rigid spinnaker [Bot et al., 2014] have been studied. However for full-scale experiments, before this PhD work, there was no published result on fluctuations of loads, pressures or flying shapes of spinnakers. Some dynamic results have been published thanks to



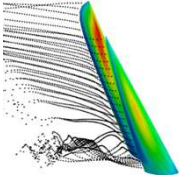
Upwind	Static approach	Dynamic approach
Full-Scale 	<ul style="list-style-type: none"> • [Van Hemmen, 1986], load measurement on 12-Meter class boat • [Herman, 1989], MIT sailboat dynamometer "Amphetrete" • [Hochkirch and Brandt, 1999], Sailboat dynamometer "Dyna" • [Flay and Millar, 2006], Pressures • [Puddu et al., 2006], Full scale catamaran • [Lozej et al., 2012], pressures • [Masuyama, 2014], Sailboat dynamometer "Fujin" • ... 	<ul style="list-style-type: none"> • [Masuyama and Fukasawa, 2011], tacking measurements • [Augier et al., 2012], loads+flying shape • [Bergsma et al., 2012], loads+flying shape • [Schutt and Williamson, 2016], body-weight motions • ...
Wind Tunnel 	<ul style="list-style-type: none"> • [Claughton and Campbell, 1994], Wind Tunnel Testings • [Flay, 1996], Twisted Flow Wind Tunnel • [Fossati et al., 2006], Wind Tunnel Techniques • ... 	<ul style="list-style-type: none"> • [Gerhardt et al., 2009], tacking meas. • [Gerhardt et al., 2011], pitching meas. • [Fossati and Muggiasca, 2011], harmonic pitching • [Aubin et al., 2016], dynamic trimming • ...
Numerical 	<ul style="list-style-type: none"> • [Gentry, 1971], sail interaction • [Kerwin and Newman, 1979] • [Milgram et al., 1993], sail forces ACC • [Clauss and Heisen, 2005], Num/Full-Scale comparison • [Braun and Imas, 2008], RANS upwind • [Chapin et al., 2011], FSI interaction • [Viola et al., 2013], Comparison with Wind Tunnel pressures • [Ranzenbach et al., 2013], FSI TP52 • [Nava et al., 2016], comparison RANS-LES • ... 	<ul style="list-style-type: none"> • [Schoop and Bessert, 2001], instantaneous aeroelastic model • [Masuyama and Fukasawa, 2011], tacking • [Fossati and Muggiasca, 2010], pitching • [Augier et al., 2013], Num/Full-Scale comparison • [Augier et al., 2014], FSI pitching • ...

Table 1.3 – Non exhaustive state of the art for upwind sailing.

this PhD project where full-scale experiments were developed in collaboration with Dario Motta's PhD ([Deparday et al., 2014, Motta et al., 2015, Motta, 2015, Deparday et al., 2016]).

Downwind	Static approach	Dynamic approach
Full-Scale 	<ul style="list-style-type: none"> • [Viola and Flay, 2010], pressures • [Mausolf et al., 2011], Flying shape • [Motta et al., 2014], pressures + Flying shapes • [Campbell, 2014b], comparison Full Scale/Wind Tunnel loads • ... 	<ul style="list-style-type: none"> • [Deparday et al., 2014] <i>Analysis of flapping</i> • [Motta et al., 2015] <i>Pressure fluctuation pattern</i> • [Deparday et al., 2016] <i>modal analysis on pressure fluctuations</i>
Wind Tunnel 	<ul style="list-style-type: none"> • [Ranzenbach and Kleene, 2002], flying shapes • [Hansen et al., 2002], Full Scale/Wind Tunnel sail force • [Richards et al., 2006], rigid sails • [Graf and Müller, 2009], flying shapes • [Viola and Flay, 2009], forces and pressures • [Renzsch and Graf, 2013], forces + flying shapes • [Campbell, 2014a], Comparison Wind Tunnel testings • ... 	<ul style="list-style-type: none"> • [Banks et al., 2010], forces during gybe • [Bot et al., 2014], time series pressure
Numerical 	<ul style="list-style-type: none"> • [Hedges et al., 1996] • [Lasher and Sonnenmeier, 2008] • [Renzsch and Graf, 2010] FSI • [Viola and Flay, 2011], comparison Full scale, Wind Tunnel, numerical • [Trimarchi et al., 2013] FSI shell • [Viola et al., 2014] DES • ... 	<ul style="list-style-type: none"> • [Lombardi et al., 2012] dynamic FSI • [Durand et al., 2014] automatic dynamic trimming

Table 1.4 – Non exhaustive state of the art for downwind sailing. References in *italics* are articles using results obtained within this PhD project.

1.6.3 Full-scale testing

1.6.3.1 Full-scale testing as a complement to wind tunnel testing and numerical computations

Wind tunnel testing is the main experimental tool to improve the understanding of sail aerodynamics. Whereas wind tunnel tests are efficient to assess the sail performance and to provide comparative data between different sail designs or numerical simulations, it is more difficult to reproduce the dynamic aspects occurring on water. Not only is there a too small Reynolds number (about $4 \cdot 10^6$ for full scale testing and $4 \cdot 10^5$ for a 1/10th model) but also a different ratio of fabric weight to wind pressure is encountered as well as a different ratio of membrane stress to wind pressure. Thus full-scale experiments would make it possible to compare the dynamic behaviour of downwind sails with wind tunnel experiments. Also it is difficult to correctly reproduce the twisted wind flow even in twisted flow wind tunnels.

Computational Fluid Dynamics (CFD) has become the most common method for studying sail aerodynamics. A lot of different environmental conditions can be set, and it can be faster and easier to set than full-scale or wind tunnel experiments. However, as explained by [Gentry, 1971] and also cited in [Motta, 2015]: *"the limits of CFD are that it is only as good as the mathematical equations and assumptions used in representing the physical flow. All CFD codes require precise input of the geometry of the shapes to be studied. In the case of soft thin sails, this is difficult. Under sail, the crew can adjust the sails precisely to the flow conditions, but this is difficult to accomplish in a computer program."* Furthermore for downwind sails, viscous RANS methods with turbulence models still need validation and are not fully reliable in modelling the separation on the sails. Large Eddy Simulation (LES) or Detached Eddy Simulation (DES) require much larger computational resources and still need validation from wind-tunnel and full-scale testings.

Understanding the sail behaviour in real sailing conditions can only be done by full-scale testing. The unsteadiness of the environment (wind variations in strength and direction, sea state, continuous changes made by the crew on board) makes the sail performance vary.

1.6.3.2 Different types of full-scale experiments

Different types of full-scale experiments have been conducted using different methods:

Sailboat dynamometer [Herman, 1989] was the first to equip a sailing boat called "Amphetrete" with an internal frame with 6 strain gauges assessing the aerodynamic load transferred to the hull. Then the University of Berlin built a 33-foot sail dynamometer boat "DYNA" [Hochkirch and Brandt, 1999]. The measured aerodynamic forces were compared with wind tunnel experiments [Hansen et al., 2002], and CFD computations [Clauss and Heisen, 2005]. [Masuyama, 2014] built another sailboat dynamometer "Fujin" to relate sail shape and loads to yacht performance. And lastly [Fossati et al., 2015a] has started to build a new sailboat dynamometer "Lecco" equipped with sensors using the latest technologies for flying shape [Fossati et al., 2015b] and pressure measurements [Fossati et al., 2016]. With this last sail dynamometer boat, downwind experiments are planned to be carried out unlike the other ones that focused only on upwind sailing.

Rigging load measurement Another technique consists in fitting the running and/or standing rigging with stress gauges to measure aerodynamic loads. On a 12-Meter America's Cup design yacht, [Van Hemmen, 1986] was the first to present load measurements. More recently [Augier et al., 2012] equipped a J/80 class sailing yacht with strain gauges at the corners of the sails (head, tack and clew) as well as on the shrouds, forestay and backstay. The combination of boat motion, rigging loads, flying shapes in unsteady conditions made it possible to validate the FSI numerical model ARAVANTI [Augier et al., 2013] for upwind sailing in waves. For downwind sails, the Yacht Research Unit of the University of Auckland developed the Directional Load Cell (DLC) [Le Pelley et al., 2015]. Not only is the magnitude of loads measured with the DLC but also the direction that is valuable for downwind flying sails. In this PhD project, the load acquisition system developed by Benoit Augier and the DLCs developed by David Le Pelley were further developed and used.

Pressure measurement The last technique used to assess the aerodynamic performance of full-scale sails consists in measuring the pressure generated by the sail. [Puddu et al., 2006] performed a full-scale test on the mainsail of a Tornado class catamaran with 25 pressure taps arranged in 6 rows. [Graves et al., 2008] measured pressures on the mainsail and the jib of an America's Cup sailing yacht of the Oracle BMW team. Compared to other pressure measurements carried out at full-scale, wireless sensors were used. [Viola and Flay, 2010] were the first to measure full-scale pressures on an asymmetric spinnaker. The windward and leeward pressures were measured separately thanks to a change of tack. [Lozej et al., 2012] presented pressure measurements on a mainsail sailing upwind. Finally the Yacht Research Unit of the University of Auckland developed its own system [Flay and Millar, 2006] and then [Le Pelley et al., 2012, Bergsma et al., 2012] presented pressure data in association with the acquisition of the flying shape thanks to the system Visual Sail Position And Rig Shape (VSPARS) developed by Le Pelley [Le Pelley and Modral, 2008] to assess the global aerodynamic force produced by sails. [Motta et al., 2014, Motta et al., 2015, Motta, 2015] improved this system now called Force Evaluation via Pressure and VSPARS (FEPV). In this PhD project, in collaboration with Dario Motta [Motta, 2015], we used their pressure acquisition system.

1.6.4 Flying shape acquisition

Finally an important part of this PhD project has been on developing a flying shape acquisition system. This last section presents the state of the art of shape measurements.

1.6.4.1 Surface shape acquisition

Different methods used to measure of surface shapes can be divided into 2 main categories: contact and non-contact methods. By placing some embedded sensors, like Inertial Measurement Units (IMUs), a deformable surface can be reconstructed from these discrete measurements. But due to the lack of accuracy, and the weight of the sensors, this solution is not convenient for spinnaker flying shape measurement. Used in some industries and even in a wind tunnel to measure flying shapes of flexible spinnakers [Ranzenbach and Kleene, 2002], Coordinate Measuring Machines are also too complex to set at full-scale.

Non-contact methods seem more appropriate to measure a spinnaker flying shape since they ensure no load effect or any perturbation onto the highly deformable sailcloth. Indirect, reflective methods and especially using optical measurements would be better thanks to smaller measurement systems and faster setup and measurements. To measure the shape of a thin flexible surface several methods have been developed.

The optical profilometric technique ([Cobelli et al., 2009]) measures the displacement of a surface using fringe pattern projection. However for these methods controlled environment and light are required.

Photogrammetry and videogrammetry using triangulation with projection of dots have been used on solar sails by NASA ([Pappa et al., 2003]). Photogrammetry is a triangulation method using several object points seen by several photographs (cf. figure 1.23). It can be used to recompute the 3D shape of the object. The perspective lines of one object-point from different photographs intersect each other at one location. These intersecting lines are used to compute the location of an object-point in three dimensions. For further details, the reader is referred to appendix A. Videogrammetry uses the same principle than photogrammetry, but in addition the object points are tracked in time, and therefore the photogrammetry process at every frame is optimised and faster.

There is also stereophotogrammetry that can measure deformations of a flexible wing in a wind tunnel ([Black et al., 2010]). Only 2 cameras are used instead of multiple cameras. However unlike photogrammetry, the 3D distance between them must be fixed and known precisely. Similarly [Giovannetti et al., 2015] used Digital Image Correlation with 2 digital cameras in stereo configuration. But large displacements are more complicated to measure with these two last techniques, especially in full-scale experiments. Thin flexible surfaces like a spinnaker can have large displacements, in an order of magnitude of 1 to 5 m for the spinnaker used on the J/80 class sailing boat.

In recent years laser measuring tools like LIDAR (LIght Detection and RAnging) have been improved and can be used to measure flexible surfaces [Fossati et al., 2015b]. They rely on Time Of Flight technology. A laser impulse is projected (in the visible or near infrared range) and the time of flight is measured to reach the object and return.

1.6.4.2 Sail shape acquisition

At full-scale, sail shape measurements have already been carried out by the sail dynamometer boat "Fujin" [Masuyama, 2014] and "DYNA" [Clauss and Heisen, 2005]. However these sail dynamometer boats mainly focused their experiments on upwind situations. Many systems use only one camera filming stripes painted or glued on the sails, and via a post-processing software, parameters of the stripes (entry angles, camber, draft, ...) are extracted. The first known software is ISIS developed by the Nivelleanus for the America's Cup. Another software program commercialised for the America's Cup was SailVision developed by BSG Développements. Nowadays a sail analyser method called Visual Sail Position And Rig Shape (VSPARS) has been developed by the Yacht Research Unit at the University of Auckland ([Le Pelley and Modral, 2008]). The sailmaker NorthSails has also developed its own tool called Advanced Sail Analyser (ASA). [Schutt and Williamson, 2016, Doyle et al., 2016] used OpenCV ([Bradski and Kaehler, 2008]) to reconstruct sail shape from different stripes. However, all these systems need a strong hypothesis for accurate measurements: the stripes painted or glued on the sail are supposed to remain in the same plane and perpendicular to the line of sight, which is satisfactory for upwind sails

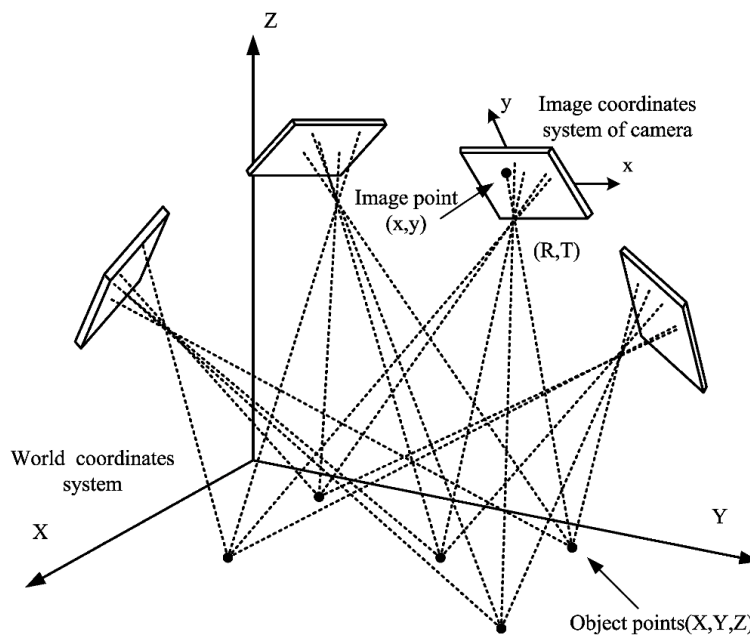


Figure 1.23 – Principle of photogrammetry using triangulation. Several object-points are projected onto different image planes (photographs).

but not for downwind sails on a large range of apparent wind angles.

With the use of only one camera, [Salzmann and Fua, 2011] developed a model using a deforming mesh corresponding to the size of the object. Nevertheless given the large area of the spinnaker, nothing can guarantee the whole sail is in the field of view of only one camera fixed on the deck of the sailing yacht.

Different tools have been used to measure flying shapes of downwind sails during wind tunnel experiments at smaller scale: Coordinate Measuring Machine ([Ranzenbach and Kleene, 2002]), Photogrammetry [Renzsch and Graf, 2013] and ([Fossati, 2009, part8.1 pp227-232]) using custom built Infrared cameras. At the same time of my PhD project, [Fossati et al., 2015b] developed a patented system using a "Time Of Flight radar". In theory, measurements should be more precise than with the photogrammetry method. However with this last solution, a significant time is necessary to scan the whole sail, hence dynamic measurement might be difficult to obtain. Furthermore strong variation of the lighting can alter the quality of measurement, as can happen during a sunny full-scale experimental session.⁷

In [Mausolf et al., 2011], full-scale flying shapes of a spinnaker were captured using a photogrammetry process with 4 cameras placed on motorboats all around the sailing yacht, requiring manpower. In addition to independent and spaced cameras, synchronization is hard to obtain for dynamic measurements between all the cameras and the other time-resolved data. Moreover they are on moving spots relative to the sailing yacht, which is not convenient for time-resolved flying shape measurements. Furthermore rigid-inflatable boats create waves and can disturb the experiments.

To obtain a 3D-shape of a flying spinnaker, I decided to use a photogrammetry measurement with

⁷And surprisingly, during this PhD project carried out in the Bay of Brest, the extreme west of Brittany, quite well known for not having a very good weather, we always had sunny and pleasant conditions when we planned and carried out full-scale experiments!

all cameras placed on-board the sailing boat in order to operate the acquisition system on-board easily. Fixed cameras relative to the boat frame simplify time-resolved measurements. A careful set-up of the cameras is required to obtain good quality results. This will be further explained in the next chapter.

1.7 Conclusions and motivations

In this first chapter, the motivations to carry out this PhD project were explained. The flow around downwind sails is complex. A 3D, turbulent and twisted flow encounters a highly cambered, non-developable shape. There is a massive flow separation with several vortices created. Furthermore the sail shape is strongly linked to the aerodynamic pressure. The coupling of the 3D flow with a thin and flexible membrane results in a complex FSI system. It involves large displacements of a light sail. Therefore the added mass effect is preponderant. Measuring accurately the *flying shape*, loads and pressures of the spinnaker would allow us to better assess the fluid-mechanical phenomena present on a downwind sail.

The dynamic behaviour of downwind sails is due to the intrinsic dynamic instabilities of the sail, and also due to the waves and wind variations. Furthermore the optimum trim is often dynamic by keeping the luff of the sail flapping. The dynamic behaviour can hardly be reproduced in a wind tunnel. Some numerical simulations resolved in time have been developed [Durand, 2012, Durand et al., 2014] but still need validations. With full-scale measurements at sea, we can quantify the actual forces at work and better apprehend the dynamic FSI of sails. These data can be compared with wind tunnel testing and numerical results.

Design shapes of downwind sails are quite different from flying shapes on water. Acquiring the flying shapes would make it possible to compare them, and therefore help to improve their design. A database or a method to quantify the shapes might help to generalise this comparison. Before this PhD project, no method to measure accurately offwind sails synchronised with other time-resolved data existed.

During this PhD project, a system to dynamically acquire the flying shape of the spinnaker has been developed. It is synchronised with rigging loads and boat data. The evolutions of the flying shapes, loads, pressures on the spinnaker and boat data were analysed according to the speed and the angle of attack of the flow. Not only have stable data been analysed but also unsteady behaviour of the flying sail. The flapping of the luff has been investigated, which is the most efficient trim according to sailors.

Contents

2.1 Set up of the experiments	46
2.1.1 Conditions	48
2.1.2 Procedure	48
2.2 The J/80 class sailing yacht	49
2.2.1 Standing Rigging	50
2.2.2 Sails	50
2.3 Flying shape acquisition	51
2.3.1 Main parameters affecting photogrammetry measurements	51
2.3.2 Set-up of the flying shape acquisition	54
2.3.3 Calibration	56
2.3.4 Photogrammetric measurements	59
2.3.5 Accuracy of the flying shape acquisition system	59
2.3.5.1 Precision	59
2.3.5.2 Accuracy	61
2.3.6 Synchronization with other data	62
2.3.7 Further improvements	63
2.4 Load measurement	64
2.4.1 Load sensors on standing and running rigging	64
2.4.1.1 Description	64
2.4.1.2 Calibration	65
2.4.2 Spinnaker load sensors	66
2.4.2.1 Wireless shackles	67
Description	67
Dynamics	67
2.4.2.2 Directional Load Cells (DLCs)	68
Description	68
Load calibration	69
Dynamics	70

Load direction	70
Precision of the load directions	71
2.4.2.3 Conclusions on spinnaker load acquisition	72
2.5 Pressure acquisition system on spinnaker	73
2.5.1 Description of the pressure system	74
2.5.2 Zeroing and accuracy of pressure sensors	75
2.5.3 Dynamics of pressure sensors	76
2.6 Wind measurement	77
2.6.1 Presentation of wind sensors	77
2.6.2 Difficulties to measure wind	78
2.7 Boat data acquisition	80
2.7.1 Boat motion	80
2.7.1.1 Description	80
2.7.1.2 Calibration	81
2.7.2 Speeds and courses	83
2.7.2.1 Speed Over Ground (SOG) and Course Over Ground (COG)	83
2.7.2.2 Speed Over Water (SOW) and Course Over Water (COW)	84
2.8 Acquisition systems	85
2.8.1 RTMaps architecture	85
2.8.2 CompactRio architecture	86
2.9 Procedure and Post-processing	87
2.10 Conclusions	88

2.1 Set up of the experiments

Experiments were carried out on-water at full-scale on a J/80 class sailing yacht to assess the actual aerodynamic loads created by the sails. My main efforts had been devoted to measurements of flying shapes of sails. We also measured the loads on the sails and rigging and the pressures on the spinnaker. Their evolutions according to different conditions, such as a function of wind, boat speed or boat attitude were analysed. Therefore the yacht was also equipped with an anemometer, GPS and an Inertial Measurement Unit (IMU).

During this PhD project, two main experiments were carried out: one in June 2013 with a focus on pressures, with the support of colleagues from the Yacht Research Unit, University of Auckland, New-Zealand (see the general arrangement of the system apparatus in Figure 2.1) and a second one in July 2014 with a focus on flying shapes (see the general arrangement of the system apparatus in Figure 2.2). Unfortunately, no experiment (yet) has been carried out with a focus on pressures and shapes at the same time.

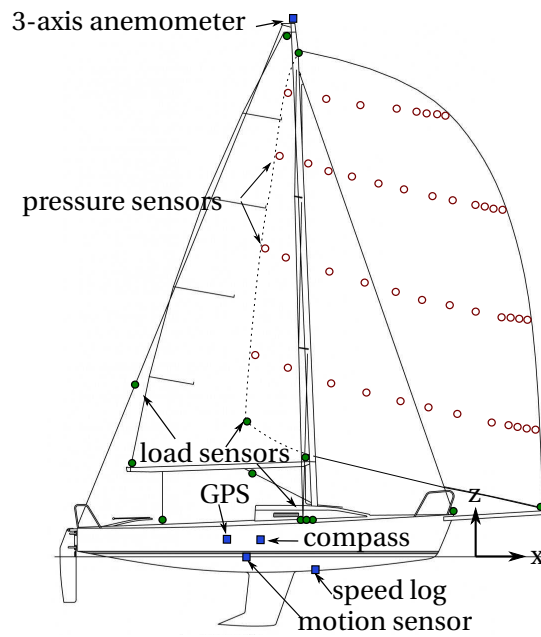


Figure 2.1 – General arrangement of the experimental set-up on the J/80 in 2013. 16 load sensors (green discs), 44 pressure taps (red circles), and wind and boat sensors (blue squares).

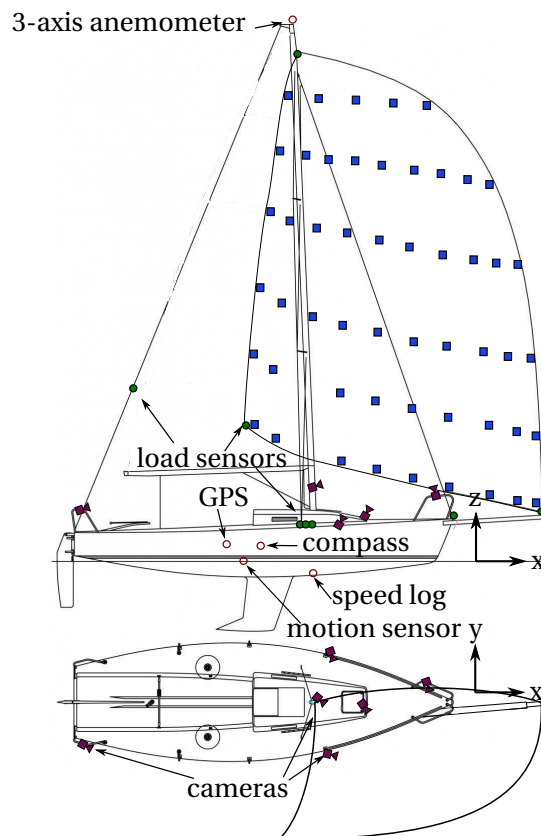


Figure 2.2 – General arrangement of the experimental set-up on the J/80 in 2014. 16 load sensors (green discs), wind and boat sensors (red circles) as in the experiments in 2013. 54 targets on the spinnaker for photogrammetry measurement (blue squares) were added and pressure sensors not used.

2.1.1 Conditions

Both experiments were performed in the bay of Brest, France, offshore Ecole Navale. During both experiments the weather conditions were stable (cf. table 2.1). In 2014, the wind was slightly lighter and a bit more shifty. Nevertheless conditions were relatively similar and data from both experiments could be used together for comparison when needed.

Conditions in:	2013	2014
Average True Wind Speed	6 m/s (12 kn)	5 m/s (10 kn)
Gust speed	8 m/s (16 kn)	8 m/s (16 kn)
Wind direction	270° (westerly wind). Stable.	40° (North-easterly wind). Slightly shifty.
Wave height	≈ 0.1 m. Flat water.	≈ 0.1 m. Flat water.

Table 2.1 – Weather conditions for the two main experiments carried out during this project.

2.1.2 Procedure

During the experiments carried out in 2014, different objectives were aimed at, thanks to the expertise gained with the experiments carried out in 2013. We wanted to obtain experimental results for comparisons on average and in time domain with potential numerical simulations. To ease numerical simulations, most of the full-scale experiments were carried out with the spinnaker only, the mainsail not hoisted. Another goal was to acquire data to analyse the evolutions of loads and flying shapes at different AWA whether with the spinnaker flapping or not flapping. Therefore, a detailed procedure was defined to allow correct measurements to be repeatable and usable. Every test was repeated several times for every AWA:

- Sail at a constant given AWA previously chosen between 70°, 100°, 120° or 140°.
- Phase 1: Spinnaker is slightly overtrimmed (not flapping).
- Phase 2: Spinnaker sheet is eased at a constant speed until first flapping. The distance of the eased clew sheet is measured.
- Phase 3: Spinnaker is dynamically trimmed on the verge of luffing for one minute minimum.
- Phase 4: If the conditions are correct, a periodic trimming "ease-trim", like pumping is done.
- Feelings of the helmsman and the trimmer are recorded.

Phases 1 to 3 can be used for comparison with numerical experiments. During phase 1, stable and not folded flying shapes can be measured.

All main actions and remarks were recorded live during the measurements thanks to a dictaphone.



Figure 2.3 – The J/80 *Thetys* -used for our experiments- during the regatta *Grand Prix Ecole Navale* in 2013. Credit Pierrick Contin.

Hull	
Length Over All	8 m
Length at Water Line	6.7 m
Beam	2.5 m
Draft	1.5 m
Displacement	1.5 t
Sails	
mast height	11.5 m
I	10 m
P	9.14 m
J	2.9 m
E	3.9 m
mainsail area	17.4 m ²
jib area	14 m ²
spi area	65 m ²

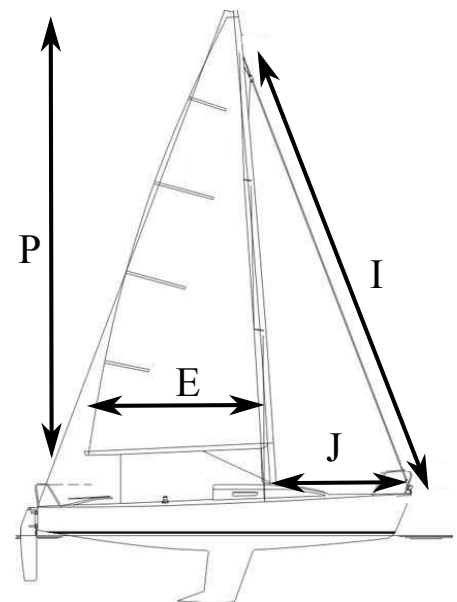


Table 2.2 – Main characteristics of the J/80 sailing yacht.

2.2 The J/80 class sailing yacht

The J/80 class sailing yacht is a fixed keel one-design sportboat (cf figure 2.3 and specifications in table 2.2) widely used in Europe and in the United States of America in competitive regattas. Participating successfully in the French championship, my supervisors Patrick Bot and Frédéric Hauville have great experience and knowledge about this yacht. They know the good trim settings to be competitive. Moreover their yacht *Thetys* is used for these experiments because she is located at Ecole Navale and can be on water relatively easily.

2.2.1 Standing Rigging

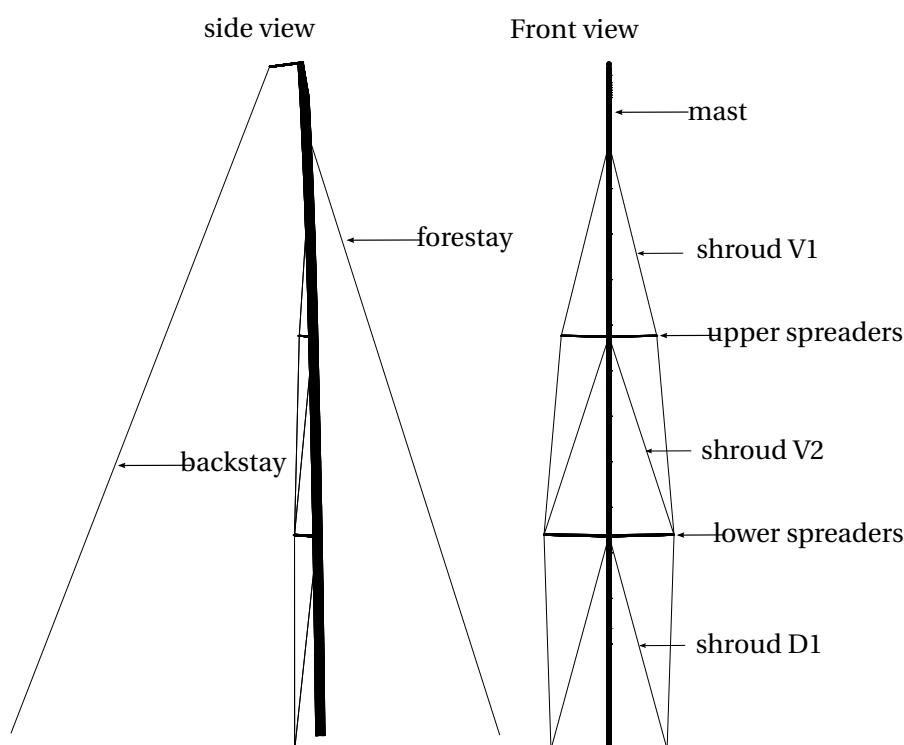


Figure 2.4 – Standing rigging of the J/80 class sailing yacht.

The standing rigging is composed of the mast, the boom, the shrouds V1, V2 and D1, the spreaders, the backstay and forestay. It is a fractional rig: the foresail does not reach the top of the mast. The forestay is fixed at 7/8th of the mast height. The difference in height between the forestay point and the backstay point provides a better control of the mast camber and therefore of the shape of the sails. It is particularly efficient for upwind sails.

The forestay and backstay sustain the mast longitudinally. The shrouds support the mast laterally and longitudinally thanks to the spreaders. On a J/80, the spreaders are slightly angled to take some of the longitudinal force. Thus thanks to turnbuckles at the deck-shroud connection, the bending of the mast can be tuned, by setting the tension in the shrouds applying compression loads on the spreaders.

2.2.2 Sails

The upwind sail area of the J/80 is 31.5 m² with a jib and a mainsail. For downwind courses, the spinnaker has a much larger area -65 m² according to the class measurement method. Compared to the size of the boat and other boats of the same type, the spinnaker is rather large, which makes the J/80 a "powerful" boat.

Figure 2.5 indicates the measured lengths according to the class rules. The long curved luff (G=12 m) is

1.25 times longer than the leech ($C=9.55$ m) and 1.7 times longer than the foot ($B=7.14$ m) and 1 m longer than the distance between the head and tack points. Compared to upwind sails, the luff is much more rounded.

The spinnaker point on the mast is 0.7 m above the forestay point, but still 0.6 m below the backstay point. On the hull, the tack point is maintained at 2 m in front of the bow by a retractable bowsprit. The tack point is therefore 4.9 m in front of the mast foot. The clew point is connected with a spinnaker sheet to the hull on a block at the foot of a forward stanchion of the pushpit.

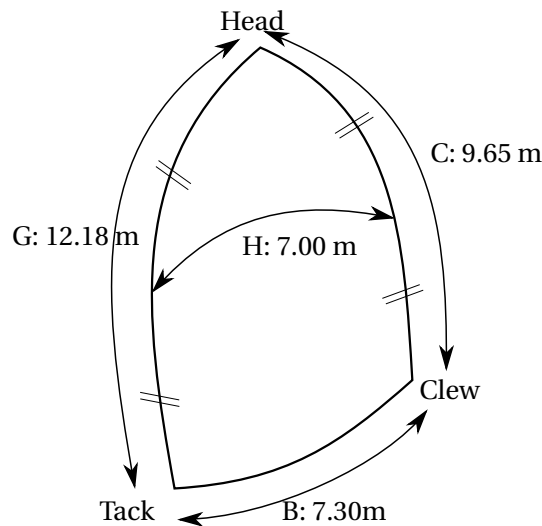


Figure 2.5 – Class dimensions of the spinnaker laid down on ground.

2.3 Flying shape acquisition

This section describes the acquisition system developed to measure the full-scale flying shape of sails. But before describing the system, we should examine the main parameters affecting the accuracy of photogrammetry measurements. We will then deduce the required specifications of the acquisition system. The main principles of photogrammetry are explained in appendix A. Photogrammetry is a triangulation method to measure the positions of targets using several photographs placed at different locations.

2.3.1 Main parameters affecting photogrammetry measurements

For this PhD project, we used the software *Photomodeler* [Eos Systems Inc., 2015]. I already had some experience with this software, which is quite efficient and enables automatic processing of target tracking for time-resolved photogrammetry also called videogrammetry. Figure 2.6 shows a table presenting the parameters affecting accuracy in photogrammetry measurements. These parameters are described with the settings used in our measurements.

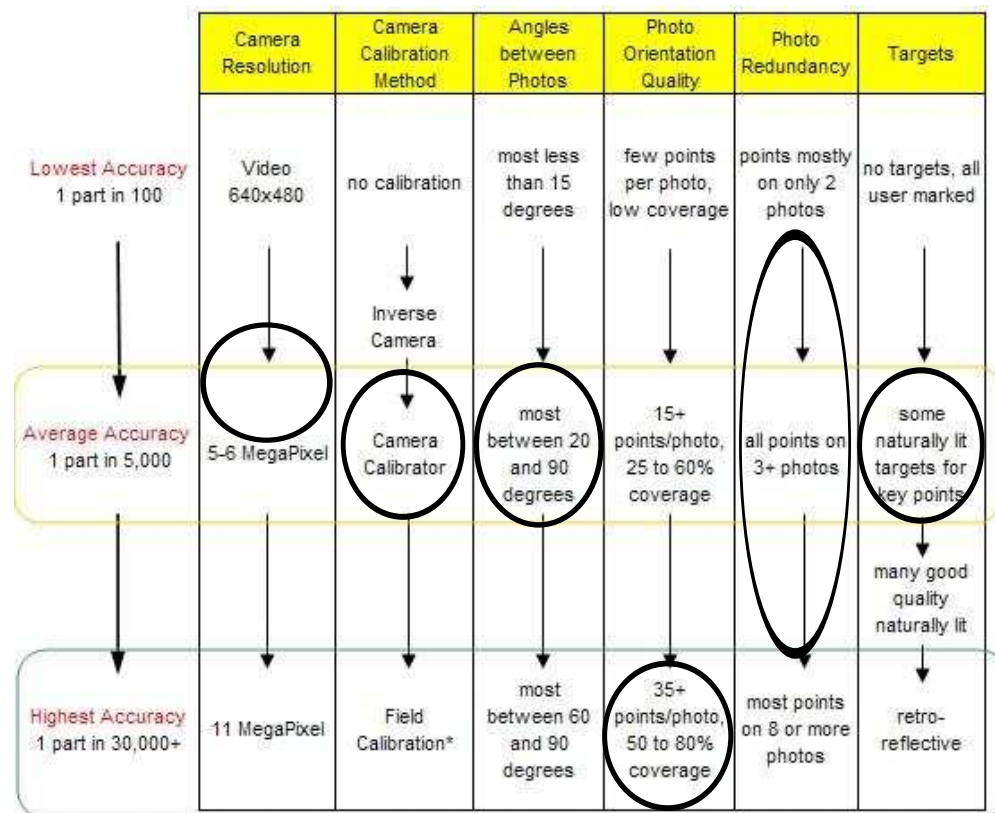


Figure 2.6 – Parameters affecting accuracy in photogrammetry. From the website www.photomodeler.com. Circles show the accuracy obtained for the experimental setup defined in this thesis. The accuracy figures "1 part in NNN" are the one σ standard deviation accuracies. For example at 1 part in 30,000 on a 9 m object, point positions would be accurate within 0.3 mm at 68% probability (one σ).

Resolution A better resolution involves a finer precision of the edges of the object points. The resolution used during the experiments was between 2 MegaPixel and 3.7 MegaPixel. A common reflex camera can have a better resolution usually around 10 MegaPixel. However for dynamic measurements, we needed videos that have better resolutions. Anyway, the resolution is sufficient for most of the points but only just satisfactory for the points near the head of the sail at 10 m high that are not easily detected.

Camera calibration method Each camera has its own specificities, its proper focal length, its own principal point position. The more precisely these specificities are determined, the better the measurements. Furthermore the image can be distorted due to the shape of the lens. To carry out high accuracy measurements, a lot of effort has been put into the calibration method to accurately quantify all these specificities. The procedure is more detailed in section 2.3.3. Thanks to these efforts, the "averaged accuracy" standard is reached which is good for our application.

Angles between photos Smaller angles reduce the accuracy of measurements. Figure 2.7 shows that extreme angles (below 10° and above 160° about) increase the potential error of the intersecting area thus altering the quality of the photogrammetry measurements. According to the small distance

between the large spinnaker and the cameras placed on the boat, a particular effort was put into this point during the set-up of the system in order to maximise angles between cameras. Finally, the average angle obtained during our measurements is around 40° . Despite a few object points near the head of the sail where we found angles lower than 5° , the results were satisfactory.

Photo orientation quality The more points spread on the whole image plane, the better the precision on the position and on the orientation of the cameras. A good precision on the position of the cameras reduces the residuals and enhances the quality of the projects. More than 80% of the photographs were covered by targets. We used 51 targets on the spinnaker seen by almost all the cameras, in addition to about 50 specific points on the mast and on the hull giving us the highest accuracy possible for this parameter.

Photo redundancy Similar to the previous parameter, an object point seen by many photographs improves the quality of the measurements. For our measurements, there is an equidistribution of points seen by a different number of photographs. About 20% are seen by only 2 photographs, and 20% seen by the 6 cameras. Given the large area covered by the sail, and the small distance between the cameras and the sail, we are satisfied with this accuracy.

Targets On the sail, we stuck targets made of dark blue squares of 100 mm x 100 mm that can be automatically detected but not automatically differentiated. They are called sub-pixel targets; because by detecting the edges of the target, *Photomodeler* defines the image point as the calculated geometric centre of the target hence giving a precision of the image point of less than a pixel. Some specific points on the mast and the hull were manually marked hence less accurate than sub-pixel targets. But they are used to increase the overall accuracy of the project, and to place the sail in the boat frame.

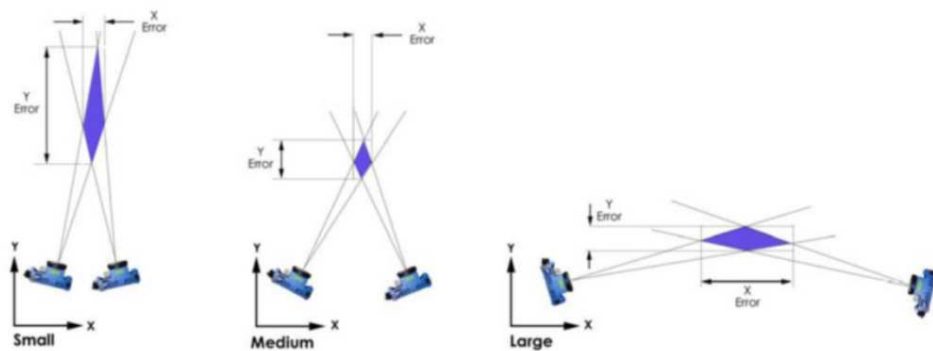


Figure 2.7 – Importance of angles in precision of photogrammetry measurement. From www.geodetic.com

According to Figure 2.6, the expected accuracy obtained should be 1 part in 5000. It means the point positions would be accurate to 2 mm at 68% probability (one standard deviation). This accuracy (probably optimistic) would be largely sufficient for our purpose where an accuracy of 100 mm would be satisfactory. These main parameters affecting the accuracy of photogrammetric measurement will partly define the specifications of the set up of the flying shape acquisition.

2.3.2 Set-up of the flying shape acquisition

The main objective is to measure different full-scale flying shapes of spinnaker for a wide range of Apparent Wind Angle (AWA), between 60° and 150°. The second objective is to measure time-resolved evolution of the flying shape of spinnaker.

From these goals, 6 main constraints were determined:

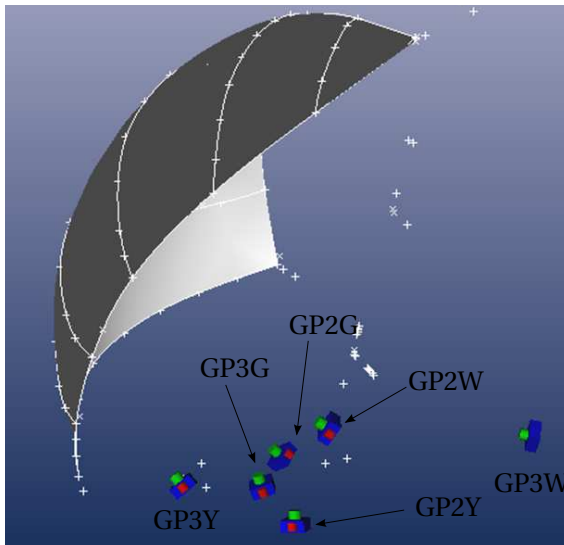
- C1 See most of the spinnaker for a wide range of AWA.
- C2 In order to measure time-resolved flying shape of spinnaker, camera positions should remain steady for every frame. The idea is to measure the flying shape of the spinnaker once for the first frame, and to track targets on the following frames. Therefore cameras must be fixed in the chosen boat reference. This constraint implies the following two points:
 - C2-a) Cameras must not move during experiments.
 - C2-b) Cameras must be placed on the boat.
- C3 Cameras must be watertight since experiments are carried out on water.
- C4 Angles between cameras should be kept as wide as possible to achieve good quality projects.
- C5 A minimum of 3 cameras should be used for good quality projects.
- C6 Cameras should have a good resolution (> 2 Mpx)

To determine the positions of the cameras during post-process, at least 3 points must be seen by 3 photographs. However it is highly recommended to have more points seen by more photographs. Nonetheless, because of C2-b), if too many cameras are positioned on the boat, angles between perspective lines of cameras would be too tight. A good compromise has been achieved with the use of 6 cameras. To respect C4, cameras were placed as widely spaced as possible, thus at extremities of the yacht (outboard at the hull-deck connection, on the pushpit and pulpit), on the fore deck and on the mast (cf. figures 2.8 and 2.2). To comply with C2-a), specific articulated mounts -sticked or clamped on the pushpit and pulpit- were used. The camera on the mast was placed at 1.5m up from the deck-mast connection in order not to be affected by mast movements.

A short focal length -thus a wide field of view- helps to satisfy C1 and C2-b). Since the cameras must be placed on the boat, there is a short distance between the cameras and the 65 m² spinnaker. Therefore a wide field of view is also required for C2-b). Furthermore a wide field of view improves large angles between perspective lines from all cameras (C4) (cf. figure 2.9).

GoPro cameras (cf. table 2.3) were chosen because the image quality is adequate, they are built for outdoor purposes thus watertight and shockproof and they have wide fields of view. Moreover various off-the-shelf mounts can be used to easily fit them wherever is needed.

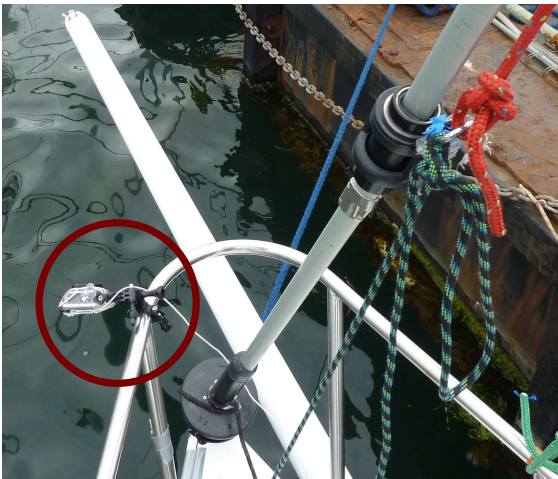
Nonetheless, this short focal lens (about 3 mm, i.e. 35 mm equivalent focal length of 17 mm) gives a barrel effect which must be corrected for photogrammetry measurements. A careful calibration should be carried out first.



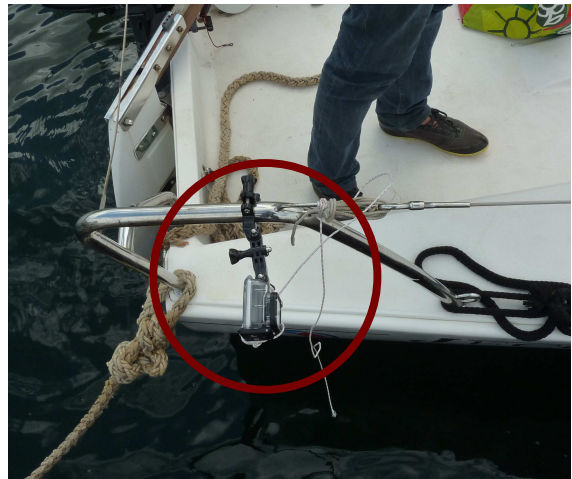
(a) Position of the 6 cameras used for the photogrammetric flying shape measurements (green dots).



(b) Position of camera GP3G on the foredeck.



(c) Position of camera GP3Y on the pulpit.



(d) Position of camera GP3W on the pushpit.



(e) Position of camera GP2G on the deck-hull connection on starboard side.



(f) Position of camera GP2Y on the deck-hull connection on portside and camera GP2W on the mast.

Figure 2.8 – Positions of cameras onboard the instrumented J/80 sailing yacht.

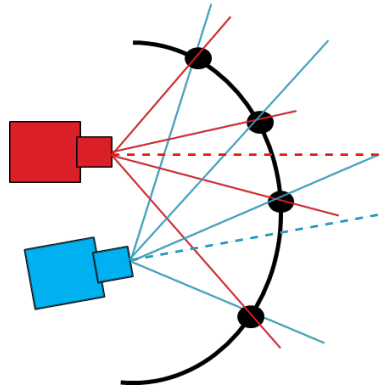


Figure 2.9 – Even if there is a small angle between the principal perspective rays (in dashed lines) of both cameras, due to their wide fields of view, for targets on the edges (black points) angles between perspective rays can be wider.

camera type	GoPro Hero2	GoPro Hero3 White	GoPro Hero3 Black
number of cameras used	3	1	2
focal length (mm)	3	3	3
aperture	f2.8	f2.8	f2.8
sensor size (Mpx)	11	5	12
optical size	1/2.3"	1/2.5"	1/2.3"
sensor type	CMOS rolling shutter	CMOS rolling shutter	CMOS rolling shutter
video resolution	1920x1080	1920x1080	2560x1440
video format	16:9	16:9	4:3
field of view (hor x ver)	120°x64°	120°x64°	120°x90°
frame rate (fps)	25	25	25
output format	mpeg4 h264	mpeg4 h264	mpeg4 h264
size with housing (mm)	72x65x46	72x65x37	72x65x37
weight with housing (g)	190	180	180

Table 2.3 – Technical specifications of cameras used for flying shape measurements

2.3.3 Calibration

Prior to photogrammetry measurement, a calibration process is required to evaluate the focal length, the principal point position and also the lens distortion for each used camera. Further details on the equations used for calibration are in Appendix A.

Figure 2.10 shows the strong distortion due to the "fish eye" lens of a GoPro and demonstrates the importance of a good calibration process. Note the straight forestay on the corrected photograph which appears curved on the raw image due to the barrel effect.

In this project, to calibrate the cameras, the principle of photogrammetry is used in a "reverse-engineering" way. Many fixed targets are seen by photographs taken by a unique camera from different

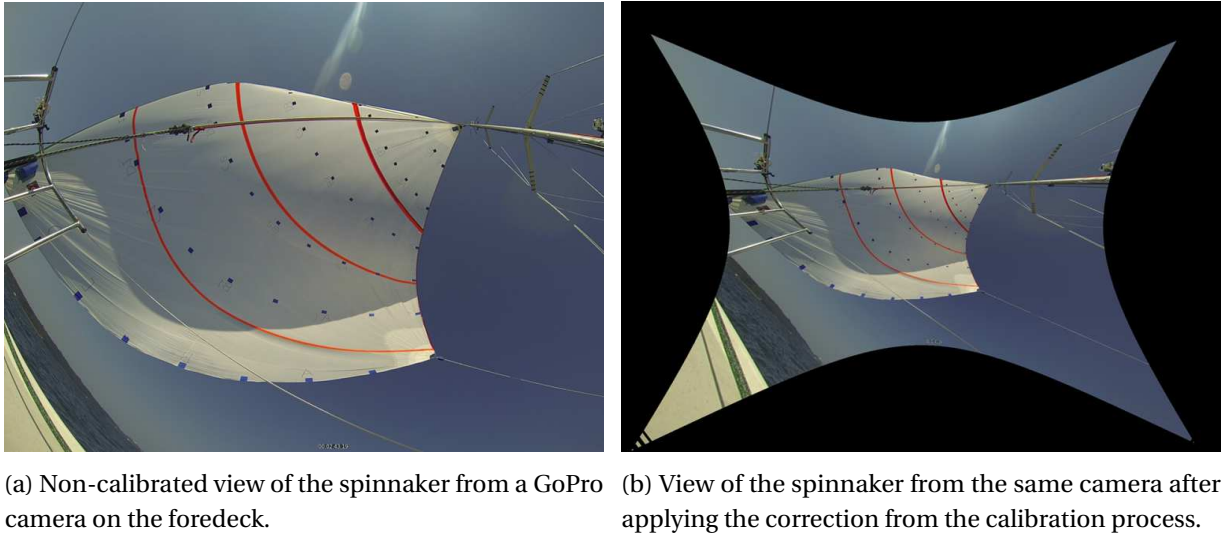


Figure 2.10 – Same photograph before and after the corrections from the calibration process which removes the barrel effect of the GoPro lens.

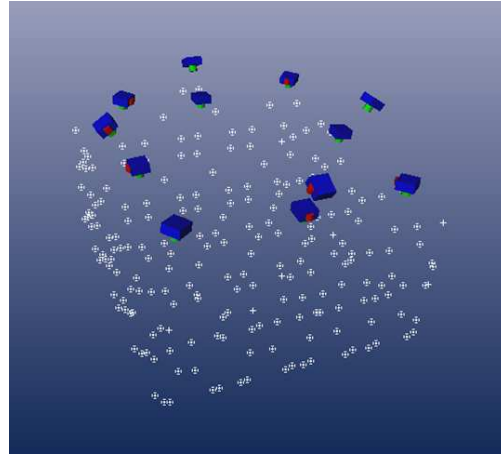
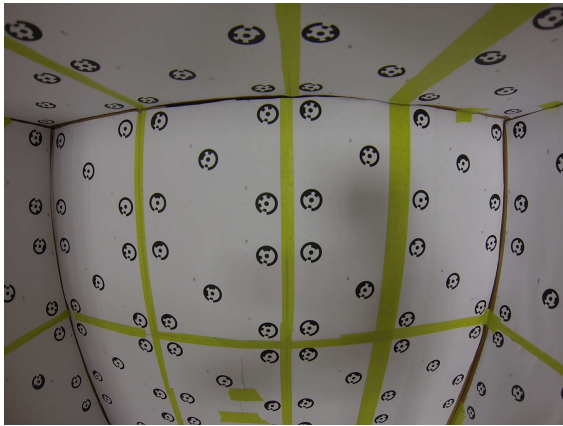
locations. For every target, all the perspective rays from the different photographs displaying the target should cross each other correctly at a unique location, if a perfect calibration is set. An optimisation algorithm finds the optimal calibration parameters to satisfy these conditions with the minimum uncertainty. Cameras with a wide field of view are used. Thus a box with targets is created. Photographs were taken inside the box (cf. figure 2.11) to get most of the perspective lines perpendicular to the target planes (sides of the box).

For calibration, the cameras were equipped as they are during the on-water experiments. Each camera has its own transparent watertight case, with some rain-repellent applied on it. Videos were recorded and frames were extracted to create photographs for calibration.

The calibration results (cf. table 2.4) confirm what we explained in subsection 2.3.1 and in Figure 2.6: with GoPro cameras, it would be possible to reach the "average accuracy" standards according to the thresholds set by *Photomodeler*. Calibration of cameras with a big fish eye effect is complicated, and it is hard to reach the criteria for highest accuracy projects with subpixel precision. Nevertheless, according to the developers of the software *Photomodeler*, we achieved good calibrations with low-cost cameras. Detailed calibration parameters for each camera are presented in Appendix A.

Table 2.4 displays the tightness. The tightness of a point relates to how well its defining perspective rays intersect. The better and closer they intersect in 3D space, the smaller the tightness value. The percentage is the ratio between the minimum distance between the perspective rays of one point and the maximum diagonal extents of the 3D data in the project.

Table 2.4 displays also the residual error. When the 3D position of a point is calculated, PhotoModeler can project it back onto the photograph (using the perspective ray). The distance between this projection and its actual marked position on the photograph is calculated and gives the residual error. The RMS residual of one point is the Root-Mean-Squared of the residual of this point on all photographs where it is marked.



(a) An example of photographs used for calibration. (b) 3D photogrammetric representation of the calibration box with the position and orientation of photographs used for calibration.

Figure 2.11 – Calibration box used to determine intrinsic parameters of lens distortion of cameras.

Resolution	Tightness (%)		Max angle (°)		RMS Residual (px)		Largest Residual (px)	
	average	max	average	min	average	max	average	max
GP2G 1920x1080	0.08	0.22	63.8	33.3	0.81	2.91	1.21	3.88
GP2W 1920x1080	0.07	0.21	63.7	34.7	0.74	2.11	1.10	3.06
GP2Y 1920x1080	0.06	0.21	62.8	32.5	0.55	1.73	0.85	2.20
GP3G 2560x1440	0.05	0.20	61.7	75.6	0.49	2.61	0.79	2.87
GP3W 1920x1080	0.05	0.12	59.9	20.8	0.46	1.68	0.71	2.12
GP3Y 2560x1440	0.04	0.13	64.0	30.9	0.36	0.49	0.75	2.67
"Highest accuracy"		0.03		30		0.9		1
"Average accuracy"		0.1		20		3		5

Table 2.4 – Results of calibration for each camera.

"Max Angle" indicates for each point the maximum angle (the largest, best angle between all perspective ray pairs). In Table 2.4, for every camera, the average maximum angle and the smallest maximum angle for one point are displayed.

"Highest accuracy" refers to thresholds set by *Photomodeler* to obtain high-accuracy industrial surveys with a sub-pixel precision. "Average accuracy" refers to thresholds set by *Photomodeler* to obtain good quality projects.

Calibration of the cameras used for the flying shape acquisition is on average closer to the "Average accuracy" thresholds and extreme values are closer to the "Highest accuracy" thresholds. According to the calibration results we obtained, it is possible to reach an accuracy of 1 part in 5000 meaning an accuracy of 2 mm at 68% probability (one standard deviation) which is completely satisfactory for our measurements.

2.3.4 Photogrammetric measurements

To measure the flying shape of the spinnaker, the sail is fitted with 100 mm × 100 mm wide dark blue markers at 51 selected locations (cf. fig E.9a and fig 2.2). There are six rows of markers stuck on the sail cloth, that divide the luff and leech lengths in 6 equidistant sections. For every row, the markers are evenly distributed. Since more curvature is expected at the luff, an extra target is added in the first 10% of the row near the leading edge. The corners of the sail (head, tack and clew) are also marked.

During the experiments, movies of the sails are recorded locally in cameras in their micro-SD cards. After synchronization (more explained in subsection 2.3.6), videos are extracted frame by frame as .png images. A set of 6 synchronized photographs are used to reproduce the 3D shape of the sail at a specific timestamp. For motion projects, targets are tracked frame after frame to recompute the flying shape resolved in time. These targets create a 3D point cloud.

However this point cloud is not scaled or oriented in a specific frame. The "Z" axis is defined by 2 points located on the bottom half of the mast, and the Y axis by 2 points on the pulpit on portside and on starboard side. The scaling is done by referencing many distances measured on the boat after the experiments (i.e. between spreaders, from tack point to mast foot, from tack point to head point, etc.). These distances should be as far as possible in the order of magnitude of the size of the sail. Strong hypotheses have been made here: we assume some distances between points are fixed during the experiments, and the points defining the frame are correctly vertically or horizontally aligned. It is debatable but it gives the best achievable compromise. In further experiments, targets on the boat should be purposely placed to define a precise boat frame.

Finally point rows are lofted to create spline curves. From these curves, a Non Uniform Rational B-Splines (NURBS) surface is created to represent the 3D shape of a flying spinnaker. This 3D surface is inserted in a 3D model of the J/80 sailing yacht created with the software Rhinoceros 3D. Small adjustments in rotation and translation of this surface can be made to fit the 3D-model.

2.3.5 Accuracy of the flying shape acquisition system

To quantify the accuracy obtained by this flying shape acquisition system, we used 4 flying shapes measured at different Apparent Wind Angle (AWA) (from 64° -tight AWA- to 141° -deep AWA-). They are characteristic of the range of shapes we want to acquire.

2.3.5.1 Precision

Calculating the positions of the cameras and points on the spinnaker is an iterative process. Thus the uncertainties on positions - the residuals - are analysed.

Table 2.5 shows the precision defined as one standard deviation based on the post-processing covariance matrix of the 3D object points. The second column shows the average precision of all points computed for each apparent wind angle. The next three columns are the breakdown of this average precision in the boat frame. The precision is displayed and scaled up 20 times in Figure 2.12 as the "confidence region" for every point.

AWA	Average Precision (mm)	X Precision (mm)	Y Precision (mm)	Z Precision (mm)
64°	38	13	12	29
96°	30	12	10	24
124°	27	11	9	21
141°	21	9	7	16

Table 2.5 – Standard deviation in mm based on the post-processing covariance matrix of the 3D object points. The three last columns analyse the average precision in the boat frame (X longitudinal, Y portside and Z upwards).

The precision is on average better by 40 mm. We are far from the precision of 2 mm expected in subsection 2.3.1. Nonetheless this precision of 0.3% of the luff length is satisfactory. Precision in Z axis (upwards) is worse than in other axes due to similar height positions of camera -on the deck. At the head of the spinnaker, about 10 m away from the cameras, the angles between the perspective rays from cameras are sharp and the markers at the top of the spinnaker have lower resolution. This is why in Figure 2.12 points near the spinnaker head have a larger confidence region. Only 3% of all the computed points have an error larger than 100 mm. The principal direction of the confidence region is perpendicular to the spinnaker surface. Thus we might be less precise on the camber of the sail. More details on the precision of the flying shape acquisition system can be found in Appendix A.

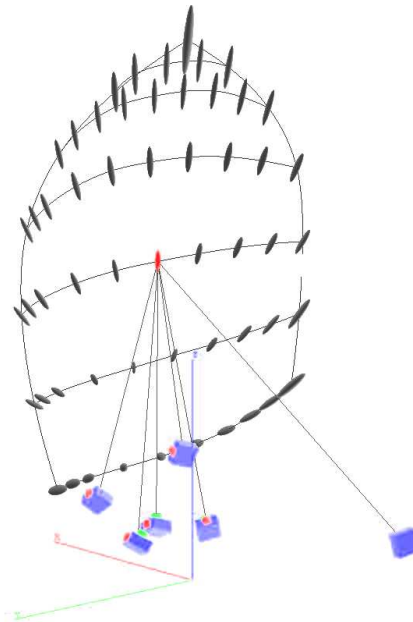


Figure 2.12 – Perspective rays (black lines) from cameras (in blue) to one point on the spinnaker (in red). Every bulb represents the confidence region for every point. Bulbs are scaled up 20 times.

Reference	Design shape			Curved stripe lengths					Sail area (m ²)
	foot (m)	luff (m)	leech (m)	S1/6 (m)	S2/6 (m)	S3/6 (m)	S4/6 (m)	S5/6 (m)	
	7.30	12.18	9.65	7.45	7.60	6.85	5.05	2.50	68.5
AWA 64°	7.24 -0.84%	12.26 0.64%	9.72 0.77%	7.73 3.73%	7.80 2.62%	6.89 0.65%	4.93 -2.28%	2.50 -0.05%	66.5 -2.92%
AWA 96°	7.09 -2.90%	12.20 0.14%	9.66 0.06%	7.52 0.99%	7.62 0.26%	6.87 0.24%	5.01 -0.87%	2.55 2.15%	65.1 -4.96%
AWA 124°	7.24 -0.89%	12.39 1.69%	9.83 1.91%	7.72 3.65%	7.87 3.50%	7.07 3.17%	5.17 2.31%	2.59 3.68%	68.7 0.29%
AWA 141°	7.20 -1.38%	12.33 1.19%	9.77 1.19%	7.68 3.07%	7.83 2.98%	7.01 2.37%	5.07 0.31%	2.52 0.66%	67.4 -1.61%

Table 2.6 – Lengths measured with the flying shape acquisition system for different apparent wind angles compared with lengths measured on the design shape for the foot, luff and leech and measured on ground with a measuring tape for the other stripes (first lines). SX/6 are the spline curves created from the rows of targets at different heights (1/6th, 2/6th, 3/6th, 4/6th and 5/6th of the spinnaker height starting from bottom). Percentages are the ratio between the difference of measurements and the reference measured lengths (on design shape or on ground).

2.3.5.2 Accuracy

Comparing the lengths measured on the design shape with those from the flying shapes is a way to evaluate the accuracy of our system. Table 2.6 shows the lengths of the luff, leech and foot for the four different apparent wind angles calculated by our photogrammetry acquisition system. It also shows the lengths of the spline curves created from the different rows of targets. The lengths of the rows of targets are measured with a measuring tape on ground with no tension applied in the sail cloth.

For the edges of the sail compared with the lengths of the design shape, the errors are on average less than 1.2% for all apparent wind angles. The maximum error is found at the foot for AWA 96° with an error of -2.90%. The absolute difference is 0.11 m on average. The maximum absolute difference is found for the longest length, the luff, with 0.21 m at AWA 124° and at the foot for AWA 96° with -0.21 m.

For the stripes, the uncertainty of measurement of long curved lines on ground with a measuring tape is about 0.1 m mainly due to the stretch applied on the sail while measuring. Therefore any comparison with these stripes is only indicative and are not as precise as the lengths of the edges from the design shape. The errors for these stripes are less than 4% with an absolute difference of 0.28 m for AWA 64°. Most of all the stripe dimensions displayed in Table 2.6 are overestimated. To cancel out this average difference, ground measured lengths should be increased by 1.7%, which is consistent knowing the possible measurement errors with a ruler and the elasticity of the sail. This ratio is indeed of the order of magnitude of elongation of a spinnaker cloth for the loads measured during our experiments (around 400 N). If we apply this correction on the referenced lengths, the absolute maximum difference is now 0.15 m (instead of 0.28 m), and the average absolute difference is 0.09 m (instead of 0.20 m). These errors with correction are similar to the errors from measurements of the foot, luff and leech: about 0.10 m of difference on average and 0.20 m for the maximum absolute difference.

The errors on the Sail Area is higher than for the lengths. Small variations of length might affect even more

the sail area variations. The sail area is mainly underestimated with a maximum absolute difference of -4.9%. Figure 2.12 highlights that the principal direction of the uncertainty in the measurement of the points is perpendicular to the sail, and is also the depth of most of the cameras. Therefore the camber of the sail is less accurately measured and the sail area is underestimated if the sail is measured with less camber.

The utopic accuracy of 2 mm as forecasted in subsection 2.3.2 is not achieved as could be expected. The precision is better by 40 mm and the accuracy on measured lengths on the sail is no more than 200 mm and on average about 100 mm only. This accuracy of less than 3% (1.5% on average) is correct and can give us some reliable data on the overall dynamic flying shape of the spinnaker. Better cameras could improve the accuracy of our measurements. It is further described in subsection 2.3.7.

2.3.6 Synchronization with other data

At the time the experiments were imagined and prepared, the latest accessories that appeared with GoPro cameras or other outdoor purpose cameras such as remote control, wifi connection etc. did not exist. These accessories could have made the experiments easier. However, at the back GoPro Hero 2 has a bus interface connector. The functions of the pins of this connector were identified and used to switch the camera on and off as well as to start recording or to watch what the camera was filming. A custom-modification at the rear of the camera and its housing enabled us to control all the GoPro Hero 2 cameras at the same time from inside the boat via cables connecting the cameras with a control station. Later, we were able to use GoPro Hero 3 cameras as well that can be controlled together via a remote control.

During the experiments, the Hero 2 and Hero 3 cameras were switched on and they started recording respectively thanks to the control station and the remote control. Then the recording of other data (loads, wind, etc.) on the acquisition system was launched. Because the cameras recorded the videos locally on an SD-card and the acquisition system the other data on its own hard disc drive, synchronisation between them was required. A clear physical impact on the forestay is filmed by the cameras and is recorded by the forestay load measurement in the acquisition system at the beginning and at the end of the run. This hit makes it possible to adjust the videos and the data together. Moreover for precise synchronisation, a laser aiming the sail was switched on every 10 s for 10 ms (about 2 frames). This laser was controlled by a TTL signal from the acquisition system. Therefore thanks to the laser signal seen on the sail in the videos, a precise adjustment was possible. It proved there was no noticeable drift of the internal clocks of the cameras during runs of 4 minutes. With this system, synchronisation between the flying shape measurement and the other data has a precision of one frame period: $1/25 = 0.04$ s. For dynamic behaviour of the order of 1 s, this precision is sufficient.

2.3.7 Further improvements

As described before in subsection 2.3.2, GoPro cameras have many advantages:

- outdoor purpose. Shockproof and waterproof
- affordable price
- Wide field of view
- Widely used, many advice to tune and improve GoPros.

However they also have some drawbacks that reduce the quality of our measurements:

- Rolling shutter
- Moderate lens quality
- Process of the image and compression not really known and not customisable
- Cannot be manually synchronized on specific timestamps.

To improve the precision of our measurements, it has been decided to look for higher quality cameras that have the same advantages as the GoPro cameras but also do not have their drawbacks. The chosen cameras are Basler acA2040-25gc with a KOWA lens LM6HC (see specifications in table 2.7). Despite a slightly smaller field of view, they have a bigger optical sensor (1" instead of 1/2.3") which can receive more light and has a better resolution. Moreover they possess a global shutter and not a rolling shutter. A global shutter captures the whole scene on the sensor at a single instant in time. While a rolling shutter scans across the scene rapidly. This produces distortions for fast-moving objects which might affect the quality of our measurement. Furthermore these new cameras can be synchronised with the other data thanks to an external trigger signal. Better simultaneity between photographs would improve the measurement accuracy. The video format can be chosen. Specific watertight housings have been purchased that prevent cameras from overheating. These cameras will be used in future experiments, not yet carried out at the time of writing of this thesis.

Furthermore the choice of squares as sub-pixel targets was not the most appropriate. It did facilitate the cut and the preparation on the sail, but the automatic detection algorithm looks for circles or ellipses and not squares. Therefore sub-pixel rounded targets would improve the accuracy and increase the speed of the detection and tracking process.

Finally to place the spinnaker onto the boat frame more precisely, precise target points with known positions should be placed on the deck and mast.

Now that the photogrammetry flying shape acquisition system has been described, the other sensors are presented. In the next section, load sensors are described.

BaslerA2040-25gc with a Kowa lens LM6HC	
number of cameras used	4
focal length (mm)	6
aperture	f1.8-16
sensor size (Mpx)	4
optical size	1"
sensor type	CMOS global shutter
video resolution	2046x2046
video format	1:1
field of view (hor x ver)	100°x80°
frame rate (fps)	up to 25Hz
output format	various choice
power supply	2.9 W using Power Over Ethernet

Table 2.7 – Specifications of new cameras to be used in future experiments.

2.4 Load measurement

One way to acquire aerodynamic loads produced by the sail and transmitted to the yacht is to measure the loads on standing and running rigging. Even though the total aerodynamic load transferred to the hull and thus opposed to the hydrodynamic load is not completely quantified (the loads in the mast transferred to the hull is not measured for example), loads monitored on the corners of the sails, on the shrouds and on the forestay and backstay provide many useful data.

2.4.1 Load sensors on standing and running rigging

2.4.1.1 Description

For the instrumentation of the rigging, the acquisition system used for these experiments was the one developed during the PhD project of Benoit Augier ([Augier, 2012]).

Sixteen load sensors are used, 7 on turnbuckles (3 shrouds on each side plus the forestay), and 9 on shackles.

The load sensors are custom-built by assembling strain gauges on off-the-shelf Sparcraft turnbuckles and on Wichard shackles (cf. figure 2.13). Therefore the usual sailing configuration of the sailing yacht is maintained except that cables from the shackles and turnbuckles need extra care when preparing the yacht for experiments and sailing. Sail and rig tuning used in regattas can be applied and experiments in real sailing conditions can be carried out. The strain gauges are set in a Wheatstone bridge configuration on each side of the shackles or turnbuckles where a flat surface has been machined. The loads applied where the strain gauges are located are traction loads only. It is a bit more complex for the "U-shape" shackles. Nevertheless having the strain gauges on each side of the "U" means that the flexion load can be cancelled out. For more details, the reader is referred to [Augier, 2012].



Figure 2.13 – Picture taken during experiments showing load sensors on the shackle of the jib sheet, and on the shrouds on portside.

All wired load sensors are connected to the acquisition system via a specific Analog-Digital Converter (A/D converter). In 2013, A Spider8 from *HBM* was used, and in 2014 a specific module of the CompactRio from *National Instruments* was used. Nevertheless both have the same function and similar specifications. They convert electric measurement of the strain gauges to digital signals. They also amplify the signals and balance the Wheatstone bridges for correct measurements without noise. Each channel works with a separate A/D converter that is synchronised to ensure simultaneous measurement of all channels. A high resolution clock make instantaneous measurements possible without any time lag. The sampling rate of 25 Hz ensures the dynamical evolutions of loads for the dynamics we want to measure are correctly resolved.

The shackle measurement range is 5000 N. The turnbuckles plus one shackle for the mainsail sheet have a measurement range of 10 000 N. These measurement ranges correspond to the maximum working loads.

2.4.1.2 Calibration

A thorough calibration was carried out. The calibration process is strongly inspired from [Augier, 2012] to quantify the errors of trueness, precision, hysteresis and finally accuracy of the strain gauges. Load sensors are assembled in series hanged on a hook linked by textile shackles (cf. figure 2.14). They are

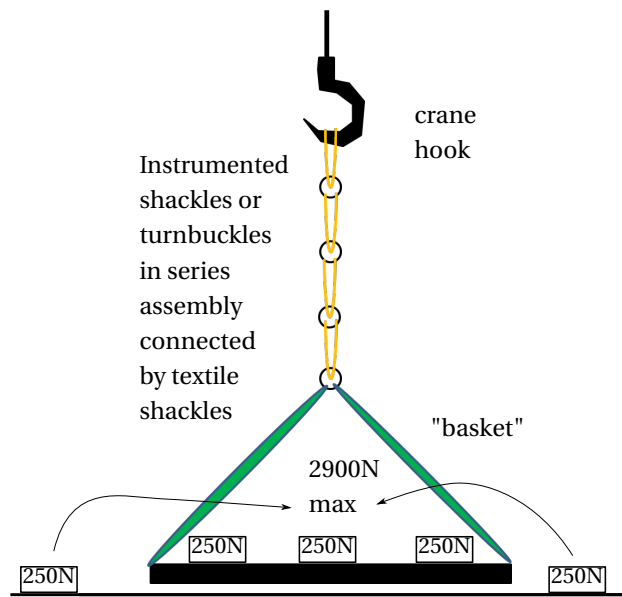


Figure 2.14 – Scheme of arrangement used for calibration of load sensors.

loaded several times thanks to known calibrated weights added in a basket and then removed in 12 steps. At each step, the voltages of the load sensors are recorded. The calibrated weights are from 190 N up to 2900 N for the shackles and from 2300 N up to 5000 N for turnbuckles. These weights are in the range of actual loads in real sailing conditions. This procedure is repeated 5 times to quantify the different errors.

Finally the errors on the measurement range were below 2% maximum which represents an uncertainty of 100 N for the shackles and 200 N for the turnbuckles. On average the accuracy is below 0.6% which represents an uncertainty of only 30 N for the shackles and 60 N for the turnbuckles. For detailed results, the reader is referred to Appendix B. As in [Augier, 2012], we wanted an accuracy lower than 2% of the measurement range. The lowest loads we recorded were at very large AWA (about 140°), for a True Wind Speed (TWS) of 12 kn. They were of the order of magnitude of 250 N. The achieved precision is sufficient for this specific worst case, and very good for other conditions (where we recorded loads mainly from 500 N to 1200 N).

Finally, at the beginning of every day of experiments, a "zero" was recorded. After a warm-up of the load sensors, gauge voltages were recorded with no load applied. These values were used to determine the offsets during the post-processing.

2.4.2 Spinnaker load sensors

Spinnaker points can move significantly. While sailing the clew point is only held by a line, the clew sheet from the aft of the boat, hence can be at various distance from the yacht. Moreover the spinnaker needs to be hoisted and lowered. Thus head and tack points shall not be wired to the acquisition system inside the boat. Two different configurations were used to measure loads at the 3 corners of the spinnaker.

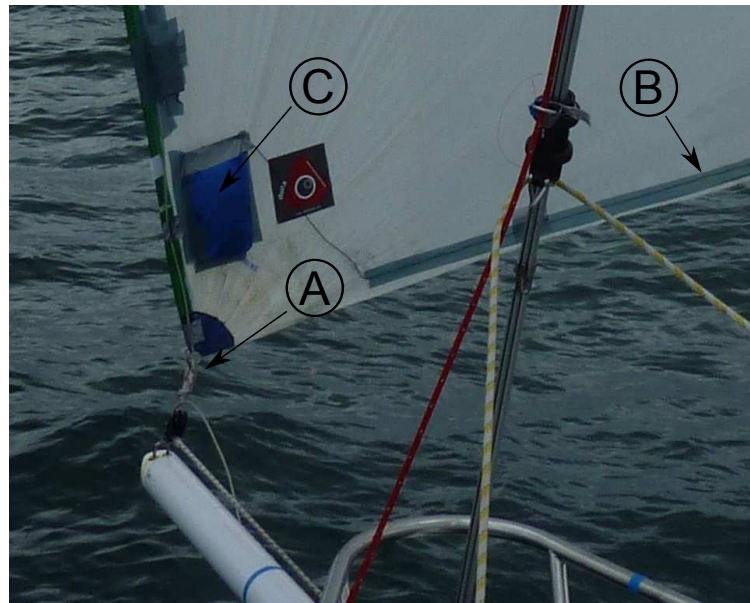


Figure 2.15 – Photograph of the spinnaker tack. Ⓐ: tack shackle wired to the acquisition box. Ⓑ: wire running along the foot from the clew shackle to acquisition box. Ⓒ: Acquisition box with strain gauge amplifiers, a microcontroller, a wireless transmitter and a battery.

2.4.2.1 Wireless shackles

Description In 2013, the same shackles presented in subsection 2.4.1 are used for the three corners of the spinnaker (Head, Tack and Clew). However they are not wired to the acquisition system and are linked to boxes placed at the head for the head corner and placed at the tack point for the tack corner and the clew corner thanks to a wire running along the foot through a facing (cf. figure 2.15). In each of the acquisition boxes, there is a strain gauge amplifier XN3 developed by *Texense* for each strain gauge. A microcontroller Arduino receives the amplified analogue signals and transmits them wirelessly to the acquisition system via a Zigbee network with a sampling rate set at 25 Hz.

Dynamics Since the configuration is different between wired and wireless shackles, I checked that no measurable delay was induced by the wireless communication for the load sensors at the spinnaker corners. A test before the experiments was carried out using the calibration experiment with some peaks of load. In series configuration, the three wireless shackles were placed with two wired shackles. The acquisition system was positioned about 10 m away from the calibration setup to represent the distance between the strain gauge at the head of the spinnaker when hoisted and the acquisition system. Signals from instrumented wireless shackles were just a bit noisier, but no delay was noticed on signals during a 5 min record. The wireless communication is fast enough to resolve the actual load dynamics.

Nevertheless, this wireless configuration is not ideal. The Wheatstone bridge needs to be well balanced (in a range of ± 2 mV) which cannot always be guaranteed even if a lot of effort had been put into

it. Moreover, the amplifier is not close to the strain gauge. Despite shielded cables, very low voltage signals transferred over several meters might become noisier.

Furthermore, this type of sensors records only the magnitude of the load vector. A downwind sail has strong variations of shape and therefore has a wide range of load direction. The same corner load for a specific AWA can contribute mainly to the heeling moment while for another downwind course (different AWA), it will mostly contribute to the driving force.

In order to resolve this issue, we used Directional Load Cell (DLC) for the experiments carried out in 2014.

2.4.2.2 Directional Load Cells (DLCs)

Description For the experiments carried out in 2014, 3 Directional Load Cells (DLCs) were used. They were conceived and manufactured by David Le Pelley, at the Yacht Research Unit at the University of Auckland in New-Zealand [Le Pelley et al., 2015]. A DLC measures the entire load vector: magnitude and direction. The norm of the load vector is measured thanks to strain gauges glued on a steel bar. The directions projected onto the boat frame are measured thanks to an IMU placed on this steel bar and compared with the attitudes of the yacht (heading, heel and trim) measured by another IMU placed inside the boat. In addition, in the wireless DLC, signals from strain gauge and IMU are converted into string sentences by a microcontroller and sent by a XBee emitter to the acquisition system at a sampling rate of 25 Hz. A Lithium-Ion battery powers the DLC with a 3 to 4 hours of autonomy. Figure 2.16 shows the DLC. Table 2.8 describes the specifications of the DLC components. The DLC is placed between the line (clew, head or tack line) and the corners of the spinnaker thanks to shackles in specific holes at the extremity of the steel bar.

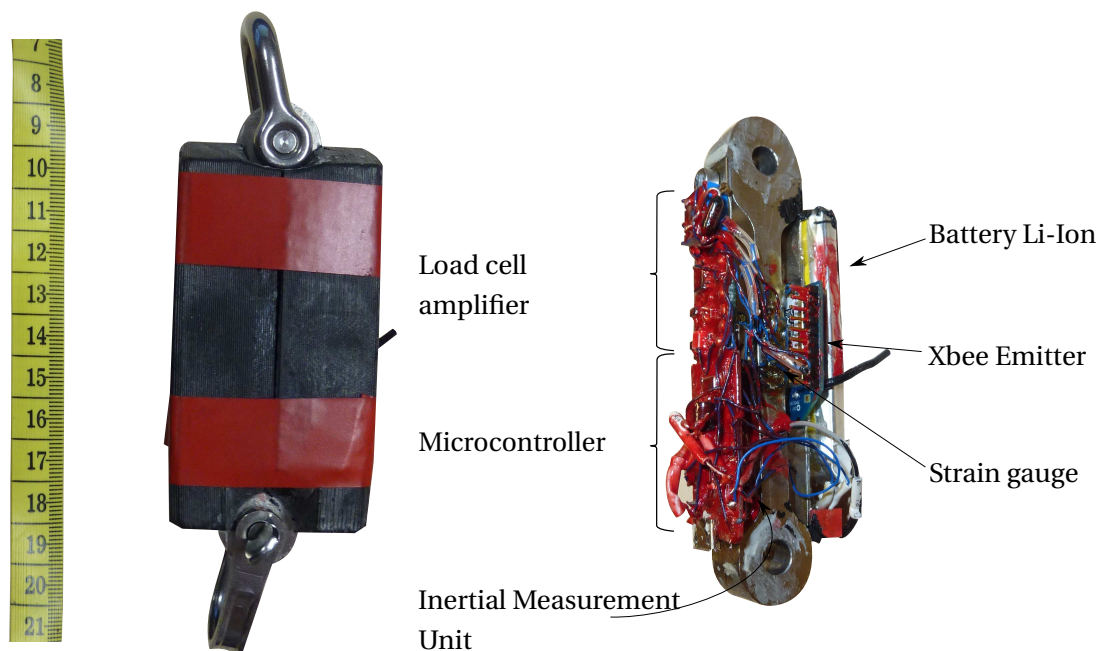


Figure 2.16 – Directional Load Cell (DLC) with its case and shackles (left), inside view (right).

Name	DLC			
Sensor used	Inertial Measurement Unit			Load Cell
	9 DOF sensor-stick SEN 10724			
	Accelerometer	Gyrometer	Magnetometer	
	ADXL345	ITG3200	HMC5883L	
Range	±4 g	±2000°/s	±1.3 G	0 N to 5000 N
Resolution	4 mg/unit	14.375 unit/(°/s)	0.92 mG/unit	0.3 N/unit
Precision	1%	2%	2°	<1.5%
Communication	i2C			i2C via A/D-C
Microcontroller	Sparkfun ProMicro 3.3V/8MHz			
Sampling rate	25Hz			
Communication	Serial digital using Zigbee network			
Power supply	5 V via Li-Ion battery			

Table 2.8 – Specification of a Directional Load Cell (DLC)

Like other load sensors, calibration is required to determine the gain and the errors to be applied to compute the actual load. Moreover specific calibration for the IMU is needed to measure directions as accurately as possible. This last calibration will be explained in more detail in the next subsection.

Load calibration The same calibration test as described in section 2.4 was applied to the DLCs. One would expect lower errors since the steel bar fitted with the gauges works in pure traction. However, the reference voltage depends on the charge of the battery. If the battery is low, the reference voltage used in the strain gauge will be affected and therefore the output voltage giving the actual load will be affected too. Moreover, when the XBee emitter starts sending data, it slightly lowers the reference voltage. The reference voltage returns to its initial value after a short but non insignificant time. This is the reason why I optimised the code in the microcontroller to reduce calculation time during measurements and to place the emission in the algorithm loop as late as possible from the reading of the strain gauge voltage. Nevertheless, the calibration of the load sensor depends on the sampling rate defined in the microcontroller.

	Sensitivity unit/kg	Offset unit	Errors % on Measuring Range			
			hysteresis	trueness	precision	Accuracy
DLC6-Head	36.94	9477.8	0.04	0.23	0.34	0.41
DLC7-Tack	36.87	10365.9	0.05	0.24	1.60	1.62
DLC8-Clew	34.47	10583.2	0.12	0.20	1.47	1.49

Table 2.9 – Load calibration errors for Directional Load Cell (DLC) in 2014 for a 25 Hz sampling rate.

Table 2.9 shows the results for a sampling rate of 25 Hz used during the experiments. It demonstrates that when the battery is sufficiently full, the precision is below 2% (100 N of precision). Therefore, we

were confident in the load data of the DLC. Nonetheless a good battery voltage is required to keep this precision. If the battery is low, the imprecision is increased by a factor 10. The signal is much noisier and measurements are rejected.

Dynamics Between the reading of the sensors and the reception of data in the acquisition system, the sentences sent by every DLC are timestamped as soon as they are received by the acquisition system. There are several steps that can take time. The microcontroller in the DLC communicates with the sensors using i2C protocol which enables fast communication at a high rate (about 100 Hz). I optimised the algorithm loop "reading-emitting" in order to have as few calculations as possible made by the microcontroller and thus try to prevent any lag. Finally the three DLCs send wirelessly at their own flow their signals to a unique XBee receiver. The Zigbee¹ protocol is used to deal with multiple emitters on one receiver. However one cannot guarantee the precision in time on the data received. The microcontroller timestamps with its own clock when it reads the load values. Therefore in every sentence in addition to the IMU and the load data, there is one timestamp given by the microcontroller and one timestamp given by the acquisition system at reception. However the internal clock of Arduino is known to deviate in time and to be not really accurate. Therefore only the timestamp of the acquisition system at the reception is used.

During a calibration test of DLCs, a wired shackle defined as a reference was also assembled in series. A small delay was detected for the DLC load signal -timestamped with the acquisition system- compared with the load of the wired shackle (cf. figure 2.17). This shift is not constant but is about 0.1 s. We could not really determine why this shift is present. For loads recorded at 25 Hz, this incertitude of 0.1 s is rather large. But the DLC architecture should have been modified significantly to correctly deal with dynamic data, which was not the first aim of the DLC. This is out of the scope of this PhD project and we just have to keep in mind, a shift of order 0.1 second might exist in the DLC data.

Load direction One of the main interesting features of the DLC is the measurement of the load direction, hence the measurement of driving and side forces if they are projected onto the boat frame. In each DLC, an IMU gives the attitude of the sensor, the load frame. Another IMU called *Base Unit* is located inside the boat near its centre of rotation and determines the orientation of the boat, the boat frame. These frames measured by IMUs are represented in the Earth's frame (\underline{X} pointing towards the magnetic North, \underline{Y} to the West and \underline{Z} pointing in the opposite direction to gravity). The load frame therefore needs to be projected onto the boat frame to compute driving and side forces. For this project, the quaternion representation is used. Using the quaternion representation makes calculations easier without any special cases -like the gimbal lock²- as could happen with Euler angles. For further details on quaternions and the calculation to project the force on the boat frame, the reader is referred to Appendix C.

¹Zigbee is a specification for wireless communication protocols used in systems where small and low-power electronics are used. XBee are product names for radio communication modules using the Zigbee protocol.

²When the orientation can be defined by only 2 Euler angles, losing a degree of freedom, like an orientation pointing upwards. Mathematically, a singularity is reached which needs a specific case in the algorithm.

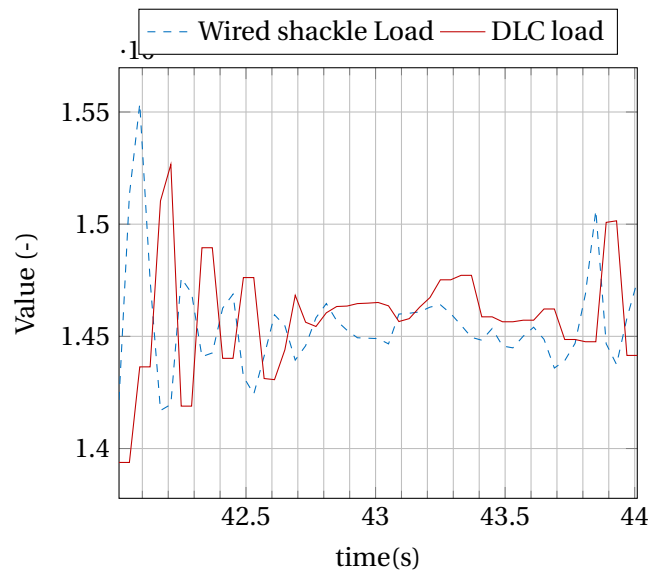


Figure 2.17 – Evolution of loads in time. A delay of about 0.1 s is found for the load measured by the DLC compared with the load measured by a wired shackle.

The vectorial sum of all DLC loads gives the total aerodynamic force created by the spinnaker in the boat frame. However, one should be aware that computing the loads relative to the boat frame can deal with small angles and especially with the heading angle. And yet, it is known to be difficult to measure the heading angle precisely with an IMU because the measurement depends on the magnetic environment. Moreover the heading of the DLC is compared with the heading of the boat via a reference which is the magnetic North, difficult to pick up. Furthermore, the *Base Unit* is placed inside the boat -where we do not have any easy visual references- with a precision of about 5° .

Precision of the load directions To assess the precision of the load directions measured by the DLC, I used the same AWA used for the verification of accuracy of the flying shape acquisition system described in subsection 2.3.5. The total aerodynamic load created by the spinnaker is calculated for these 4 AWA. Since we had an incertitude of about 5° on the orientation of the *Base Unit*, the projected loads were calculated with virtual shifts of 5° of the *Base Unit* independently in heel, in trim, or in heading.

In figure 2.18(left), the variations of the total aerodynamic loads FX, FY and FZ are plotted as a function of the AWA, if the *Base Unit* -the boat reference frame- is shifted by either 5° in heel, or in trim or in heading. The load projected onto the axis of rotation is not affected by this rotation. Thus only two projected loads are plotted for each rotational shift. Figure 2.18 demonstrates that projected aerodynamic loads vary no more than 100 N which is also the precision in load of the DLCs. A change of 5° in trim affects mostly FZ, and a change of 5° in heading, FY.

Figure 2.18(right) shows for each AWA the ratios of the variations of projected aerodynamic loads due to a rotational shift of the *Base Unit* with their measured loads. FX is only slightly affected with a reduction

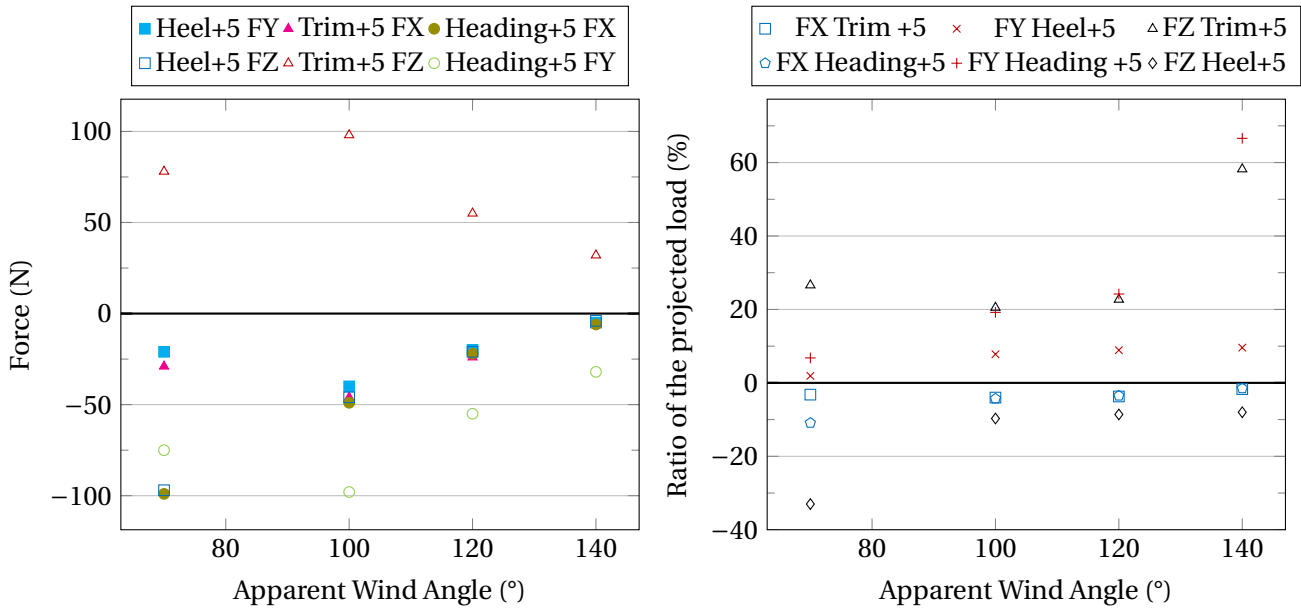


Figure 2.18 – Difference of projected loads (left) and Ratio of projected loads (right) if the Base Unit is shifted by 5° in three directions.

of its magnitude of 5% on average. FY is overestimated by 10% if the *Base Unit* is shifted by 5° in heel. With a rotational shift of 5° in heading, FY is more and more overestimated when the AWA is increased because FY decreases: at AWA 70°: +7% ($F_{Y_{AWA70}} = 1100N$); and at AWA 140°: +67% ($F_{Y_{AWA70}} = 50N$).

There are two main imprecisions: the *base unit* should be precisely positioned and the DLCs can hardly measure directions with a precision better than 5°. As explained before, an IMU is strongly influenced by its magnetic environment even after calibration and the algorithm estimating the Euler angles or quaternions from raw measurements from the accelerometer, gyrometer and magnetometer is not perfect. There are several algorithms that are open source or not having their own advantages and drawbacks. For all the IMUs used for these experiments, we used an open source algorithm from [Madgwick et al., 2011]. This algorithm is nowadays widely used in the Open Source community and therefore the code is available with many feedbacks and comments.

Finally the precision in the load direction is in the order of the precision of the load magnitude (about 100 N). However when the total aerodynamic loads measured at the head, tack and clew are projected onto the boat frame, better precision is needed. The projected loads can be modified by 10-20%.

2.4.2.3 Conclusions on spinnaker load acquisition

For both experimental campaigns, spinnaker load sensors were used (wireless shackles or Directional Load Cells (DLCs)). Wireless shackles have a slightly better precision (less than 1%) which is not affected by the voltage of the battery as is the case for the DLCs. The signal recorded by wireless shackles is also less noisy. Wireless shackles measure loads more precisely but do not measure any direction of the load. For DLC, the accuracy for measurement of the load magnitude is correct (lower than 2% of the measurement

range, thus about 100 N). This precision is however not very good for running courses (large AWA) where small loads (about 250 N) are measured.

The precision in time of the wireless shackles seems to be good enough for the dynamics we want to measure (easing of the clew sheet, flapping of the luff, dynamic behaviours of the order of magnitude of 1 s). For the DLCs, a time lapse of about 0.1 s exists which is not constant. However this imprecision is still reasonable if we do not look for any small phase shifts between loads and/or motion.

Wireless shackles cannot measure the direction of loads whereas DLCs measure the magnitude and the directions of the loads on the three corners of the spinnaker. The precision in direction is of the same order of magnitude as the precision of the strain gauges. The directions seem reasonably well estimated if we look at the main evolution of the loads according to the AWA. But we might lack precision if we want to project aerodynamic loads with a precision better than 10%.

2.5 Pressure acquisition system on spinnaker

During the experiments carried out in 2013, pressure distribution was measured on the spinnaker thanks to a system developed and built by the Yacht Research Unit of the University of Auckland, New Zealand [Le Pelley et al., 2012] which participated in these experiments.

Measuring pressures on downwind sails is not an easy task due to the light sail cloth, high displacement of the spinnaker and the high range of pressure encountered in downwind courses. The pressure difference is measured between the suction and the pressure sides and not between the absolute pressure on one side only and a pressure reference that is complex to precisely acquire. Table 2.10 shows the estimated differential pressure ($\frac{1}{2}\rho AWS^2 \Delta C_p$) for a TWS of 12 kn (6 m/s) should vary between 6 and 110 Pa. The orders of magnitude of ΔC_p are found in [Larsson et al., 1994, Fossati, 2009, Viola and Flay, 2009]. With stronger winds the expected maximum differential pressure should be around 250 Pa.

TWS ρ_{air}	12 kn (6 m/s) 1.25 kg/m ³	
AWA AWS	80° 15 kn (8 m/s)	140° 6 kn (3 m/s)
average $ \Delta C_p $ $P_{average}$	1 37 Pa	1 6 Pa
Peak $ \Delta C_p $ $P_{average}$	3 110 Pa	3 18 Pa

Table 2.10 – Order of magnitude of differential pressure expected for a TWS of 12 kn (6 m/s).

2.5.1 Description of the pressure system

This pressure measurement system is made up of 44 differential pressure sensors located on the spinnaker surface along 4 horizontal stripes at 1/4, 1/2, 3/4 and 7/8 height of the spinnaker from the foot (cf. figure 2.1). The first 3 bottom stripes have 12 sensors and the top one 8 because of the shorter curve length. Since the spinnaker is asymmetric, the leading edge is the same for both tacks. Thus on every stripe, we may specifically breakdown the pressure taps as more variation of pressure is expected at the leading edge. About half of the pressure taps are located in the first 25% of the curves.

Off-the-shelf piezoresistive sensors were chosen (cf. table 2.11). The sensor range is ± 1 kPa which is large enough not to deteriorate them. The resolution of 0.5 Pa is satisfactory for our purpose. Sensors with a better resolution and with a large enough range are rare and more expensive. These sensors are stuck on one side of the sail -at the pressure side when sailing on portside tack- and are positioned facing 2 mm-diameter holes on the sail to measure the pressure jump across the sail without significant air leak. On the side where the sensors are stuck, punctured light sail cloth patches, approximately 150 mm x 150 mm are placed over the sensor housings in order to smoothen the surface and not disturb the flow, hence the pressure measurement. It was decided to place the transducers at measuring locations to avoid noise and issues with long tubings that damper the dynamics (cf. figure 2.19).

Sensor type	Piezoresistive pressure sensors
Number used	44
Name of sensor	Honeywell XSCL04DC
Range	± 1 kPa
Resolution	0.5 Pa
Precision	< 8 Pa
Communication	Serial Peripheral Interface and Serial digital
Sampling rate	6 Hz to 7 Hz
Size	diam 40 mm x 10 mm thick
Power supply	5 V via USB

Table 2.11 – Specification of sensors used in the pressure acquisition system.

A piezoresistive sensor provides an analogue output which is amplified by an operational amplifier circuit located just next to the sensor in order to limit noise. A ± 2.5 V signal is transmitted via a ribbon cable which can handle amplified signals up to 8 transducers. In addition to the 8 wires for pressure signals, three more wires are needed in this ribbon cable (5 V to power transducers, 2.5 V for amplifier circuits, and GND). On the edge of the sail, an Analog-Digital Converter (A/D converter) terminates the ribbon cable. It converts the 8 analogue signals into 12-bit digital signals. A cable runs along the leech or the luff and links the A/D converters to an Arduino microcontroller placed on the foredeck (cf. figure 2.20). The microcontroller communicates with A/D converters via a Serial Peripheral Interface (SPI) protocol. It is a master-slaves communication. The microcontroller uses a clock signal to read the data one by one. The microcontroller sends a unique sentence to the acquisition system with all pressure values gathered. For further details on the pressure system acquisition, see [Motta et al., 2015].



Figure 2.19 – Top of the spinnaker where the 7/8 stripe and its 8 pressure taps are visualised. The squares around them corresponds to the contour of light sail cloth patches.

2.5.2 Zeroing and accuracy of pressure sensors

Several tests carried out on the pressure acquisition system are described in [Motta, 2015]. Variations of temperature in a range of 2°C to 3°C do not alter the pressure measurements. However the orientation of the transducers makes the measured pressure vary because of the sensor membrane weight. The difference of pressure has been measured between a transducer at a horizontal position and the same transducer rotated by 180° - now the face which was up is down-. The average difference between both positions is 7.9 Pa, and the average difference between a horizontal position and a vertical position (rotated through 90°) is 4 Pa.

A zeroing procedure is therefore applied. With the spinnaker in the bag, before hoisting and after lowering the spinnaker, a pressure measurement is carried out for 10 s. The bag is flipped over (the face which was up is now down) and another pressure measurement is carried out. The average of the two measurements gives the zero for each transducer. The zero value obtained through this procedure is close to the correct value for a sensor oriented vertically as most of them are on the sail while sailing. Better zeroing procedure could have been followed such as laying down the spinnaker on both sides before going on water for example. However the one described before is by far the most practical.

Another conclusion of this orientation test is the low accuracy expected for a deep angle course, running downwind. As shown in Table 2.10, at an AWA of 140° , the average pressure difference is of 6 Pa. Moreover the flying shape at this AWA has a large camber. The normal vector of the spinnaker surface is almost horizontal at the bottom of the sail and almost vertical at the top of the sail. The orientation of pressure transducers is different between those placed at the bottom and those placed at the top of the spinnaker. The errors on zeroes are then in the same order of magnitude as pressures to be measured.

A last remark is the influence of the acceleration on the pressure sensors. The difference of pressure between the two opposite orientations should come from the weight of the membrane. Thus an acceleration

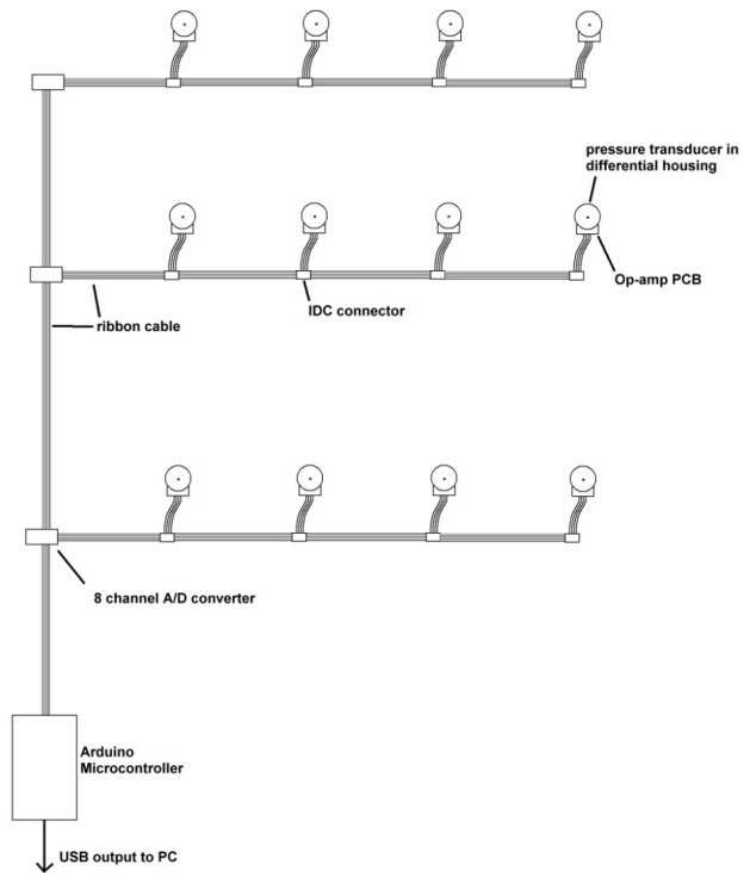


Figure 2.20 – General layout of the pressure sensors of the Yacht Research Unit Pressure System. Diagram from [Motta et al., 2014].

of $g = 9.81 \text{ m/s}^2$ overestimates the pressure by about 4 Pa. Therefore during flapping, if there are fast variations of shape, hence significant accelerations or decelerations, pressures might be biased.

2.5.3 Dynamics of pressure sensors

The Arduino microcontroller sends data with all the pressure values gathered at a sampling rate of 40 Hz. However because of the SPI communication, between each sentence only one A/D converter -thus 8 pressure taps- is updated. On the spinnaker the 44 transducers are split in 6 A/D converters (1 for the 8 transducers at the 7/8 stripe, 3 gathering the first 8 transducers at the luff for each stripe, 1 gathering the last 4 of the 1/4 stripe and the last 4 of the 1/2 stripe, and another A/D converter for the last 4 of the 3/4 stripe). Therefore each A/D converter (hence group of 8 pressure taps) is updated only every $40/6 = 6.7 \text{ Hz}$ (cf. table 2.12).

The final sampling rate is quite low but also comes from a compromise with the reduction of noise. Raw pressure measurements are noisy. The microcontroller sampling rate could go up to 100 Hz but it has been decided to restrict the rate at 40 Hz using a moving average to reduce noise.

Timestamp	ADC A	ADC B	ADC C	
t1	Ua1 (8 values)	Ub1 (8 values)	Uc1 (8values)	etc
t2=t1+1/40	Ua2(8 values)	Ub1 (8 values)	Uc1 (8values)	etc
t3=t2+1/40	Ua2 (8 values)	Ub2(8 values)	Uc1 (8values)	etc
t4=t3+1/40	Ua2 (8 values)	Ub2 (8 values)	Uc2(8values)	etc
...
tn=t1+n/40	Ua3(8 values)	Ub2 (8 values)	Uc2 (8values)	etc

Table 2.12 – Description of the synchronisation of pressure values. In our case, there are n=6 A/D converters.

2.6 Wind measurement

2.6.1 Presentation of wind sensors

Wind measurement is important because the Apparent Wind Speed (AWS) is used to calculate non-dimensional coefficients and the Apparent Wind Angle (AWA) classifies all records to analyse their evolutions. It can also determine the type of navigation for each measurement: reaching course (approximately perpendicular to the wind) or running (wind almost from the aft).

An ultrasonic anemometer measuring the wind in the 3 axes was placed at the top of the mast head (cf. table 2.13). In 2014, we designed a custom installation to add other anemometers for another purpose not used in my PhD project (cf. figure 2.21).

	3-Axis Ultrasonic Anemometer	ultrasonic anemometer
Name	Gill Instruments Windmaster	LCJ capteurs CV7
Range speed	0 m/s to 45 m/s	0.15 m/s to 40 m/s
Resolution speed	0.01 m/s	0.05 m/s
Resolution direction	0.1°	1°
Precision speed	<1.5% RMS @ 12 m/s	0.25 kn
Precision direction	2° @ 12 m/s	±1°
Communication	Serial digital RS232	Serial digital NMEA
Sampling rate	10 Hz	2 Hz
Weight	1 kg	200 g
Size (mm)	750x240	300x120
Protection class	IP65	IP67
Power supply	12 V	12 V

Table 2.13 – Specifications of the different wind sensors used for this PhD.

Table 2.13 gives the specifications of the 3-Axis Ultrasonic anemometer used during our experiments. Unlike common wind sensors that measure the wind only in a plane, we can acquire the global wind vector in the 3 axes. It is particularly advantageous when the boat is heeled. The sample rate of 10 Hz is sufficient for our measurements. The wind sensor CV7 was used for tests presented in the next subsection.

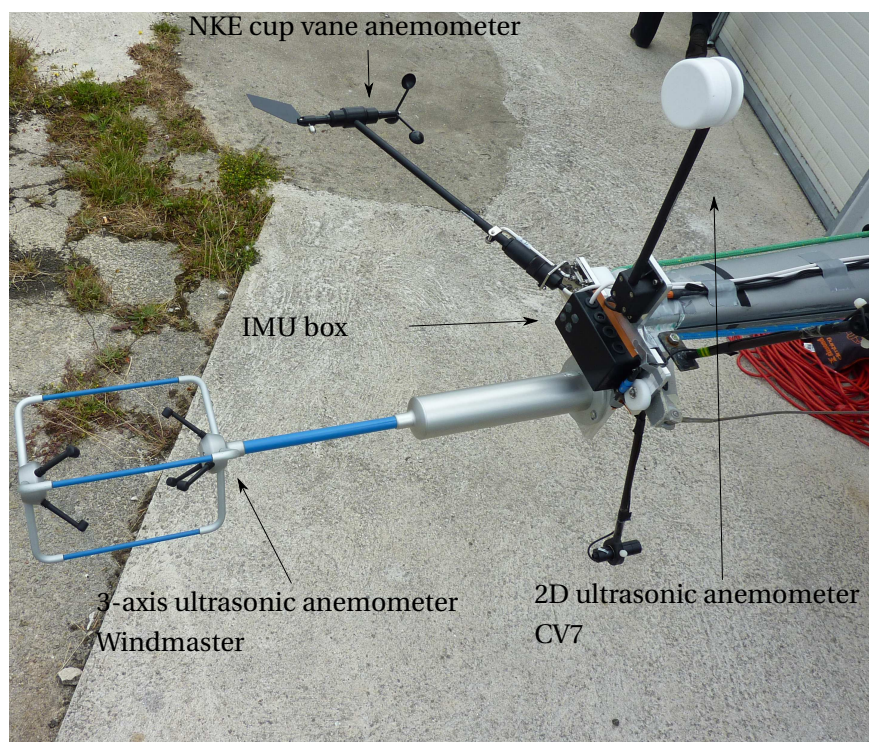


Figure 2.21 – Photograph of the headmast when preparing experiments in 2014. 3 anemometers + an IMU box are visible on a custom-made platform.

2.6.2 Difficulties to measure wind

Measuring the wind on a yacht is a difficult problem (see 1.3). We decided to place the wind sensors at the top of the mast as is common in most sailing boats, even though the measurements are affected by the flexibility of the mast and the yacht motion. [Masuyama, 2014] placed the wind sensors at the extremity of a pole in front of the bow of the yacht, but this is not practical especially with a spinnaker.

Another issue is the upwash effect more prominent for downwind sails than for upwind sails. It is the deflection of the wind made by the sails. To illustrate this effect on the wind sensor at the top of the mast, we carried out experiments in 2012 with the J/80 yacht placed on her trailer. The 3-axis ultrasonic anemometer was placed at the top of the mast and the ultrasonic anemometer CV7 was located about 10 m upstream and at a height of 4.5 m and oriented in the same direction as the yacht (cf. figure 2.22).

Figure 2.23 shows the evolution of wind angle during the hoist of the spinnaker without the mainsail up. Before the hoist of the spinnaker, both wind signals have a similar direction of about 115° . As soon as the spinnaker is hoisted and inflated, the direction of the wind measured at the top of the mast is shifted by 15° , coming more from the aft of the boat. The AWA fluctuations are also larger at the top of the mast maybe due to stronger wind, the variations of the spinnaker shape and the movements of the mast. The wind speed measured at the top of the mast does not change when the spinnaker is hoisted. It is not in the scope of this PhD project to correct wind measurement³, and the wind data presented in this thesis

³There is ongoing PhD research on this topic supervised by the company NKE, Université Bretagne Sud and IRENav. The PhD

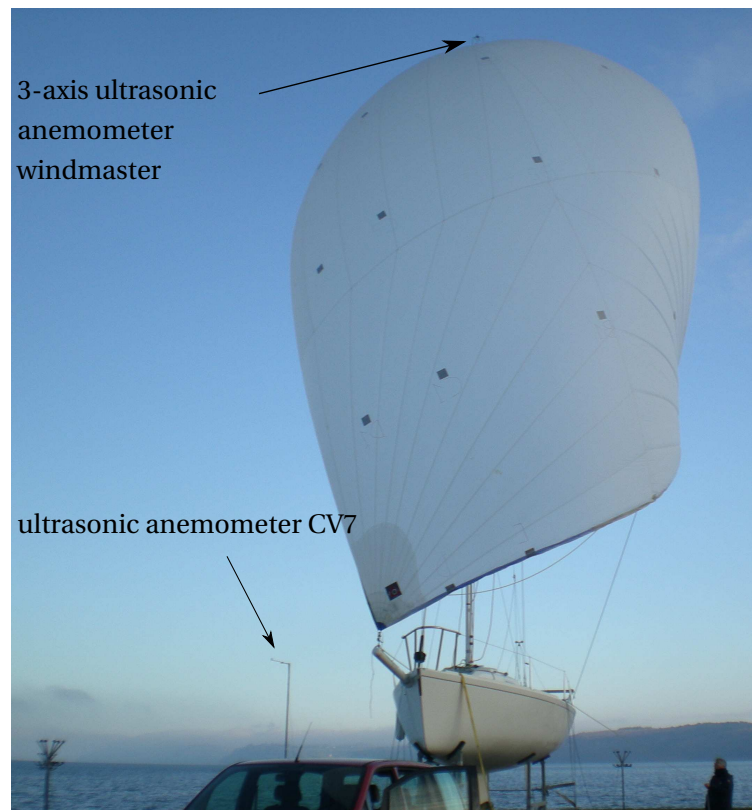


Figure 2.22 – Photograph presenting the configuration of the anemometers during the experiments carried out in Decembre 2012 where the spinnaker was hoisted on ground.

are given by the 3-axis anemometer at the top of the mast corresponding to the AWA measured by sailors. However one must be aware of the importance of the upwash effect for downwind sails in addition to the large twist of the apparent wind angle (explained in subsection 1.3).

candidate, Hugo Kerhascoët, carries out research on denoising the wind signal by removing the yacht and mast motion and also by considering the physical sensor dynamics using Kalman filters.

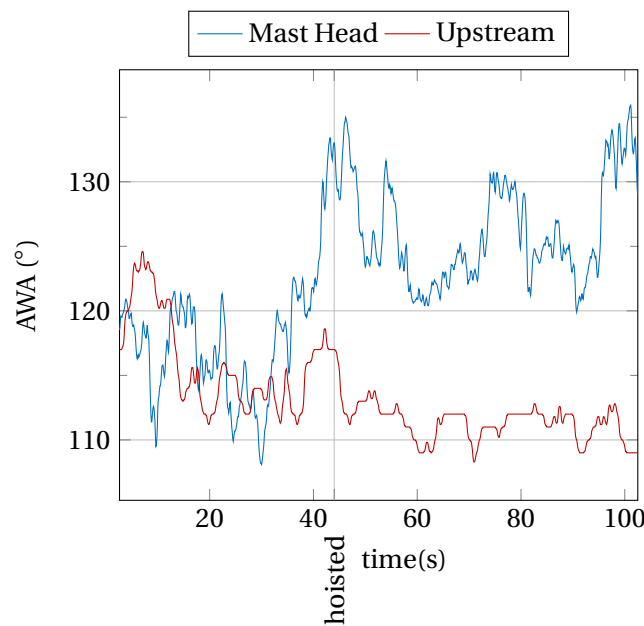


Figure 2.23 – Evolution of the measured AWA when hoisting the spinnaker only with a measurement at the top of the mast and another measurement 10 m upstream at 4.5 m height. The spinnaker is fully hoisted and inflated at $t = 44$ s.

2.7 Boat data acquisition

This section describes the more usual data measured on a racing yacht. These measurements are useful for comparison of performance with load and pressure data. The integration of all the sensors has evolved between the experiments in 2013 and in 2014. In 2014, a NKE bus was gathered data from different NKE sensors and was able to obtain more consistent and reliable data.

2.7.1 Boat motion

2.7.1.1 Description

The recorded boat motion is defined by the angles of the boat frame relative to the Earth's frame (Heel, Trim, Heading) and their corresponding rotation velocities (Roll, Pitch, Yaw). These angles result from the balance between the measured aerodynamic and hydrodynamic forces. These attitudes are recorded thanks to an Inertial Measurement Unit (IMU). An IMU is composed of 3 sensors: a 3-axis accelerometer to measure the direction of the gravity and the accelerations of the yacht in the IMU frame, a 3-axis magnetometer to measure the magnetic North and a 3-axis gyrometer measuring the rotation velocities. It is sometimes called a 9 Degrees of Freedom IMU. Many algorithms (mostly using Kalman filters) have been developed to compute the attitude (heel, trim, heading) of the IMU. It is placed inside the boat, just behind the companionway in order to be as close as possible to the centre of rotation for small angles of the J/80 sailing yacht to better measure the position of the boat frame relative to the Earth's Frame.

During the experiments carried out in 2013, an off-the-shelf IMU, Xsens MTI-G, was used (cf. table 2.14). Despite its fast sampling rate, an efficient algorithm and its plug-and-play capability, we had several issues with this sensor during the experiments. Therefore we decided to change our tune for the experiments in 2014, and the NKE compass plus Open-Source IMUs were used (cf. table 2.15). The NKE compass was part of the pack of NKE sensors gathered by the NKE bus, the *Base Unit* was part of the DLC system (cf section 2.4.2.2), and a *FreeIMU* was available and therefore added for redundancy. The *FreeIMU* has a faster sampling rate than the others, a different configuration and is a complete open hardware framework, thus highly configurable. It also computes the boat attitude in a quaternion format which can be used to check our calculations.

To compute values of heel, trim and heading from the 9 Degrees of Freedom IMU, many algorithms are available. A non-linear estimation algorithm such as the Extended Kalman filter is commonly used and customised. In our case, an algorithm developed by [Madgwick et al., 2011] is used. It uses a quaternion representation as is used in our post-process. It does not use a Kalman filter but an optimised gradient descent algorithm. This algorithm is nowadays widely used in the Open Source community and therefore the code is available with many feedbacks and comments. Nevertheless, in order to compute precise angles, any algorithm needs calibrated values as input.

Sensor used Name of sensor	Inertial Measurement Unit Xsens MTI-G
Resolution angle	0.05°
Precision static	< 1° for trim and heel angles
Dynamic precision	< 2° RMS
Gyrometer Range	±300°/s
Gyrometer precision	1 °/s
Accelerometer range	±50 m/s ²
Accelerometer precision	0.02 m/s ²
Magnetometer range	±750 mG
Magnetometer precision	0.1 mG
Communication	Serial digital RS232 converted in USB
Sampling rate	100 Hz
Power supply	USB

Table 2.14 – Specifications of the IMU used during the experiments carried out in 2013.

2.7.1.2 Calibration

The boat motion sensors (FreeIMU and the *Base Unit* using the 9 DOF sensor-stick) as well as the IMUs in the DLCs (9 DOF sensor-stick) were carefully calibrated.

Calibration for IMU is important and yet not an easy task especially for the magnetometer. For example the magnetic environment of the sensor needs to be taken into account. A rather common and simple calibration ([Camps et al., 2009]) is to characterise the sensors by finding the offsets of the three sensors

Name of IMU	9 DOF sensor-stick SEN 10724			FreeIMU v0.4		
Type of sensor	Accelerometer	Gyro	Magneto	Accelerometer	Gyro	Magneto
Name of sensor	ADXL345	ITG3200	HMC5883L	MPU6050		HMC5883L
Range	$\pm 4\text{ g}$	$\pm 2000^\circ/\text{s}$	$\pm 1.3\text{ G}$	$\pm 4\text{ g}$	$\pm 2000^\circ/\text{s}$	$\pm 1.3\text{ G}$
Resolution	255 unit/g	14.4 unit/ $^\circ/\text{s}$	1087 unit/G	8192 unit/g	16.4 unit/ $^\circ/\text{s}$	1087 unit/G
Precision	1%	2%	2°	-	-	2°
Communication		i2C			i2C	
Sampling rate		25 Hz			40 Hz	
Communication		Serial digital String sentence			Serial digital String sentence	
Power supply		5 V			5 V	

Table 2.15 – Specifications of the 2 IMUs used during the experiments carried out in 2014.

gyrometer, magnetometer and accelerometer and to find gains of the accelerometer and magnetometer. The magnetometer measures the magnitude of the Earth's magnetic field in the magnetometer frame $\underline{H} = [h_x(t) \ h_y(t) \ h_z(t)]^T$ in every direction. In an undisturbed environment, the norm of the vector measured by the three orthogonal axes of the magnetometer should give the constant value of the local Earth's magnetic field.

$$\forall t, ||H|| = \sqrt{h_x^2(t) + h_y^2(t) + h_z^2(t)}$$

The variations of this norm highlight deviations from the magnetic field due to spatial drift and uncertainties of the sensor which can be modeled as follows:

$$\begin{bmatrix} V_x(t) \\ V_y(t) \\ V_z(t) \end{bmatrix} = \begin{bmatrix} \alpha_x & 0 & 0 \\ 0 & \alpha_y & 0 \\ 0 & 0 & \alpha_z \end{bmatrix} \begin{bmatrix} h_x(t) \\ h_y(t) \\ h_z(t) \end{bmatrix} + \begin{bmatrix} \beta_x \\ \beta_y \\ \beta_z \end{bmatrix}$$

with α_x, α_y and α_z the gains for every axis of the magnetometer and with $\underline{\beta} = [\beta_x \ \beta_y \ \beta_z]^T$ for offsets of the sensor.

Using a 3D representation in the sensor frame, the output geometric form of the computed vector should be a sphere in an undisturbed environment ($\underline{\beta} = \vec{0}$ and $\alpha = \alpha_x = \alpha_y = \alpha_z$). But if we take into account distortions, when we rotate the sensor sweeping almost all possible orientations to create a point cloud, we can estimate the point cloud created by an ellipsoid:

$$\forall t, ||H|| = \sqrt{\left(\frac{V_x(t) - \beta_x}{\alpha_x}\right)^2 + \left(\frac{V_y(t) - \beta_y}{\alpha_y}\right)^2 + \left(\frac{V_z(t) - \beta_z}{\alpha_z}\right)^2}$$

The values of the centre position $\vec{\beta}$ and the radii of the main axes α_x, α_y and α_z give the offsets and gains in each direction. Moreover, in the calibration we also take into account that the main axes of the ellipsoid might not be the main axes of the sensor. A rotation matrix is applied and therefore the gain matrix used for calibration is no more diagonal but full.

The same process can be applied to the accelerometer measuring the Earth's gravity, if the rotation of the sensor is made at a constant speed, without any acceleration.

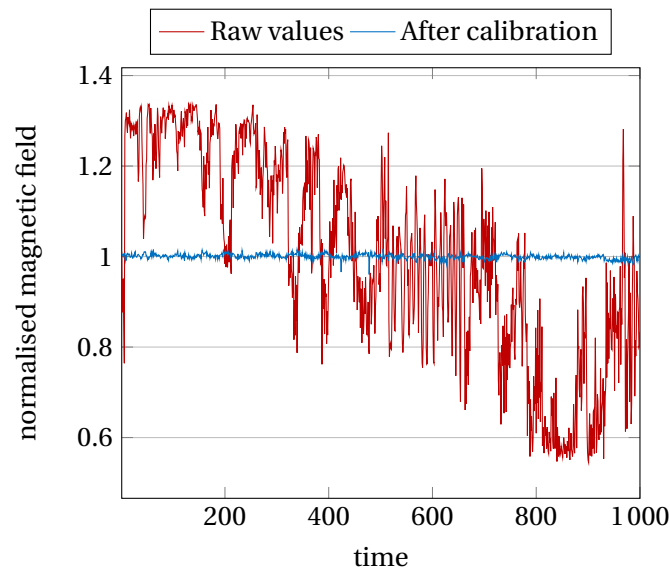


Figure 2.24 – Calibration of the magnetometer. 10000 values recorded during 5 minutes of calibration rotating the sensor in different positions. Raw values are in red, and corrected values in blue after finding 3D gains and bias. The data are normalised so that the Earth magnetic field value corresponds to 1.

Figure 2.24 shows the values measured during a calibration measurement where the sensor swept progressively all directions. The displayed values are the norm of the magnetic field before and after calibration. One can notice the much reduced noise and more constant value around 1 for the calibrated values. This calibration is carried out in an undisturbed magnetic environment. Nevertheless to be more accurate, the calibration should be done in the environment where the sensor is used. It is not possible in our case because that would mean to stick the sensor inside the boat and rotate the sailing yacht in all directions(!). Figure 2.25 uses red dots to show the raw values of the magnetometer before the calibration used in Figure 2.24. The green solid is the ellipsoid fitting well with the point cloud of raw values. It confirms the hypothesis of estimating the raw magnetic field measured by the magnetometer using an ellipsoid.

This calibration protocol was applied on the DLCs too.

2.7.2 Speeds and courses

2.7.2.1 Speed Over Ground (SOG) and Course Over Ground (COG)

Global Positioning System (GPS) is a common sensor used in sailing yachts for navigation. It gives the speed and the yacht motion relative to the Earth's frame, which can be different from the speed and the direction on water if there is tide.

We used a differential GPS in 2013 and a high frequency GPS from NKE in 2014. Manufacturer specifications set out in detail in Table 2.16. The sampling rates are much lower than the sampling rate of the load or pressure acquisition system. But these data will not be used for precise dynamic analysis, only for information on the boat performance.

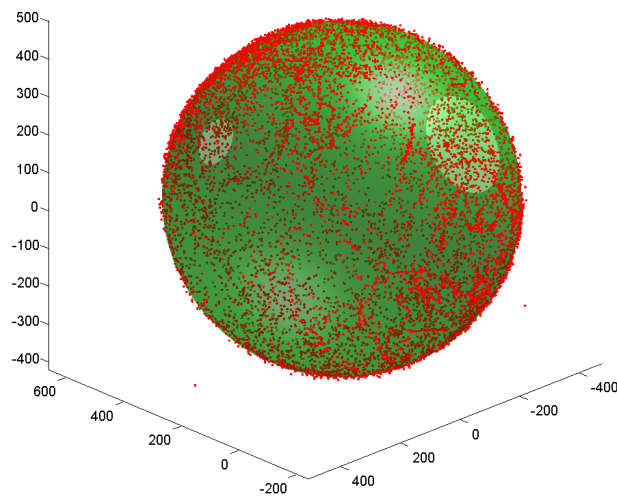


Figure 2.25 – An ellipsoid (in green) fits well the raw values of the magnetometer.

Sensor used in	2013	2014
Name of sensor	DGPS Furuno GP37	NKE GPS HF
Resolution	5 m	2.5 m
Sampling rate	1 Hz	≈ 6 Hz
Communication	Serial digital NMEA	Serial digital NMEA
Power supply	12 V	12 V

Table 2.16 – Specification of the 2 GPSs used during the experiments carried out in 2013 and 2014 to measure the Speed Over Ground (SOG) and Course Over Ground (COG).

2.7.2.2 Speed Over Water (SOW) and Course Over Water (COW)

We also measured the Speed Over Water (SOW) and the direction of the boat called Course Over Water (COW). A paddlewheel speed sensor also called log was used to measure the speed of the flow below the hull. A compass was used to measure the Earth’s magnetic field and therefore gave the direction of the boat. However the speed and the direction of the currents or waves affect the flow speed measured by the speed sensor and can make the boat go sideways which is not detected by the compass. Those data have a higher rate than the SOG and COG measured by the GPS, even if the inertia of the paddlewheel might affect the dynamics of the measurement. But like the GPS these data will only be used to visualise the boat’s performance.

In 2013, a Navman log and B&G fluxgate compass were used. In 2014, with the NKE equipment set, a NKE compass and paddlewheel speed sensor were used (cf Tables 2.17 and 2.18 for the manufacturer specifications).

Sensor used in	2013	2014
Name of sensor	Compass Fluxgate B&G Halcyon3	NKE Regatta Compass
Resolution	0.1°	0.1°
Precision	0.5°	< 1°
Sampling rate	5 Hz	≈ 6 Hz
Communication	Serial digital NMEA	Serial digital NMEA
Power supply	12 V	12 V

Table 2.17 – Specification of the compass used during the experiments carried out in 2013 and 2014 to measure the Course Over Water (COW).

Sensor used in	2013	2014
Name of sensor	Log Navman 3100S B&G Halcyon3	Log NKE paddlewheel
Resolution	0.01 kn	0.01 kn
Precision	0.2 kn	0.2 kn
Sampling rate	5 Hz	≈ 6 Hz
Communication	Serial digital NMEA	Serial digital NMEA
Power supply	12 V	12 V

Table 2.18 – Specification of the speedometer used during the experiments carried out in 2013 and 2014 to measure the Speed Over Water (SOW).

2.8 Acquisition systems

Different type of sensors are used for the full-scale experiments. Not only are there common wind and navigation sensors that need to be precisely timestamped but there are also analogue data from load and pressure sensors that need to be amplified and converted into digital signals. Every signal has its own acquisition rate from 1 Hz to 100 Hz. To acquire time-resolved data precise enough for our dynamic analysis, specific acquisition systems shall be used to deal with this rich variety of type of sensors.

2.8.1 RTMaps architecture

During the experiments in 2013, a fanless computer was used with a software RTMaps developed by Intempora which synchronises and processes real-time data streams from multiple sensors. Navigation and wind sensors are plugged into the 4 RS232-Serial communication slots. It also has 4 USB slots for the other sensors. It also contains video acquisition cards not described here since there were not used for my PhD project. To prevent any data loss in rough weather, it is equipped with an SSD hard-drive with no spinning mechanical parts.

On this fanless computer, the software RTMaps receives all data "on the flow". It does not behave in a "master-slave" communication mode, but receives the data at the sampling rate of each sensor. At the reception in the software RTMaps, each data is given a unique timestamp. Then data are stored in a specific file during the recording. This results in a set of data with a non-uniform sampling rate which

needs to be post-processed. The main advantage is that there is no loss (or very little) of data, and data are precisely time-resolved. RTMaps has a modular-diagram interface. Each type of sensor is represented by a module developed specifically by RTMaps when needed.

Nevertheless this architecture has several drawbacks. The main drawback is the lack of possible hardware development for this architecture due to the limited numbers of port on the computer. All serial slots are already used and interferences between serial signals happen quite often. A fanless computer is designed for being resistant, but in return the performance of the computer is limited. Therefore if too much data must be dealt with, lags can occur, thus data loss. In conclusion, we have reached the limits of this architecture which lacks reliability for full-scale experiments in rough conditions.

2.8.2 CompactRio architecture

This is the reason why in 2014, we decided to change the architecture and build our system around a Compact Rio (CRio) acquisition system. CRio is a real-time embedded industrial controller developed by National Instruments. It combines a real-time processor and a reconfigurable field-programmable gate array (FPGA) within the same chassis to control reconfigurable modules (cf. table 2.19). It also features communication over the network and built-in web (HTTP) and file (FTP) servers.

CRio also records data "on the flow" using an internal clock which is more precise than in the RTMaps architecture. Load sensors use a specific module, and other sensor data must use a RS232 serial protocol. The configuration of each of these modules can be made with Labview, also developed by National Instruments.

Data from each sensor are then saved individually in a text file. In each text file, one line corresponds to one measurement received by the CRio. Each line starts with the timestamp of the CRio. A post-process is needed to retrieve all data in one file with a unique timestamp for easier analysis.

NI cRIO-9024
Real-time controller ①
800MHz processor
512Mb DDR2 RAM
4Gb storage
Ethernet ports with embedded HTTP and FTP servers
On a 8-slot reconfigurable chassis NI cRIO-9114, modules controlled by the NI cRIO-9024:
4 simultaneous analogue-to-digital converters input (NI 9215) ②
16 load cell ports (NI 9237) ③
8 ports for RS232 Serial Interface Module (NI 9870) ④
4 channels for input/output TTL signal (NI 9402) ⑤

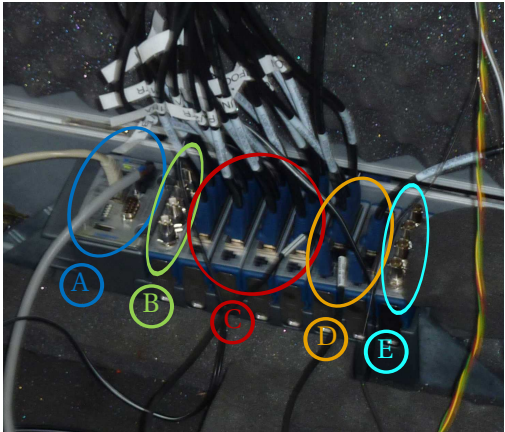


Table 2.19 – Specification of the NI CRio used during the experiments in 2014.

2.9 Procedure and Post-processing

After retrieving all data from the experiments, a routine was developed in Matlab. It imports files for one set of measurements, extracts data, converts them if needed (like voltage into load, or calculating the driving force of the spinnaker) and concatenates them in a unique Matlab structure. The routine resamples to obtain synchronous data for easier analysis. Measurements not only have different sample rates but also non-uniform sample rates. Usually resampling methods such as linear or spline interpolation or zero padding in the Fourier space can be applied if the initial sample rate is uniform. Other methods have been developed for non uniform sampling such as the Marvasti algorithm, the adaptive-weight algorithm or also the adaptive-conjugate-Toeplitz algorithm among others [Feichtinger et al., 1995, Chauvet et al., 2009]. Appendix D briefly explains the principle of these methods and their performances on a sinusoidal signal. After careful testing of different methods, for most of the cases, it was decided to use a two-step resampling method:

1. Apply a linear interpolation at the average sample rate for each sensor in order to obtain a uniform sampling with a minimum information loss.
2. Apply a linear interpolation at a specific sample rate (usually 25 Hz) for all sensors in order to obtain a unique time vector.

This resampling method proved to be the most reliable in the vast majority of cases, particularly to avoid introducing parasitic dynamics into the signals. However, when needed, spline interpolation, zeropadding interpolation or the Marvasti algorithm can be applied in the Matlab routine on specific sets of measurements. For the results presented in this thesis, it will be clearly stated when any of the latter interpolations are used.

Finally, this routine is also used to define "stable" runs. Wind is considered as the only input control of the sailing yacht system. The trim and the helm are adjusted as a function of the wind direction and force. Aerodynamic loads are considered as an output, a response to the environmental conditions. Wind variations cannot be controlled. In order to analyse the intrinsic dynamics of the aerodynamic FSI system, and not the dynamics of the onset wind flow, "stable" periods are defined according to a "stable" wind that is quantified as follows:

- The standard deviation of the AWA during the "stable" period should not be larger than a certain threshold: $\text{standard deviation(AWA)} < \text{thres}_{\text{AWA}}$.
- The standard deviation of the AWS during the "stable" period should not be larger than a fraction of the average AWS: $\text{standard deviation(AWS)} < \text{thres}_{\text{AWS}} \langle \text{AWS} \rangle$.
- The "stable" period should last a defined minimum of time: $\Delta t > \text{thres}_{\text{time}}$.

Most of the time, the thresholds used are:

$$\begin{cases} \text{thres}_{\text{AWA}} = 4^\circ \\ \text{thres}_{\text{AWS}} = 0.1 \langle \text{AWS} \rangle \\ \text{thres}_{\text{time}} = 10 \text{ s} \end{cases}$$

These criteria make it possible to find enough periods for comparison where the conditions do not change too much. If the criteria are changed for some results presented in this thesis, this will be stated. Stable periods define stable input, but not necessarily stable output. As shown in Figure 2.26, a stable wind does not necessarily mean stable aerodynamic loads.

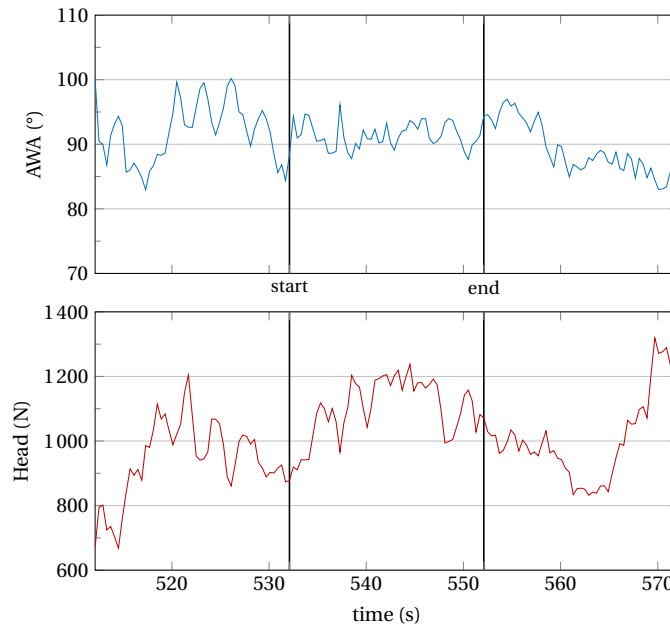


Figure 2.26 – Evolution of AWA and Head load during of a 40 s run. A 20 s "stable" run is detected between the two vertical bars.

2.10 Conclusions

A J/80 class sailing boat was instrumented to measure the flying shape of the spinnaker, the aerodynamic loads transmitted to the rigging, the pressures on the asymmetric spinnaker and the boat and wind data, with the constraint of still being able to sail as in regatta conditions. Our goal is to measure averaged data and also dynamic behaviours of the sail with a typical time scale of 1 s. Note that pressure distribution and flying shape of the spinnaker were never measured simultaneously. The instrumented full-scale boat started to be developed during the PhD project of Benoît Augier [Augier, 2012], for upwind tests.

The major evolution during my PhD has been the development of the flying shape acquisition system using photogrammetry measurement. This new system is based on 6 cameras placed on the yacht.

Simultaneous images from different view points are processed with Photomodeler in order to determine the 3D flying shape of the spinnaker. A careful design of the system and a thorough calibration make it possible to obtain an averaged spatial accuracy better than 1.5%. It corresponds to about 0.15 m for the size of the spinnaker. This global accuracy may not seem outstanding in absolute terms, but considering the objectives of this project it is totally satisfactory. For time-resolved flying shape, a high frame rate (25 Hz) was required, thus a lower resolution of images decreasing the precision. A compromise had to be found between the spatial precision and the time resolution of the data.

For load sensors on the rigging and on the corners of the sail, the accuracy is better than 2% of the measurement range, namely 100 N, and the frequency rate is of 25 Hz. The accuracy is of good quality for the rigging, but just correct for load measurement on the corners of the sail. For large AWA, loads at the head, tack and clew are around 250 N. For experiments in 2013, wireless shackles were used, with a good precision in time and in the measurement of load but no information on the directions. For the experiments in 2014, Directional Load Cells (DLCs) were used to acquire the magnitude and the directions of the loads on the corners of the spinnaker. While the accuracy of the strain gauges is similar to wireless shackles, there is an uncertainty in the directions of the loads of about 10%. Moreover a small shift in time of 0.1 s might appear, which is still reasonable with regard to typical time scales of the Full Scale spinnaker dynamic behaviour.

The pressure acquisition system was developed and used during the PhD project of Dario Motta [Motta, 2015]. The sampling rate of 7 Hz prevents us from looking closely into small time shifts between pressures and loads for example, but is sufficient for analysing the evolution in time of the pressure distribution on the spinnaker. The precision of 4 Pa is good, but is only just enough for large AWA, where the AWS is low thus pressures and aerodynamic loads as well.

Boat and wind data have sampling rates varying from 1 Hz to 20 Hz and are used to analyse the average performance of the sailing boat.

Considering the difficulties to achieve full-scale testing in real sailing conditions, we are satisfied with the accuracy of all the sensors set on the instrumented sailing yacht. It would make it possible to analyse for different AWA, the flying shapes, loads and pressures as well as dynamical FSI phenomena such as the flapping of the luff.

General behaviour of the spinnaker

Contents

3.1 Flying shapes	92
3.1.1 Presentation of flying shapes at different AWA	92
3.1.2 Comparison of flying shapes	94
3.1.2.1 Intrinsic stripes of the spinnaker	94
3.1.2.2 3D camber representation	96
3.1.3 Comparison with Design Shape	98
3.1.3.1 General overview of the differences	98
3.1.3.2 Comparison using intrinsic stripes	99
3.1.3.3 Comparison using the 3D camber representation	99
3.1.4 Bézier surface	101
3.1.4.1 Presentation of a Bézier surface	102
Bézier curve	102
Rectangular Bézier surface	104
Triangular Bézier surface	106
3.1.4.2 Create a triangular Bézier surface to represent the shape of a spinnaker	106
3.1.4.3 Precision of the reconstruction by a Bézier surface	108
3.1.4.4 Utility of a Bézier surface for sail design	110
3.1.4.5 Evolution of control points according to Apparent Wind Angle (AWA)	110
Comparison with the Design Shape	113
3.1.5 Conclusions	113
3.2 Loads on the spinnaker	114
3.2.1 Evolution of the spinnaker loads with the AWA	114
3.2.1.1 With the mainsail hoisted	114
3.2.1.2 With the mainsail lowered	116
Comparison between 2013 and 2014 results	116
Projection of load onto boat frame	117

Loads in shrouds	117
Comparison with Wind Tunnel experiments	118
3.2.2 Load fluctuations	121
3.3 Evolution of pressures	124
3.3.1 Average pressure distributions	124
3.3.2 Fluctuations of pressures	127
3.4 Conclusions	128

In this chapter, the overall behaviour of the spinnaker is presented thanks to experimental results. The change of shape and the generated aerodynamic loads affected by the pressure distribution are presented mostly according to the Apparent Wind Angle (AWA) (and hence by the corresponding Apparent Wind Speed (AWS)). In this chapter, stable time-averaged data are selected as explained in section 2.9.

3.1 Flying shapes

This section describes 4 different flying shapes measured by the flying shape acquisition system described in section 2.3 during full-scale on water experiments at distinct apparent wind angles presented in Figure 3.1: 64°, 96°, 124° and 141°. For each apparent wind angle, the spinnaker is slightly overtrimmed (the luff does not flap). The flying shape is fairly constant for 20 second “stable” periods described in section 2.9. Thus the flying shape of one timestamp has been chosen to be representative of the average flying shape. Different representations are used to highlight the difference of shapes for different AWA. The common representation by stripes might indeed not be the most appropriate for 3D shapes of downwind sails. New types of representations developed during this PhD project are therefore presented: 3D-camber and Bézier surface representations. These flying shapes are also compared with the design shape to highlight the differences.

3.1.1 Presentation of flying shapes at different AWA

Figure 3.1 presents 4 measured flying shapes from AWA 64° to 141° with the corresponding measured heel. Figure 3.1c displays the bird’s eye view above the mast perpendicular to the X-Y plane of the boat. The arrow represents the apparent wind direction measured at the top of the mast. At 64°, the clew point is aft of the mast and the whole luff is on the leeward side of the boat. The luff is highly curved -but not flapped- as it is common at tight apparent wind angles. When the apparent wind angle is increased, the clew point goes further forward and upward. Between AWA 64° and 141°, the clew point position is 2.3 m further forward and 1.4 m higher and goes only 0.5 m more to the leeward side. Thus the clew point is closer to the “tack-head” line. Still, the same sail area is held by these 3 points while the area of the triangle head-tack-clew is smaller. Thus for deeper AWA, the spinnaker has a more rounded shape with the luff rotating to the windward side and with the leech more twisted at 3/4 of the height.

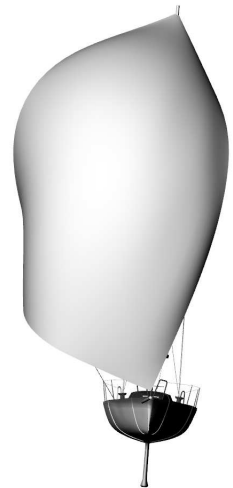
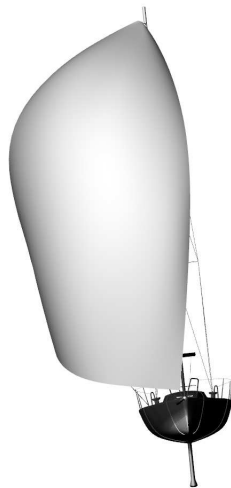
Figure 3.1 also displays the wind data and loads on the three corners of the spinnaker. When the AWA is

AWA: 64°
 AWS: 7.0 m/s
 Head: 897 N
 Tack: 730 N
 Clew: 407 N

AWA: 96°
 AWS: 5.3 m/s
 Head: 803 N
 Tack: 608 N
 Clew: 325 N

AWA: 124°
 AWS: 4.4 m/s
 Head: 518 N
 Tack: 351 N
 Clew: 211 N

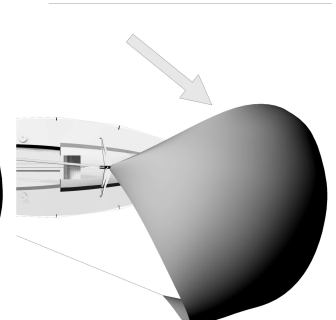
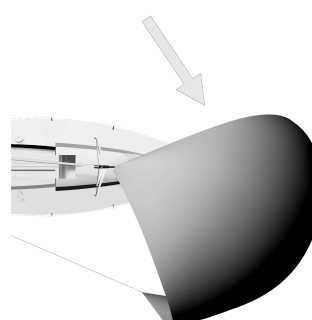
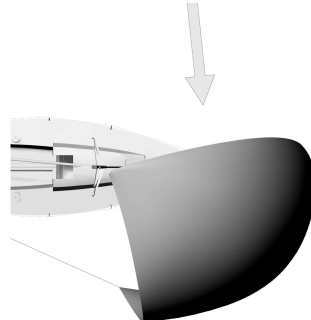
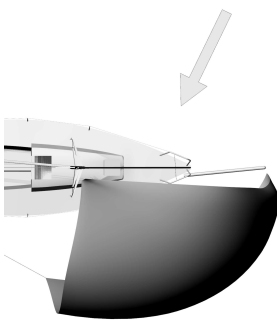
AWA: 141°
 AWS: 3.1 m/s
 Head: 259 N
 Tack: 90 N
 Clew: 86 N



(a) View from front



(b) View from starboard



(c) Bird's eye view just above the mast head

Figure 3.1 – 3D views of 4 flying shapes from photogrammetric measurements with corresponding loads at the head, tack and clew. From left to right AWA: 64°, 96°, 124°, 141°.

increased, the AWS and also the loads on the corners decrease. These evolutions will be further explained in the next section 3.2.

3.1.2 Comparison of flying shapes

3.1.2.1 Intrinsic stripes of the spinnaker

Sail designers commonly use sections at different heights to create design shape of spinnaker. Leech and luff are divided into equidistant segments. On the design shape, each division on the luff linked by a straight line to a division on the leech defines a section at a specific height. They are convenient to design a sail or compare the flying shape evolution. The lines of targets points used for the photogrammetric flying shape acquisition system (see Figures E.9a and 2.12) have a definition similar to the design stripes. However they are not the design stripes as they are placed at different heights.

For two significant apparent wind angles, 64° and 124° , table 3.1 displays some typical surface geometric parameters for 6 sections defining the spinnaker. The spinnaker bottom is flatter at AWA 64° than at AWA 124° with a lower camber and longer chord for a similar draft position. Table 3.1 indicates there is a small twist for the AWA 64° on the whole height of the spinnaker, while at AWA 124° the twist increases constantly from bottom to top of the sail up to the 3/6th of the height of the sail producing longer chord lengths than at AWA 64° . For larger AWA, the clew position is more forward and higher allowing a more twisted shape.

Section	curve length (m)	AWA 64°				AWA 124°			
		chord (m)	max camber	draft	twist	chord (m)	max camber	draft	twist
foot	7.19	6.58	20%	49%	-	5.93	31%	41%	-
1/6	7.66	6.51	28%	44%	3°	6.29	32%	46%	10°
2/6	7.78	6.31	27%	39%	6°	6.5	28%	46%	18°
3/6	6.96	5.8	26%	44%	6°	6.16	24%	48%	23°
4/6	5.04	4.53	18%	45%	3°	4.69	20%	49%	25°
5/6	2.54	2.33	15%	61%	4°	2.4	18%	67%	26°

Table 3.1 – Main surface geometric parameters for 6 sections for two different apparent wind angles. The reference for percentages is the chord length. Twist is defined as the horizontal angle between the chord of a stripe and the chord of the foot. All data is measured by the photogrammetry flying shape acquisition system.

Figure 3.2 shows, for the 4 AWA, the evolution of the ratio of the chord lengths with the lengths of the curves at the different virtual stripes of the sail (from the foot up to 5/6 of the height of the spinnaker). It also shows the ratio of the chord lengths with the curved lengths for the design shape. According to sail designers, the design shape is not designed for any specific AWA. This plot will be used in subsection 3.1.3. The flying shape for AWA 64° has a lower ratio at mid-height of the sail than at the bottom and at the top of the sail, meaning a more rounded shape at mid-height of the sail. For AWA 96° 124° and 141° , the trend is different with the ratio increasing with the height.

Figure 3.3 shows the evolution of the twist for the 4 AWA according to the height. The reference is the chord of the foot stripe. The twist for the design shape is also plotted and will be compared with the

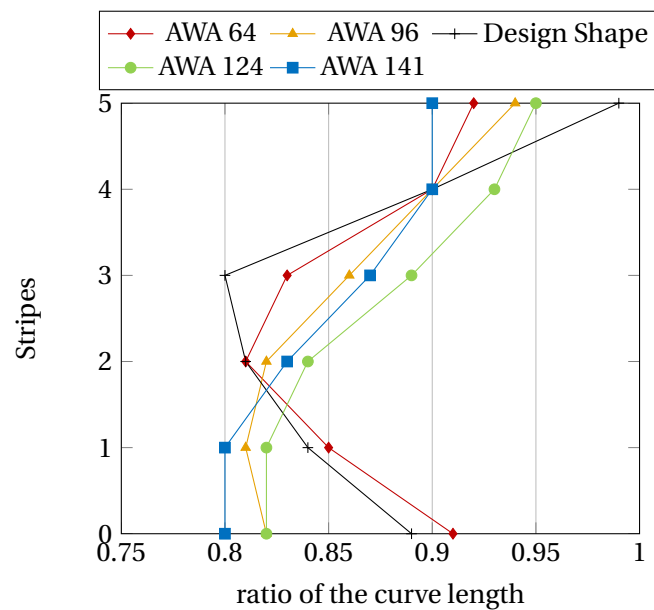


Figure 3.2 – Ratio between the chord and the curve lengths for different AWAs and for the design shape at different heights of the spinnaker (from the foot (0) and every 1/6 of the height of the spinnaker (1-5)).

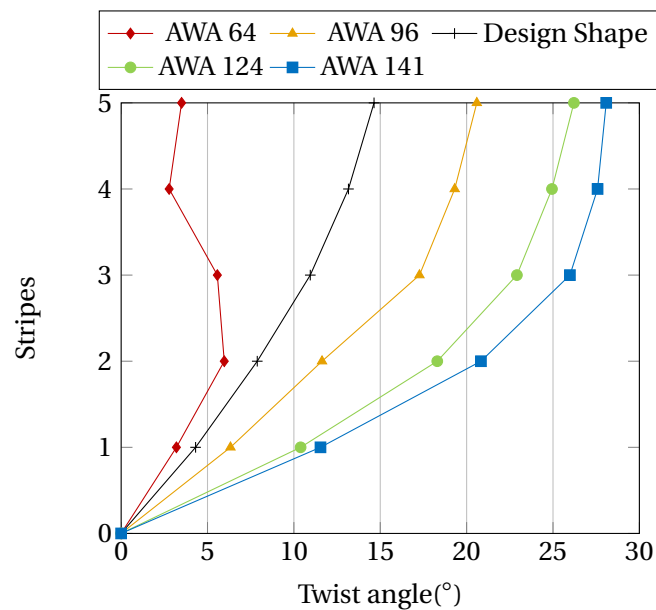


Figure 3.3 – Twist angle between the chord of the foot (0) and the other stripes at different heights of the spinnaker (1-5, every 1/6 of the height of the spinnaker) for different AWAs and for the design shape.

other flying shapes in subsection 3.1.3. For AWA 64°, the maximum of twist is at about half the height of the sail where the spinnaker is also more rounded. The top half part of the spinnaker is seemingly bridled and forced to stay tight. Similar to figure 3.2, for other AWA, behaviours are different from AWA 64° with a twist increasing constantly from bottom to 3/6 (half) of the height of the sail. At the top half part, the twist angle increases with a lower rate. The main difference between these AWA having similar evolution of

twist, is the absolute maximum twist. For AWA 96°, the maximum twist is a bit more than 20°, and for AWA 141° the maximum twist reaches 28°.

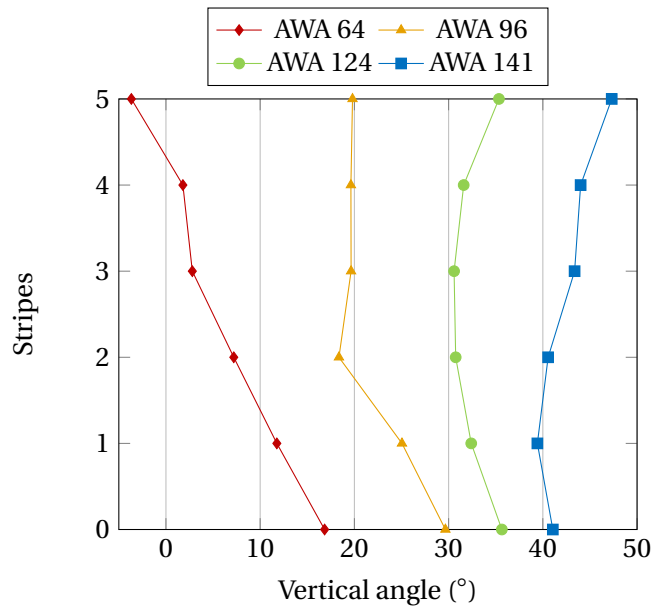


Figure 3.4 – Vertical angle of the chord of the foot (0) and of the other stripes at different height of the spinnaker (1-5, every 1/6 of the height of the spinnaker) for different AWAs. Negative means stripe is going down from luff to leech.

Figure 3.4 displays the angle between the horizontal (X-Y) plane of the boat and the chord length for the different stripes projected onto the X-Z plane. Since the design shape is not given for a specific AWA, and can only be placed arbitrarily on the boat, the angle between the horizontal plane and the chord lengths for different stripes of the design shape cannot be measured. Similar to previous figures, the flying shape for AWA 64° has a different behaviour from the other AWA. The vertical angle is decreased when the height is increased starting from 17° at the foot and going down to -4°. For the other flying shapes and more specifically AWA 124° and 141°, the vertical angle is larger at the foot (around 35°) decreasing a bit up to the half height. The vertical angle increases again in the top half part of the sail.

This figure 3.4 demonstrates the flying shape is deformed not only curvewise but also spanwise. Unlike upwind sails, spinnakers are far from 2D-extruded shapes. Downwind sails are 3D objects. However, the stripes are not always contained in a plane. They can be curved, and have different heights at the luff and leech points. Since these stripes are intrinsic to the sail, these 3D curved lines evolve with the AWA. They might not be the most convenient way to quantify the 3D geometry of a spinnaker. A more global view taking into account the 3D aspect of the shape could be more appropriate to define the flying shape and its evolution according to the AWA. The following subsections will describe a 3D camber representation and a Bézier surface representation using control points.

3.1.2.2 3D camber representation

Figure 3.5 presents the shape of the spinnaker in a different way. It shows the "3D camber", the depth of the sail projected onto the plane created by the 3 corners of the spinnaker. The "H" point is the head of

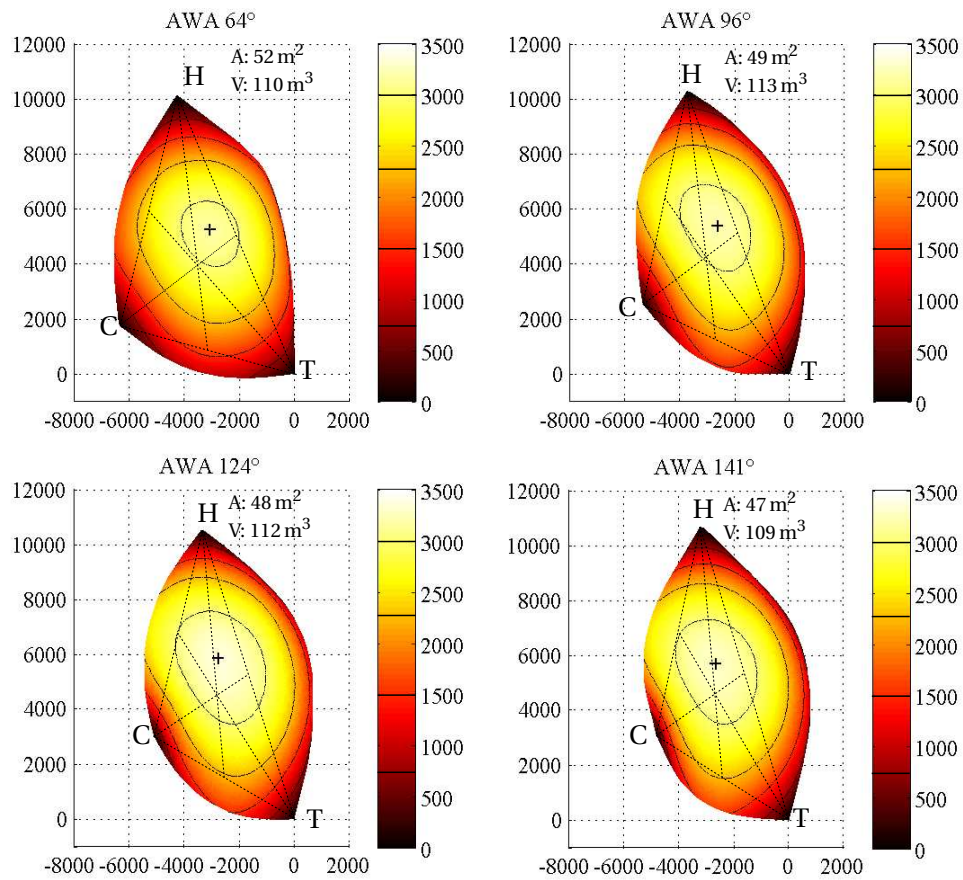


Figure 3.5 – Depth of the spinnaker in mm projected onto the plane created by the 3 corners head (H)-tack (T)-clew (C) for different apparent wind angles. Black lines on the spinnaker represent isodepths. The cross marker represents the maximum depth location. The medians of the triangle HTC are also displayed. For each AWA, the projected area (A) of the spinnaker onto the plane and the volume (V) between the spinnaker and the plane are given.

the spinnaker fixed on the mast and "T" is the tack point fixed on the bowsprit of the boat. Assuming these points to be fixed, with this representation the position of the clew "C" is defined with the angles of the triangle HTC. This representation could facilitate the comparison between shapes.

The cross marker showing the location of the maximum of "3D camber" is located slightly above and forward of the centroid -The intersection of the medians- of the triangle "Head-Tack-Clew" (HTC). At AWA 64°, the volume distribution is mainly homogeneous and circular. When the apparent wind angle is increased, the "bulb of camber" tends to have a more elongated and bended shape similar to a bean shape. Furthermore, for deeper AWA, the maximum depth goes closer to C. At AWA 141°, it is located at the middle of the Head median. Finally when the AWA is increased, the projected area decreases a bit while the volume between the spinnaker and the HTC plane remains almost constant. The volume is calculated as the integral of the depth of the spinnaker relative to the HTC plane.

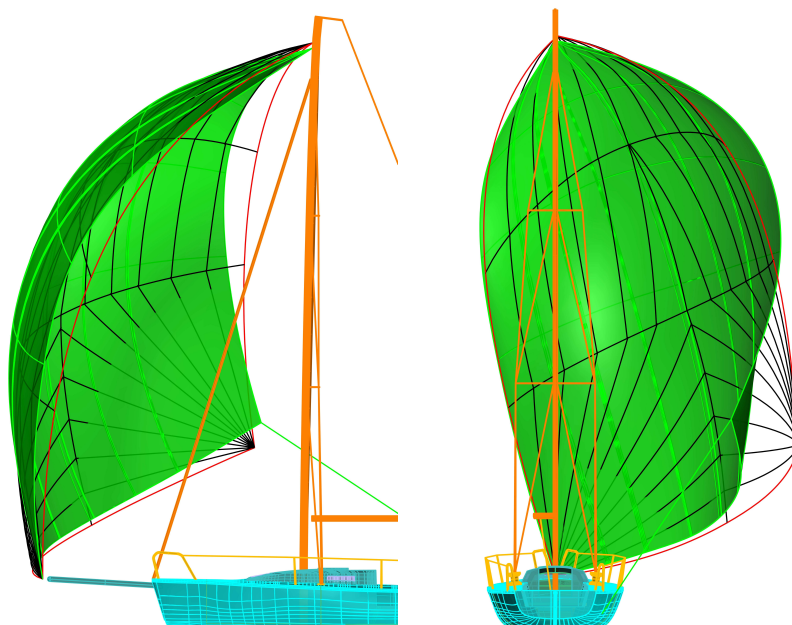


Figure 3.6 – Comparison of design shape (in black lines and edges in red) and measured flying shape for AWA 124° (in green).

3.1.3 Comparison with Design Shape

3.1.3.1 General overview of the differences

Figure 3.6 shows two distinctive shapes, the design shape of the spinnaker used during these experiments (in black lines and red edges) and the measured flying shape for AWA 124° (the green surface). The design shape is a generic shape. No specific trim or apparent wind angle is assumed during the design phase of the sail. The flying shape for AWA 124° was chosen because it corresponds to the best angle course downwind (best Velocity Made Good for a J/80 is around 120° in 12-16 knot true wind). Compared with the flying shape, the design shape has less volume at half height of the sail with less rounded edges. In reality, the leech is more curved, more twisted at 3/4 height and closed at bottom due to the only control we have with the clew point. The design shape clearly diverges from the actual flying shape for best angle course downwind.

Another method to place the spinnaker in the boat frame is by using the tangential plane of the sail at the clew point which must reach the spinnaker sheet block on the deck. Hence the clew sheet is included in the tangential plane. By placing the design shape that way, the flying shape AWA 64° is the closest to the design shape (cf. figure 3.7). The foot and clew points are close. However the luff of the design shape is on the windward side whereas the luff of the flying shape is on the leeward side and more curved in the 3/4 height of the sail. The leech is more curved for the flying shape than for the design shape. We do not know if the design shape is potentially more propulsive than the real flying shape at AWA 64°.

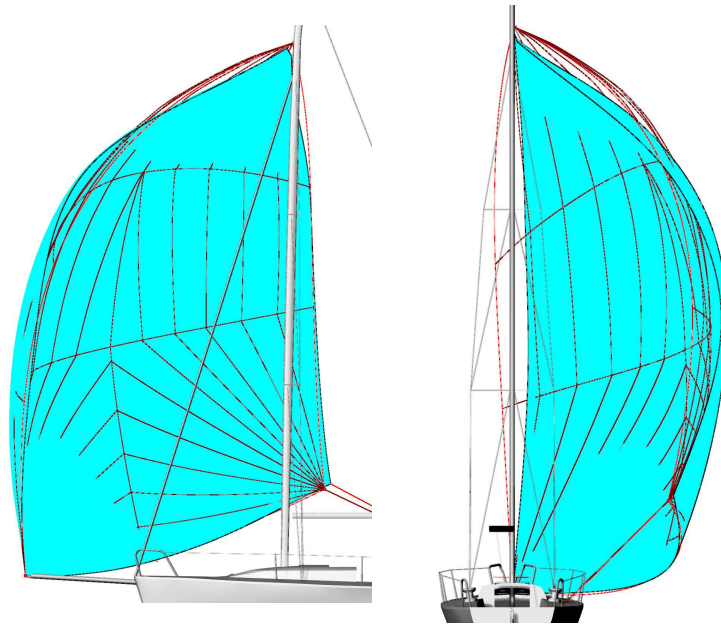


Figure 3.7 – Comparison of design shape (in black lines and edges in red) and measured flying shape for AWA 64° (in cyan).

3.1.3.2 Comparison using intrinsic stripes

The design shape is compared with the 4 flying shapes by analysing the camber (cf. figure 3.2) and the twist (cf. figure 3.3) of the intrinsic stripes. The design shape has a similar evolution of the camber to the flying shape AWA 64°. However the twist has a trend similar to the large AWA (linear increase in the bottom half and at a lower rate in the top half part of the sail). Nonetheless the absolute twist angle is between the twist of AWA 64° and AWA 96°.

3.1.3.3 Comparison using the 3D camber representation

Figure 3.8 presents the design shape using the 3D camber representation described before. It is compared with the 3D cambers of the different flying shapes presented in figure 3.5.

Even if the design shape is not represented in the boat frame, with this representation we can compare the clew positions. With the points "T" and "H" fixed, the "head-tack-clew" triangle defines the position of the clew point. The clew angle \widehat{TCH} for the design shape is 93° (91° for AWA 64°) and the tack angle \widehat{CTH} is 52° (52° for AWA 64°). Moreover the projected area for the design shape is equal to the projected area for AWA 64° ($A=52 \text{ m}^2$). The clew positions are similar. The design shape is closer to the flying shape at AWA 64°.

However, not only is an apparent wind angle of 64° an extreme sailing navigation for this type of spinnaker, but also the design shape does not really correspond to any flying shapes presented in Figure 3.5. The "bulb of camber" is clearly elliptic, is not circular and does not have a "bean shape". The maximum of camber is slightly less than 3 m for the design shape while the maximum camber on flying shapes is 3.3 m at AWA 124° and 3.1 m for AWA 64°.

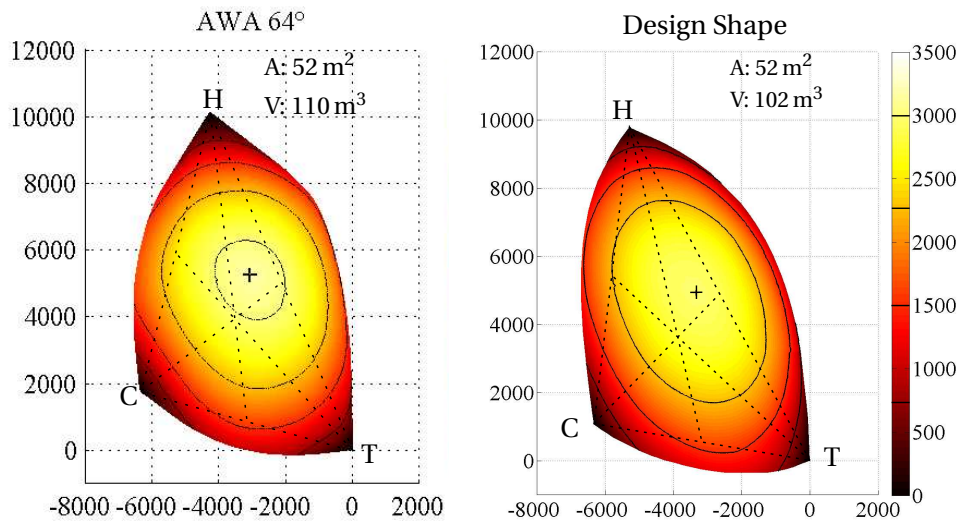


Figure 3.8 – Depth of the flying shape AWA 64° (left) and of the design shape (right) in mm when projected onto the plane created by the 3 corners head-tack-clew. The projected area of the spinnaker onto the plane and the volume between the spinnaker and the plane are given.

Table 3.2 summarises the projected area onto the "Head-Tack-Clew" plane and volume between the spinnaker and the HTC plane measured for the different spinnaker shapes. The volume is calculated as the integration of the depth over the whole spinnaker surface. For every volume calculated, the whole sail was on one side of the HTC plane. Therefore no negative depths were found. Another shape, presented in table 3.2, was computed using a structural solver called ARA dedicated for the sails and riggings of sailing boats. The structural model is a finite element model composed of beams (spars and battens), cables (wires and running rigging) and membranes (sails). The sail model is based on CST (Constant Strain Triangles) membrane model elements extended in 3 dimensions. It can be coupled with a fluid solver ISIS or AVANTI ([Durand, 2012]) for numerical FSI simulations.

The projected area decreases when the AWA is increased. The projected area is the same for AWA 64°, the design shape and also the flying shape computed by the solver ARA. To compute this shape, the properties of the design shape given by the sailmaker *Delta Voile* (panels, seams, sail cloth, ...) are modelled in ARA. The head, tack and clew positions are similar to the flying shape at AWA 64°. A constant pressure distribution of 40 Pa was applied to the sail. It is of the same order of magnitude as the pressure distribution measured for this AWA, but a constant differential pressure distribution is not representative to what is measured (cf section 3.3). Nonetheless, the projected area and the volume of the numerically calculated spinnaker shape are equal to the ones for AWA 64° (52 m² and 110 m³), whereas the volume is different (102 m³), even though the positions of the 3 spinnaker points (head, tack and clew) and the projected area are identical. Thus the difference between the design and the flying shapes is not only due to a difference of trim but also results from the fluid-structure interaction between the wind and the sail¹.

It is also interesting to note that for flying shapes measured or numerically calculated the volume does

¹The spinnaker was used for 2 regatta seasons, and the sail might now be a bit stretched compared to its original shape. Nonetheless this deformation is negligible in comparison with the difference of shape found.

not vary whereas the volume is lower for the design shape. The integral of the depth of the sail can be linked to the curvature. And the product of the curvature with the tension in the sail balances the pressure according to equation 1.13 for a static problem: $\Delta p + \underline{\chi} \cdot \underline{\kappa} = 0$. As first order, it might appear that for all pressure distribution the integration of the depth of the sail from the HTC plane might be constant. However a quick analytical analysis linking the curvature with the depth of the sail has not brought any evidence and confirmation to this idea yet.

spinnaker shape	area measured (m ²)	projected area (m ²)	volume (m ³)
AWA 64°	66.6	52	110
AWA 96°	65.4	49	113
AWA 124°	68.9	48	112
AWA 141°	67.6	47	109
Design Shape	68.5	52	102
ARA Shape	68.6	52	110

Table 3.2 – Areas and volume measured for different flying shapes, the design shape, and the flying shape calculated by ARA, a structure solver. Projected area is the area of the spinnaker projected onto the "Head-Tack-Clew" plane. Volume is the integral of the depth of the spinnaker between the "Head-Tack-Clew" plane and the spinnaker.

3.1.4 Bézier surface

Sail designers mainly use classical parameters of aerodynamic stripes to design a spinnaker. However a spinnaker is a 3D shape which changes with the AWA and these stripes are not always in a plane. The 3D camber representation provides a simple 3D visualisation to easily compare the shapes but it is not suitable for designing sails. Thus another representation using the Bézier surface was also developed during this PhD project to represent the flying shape of a spinnaker. Such a representation has the major advantage of defining the spinnaker as a 3D surface with only a few control points. (cf. figure 3.9). The evolution of these control points makes it possible to define the evolution of the flying shape of a spinnaker according to the AWA. Moreover for sail designers, it would be useful to develop a large database of flying shapes [Ranzenbach and Kleene, 2002, Fossati et al., 2015b]. Using control points instead of a whole surface would lead to a reduction and simplification of data storage.

Bézier representation was preferred to spline or NURBS because the blending functions have a more general impact on the whole surface. A sail has a triangular shape with 3 edges. Therefore triangular Bézier patches are more suitable for sails, and give similar errors with less control points than more common rectangular Bézier patches. For a better understanding, before showing the results, the main principles and properties of this representation are explained. For further details, numerous books and articles describe the Bézier curves and surfaces ([Prautzsch et al., 2002, Farin, 1986, Pastva, 1998, Patrick, 2007] among others).

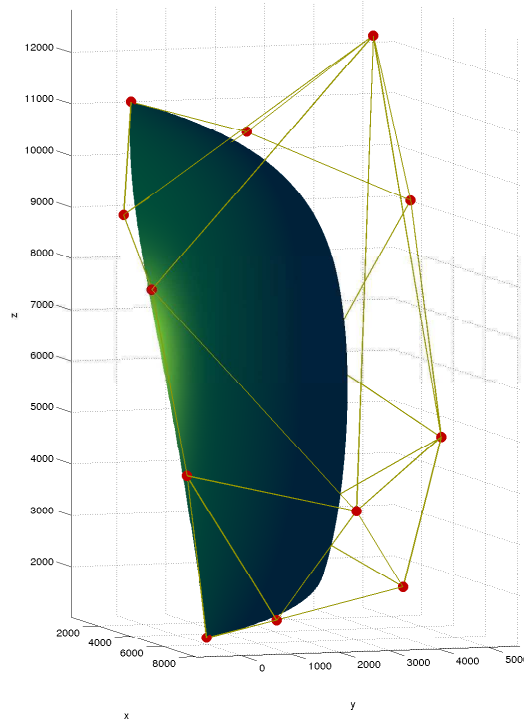


Figure 3.9 – Bézier surface and its control points (big red dots) representing a flying shape at AWA 96° using a triangular Bézier patch of degree 4.

3.1.4.1 Presentation of a Bézier surface

The use of Bézier curves and surfaces are named after Pierre Bézier a French engineer who worked at the French car manufacturer Renault [Bézier, 1968]. He developed this representation in order to have better control on the shape of the car body. It is now widely used for 3D computations of surfaces for example in design and video games. It can also be used for other purposes like characterising the different radar electromagnetic sources [Digne, 2013]. In this project, we used the Bézier surface to represent the shape of a sail and to characterise it.

Bézier curve Bézier curves are first explained to set the main properties that are still valid for Bézier surfaces. Bézier curves in 2 dimensions are parametric polynomial curves that can be written with the Bernstein polynomials:

$$Q(u) = \sum_{i=0}^n P_i B_i^n(u), \quad u \in [0, 1] \quad (3.1)$$

$$\text{with } B_i^n(u) = \frac{n!}{i!(n-i)!} u^i (1-u)^{n-i}, \quad u \in [0, 1] \quad (3.2)$$

$(P_i)_{i \in \{0, n\}}$ are the control points which define the curve, u is the curvilinear abscissa from 0 (beginning of the curve) to 1 (end of the curve), and $B_i^n(u)$ the Bernstein basis functions (sometimes also called blending

functions) (cf equation 3.2).

To better understand the properties of the Bézier curves, let us look at a simple example of a third order mathematical form of the Bézier curve. Figure 3.10 represents a cubic Bézier curve $Q(u)$ defined by 4 control points $P_0 = (0,0)$, $P_1 = (0,1)$, $P_2 = (1,1)$ and $P_3 = (1,0)$ arranged as a polygon. According to equation 3.1, if $n = 3$, we obtain:

$$Q(u) = B_0^3 P_0 + B_1^3 P_1 + B_2^3 P_2 + B_3^3 P_3, \quad u \in [0, 1] \quad (3.3)$$

$$Q(u) = (1-u)^3 P_0 + 3u(1-u)^2 P_1 + 3u^2(1-u) P_2 + u^3 P_3, \quad u \in [0, 1] \quad (3.4)$$

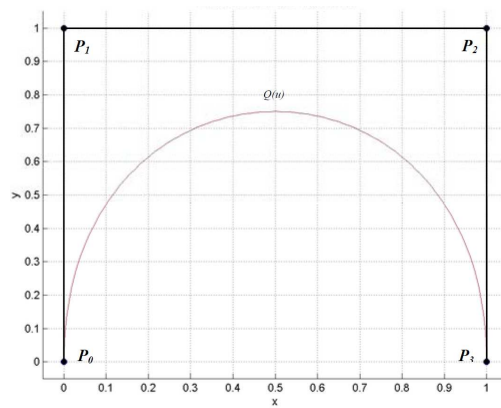


Figure 3.10 – Cubic Bézier curve $Q(u)$ and its 4 control points P_0 , P_1 , P_2 and P_3 .

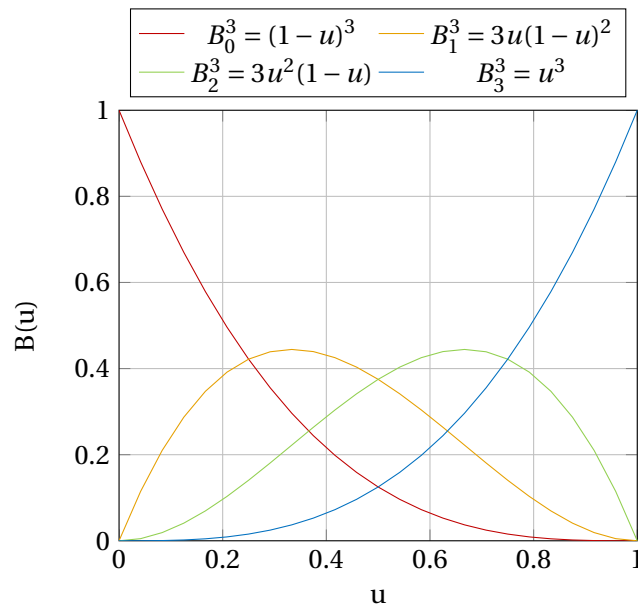


Figure 3.11 – Cubic Bézier blending functions as a function of the parameter u , the curvilinear abscissa.

Figure 3.11 shows the four Bernstein polynomials used to describe the cubic polynomial in equation 3.3. For all u , the sum of the four functions is equal to 1. One can notice that P_0 has a strong influence

on the curve at $u = 0$ and then its influence decreases when u is increased. B_1^3 and B_2^3 associated respectively with P_1 and P_2 do not reach 1, therefore $Q(u)$ does not pass through the points P_1 and P_2 . We can therefore draw the main properties of the Bezier curves:

- The degree of the polynomial defining the curve segment is one less than the number of control points.
- The curve follows the shape of the defining polygon formed by the connection of the control points.
- The first and last points on the curve coincide with the first and last control points.
- The tangent vectors at the first and last points are respectively parallel to the tangent of the first and last sides of the polygon.
- The curve is contained within the convex hull of the enclosed polygon. If the curvature changes sign, the polygon of the control points intersects the curve at the change of curvature. This property is a result of the convex barycentric combination of control points.
- Bézier curves are affine invariant. Scaling and rotating the control points scale and rotate the same way the curve and vice versa. An affine transformation can therefore be performed more quickly by using the control points.

Rectangular Bézier surface Bézier surfaces use also the Bernstein basis, like for the 2D case. However another dimension v is introduced. Figure 3.12 represents the parameters of a cubic surface defined by 16 control points. Figure 3.13 is a simple example of a surface defined by a control point mesh. The equation for a Bézier surface of degree $n \times m$ is:

$$Q(u, v) = \sum_{i=0}^n \sum_{j=0}^m R_{i,j} B_i^n(u) B_j^m(v), \quad \{u, v\} \in [0, 1] \quad (3.5)$$

with

$$\begin{cases} B_i^n(u) = \frac{n!}{i!(n-i)!} u^i (1-u)^{n-i}, & \{u\} \in [0, 1] \\ B_j^m(v) = \frac{m!}{j!(m-j)!} v^j (1-v)^{m-j}, & \{v\} \in [0, 1] \end{cases}$$

$(R_{i,j})_{i \in [0,n], j \in [0,m]}$ are the control points of the surface.

Bézier surfaces have similar properties to Bézier curves:

- The degree of the surface in a single parametric direction is one less than the number of control points in that direction.
- The continuity of the surface in a single parametric direction is two less than the number of control points in that direction.
- The surface follows the general shape of the defining cage.

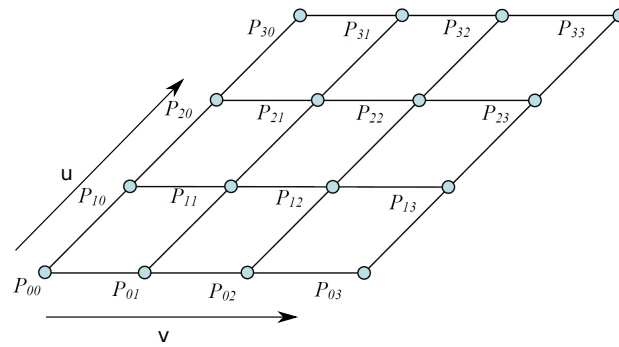


Figure 3.12 – Parameters of a cubic parametric surface with u and v directions, intrinsic of the surface and control point mesh (also called Bezier cage).

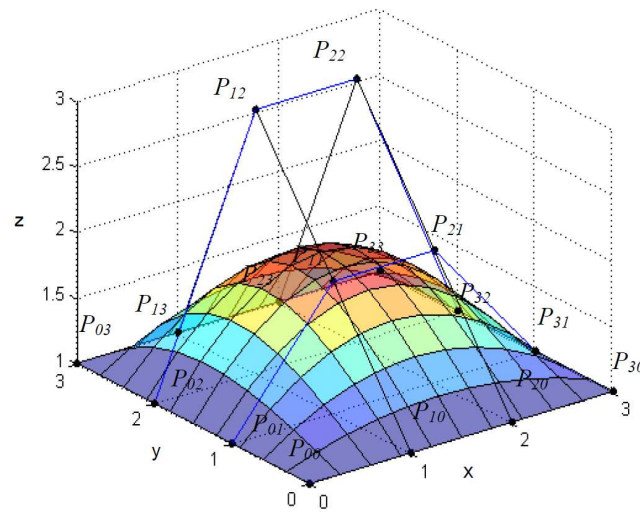


Figure 3.13 – Parametric surface and control point mesh.

- The four corners of the surface coincide with the four control points on the corners of the cage.
- The edges of the surface can be defined as a Bézier curve by the corresponding control points on the edges.
- The planes created by control points on the edges of the surface and their closest neighbours are equal to the tangential planes of the sides of the surface.
- The surface is contained within the Bézier cage, the convex hull of the enclosed control point polygon mesh. If the curvature of the surface changes sign, the polygon mesh intersects the surface at the change of curvature.
- The surface is invariant when affine transformations are applied to either the control points or the surface.

Triangular Bézier surface A spinnaker has a triangular shape with only 3 corners and 3 edges. Therefore a set of parameters defining a triangular shape should be used, such as a triangular Bézier patch:

$$Q_t(u, v) = \sum_{i=0}^n \sum_{j=0}^{n-i} T_{i,j} \frac{n!}{i!j!(n-i-j)!} u^i v^j (1-u-v)^{(n-i-j)} \quad (3.6)$$

with $0 \leq u, v \leq 1, u + v \leq 1$

$(T_{i,j})_{i \geq 0, j \geq 0, i+j \leq n}$ are the control points of the surface.

Triangular Bézier surface has the same properties than the rectangular Bézier surface.

With the use of Bézier surface to model the flying shape, the spinnaker can be defined by only one intrinsic set of parameters (u , v , and position of control points relative to u and v). Therefore to compare the flying shapes for different wind and trim conditions, the same set of control points will be used. Only their positions in space will change. A change of one control point position affects the whole sail. Therefore less control points are required to characterise a sail shape. And finally since the surface is defined by polynomials, minimum, maximum, mean or Gaussian curvatures can easily be calculated. For further details, the reader is referred to [Ratto, 2016].

3.1.4.2 Create a triangular Bézier surface to represent the shape of a spinnaker

With the help of [Ratto, 2016], and taking inspiration from [Patrick, 2007], I developed a method to represent a spinnaker with a Bézier triangular patch in 3 steps:

1. **Interpolation spline curves from photogrammetric stripes:** From the flying shape acquisition system, positions of target points, distributed on different sections of the sail, are measured (see section 2.3). From these measured points, a spline interpolation is performed in order to acquire smooth 3D curves with an increased number of equidistant points on the stripe, simplifying the calculations afterwards.
2. **Calculation of the control points to create a rectangular Bézier surface:** A rectangular Bézier patch is first created in order to use the ease and the speed of matrix equations that are not possible with triangular Bézier equations. Indeed equation 3.6 cannot be written in a matrix form because the two sums are dependent on each other, when equation 3.5 can easily be written in a matrix form:

$$Q = U_n B_n P B_m^T V_m^T \quad (3.7)$$

with:

$$U_n = \begin{pmatrix} 0 & 0 & \dots & 1 \\ u_1^n & u_1^{n-1} & \dots & 1 \\ \dots & \dots & \dots & \dots \\ u_i^n & u_i^{n-1} & \dots & 1 \\ 1 & 1 & \dots & 1 \end{pmatrix} \in \mathcal{M}_{k,n+1} \mathbb{R}$$

$$V_m = \begin{pmatrix} 0 & 0 & \dots & 1 \\ v_1^m & v_1^{m-1} & \dots & 1 \\ \dots & \dots & \dots & \dots \\ v_j^m & v_j^{m-1} & \dots & 1 \\ 1 & 1 & \dots & 1 \end{pmatrix} \in \mathcal{M}_{l,m+1} \mathbb{R}$$

Equation 3.7 needs to be inverted in order to determine the matrix P which is our unknown, while Q is known. To find the control points matrix P , the values of $(u_i)_{i \in [0,1]}$ and $(v_i)_{i \in [0,1]}$ need to be fixed. Since the number of points is equally distributed on the curves, we choose a constant step for $(u_i)_{i \in [0,1]}$ and $(v_i)_{i \in [0,1]}$. The only unknown matrix is therefore P . The matrices B_n and B_m are invertible but not U_n and U_m since they are rectangular. The Moore-Penrose pseudo inverse is therefore used [Leon, 2010]. The pseudo-inverse of a matrix A is defined in order to find the least mean squares solution and is denoted $A^+ = (A^T A)^{-1} A^T$:

$$P = (U^+ B_n^{-1}) Q (V^+ B_m^{-1}) \quad (3.8)$$

The set of control points P defines the flying shape of the sail. However, as Figure 3.14a shows, the Bézier cage is not well constructed mainly because there are too many control points at the top of the sail; a whole edge of the rectangular patch must be reduced to a single point (the head point). As explained previously, the spinnaker is better represented by a triangular patch.

3. **Conversion of a rectangular patch to a triangular patch:** After inverting the equation 3.5, the previous rectangular patch is transformed into a triangular patch. Via a change of variables:

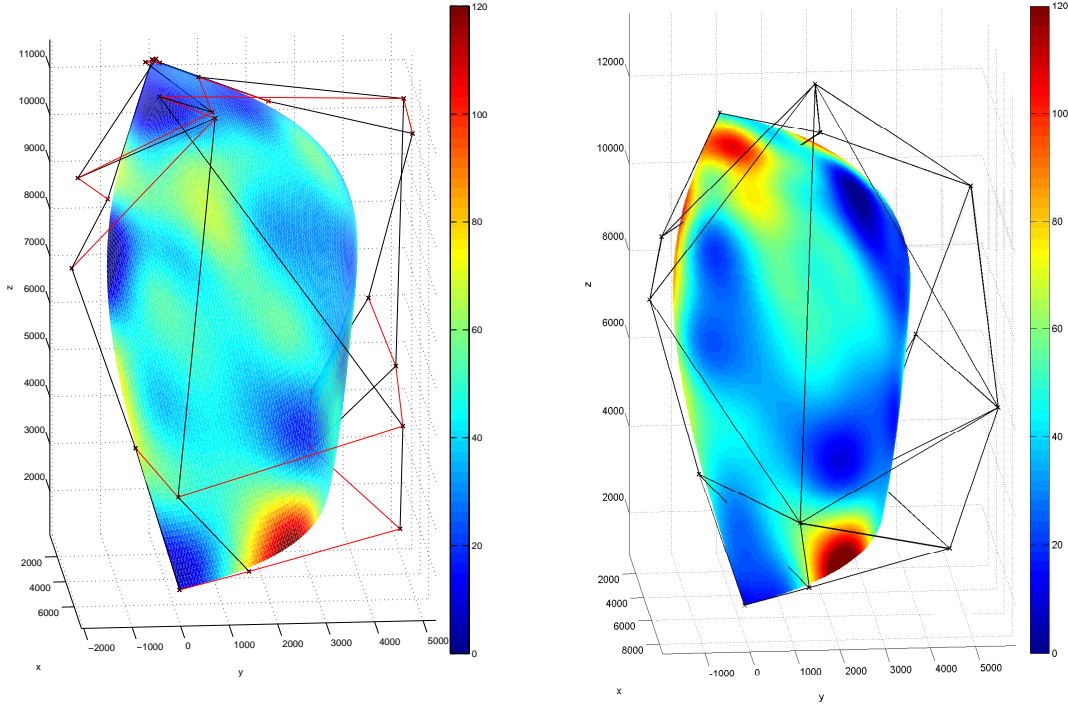
$$\begin{cases} s &= u, s \in [0, 1] \\ t &= \frac{v}{1-u}, t \in [0, 1] \end{cases}$$

we obtain:

$$Q_t(s, t) = \sum_{i=0}^n \sum_{j=0}^{n-i} T_{i,j}' B_i^n(s) B_j^{n-i}(t), s, t \in [0, 1] \quad (3.9)$$

The form of a rectangular Bézier patch can almost be recognized in equation 3.9. The idea is to use step 2 with $m = n$, to acquire a rectangular Bézier patch of degree $n \times n$ that describes the original sail and reduce every curve $C_i(v) = \sum_{j=0}^n R_{i,j} B_j^n(v)$ to the degree $n - i$. For further details, see [Ratto, 2016].

A triangular Bézier patch is presented in Figure 3.14b in comparison with a rectangular Bézier patch of an identical degree (degree 4) (Figure 3.14a). The maximum error is similar between both shapes (around 120 mm at the foot) but the average error is lower for the triangular Bézier patch. Furthermore the Bézier cage of the triangular patch is more coherent than the rectangular Bézier cage. For the rectangular patch, an entire edge must be reduced to a single point (the head), therefore there are more control points defining the narrow top of the sail than the rest of the spinnaker. The lines of the Bézier cage can cross each other, and it does not help for the visualisation of the shape. Whereas the triangular Bézier cage has a convex and coherent shape.



(a) A rectangular Bézier surface of degree 4×4 (25 control points). (b) A triangular Bézier surface of degree 4 (15 control points).

Figure 3.14 – Rectangular and Triangular Bézier surface representing the flying shape of the spinnaker at AWA 124° and their corresponding control points creating the Bézier cage. The colors plotted on the sail are the errors in mm from the points measured by photogrammetry.

3.1.4.3 Precision of the reconstruction by a Bézier surface

Finally, a flying shape of the spinnaker can be defined either by a rectangular or by a triangular patch at different degrees. For the explanations below, rectangular patches have the same degree for u and v ($m = n$).

To compute a spinnaker shape by a Bézier surface, a compromise must be found between the amount of control points used and the precision of the reconstruction. To analyse the error coming from the reconstruction by a Bézier surface, we must be certain there is no error also taken into account due to measurements. The flying shape acquisition system has a certain incertitude that might bias the reconstruction of the shape of the sail. To compare the reconstructed Bézier surface with the most defined shape (without any measurement error), we analyse the precision of the reconstruction on the design shape which comes from a 3D computed shape given by the sailmaker. Figure 3.15 shows the average and maximum errors for different degrees of rectangular and triangular patches for the computed design shape. The error is calculated as the distance between the two shapes. The number of control points is indicated on the x axis, and the figure near the marks represents the degree of the Bézier patch. For a given degree, a rectangular patch always has more control points than the triangular patch. For example at a

degree 5, a rectangular patch has 36 control points and only 21 for a triangular patch. For the same number of control points, triangular patches have much lower errors. For example with 15 control points for a triangular patch of degree 4, the average error is 40 mm. Whereas with 16 control points for a rectangular patch of degree 3, the average error is 101 mm. In conclusion, for a triangular patch, not only is the Bézier cage more consistent, but the average error is always smaller than for the rectangular patch. *A triangular patch of degree 4 is a good compromise between a good average error (40 mm) and not too many control points (15), and will therefore be used to model flying shapes of the spinnaker.*

Table 3.3 presents the average and maximum errors for the 4 flying shapes presented in Figure 3.1 for different degrees of triangular patches. The trend is similar to the errors of the design shape presented in Figure 3.15. The errors with a degree 4 are just slightly higher, with the highest average errors found at 65 mm.

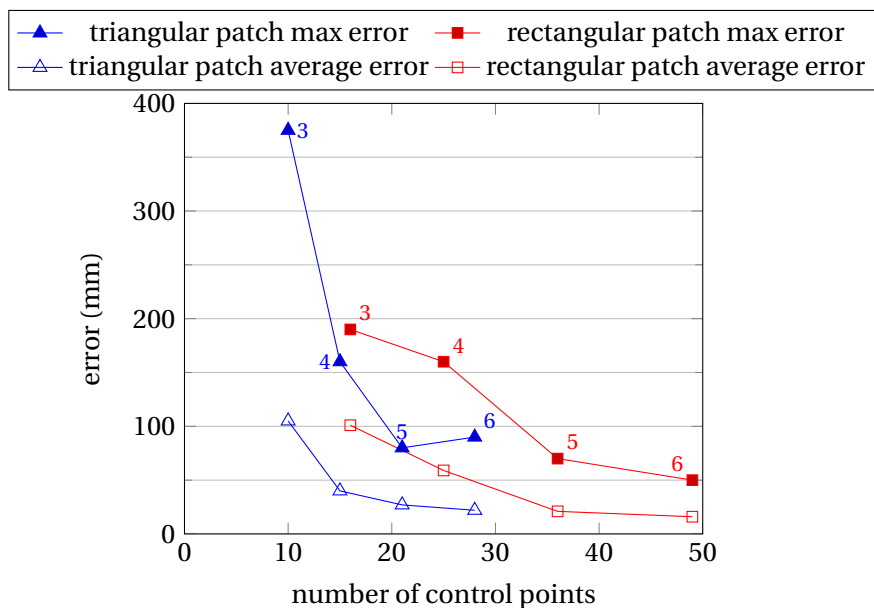


Figure 3.15 – Average and maximum errors of the Bézier surface relative to the measured surface of the design shape as a function of the number of control points. The figures near the marks indicate the degree of the Bézier surface giving this error.

Errors (mm)	Design Shape		AWA 64°		AWA 96°		AWA 124°		AWA 141°	
	average	max	average	max	average	max	average	max	average	max
Degree 3	105	375	123	375	132	325	123	325	112	350
Degree 4	40	160	65	230	57	170	65	190	61	180
Degree 5	27	80	40	120	40	100	40	90	41	100
Degree 6	22	90	43	170	30	90	43	90	36	150

Table 3.3 – Average and maximum errors of triangular Bézier surface for different degrees relative to the measured surface at different AWA and computed surface of the design shape.

3.1.4.4 Utility of a Bézier surface for sail design

With the use of a Bézier triangular surface, the spinnaker is seen as a 3D model unlike intrinsic stripes of the spinnaker. The number of control points might be similar to the number of parameters used by a sail designer to create a sail. For different stripes, he uses several parameters such as entry and exit angles, cambers at different drafts, length of the curve... All these parameters are still easily controllable thanks to the properties of the Bézier control points. For example, in Figure 3.9, the highest and furthest point from the sail will control the overall camber of the sail. The control points on the edges, like a Bézier curve, are used to design the luff, leech and foot of the sail. The control points next to them make it possible to tune the tangential plane, hence the entry and exit angles of the sail.

Moreover, a Bézier representation might be of great help to optimise the design of a sail within class rule restrictions. Usually the lengths of the luff, leech, foot and curve at mid height of the sail are restricted by the class rules. And with other constraints such as the tangential plane at the clew point which must contain the clew sheet line, or limits set on the gaussian or mean curvature, an optimisation process could be developed to restrict the allowable shift of the different control points. A boundary around each control point would help the sail designer to respect the class rule regulations.

3.1.4.5 Evolution of control points according to Apparent Wind Angle (AWA)

Another advantage of representing the flying shape by a Bézier surface is to better analyse the evolution of the flying shapes with the AWA by representing the evolution in space of the control points only. Figure 3.16 shows the evolution of the control points according to the AWA in the boat frame. From 4 flying shapes (AWA 64° in blue diamond, AWA 96° in green circle, AWA 124° in orange square and AWA 141° in red star), the evolution of each control point has been interpolated. In figure 3.16, the flying shape of AWA 96° with its Bézier cage is also represented in the boat frame.

From the top view (x-y view, bottom right), the evolution of the control points shows a rotation of the whole sail around the mast (at $(x, y) = (0, 0)$). The two control points defining the leech follow less this overall rotation, resulting in the leech being more open for larger AWA.

The side view (x-z, top left) highlights that most of the points especially at the leech and foot move upwards as well because the clew sheet is eased.

The biggest variation, as expected is for the central control points of the sail setting the general camber of the sail. Finally, from Figure 3.16, we can also notice that the variation of the control points, hence of the flying shape, is much more greater between AWA 64° and AWA 96° than between AWA 124° and AWA 141°.

Figure 3.16 presents the evolution of the control points in the boat frame. It combines the general rotation of the sail around the Head-Tack line due to the easing of the clew sheet, and the deformation of the sail. To differentiate these two parts, Figure 3.17 describes the evolution of the control points in the "spinnaker frame", with the head, tack and clew points defining the y-z plane, as computed in subsection 3.1.2.2. The Head and Tack points are therefore fixed, and the clew point evolves only in the y-z plane.

From the front view of Figure 3.17 (y-z view, top right), one can notice that the control points around the

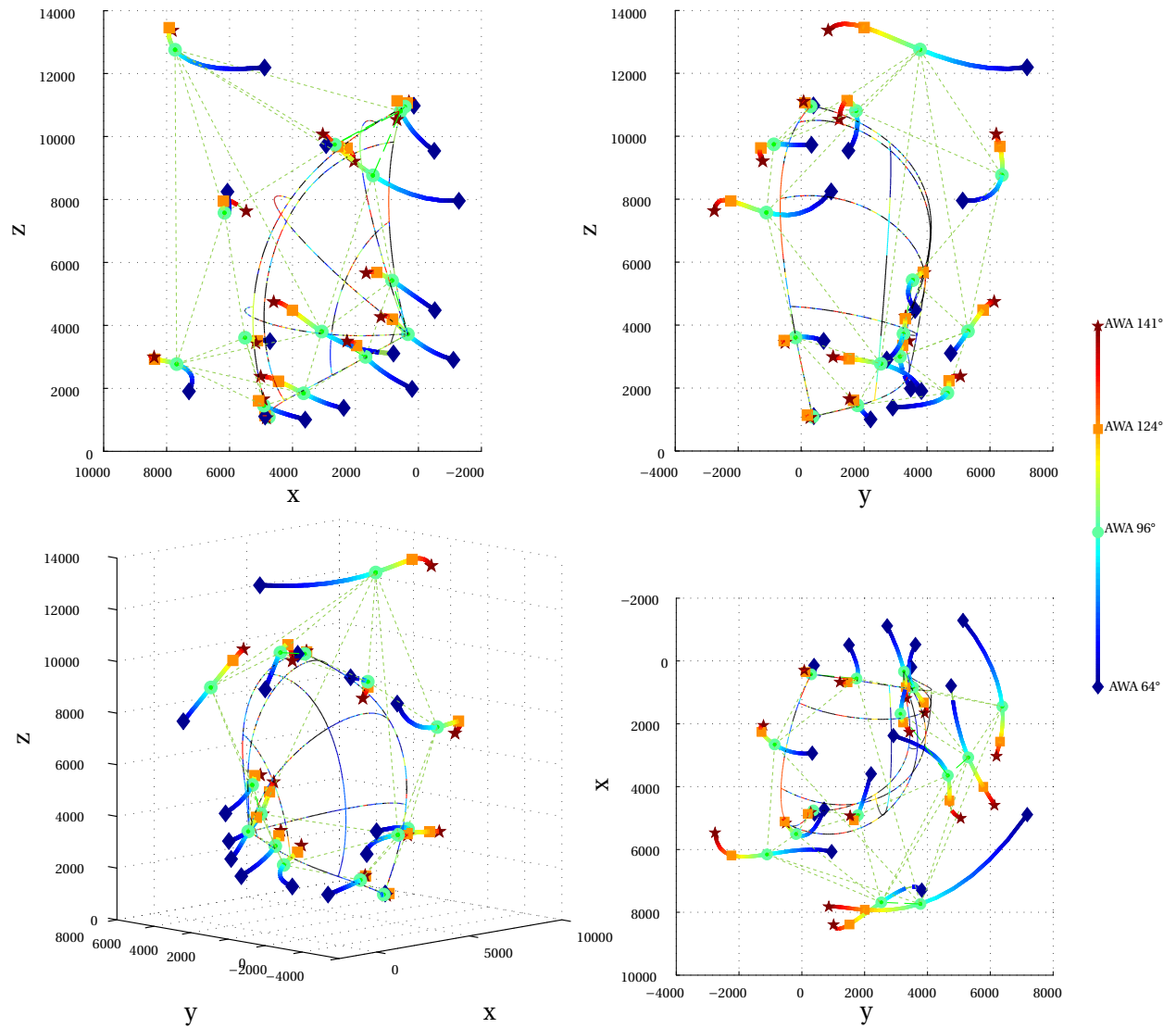


Figure 3.16 – Projections in the three planes relative to the boat frame and 3D plot of the evolution of the 15 control points from AWA 64° (in blue) to AWA 141° (in red). The black lines represent the Bézier surface of degree 4 of the shape of the spinnaker measured at AWA 96°. The light green dashed lines represent its *Bézier Cage*.

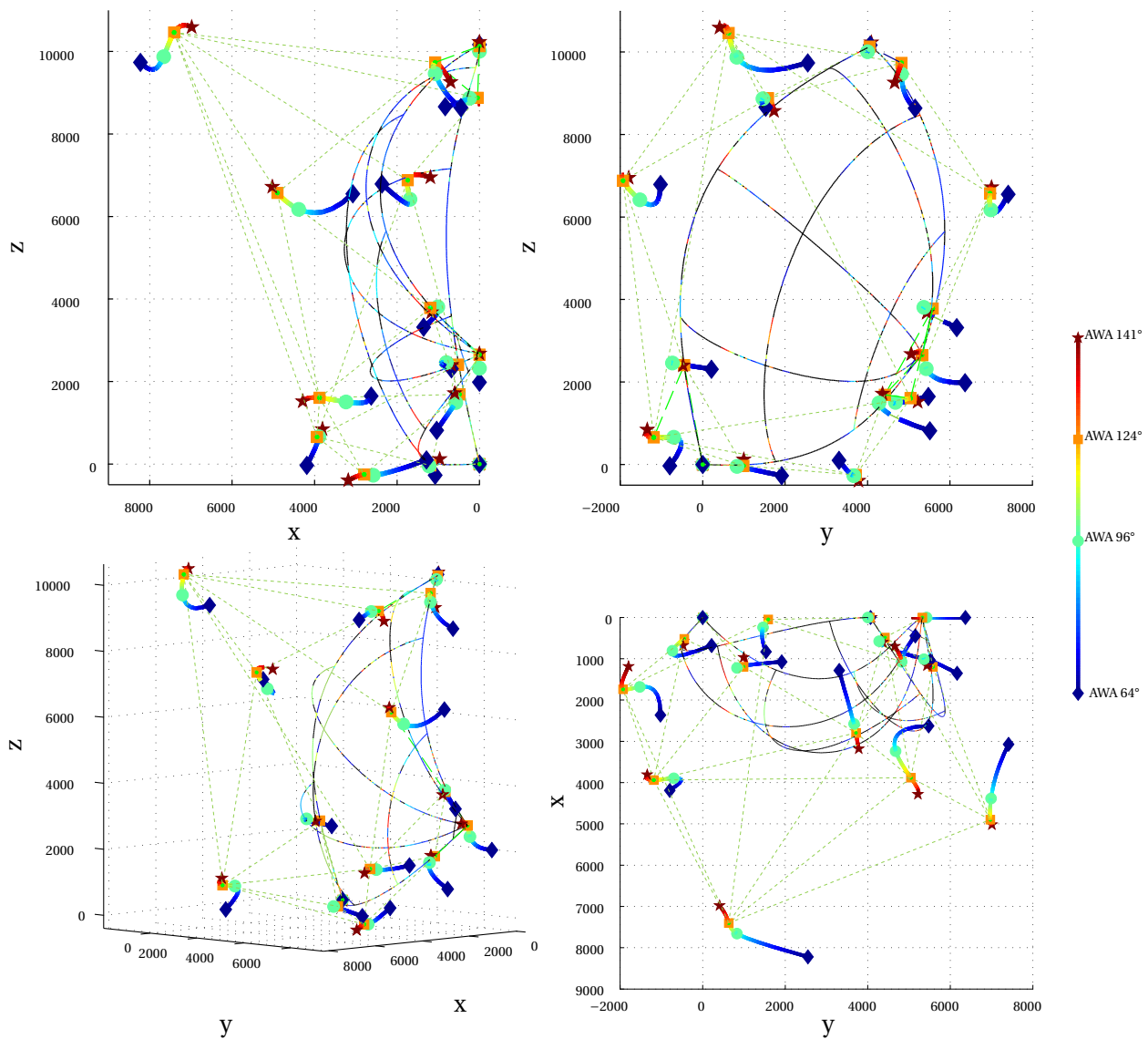


Figure 3.17 – Evolution of the control points interpolated from AWA 64° (in blue) to AWA 141° (in red) *with the Head-Tack-Clew defining the y-z plane*. The black lines represent the Bézier surface of degree 4 of the shape of the spinnaker measured at AWA 96°. The light green dashed lines represent its Bézier Cage.

clew move towards the luff, resulting in a lower projected area of the sail on the y-z plane. As a consequence the control points of the leech move forward (in +x direction). It results in a more twisted leech. However the central control point, setting the general camber of the sail, does not follow this trend and rather moves toward the luff. Most of the variations of this central control point occur between AWA 64° and AWA 96°.

With the interpolation of the different control points for one spinnaker, supposing a smooth evolution according to the AWA, it is therefore possible to interpolate the flying shape of the spinnaker for any AWA.

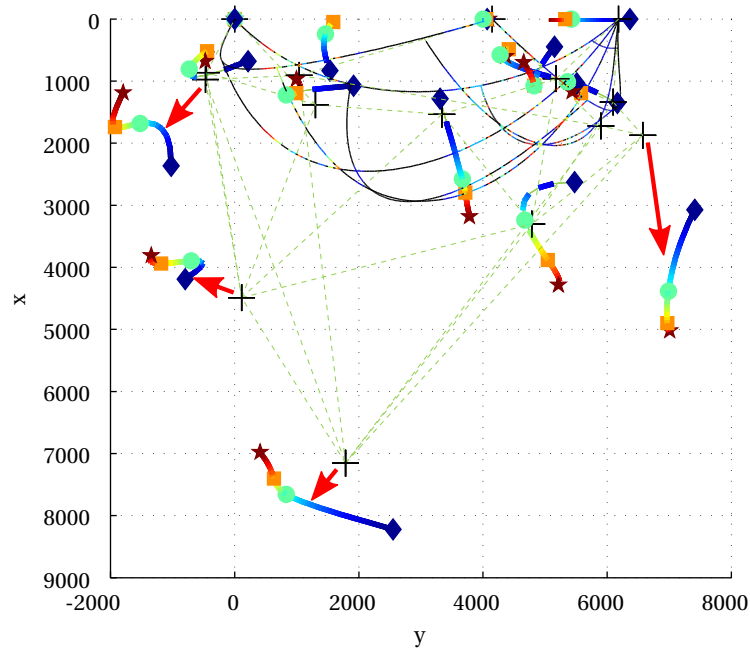


Figure 3.18 – Projection in the top view (x-y plane) of the evolution of the control points interpolated from AWA 64° (in blue) to AWA 141° (in red) *with the Head-Tack-Clew defining the y-z plane*. The black lines represent the Bezier surface of degree 4 of the *design shape* of the measured spinnaker. The light green dashed lines represent its *Bezier Cage*, and the large black crosses its control points. The red arrows highlight shifts between some control points of the design shape and some evolution curves of the control points of the flying shapes.

Comparison with the Design Shape With the use of the Bézier representation, it is also possible to compare the design shape with the flying shapes of the sail. Even if the design shape is not designed for a specific AWA, the fixed control points of the design shape can be compared with the interpolated curves of the corresponding control points. Figure 3.18 presents the evolution of the control points relative to the "Head-Tack-Clew plane" as in figure 3.17, with the design shape and its Bézier cage plotted. Its control points are represented by the black crosses. Apart from the three corners, none of the control points of the design shape is on the interpolated evolution curves of the control points. The control point of the design shape at the clew is close to a shape for an AWA near 64°. The red arrows on the top view (x-y plane) highlight the main differences with the flying shapes. The leech of the flying shapes is more open with the control points further forward (in +x direction), the luff is more curved with the control points more outwards, and the main camber of the flying shapes are larger, with the central control point further away from the "HTC" plane.

3.1.5 Conclusions

Sail designers mainly use classical parameters of aerodynamic sections (cambers at different drafts, entry and exit angles, ...) at different heights of the spinnaker to design a sail. However these stripes are not necessarily in a plane and the spinnaker is a 3D object and not a 2D-extruded shape. Plotting the depth of the sail from the plane created by the three corners (head, tack and clew) makes it possible to analyse the

"3D camber" of the sail and its general 3D form. From this projection, we have concluded the projected area of the sail onto the "Head-Tack-Clew" plane decreases, while the volume of the sail (calculated by the integration of the depth of the sail from the "HTC" plane) might be constant for all pressure distribution. With further analysis, if this first order property is verified, it might be a way to verify if the spinnaker is in an equilibrium state in numerical simulations.

The 3D shape of the spinnaker is also represented by a Bézier triangular patch. The evolution of the control points according to the AWA enables the flying shape of the sail to be well characterised for all AWA. This representation means shapes from known flying shapes can be interpolated. The sail designer could possibly use them to create an optimisation process for a sail restricted by class regulations. [Ranzenbach and Kleene, 2002, Fossati et al., 2015a] express the need to create a large database of flying shape of spinnaker for sail designers. Using Bézier surface and control points would reduce the amount of data, and would help to characterise more easily the different types of offwind sails.

3.2 Loads on the spinnaker

This section presents the evolution of the loads on the 3 corners of the spinnaker and also projected onto the boat frame (propulsive, side and vertical forces) thanks to the DLCs and the resulting loads on the rigging of the sailing boat. As explained in section 2.9, stable periods were chosen to measure the average loads and load coefficients. The load coefficient is the ratio between the time averaged load and the dynamic pressure using the time averaged AWS multiplied by the total surface of the sail $S = 68 \text{ m}^2$ over the stable period: $C_f = \frac{\langle F \rangle}{\frac{1}{2} \rho S \langle \text{AWS} \rangle^2}$.

3.2.1 Evolution of the spinnaker loads with the AWA

3.2.1.1 With the mainsail hoisted

During the experiments in 2013, some measurements of the loads with wireless shackles but without DLCs were carried out with the mainsail hoisted. The results are presented in Figure 3.19. Figure 3.19a. displays the loads in newtons. For the 3 corners the loads decrease when the AWA is increased. The highest load is found at the head of the sail (almost 1200 N). From AWA 70-80° to AWA 120-150°, the load measured at the head is divided by 3. The tack load is of the same order of magnitude (around 1000 N at 70° to 300 N at 140°) as the head load. Clew point is almost half loaded for tight angle till 90° whereas it has the same order of magnitude as the 2 other corners for AWA larger than 120°. The smaller loads at higher AWA are mainly due to the reduced AWS.

To compare without the influence of the AWS, Figure 3.19b. shows the load coefficients as defined above. This representation is from an aerodynamic point of view with a non-dimensionalisation by the incoming flow. Head and tack force coefficients are rather constant according to the AWA with a small peak at around AWA 100° with a load coefficient of 0.8. These force coefficients seem to slightly decrease down to 0.4 for AWA larger than 110°. However the clew force coefficient slightly increases in concordance with the smaller decrease rate of its load from 0.35 to 0.45 at AWA 110° and decreases for higher AWA.

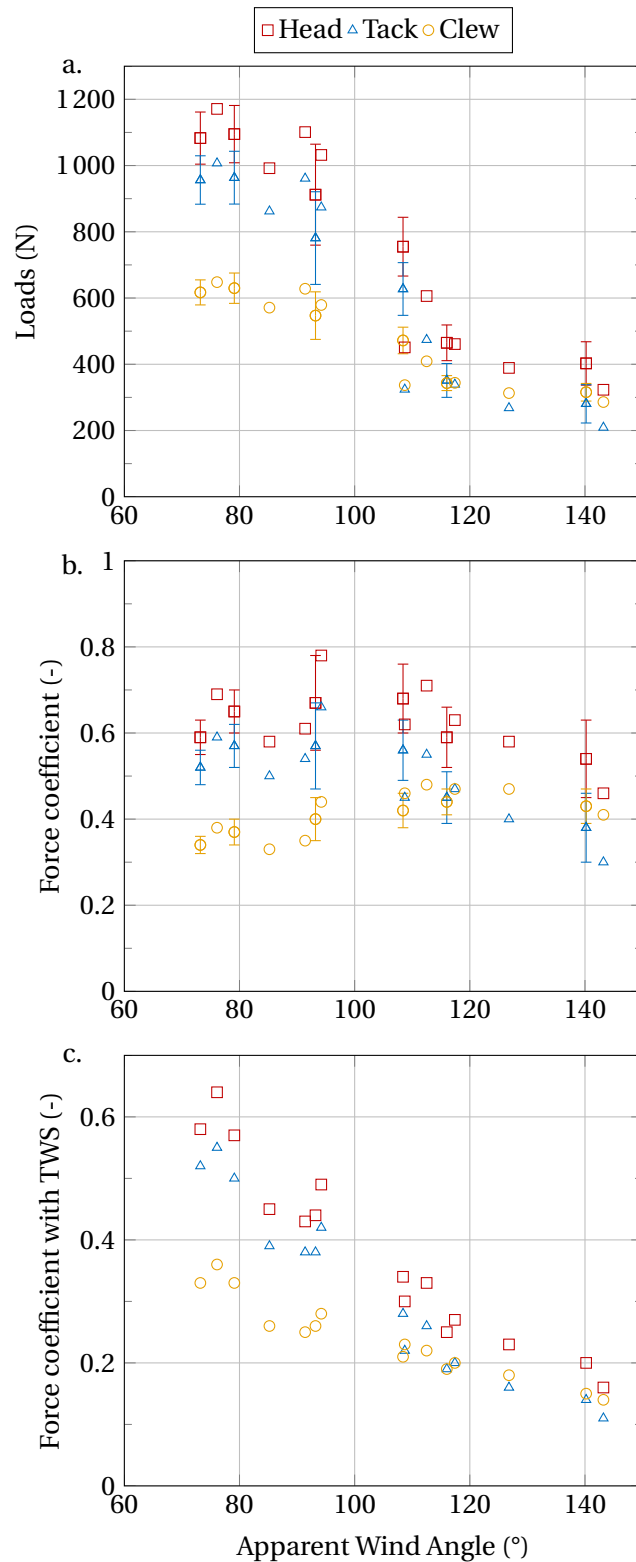


Figure 3.19 – Loads on the corners of the spinnaker for $TWS \approx 6.5 \pm 0.7$ m/s with the mainsail hoisted. **a.** Absolute measured loads. **b.** Load coefficients non dimensionalised by the AWS. **c.** Load coefficient non dimensionalised by the TWS. Error bars indicate the standard deviation obtained during one stable run.

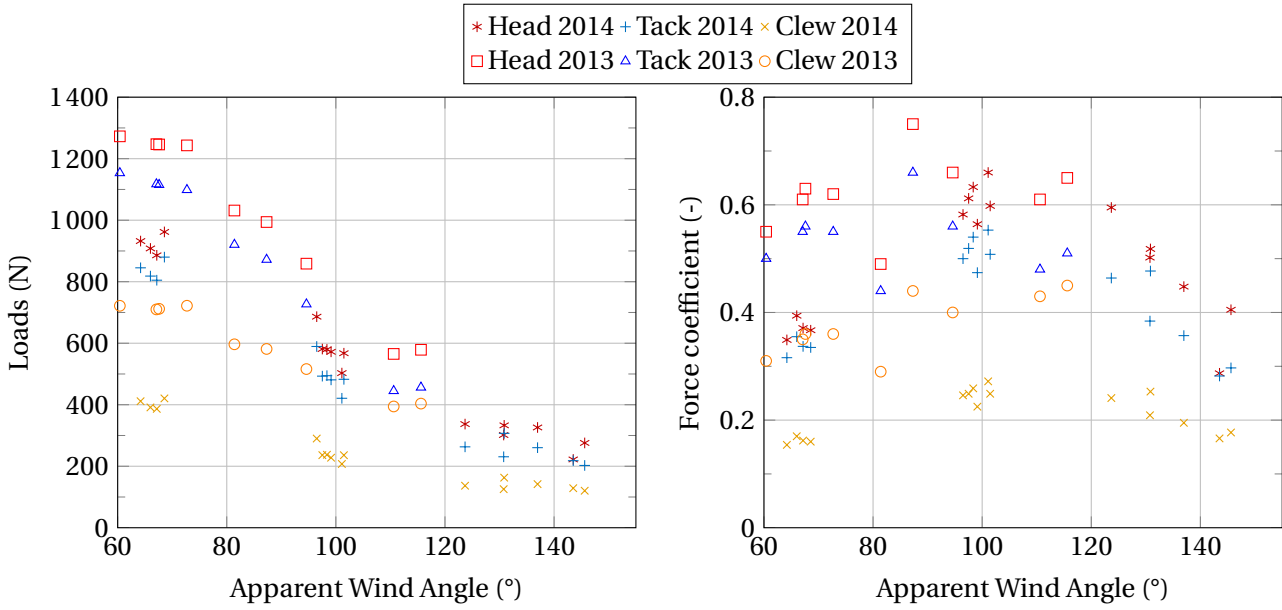


Figure 3.20 – Comparison of loads on the corners of the same spinnaker without the mainsail for different experiment campaigns in 2013 and 2014. TWS in 2013: 5.5 m/s (11 kn). TWS in 2014: 4.5 m/s (9 kn).

From a sailor’s point of view, the non-dimensionalisation is more useful by the true wind. Figure 3.19c. displays the evolution of load coefficient using the True Wind Speed (TWS) for the non dimensional coefficient: $C_f = \frac{\langle F \rangle}{\frac{1}{2} \rho S \langle TWS \rangle^2}$ using the TWS formula from [Fossati, 2009]:

$$TWS^2 = (AWS \cos(AWA) - BS)^2 + (AWS \sin(AWA) \cos(heel))^2 \quad (3.10)$$

The TWS is virtually constant for all AWA from 5.8 m/s to 7.1 m/s thus between 11.2 kn to 13.8 kn. There is a clear decrease of the load coefficient, from 0.6 down to 0.1 for the head and tack load coefficient and 0.35 down to 0.1 for the clew load coefficient.

Even during the stable runs where AWA and AWS are almost constant, loads fluctuate because of the unsteady nature of the “wind/spinnaker” system. Boat motion due to waves was found to be negligible. In Figure 3.19a, standard deviations of loads are around 8% of the averages at the head and tack of the spinnaker for an AWA around 70-90°. Standard deviations at the clew are slightly smaller. Standard deviations for an AWA between 100° and 140° are around 11 to 20% of the average loads at the tack and head. At the clew points, standard deviations are lower than 10%.

3.2.1.2 With the mainsail lowered

Comparison between 2013 and 2014 results Some measurements with the mainsail lowered were carried out both in 2013 and in 2014. In 2013, wireless shackles were used while in 2014 DLCs measured the magnitudes and the directions of the loads. In 2013, the range of AWA was shorter than for results from 2014, respectively between 60° and 120° and between 60° and 150°. However in 2014, we mainly focused

our experiments for 4 different AWA: 70°, 100°, 120° and 140°. Therefore there are voids for some AWA. Even if the AWS was similar for both experiments, Figure 3.20 shows that the loads measured in 2013 and in 2014 are rather different. For example for tight AWA (about 60°), the loads measured in 2013 is almost 1300 N while in 2014, 1000 N. This difference appears on the force coefficients too. We now analyse the possible reasons for this result.

The main differences between the two experiments were the change of installed load sensors, the change of trimmer of the spinnaker and the pressure system not on the sail in 2014. However the rigging loads were also higher in 2013. The pre-tension in the rigging was the same basic dock tuning for both experiments. Therefore the higher tension in the rigging is the result of a bigger aerodynamic load. The change of load sensors is not the main reason for this difference.

Another reason might be the difference of the wind profile on the sail, modifying the load distribution of the spinnaker. In 2013, we had stable westerly winds. While in 2014, the wind came from North-West, more unstable with a "heavier" atmosphere. There were thunderstorms in the evening. Therefore the wind gradient was probably different. Thus, even though the apparent wind measured locally at the top of the mast was similar for both experiments (AWS=7 m/s for AWA=65° and AWS=4.5 m/s for AWA=100°), the wind profile could have been different between the sea level and the anemometer. Furthermore in 2013, experiments were carried during strong tide (coefficient 104, tide range of 6.5 m) in an area of the Bay of Brest where currents can reach more than 2 knots. The difference between the boat speed (SOW) and the SOG was indeed around 1.5 kn for a boat speed of 6.5 kn. Whereas in 2014, the tide was not as strong. There was no difference measured between the SOW and the SOG. In 2013, the current was in the same direction as the wind (from west to east). The current moved the boat reducing with an offset on the whole height an equivalent apparent wind gradient without any current. To measure the same AWS at the top of the mast, the TWS should have therefore been stronger. It is confirmed with a weather buoy near the experiment area having measured a wind speed 2 kn to 3 kn higher in 2013.

Projection of load onto boat frame Thanks to the DLCs, the aerodynamic load produced by the spinnaker can be projected onto the boat frame. The results are presented in Figure 3.21. For tight AWA (around 70°) the propulsive force F_X and the side force F_Y are similar at around 1100 N. The vertical force F_Z is almost half as high as them (600 N). The loads decrease when the AWA is increased. For deeper AWA (around 120°-140°), the forces are between 0 and 400 N. The load coefficients in Figure 3.21 indicate that this spinnaker is the most efficient for AWA between 100° and 120°, since the F_X force coefficient is about 0.9 and more than twice as large as the side force. The side force is quite penalising because it makes the boat heel and increases the leeway and hence increase the hydrodynamic resistance of the hull. The side force is almost zero for AWA 130°. For large AWA, the results have less consistency because the standard deviations increase significantly. As explained in subsection 2.4.2.2, for large AWA, an error of 5° in the direction of the loads can lead to a variation of 60% of the side force.

Loads in shrouds The loads in the shrouds can confirm when the side force F_Y produced by the sails is null. The shrouds, maintaining the mast, are pre-tensioned at known values. They are called docktune settings. The name of the shrouds are introduced in subsection 2.2.1. The forestay is connected at the same height than the shroud V1, at 7/8 of the height of the mast. The head point of the spinnaker is

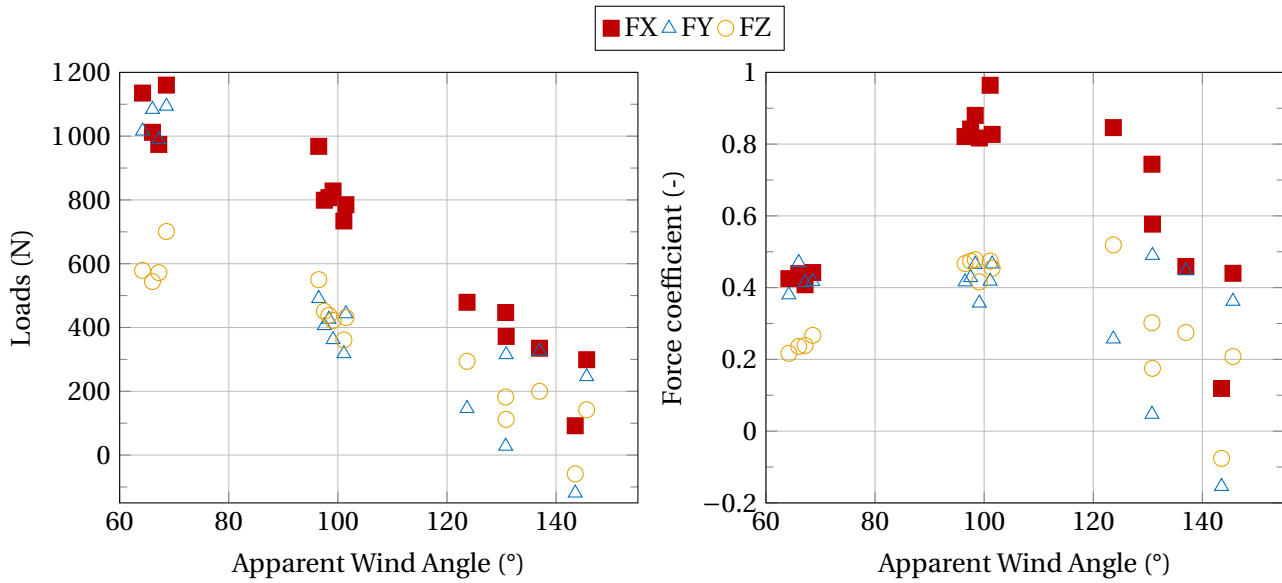


Figure 3.21 – Breakdown of the aerodynamic load of the spinnaker (without the mainsail hoisted) in the boat frame. FX is the propulsive force, FY is the side force and FZ the vertical force.

0.7 m above but not at the top of the mast. According to Figure 3.22, for small AWA, the windward side is more loaded (for V1, the loads are about 5700 N, 100% more than the docktune) and the leeward side is less loaded (600 N, -70% the docktune, for D1). For AWA larger than 120°, the loads are almost at the docktune loads. If FY is null, the loads on the shrouds on the leeward side and on the windward side should be symmetrical about the docktune, as they would take FX and FZ loads only. Figure 3.23 displays the difference between the variations of the loads at leeward and windward from the docktune:

$$\frac{(F_{windward} - Docktune) + (F_{leeward} - Docktune)}{Docktune}$$

This confirms that D1 and V2 has the highest difference of variations, with a variation relative to the docktune of +30% for the windward shroud. In Figure 3.21, the measurement for AWA 143° indicated a negative FY. In Figure 3.23 with a difference of variation at V1 almost null and negative for D1, this confirms the DLC results.

Comparison with Wind Tunnel experiments In general, to assess the performance of a downwind sail, wind tunnel experiments are carried out. In a large range of AWA, the optimum trim is sought by optimising the propulsive force generated by the sail. Several publications have been published and are set as references for downwind sails (cf. figure 3.24).

[Offshore Racing Congress, 2015] describes the methods and formulations used by the Offshore Racing Congress (ORC) VPP. The ORC VPP is the program used to calculate racing yacht handicaps based on a mathematical model of the balance of the forces in a sailing yacht. To assess the performance of sails, force coefficients are given for different type of sails. These force coefficients are determined from various wind tunnel tests. The J/80 spinnaker is an *"Asymmetric Spinnaker tacked on centreline"*.

[Campbell, 2014a] summarises tests on downwind sails he conducted between 1991 and 2007 in four

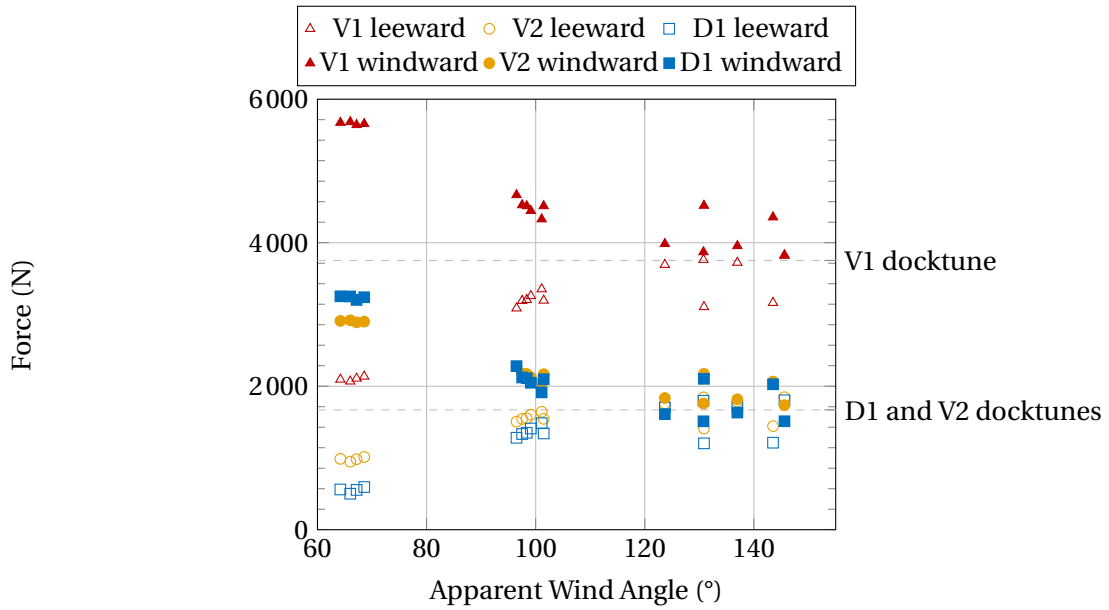


Figure 3.22 – Loads in the shrouds according to the AWA. V1 is the shroud connected on the mast at the highest point (0.7 m below the head point), V2 is the intermediate shroud and D1 the lowest.

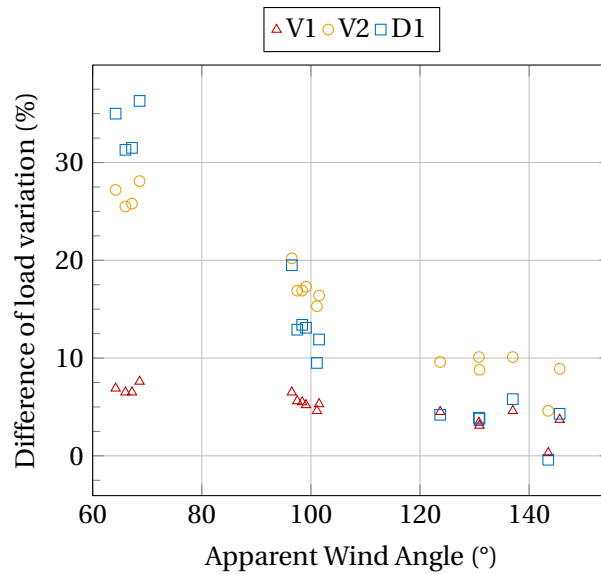


Figure 3.23 – Windward-Leeward difference of variations of loads from docktune relative to the docktune $\frac{(F_{windward}-Docktune)+(F_{leeward}-Docktune)}{Docktune}$.

different wind tunnels. The tests were conducted for racing teams during development programmes for Whitbread 60 and America's Cup Class yachts. One of these tests, at the politecnico di Milano, was conducted with a twisted flow, representing the twist of the apparent wind. Averaged downwind sail coefficients are extracted from this article.

[Renzsch and Graf, 2013] carried out Wind Tunnel tests at the Yacht Research Unit-Kiel to create validation benchmarks for downwind FSI numerical simulations. Hence the sail moulds, twisted incident flow data

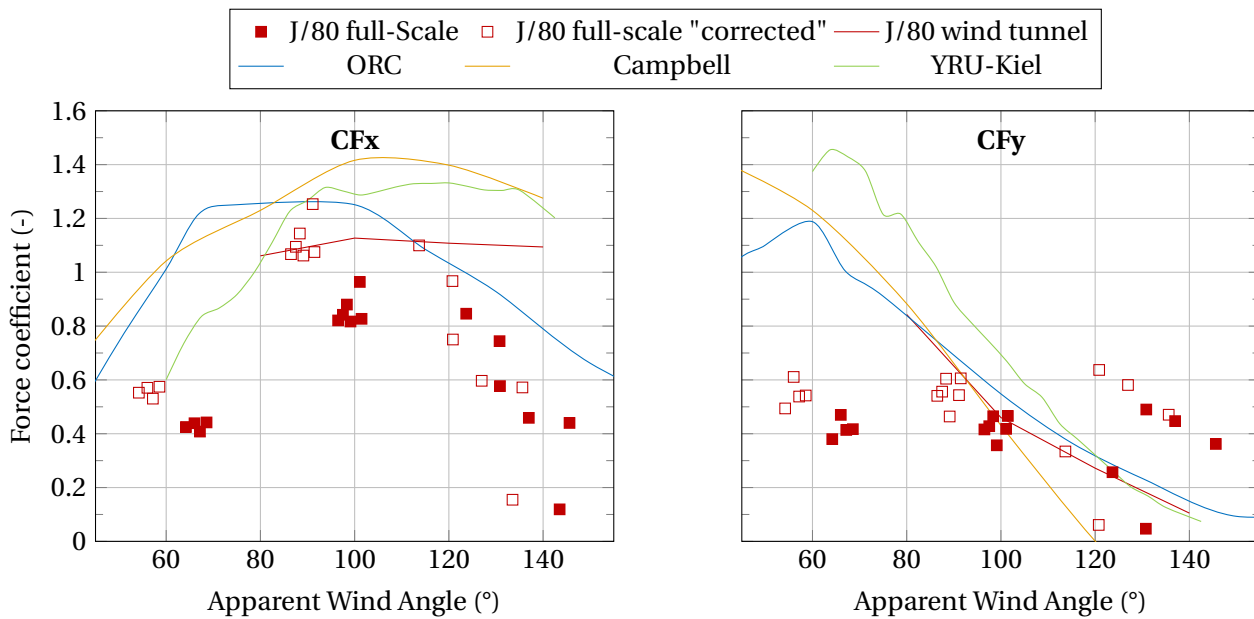


Figure 3.24 – Comparison of raw spinnaker load coefficients CF_x and CF_y measured at full scale, and same loads with a "corrected" wind, with wind tunnel load coefficients from various articles ([Offshore Racing Congress, 2015, Campbell, 2014a, Renzsch and Graf, 2013]).

as well as measured forces and flying shapes are publically available. All these wind tunnel tests were conducted with a mainsail hoisted.

Finally Nicolas Aubin, for his PhD project at IRENav, carried out experiments in the Wind Tunnel of the Yacht Research Unit at the University of Auckland on a scaled J/80 spinnaker. He investigates unsteady behaviour of the sails in a controlled environment. At the time of the writing of this thesis, results have not yet been published. For his purpose, he focused his tests on only 4 AWA (80°, 100°, 120°, 140°), with a stiff mast, and no twist of the wind.

All these results are presented in figure 3.24. They are compared with the full-scale results I obtained during my PhD, without the mainsail (full red square). The full-scale force coefficients are lower than the force coefficients generally found in wind tunnels. For example at AWA 100°, the maximum force coefficient is generally more than 1.2 for wind tunnel tests, whereas full-scale force coefficients are lower than 1.

The wind measurement largely differs between wind tunnel tests and full-scale tests. In a wind tunnel, the wind is measured upstream of the model in an undisturbed flow, whereas for in-situ measurements the wind is measured at the top of the mast. As explained in subsection 1.3 and 2.6.2, the wind can largely be deviated by the sail. With on-going FSI numerical simulations on the J/80 spinnaker, we notice that for a tight AWA (65°) measured at the top of the mast, the wind speed was 15% larger and coming 10° more from the aft than the upstream wind set as input of the numerical simulations. As a first order, empty red squares in figure 3.24 display the loads measured at full-scale non dimensionalised by a wind speed corrected by a constant value of 0.85 and a wind angle shifted by -10°. These coefficients should probably vary with the AWA but it shows that optimum values are closer to those found in wind tunnels.

For tight AWA (below 80°), the full-scale force coefficients are lower than in a wind tunnel. Tests conducted

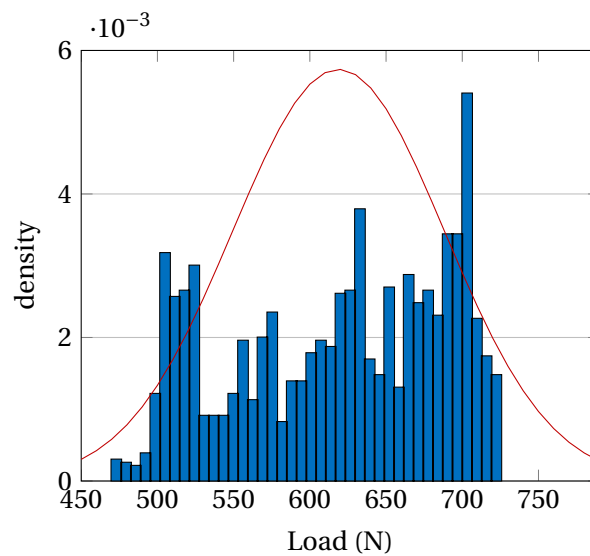


Figure 3.25 – Histogram of loads on the spinnaker head during a stable period for AWA=111°. The red plot represents the symmetrical normal distribution using the probability density formula.

in a wind tunnel at these AWA were with the mainsail hoisted except for the wind-tunnel tests with the J/80 spinnaker. This difference could be explained by the influence of the mainsail on the spinnaker. The sparsity of load coefficients found at large AWA (above 120°) might be due to the imprecision of our load measurement acquisition system as explained in section 2.4.

Wind tunnel tests on downwind sails tend to overestimate the loads measured at full-scale. This is also confirmed by [Motta, 2015] for in-situ experiments we carried out in Auckland on a larger sailing boat with a larger spinnaker. The wind-tunnel tests he conducted, reproducing the conditions found on water also gave larger aerodynamic coefficients. The measured reference wind is certainly different. Moreover, in a wind tunnel, the environment is controlled and stable whereas on water, the wind shifts, there are waves and crew moving affecting the attitude of the sailing boat. Due to a more unstable environment, an optimal static equilibrium cannot easily be found resulting in lower aerodynamic loads.

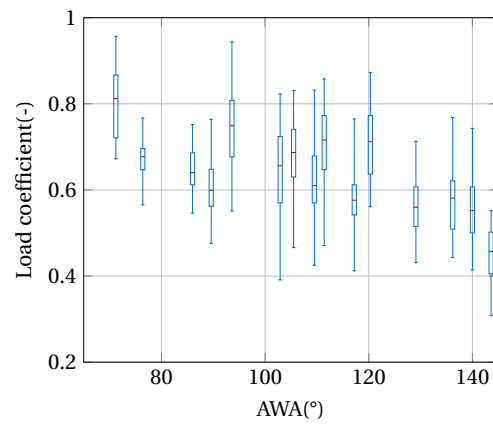
3.2.2 Load fluctuations

Even during a stable period, loads can have a wide range of values (cf. figure 3.25). Moreover, load measurements might not always fit with a gaussian distribution as figure 3.25 demonstrates for a stable period of AWA 111° of 20 s. Therefore to discuss the load fluctuations, we decided to plot boxes with quartiles and minimum and maximum whiskers.

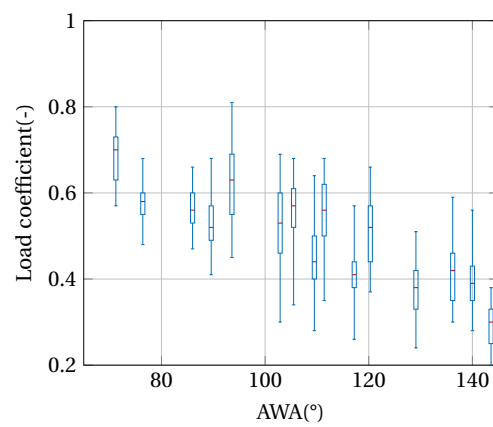
In Figure 3.26, only “stable” periods of 10 seconds minimum are taken. In figure 3.26, the interquartile range box (IQR) has almost the same relative range for every AWA, between -10% and +10% of the median for the most loaded corners (head and tack) and between -5% and +5% for the clew. Since the range of the small variations around the median load is relatively constant and small, one can conclude that for every AWA, without taking into account peaks of loads, the averaged load coefficient is fairly stable and varies

slightly.

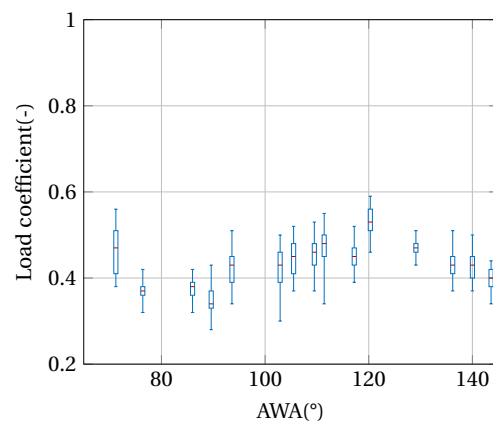
For the most loaded corners (head and tack) the upper whisker (maximum load) is about 20% higher than the median for tight angles ($AWA < 100^\circ$) and 30% for large angles ($AWA > 120^\circ$). For the clew point the upper whisker is about 15% higher than the median for all AWA. It is interesting to note that most variations of loads are present at the head and tack points, the closest points to the leading edge. While at the clew point, the relative variation of loads is smaller. One might think this is because fluctuations of load are smoothed at the clew as it moves when the flying shape evolves. However in the next section we will show that most of the pressure fluctuations occurs near the leading edge, altering mainly the loads at the tack and head points.



(a) Head load coefficient



(b) Tack load coefficient



(c) Clew load coefficient

Figure 3.26 – Boxplot for load coefficients C_F at the three corners of the spinnaker for different AWA. The central red mark is the median, the box represents the interquartile range (IQR) between the lower and upper quartiles. It contains 50% of the values. The upper and lower whiskers indicate the minimum and maximum values.

3.3 Evolution of pressures

3.3.1 Average pressure distributions

This last section of this chapter presents the evolution of average pressure coefficients according to the AWA for measurements carried out in 2013. The differential pressure coefficient ΔC_P is defined as the difference of the pressure between the leeward and pressure side divided by the dynamic pressure: $\Delta C_P = \frac{P_{leeward} - P_{windward}}{\frac{1}{2} \rho A W S^2}$. Figure 3.27 presents results for both tacks and for the two periods of the day (in the morning and afternoon) with the mainsail hoisted. In all the figures, the pressure differences are leeward minus windward, thus giving negative values. Pressure measurements performed correctly even though on the afternoon the first stripe at 1/4 height of the sail did not record any measurements. This is why only the three stripes 1/2, 3/4 and 7/8 of spinnaker height are presented in Figure 3.27. Despite an unsteady and dynamic environment (wind shear, unsteady and massively separated flow, waves, helming, etc.) which can affect the pressure distribution on a light and flexible downwind sail, the trends of the pressures along the curve are close to similar AWA at different heights of the spinnaker even for both tacks at two periods of the day. There is good repeatability for tight AWA up to about 120°.

The suctions are generally higher over the entire surface for lower AWA. At 1/2 height stripe, the differential pressure coefficient at the leading edge is almost null, followed by a peak of suction of almost -3 at about 10% of the curve. Then from 10% to 100%, the absolute differential pressure coefficient constantly decreases down to -0.5. It is not as clear for AWA around 120° where the peak of pressure is found at the leading edge. At 3/4 height stripe, the peak of suction is found at the leading edge followed by a decrease of the absolute pressure difference. At about 60% of the curve, another peak of suction emerges up to -2.5. Further the absolute differential pressure coefficient decreases to reach -1 at the trailing edge. The leading edge suction is harder to find for AWA 120°. At 7/8 height stripe, the pressure distribution is flatter at a high suction (around -3 -4 for AWA < 100° and around -2 for AWA > 100°). The absolute pressure coefficient decreases along the curve.

We sail at the optimum trim, meaning "on the verge of luffing". Theoretically, this results in the incoming flow locally tangential to the leading edge where the flow can pass from one side of the sail to the other, hence giving a flapping of the sail. It seems that for tight AWA (75° to 100°), the optimum trim is found at 1/2 height stripe because the differential pressure coefficient is null and therefore the flow might be tangential to the leading edge of the spinnaker sail. For larger AWA, around 120°, this situation is found at 3/4 of the span, because the differential pressure coefficient is null at 3/4 height and not null any more at 1/2 height stripe. The optimum trim is not present at the same time on the whole span of the sail. It also corresponds to the change of flying shape, where the shape at the top half part of the sail evolves more than the bottom half of the sail, with a more open leech, when the AWA is increased. At 7/8 height of the sail, the high suction with a small evolution along the curve might be due to a detached flow.

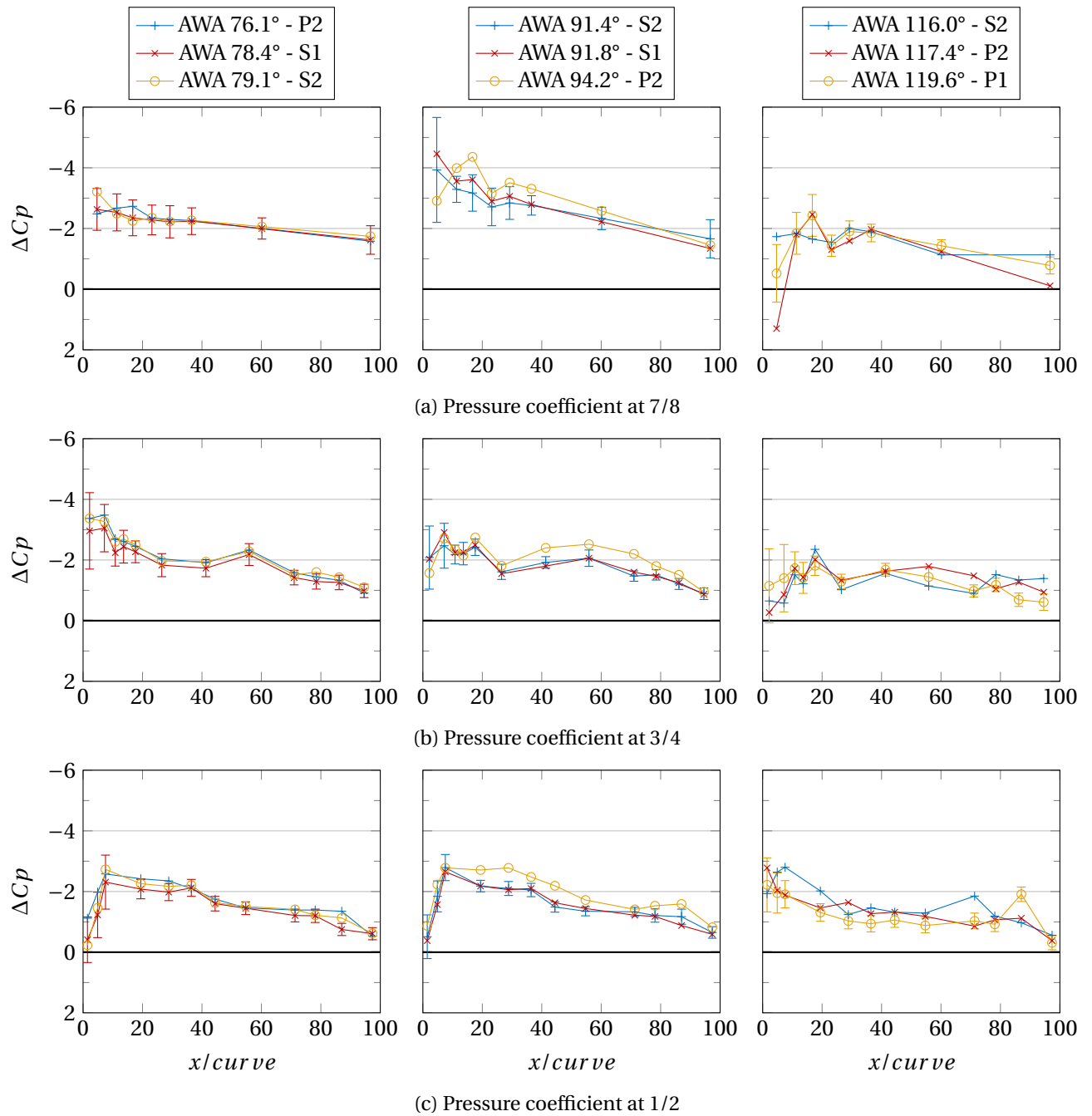


Figure 3.27 – Differential pressure coefficient at different height of the spinnaker along curve for different AWAs. P: Portside tack; S: Starboard tack; 1: Set 1 (morning); 2: Set 2 (afternoon). The error bars show the standard deviation during a stable run.

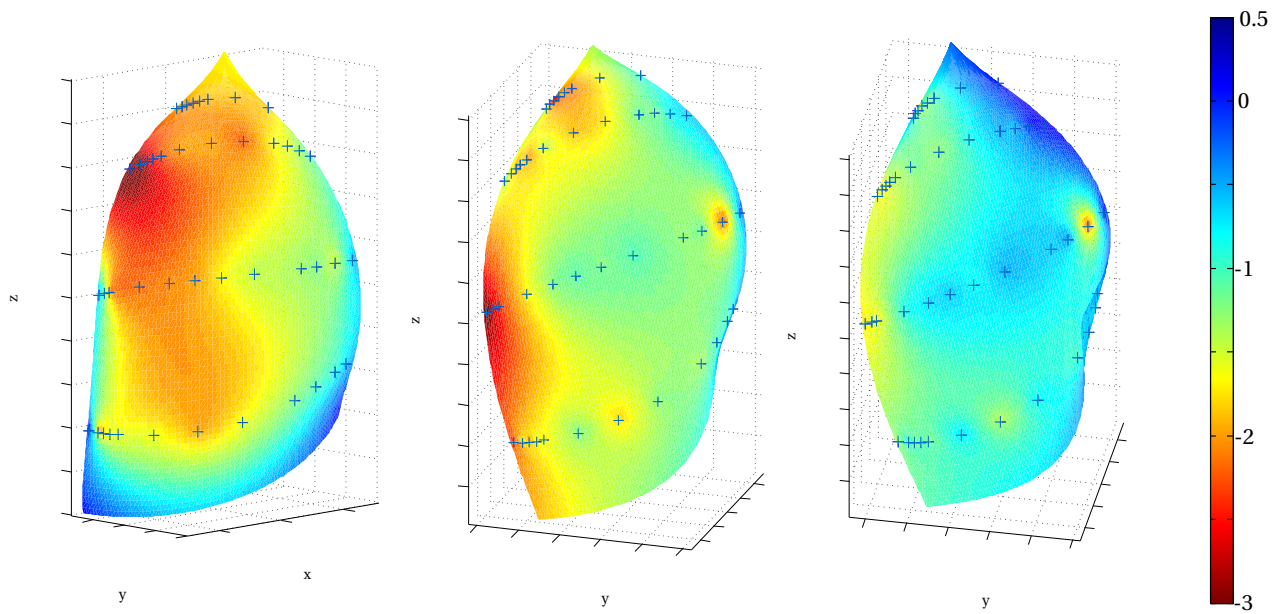
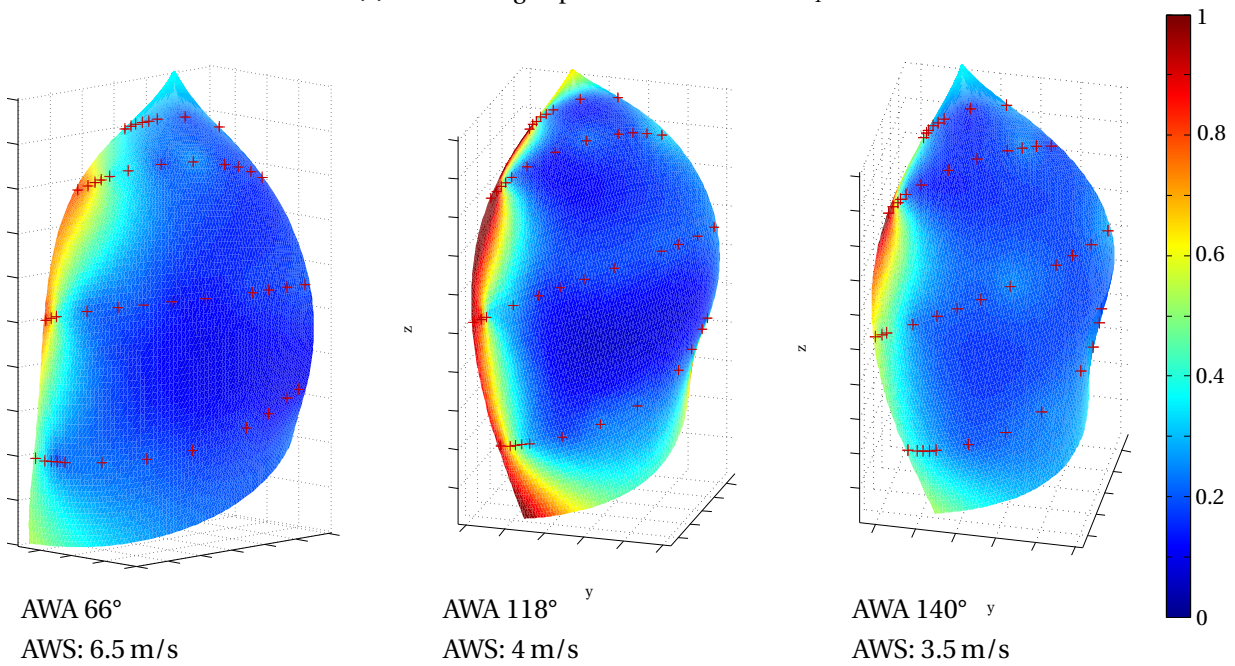
(a) Time averaged pressure coefficient ΔC_p (b) Standard deviation of pressure coefficient ΔC_p

Figure 3.28 – Pressure distributions interpolated and extrapolated on referenced flying shapes for 3 typical AWA (66°, 118°, 140°). Time averaged pressure coefficient ΔC_p (a) and the fluctuations represented by the standard deviations (b). The crosses (in blue in (a) and in red in (b)) indicate the positions of the pressure taps.

3.3.2 Fluctuations of pressures

In Figure 3.27, the standard deviation is rather small, around 0.2, except at the leading edge where it is around 0.8 and can exceed 1. This higher standard deviation might reveal the high suction peak and a possible flapping of the luff. Despite good repeatability of average pressures and loads, the standard deviations of differential pressure coefficient during a run can be of the order of magnitude of the average differential pressure coefficient.

To highlight these high instabilities at the leading edge, Figure 3.28 presents the differential pressure coefficient distribution on flying shapes presented in section 3.1. To display the pressure distribution on the whole sail from discrete measurement points, a linear Radial Basis Function interpolation was used. Blue crosses for Figure 3.28a and red crosses for Figure 3.28b show where the pressure measurement sensors were located on the sail. Thus pressures at these crosses are actual measured values. The pressure distribution is interpolated between the stripes and pressure taps. With no information on the sail boundaries, values at the top (above 7/8th) and at the bottom (below 1/4th) are extrapolated. The shapes are only used to display the pressure distributions. No conclusions can be drawn with the flying shapes because they were measured with the mainsail lowered while the pressures are measured with the mainsail hoisted. We chose data from the morning measurements when the pressures at 1/4 stripe were recorded.

At low AWA, one can notice the bulb of high suction at the leading edge in the top half part of the spinnaker ($\Delta C_p \approx -3$) which produces high aerodynamic force.

At AWA around 110° - 120° , the area where the peak of suction occurs is smaller around half of the spinnaker height and the absolute value lower. At AWA 140° , there is almost no suction peak at the leading edge.

While the AWA is increased, not only is there a clear decrease of absolute differential pressure coefficient (from -3 down to 0 about), but also the AWS decreases (from 7 m/s to 3.5 m/s about). So the absolute values of ΔP decrease even more dramatically: At tight AWA, around 65° , the order of magnitude of differential pressure is -40 Pa, and only -4 Pa at large AWA –around 140° –.

At AWA 140° , after the small leading edge suction there is a reduction of $|\Delta C_p|$ along the flow up to a positive ΔC_p at the trailing edge even on the actual measured points. Positive pressure coefficient means a collapse of the sail at the trailing edge and thus an unstable flying shape. It is consistent with what the authors have noticed during experiments: at large AWA, the spinnaker can collapse at the leech. But the averaged differential pressure measured is around 4 Pa, which is in the uncertainty of the pressure measurement system, as explained in subsection 2.5.2. Hence these differential positive pressure values might be slightly negative in reality or are compensated by the tension on the sail.

Figure 3.28b shows the standard deviation for the corresponding AWA. Standard deviation on the whole sail is interpolated from the standard deviations calculated on the pressure taps only. Despite a clear difference for the pressure distribution on the whole spinnaker depending on the AWA, pressure variations during stable runs have similar spatial patterns. Strong variations are found at the leading edge,

around 1, on the whole height for 66° and 118° while the rest of the spinnaker has a standard deviation of about 0.2. However, while the order of magnitude of standard deviation of ΔC_p is similar for each AWA, the relative variation of pressures compared with the average pressure coefficient varies. Variations are more significant for large AWA (around 120° - 140°) than for tight AWA. For tight AWA, the standard deviation is around 30 Pa thus 75% of the average pressure. For large AWA, the standard deviation is around 8 Pa thus 200% of the average pressure.

3.4 Conclusions

New sail shape representations were used to analyse the average shape of the spinnaker as measured from photogrammetry. The 3D camber representation highlights where the main camber is, and can characterise the flying shape for a specific AWA with the projected area onto the "Head-Tack-Clew" plane and with the volume of the sail. The triangular Bézier surface with control points can be used to describe quantitatively the overall 3D-shape of the sail and to characterise sails for all AWA in a database.

The global behaviour of the spinnaker evolves mostly with the AWA. To assess it, we analysed the evolutions of the flying shape, of the loads and of the pressures separately. Nonetheless, all these evolutions are coupled to each other.

For tight AWA (about 60° - 90°), it seems the spinnaker is bridled in the top half of the sail. For geometric parameters of the flying shape (camber, twist, ...), the spanwise trends are different from the trends for larger AWA. The average differential pressure coefficient is larger than for other AWA with a high suction peak in the top half of the sail at the leading edge. Since the AWS is also higher, the loads on the corners are the largest, with the head and tack loads almost twice as large as the clew load (respectively 1000 N and 600 N). The sail is fully on the leeward side. This is why if the aerodynamic load is projected onto the boat frame, the propulsive and side force are of the same order of magnitude.

For larger AWA (about 90° - 120°), the sail tends to have a "stable" shape: the shape differs less between this range of AWA and larger AWA than for tighter AWA. The ease of the sheet makes the spinnaker rotate forward and towards the windward side. The sail in the top half part is more twisted. The top part of the sail might therefore be better adjusted for the twisted incoming flow. The bulb of suction at the leading edge is located lower, at about half of the height of the sail, where the longest chord length is measured. The pressure distribution pattern is similar to lower AWA (existence of a bulb of suction at the leading edge) with globally the same average differential pressure coefficient except a lower leading edge suction. However as AWA increases the AWS is reduced, hence the absolute differential pressures are lower resulting in a lower aerodynamic load produced by the spinnaker. Nonetheless, the sail is eased and more rotated towards the bow. The side force (which was of the same order of magnitude than the propulsive force for tighter AWA) is now only half of the propulsive force. This spinnaker being optimised for this range of AWA (about 90° - 120°), the maximum of propulsive load coefficient is found in this range. For large AWA (about 120° - 150°), the shape is globally the same as for medium AWA but the spinnaker is even more rotated forward and to the windward side. However $|\Delta C_p|$ are lower (0.5 instead of 1 on average) and with a less distinct suction bulb at the leading edge. Moreover the AWS is almost divided by 2 compared with tight angles. Hence the aerodynamic loads are much smaller, the loads at head and

tack corners are almost divided by 5 compared with an AWA around 70° . The load coefficients decrease too.

Most of the variations of loads and of pressures appear near the leading edge while at clew point the variations are smaller. Even during "stable" periods, loads and pressures are unsteady. However specific patterns might be spotted and might be linked to different causes. The yacht motion and its influence on the apparent wind (pitching and rolling of the boat), gusts (pure aerodynamic cause), vortex shedding, or a change of the spinnaker shape as luffing (unsteady fluid-structure interaction) could make the spinnaker forces vary. The next chapter will be dedicated to the unsteady behaviour of the spinnaker and more specifically to the flapping of the luff, also called luffing of the spinnaker. It is a strongly coupled Fluid-Structure Interaction problem.

Flapping of the luff: an unsteady behaviour of the spinnaker

Contents

4.1	Observation of measured flapping	132
4.1.1	Global description of one flapping	132
4.1.2	Folding stage (A to C)	135
4.1.3	Unfolding stage (C to D)	135
4.1.4	3D aspects of flapping	137
4.1.5	Summary of the observations	137
4.2	Modal analysis on pressure fluctuations	137
4.2.1	Proper Orthogonal Decomposition (POD) method	137
4.2.2	Main Proper Orthogonal Decomposition (POD) results	138
4.2.3	Application of the POD method on the specific period of flappings	141
4.2.4	Mode 1, the flapping mode	144
4.2.4.1	Spatial mode	144
4.2.4.2	Time coefficient	146
4.3	Physical interpretation of flapping and discussions	147
4.3.1	Two-string membrane model	147
4.3.1.1	Beginning of flapping	148
4.3.1.2	Folding stage	151
4.3.1.3	Unfolding stage	151
4.3.1.4	3D aspects	152
4.3.2	Wave propagation model	152
4.3.3	Mechanical model	154
4.3.4	Discussions	155
4.4	Conclusions	156

After analysing from our measurements the global behaviour of the spinnaker especially as a function of wind angle and speed, we will now focus on the unsteady behaviour of downwind sails. We measured different unsteady dynamics. They can be caused by the waves, gusts, or changes of shape due to dynamic trimming or even during a fixed trim such as the flapping.

This last unsteady behaviour is typical for downwind sails and is well known by sailors. It is said that the best trim for a spinnaker to propel the boat as fast as possible is when the spinnaker is "on the verge of luffing", i.e. when the luff of the sail is slightly flapping. This phenomenon happens for all AWA, even with a fixed trim, and with or without the mainsail hoisted. It can be reproduced with wind tunnel experiments where the wind is controlled. It is an intrinsic nonstationary behaviour of the spinnaker. Physically it is a complex unsteady fluid-structure interaction problem and it is well known by sailors but not well understood.

In this last chapter the flapping phenomenon is analysed in detail. We would like to study the dynamics and if the trim of the sail which lets the luff flapping is the most efficient trim. During this PhD, a lot of experiments were carried out at different AWA from 60° to 150° . To describe this complex phenomenon, it was decided to present time-resolved measurements for only the most representative measured periods where the spinnaker flaps. The second section of this chapter analyses the global dynamic behaviour of the flapping for all AWA. In the last section, physical interpretations using different physical models are proposed to explain this complex FSI problem.

4.1 Observation of measured flapping

Flapping of the luff of the spinnaker was observed in every stable¹ measurement at the "optimum" trim (on the verge of luffing) with a fixed trim. These measurements were realised with or without the mainsail hoisted and for all AWA. To observe and precisely describe the flapping behaviour, evolutions of pressure coefficient distribution are analysed. The differential pressure is defined as the difference between the leeward side (suction side) and the windward side (pressure side) thus giving negative values. We focus on the most representative run which is a few seconds of a 20 second run without the mainsail where the average AWA was 77.8° and the standard deviation 4.7° . The most representative case is for a tight AWA, because the differential pressures applied on the sail is larger (see section 3.3), thus a more stable flying shape. In this run several flappings appear more or less periodically but we will focus on one flapping period.

4.1.1 Global description of one flapping

Figures 4.1 and 4.2 present respectively the flying shape and the pressure distributions at 4 instants evenly distributed in time (0.4 s between each instant). Table 4.1 describes the key stage of one flapping while Table 4.2 indicates the variations of loads during a flapping period.

A flapping period can be split into 2 stages: The luff of the sail folds itself (see Figure 4.1a for a flapping at

¹According to the criteria defined in section 2.9

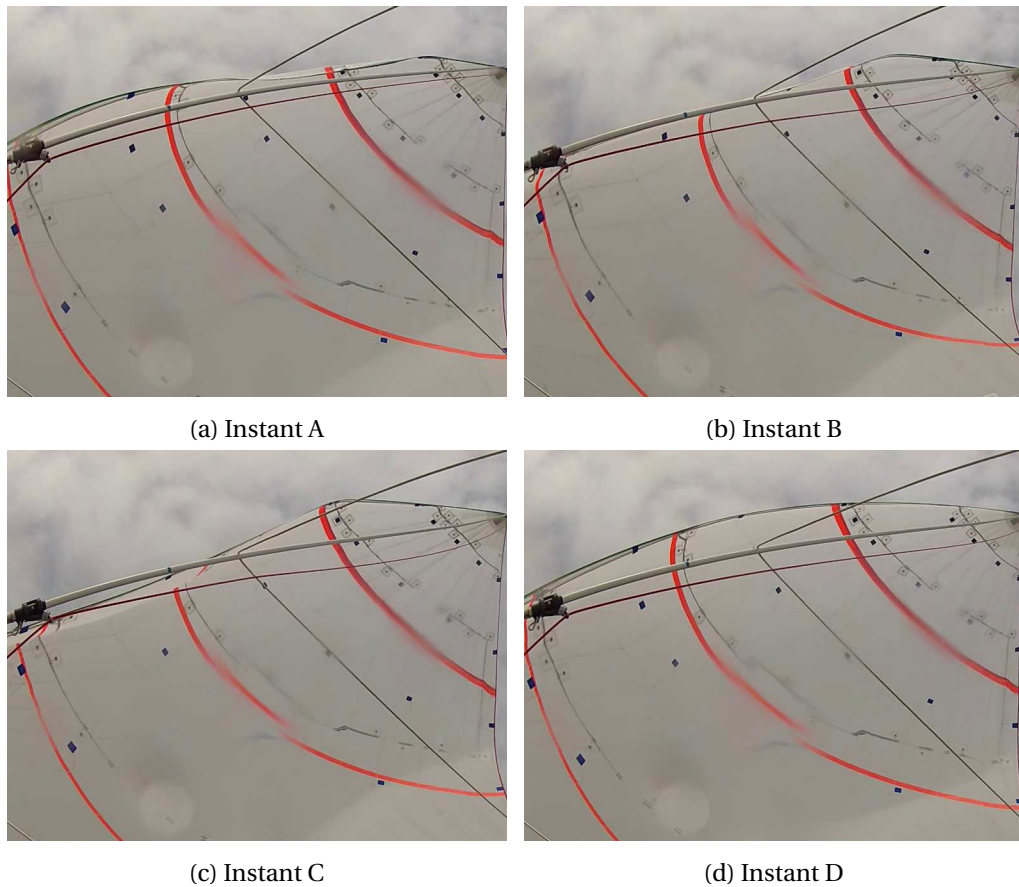


Figure 4.1 – Snapshots of the flying shape during flapping at the four selected times.

Instants	time	At 3/4 height stripe	At 1/2 height stripe	Loads
A	67.6 s	minimum of suction		minimum at head
	67.7 s			minimum at tack, clew
	67.8 s		minimum of suction	
	67.9 s	maximum of folding		
B	68.1 s			
C	68.5 s			
	68.6 s		maximum of folding	
	68.7 s	max. of suction at luff		
	68.8 s			maximum at head, tack
D	68.9 s	maximum of suction	maximum of suction	maximum at clew
	69 s		max. of suction at luff	

Table 4.1 – Pressures and forces behaviours at different instants during one flapping between 67 s and 69 s.

3/4 of the span of the spinnaker and Figure 4.1b for a flapping at 1/2 of the span) up to a maximum of folding (see Figure 4.1c), and then unfolds to recover its full flying shape (see Figure 4.1d). During a period of flapping the loads and suction increase as seen in Figure 4.2 and Table 4.2.

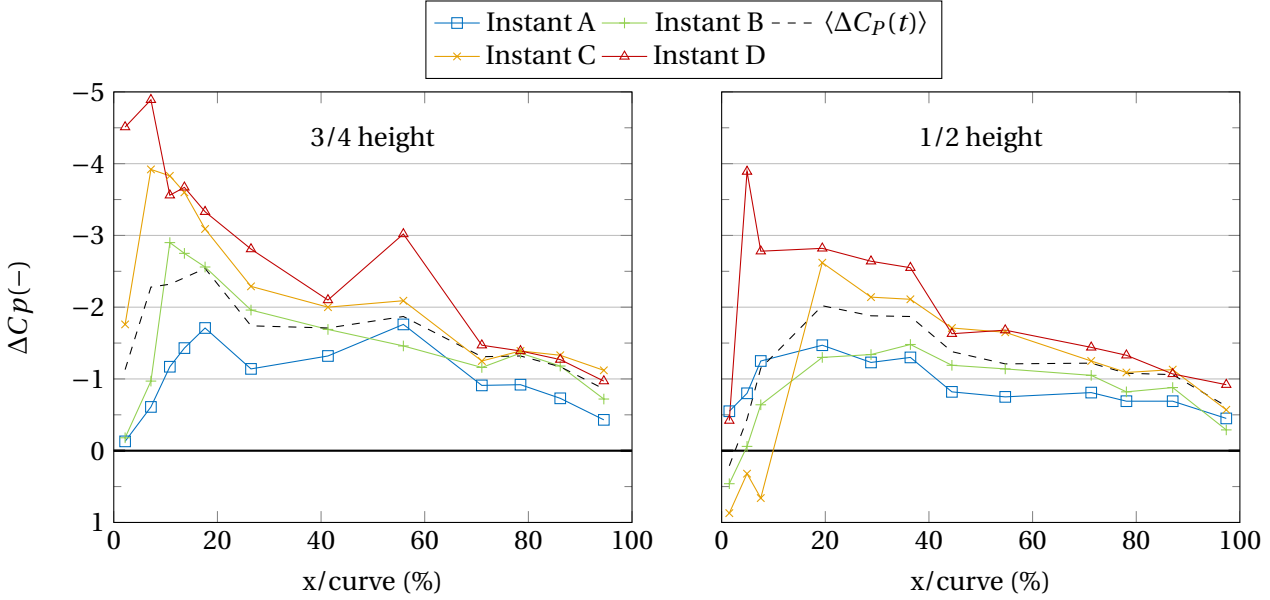


Figure 4.2 – Pressure measurements at the 4 selected instants and the time averaged value (dashed line).

	Head	difference	Tack	difference	Clew	difference
mean	0.56	to mean	0.50	to mean	0.31	to mean
A	0.41	-27%	0.36	-28%	0.24	-22%
B	0.46	-18%	0.41	-17%	0.26	-16%
C	0.64	+15%	0.56	+13%	0.34	+8%
D	0.70	+25%	0.64	+28%	0.41	+30%

Table 4.2 – Load coefficients on the corners of the spinnaker (head, tack, clew) at the four instants (A,B,C and D) during flapping.

Figure 4.3 presents space-time diagrams of $\Delta C_p(x, t)$ (a and b) at pressure stripes 3/4 and 1/2 height of the sail where flappings of the spinnaker occur. The zero differential pressure is highlighted by a white line. It also illustrates the time series of the overall pressures on these 2 pressure stripes (c). It is calculated as the integral of the pressure distribution over the curve: $\frac{1}{c} \int_0^c \Delta C_p(t) dx$. The last graph (d) describes the force coefficients on the three corners (head, tack and clew). Curly braces indicate when the spinnaker is seen folded on the synchronised video. Positive differential pressure -i.e. pressure larger on the suction side than on the pressure side- appears when the spinnaker is folded. The flapping we are focused on starts at 67.5 s and finishes at 69 s.

The dynamics of flapping is different at 3/4 and 1/2 height. The flapping at 3/4 height starts before the 1/2 height, and also finishes before. Thus firstly, for an easier description of this phenomenon, only the flapping at 1/2 height is described, because the fluctuations of pressure are better defined at 1/2 height, and the 4 instants provide a good description of the main stages of the flapping at 1/2 height. Secondly,

the time shift and differences of the evolutions of pressures at 3/4 and 1/2 height are explained.

4.1.2 Folding stage (A to C)

At *instant A* the folding stage starts at 1/2 height stripe. As seen in Figure 4.1a, the section has a full shape. Almost at the same time, the overall absolute differential pressure is at a minimum as explained in Table 4.1. In Figure 4.3a and b, the minimum pressure is marked by dashed blue and red lines. On the whole curve -the curvilinear abscissa of the pressure stripe on the sail-, the absolute differential pressure distribution is lower than the time-averaged pressure distribution according to Figure 4.2, except some pressure points at the leading edge. In concordance with the overall low suction on the sail, the loads measured at the 3 corners of the sail presented in Table 4.2 are about 25% lower than the time-averaged loads.

From *instant A* to *instant C*, the luff folds towards the windward side. The folded area at the leading edge increases. The suction is lowered, and differential pressures become positive in the folded area as shown in Figure 4.2b at *instant B* -during the flapping-. On the rest of the section, pressures are between values measured at *instant A* and time-averaged values. The loads slightly increase but are still lower than the time-averaged loads (from -28% to -16%).

At *instant C* (cf. figure 4.1c), the luff has reached its maximum of folded area -marked by blue and red lines in Figure 4.3a and b.

4.1.3 Unfolding stage (C to D)

At *instant C*, a high suction occurs just downstream of the low absolute differential pressure. In Figure 4.2, there is a clear jump of pressure at 10% of the curve, with a positive pressure at the folded leading edge (from 0 to 10% of the curve), and a high suction just afterwards. The absolute differential pressure then decreases down to values similar to the time-averaged pressures. The loads still increase and are now higher than the time averaged loads (about +13%).

From *instant C* to *D*, the spinnaker is unfolds to recover its full flying shape. With the low absolute differential pressure, the folded area decreases. Low pressures are replaced by high suction that appeared at the maximum of folding. During the unfolding stage, according to Figure 4.3b, the high suction area expands in both directions: its starting point follows the zero differential pressure point towards the leading edge, and the end of the suction area goes downstream.

At *instant D*, the sail section recovers a full shape, similarly to *instant A* (cf. figure 4.1d). The high suction area reaches the leading edge as described in Table 4.1. Figure 4.2b indicates that $|\Delta C_p|$ is much higher than the average pressure distribution from 0 to 40% of the curve length ($1.5 < |\Delta C_p| < 3$) and still slightly higher (about 0.5) up to 90% of the curve length. Consequently the maximum of loads appears at this instant with loads between 25% and 30% higher than the time-averaged values.

The duration of this high suction peak is quite short compared to the period of flapping. The large high suction area disappears 0.1 s afterwards (at 69 s).

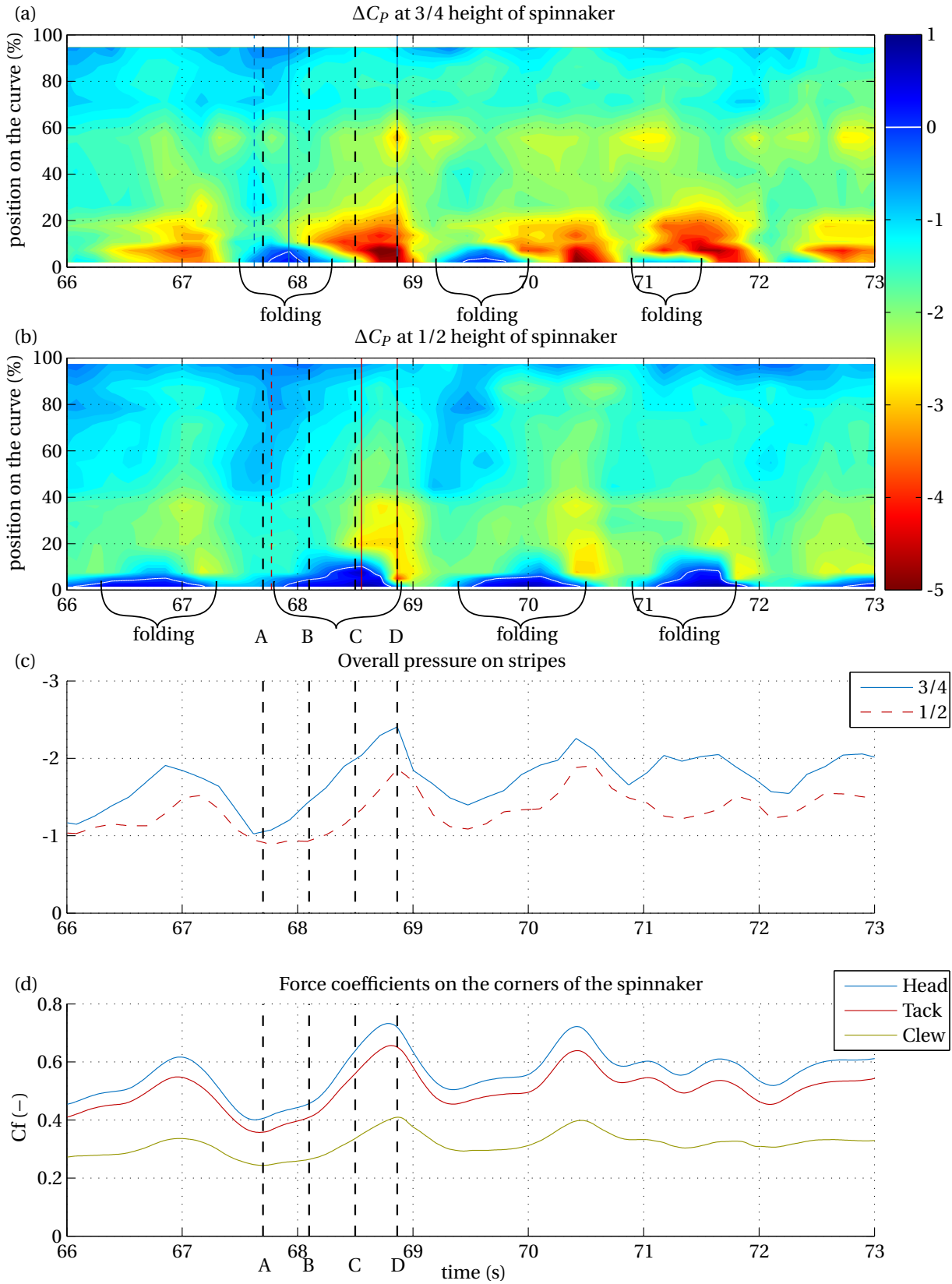


Figure 4.3 – Evolution in time of the pressure distributions and loads on spinnaker. Space-time diagrams of $\Delta C_p(x, t)$ at 3/4 height (a), at 1/2 height (b); integral of pressure ($\frac{1}{c} \int_0^c \Delta C_p dx$ where c is the curvilinear abscissa of the pressure stripe on the sail) (c); time series of load coefficients measured on the sail corners (d).

4.1.4 3D aspects of flapping

As explained previously and described in Table 4.1, the dynamics of flapping is different at $3/4$ and $1/2$ height. The flapping at $3/4$ height starts slightly before the $1/2$ height stripe, reaches its maximum of folding just before instant B, during the folding stage of the $1/2$ height stripe. Still during the folding stage of the $1/2$ height stripe, the $3/4$ stripe unfolds from instant B to C. Then the $1/2$ stripe unfolds. The flapping can be seen as a spanwise propagating wave going downwards. The flapping at $3/4$ height is shorter in space and in time.

As demonstrated in Figures 4.3 and 4.2, the pressure evolution in space and time at the $3/4$ height stripe is similar to the $1/2$ height stripe with a creation of the high suction area at the maximum of folding which increases during the unfolding stage. However, at $3/4$ height, when the section has recovered its full shape, the high suction area stays at the leading edge. It disappears when the high suction at $1/2$ stripe disappears. This is why the highest absolute differential pressure, hence the loads on the corners, are at instant D.

4.1.5 Summary of the observations

Flappings, high peaks of suction at the leading edge of the spinnaker, and extrema in forces are strongly correlated to each other. Just before the spinnaker starts folding, the minimum of loads and suction are spotted. During the folding of the spinnaker, a low suction area starts from the leading edge and evolves up to 15% of the curve. During the unfolding of the spinnaker, a high suction area replaces the low suction zone. At the full shape recovery, the load peak is found.

The description of this specific dynamics of a spinnaker is based on the most representative periods where flappings occur. It is a specific pattern which might be spotted in the other measurements carried out at different AWA with or without the mainsail on this spinnaker but also on a larger spinnaker ([Motta et al., 2015]). We would like to detect these patterns in our other measurements and analyse them. We tried different methods such as the Dynamic Mode Decomposition ([Schmid, 2010]), but the amount of data were not sufficient and the phenomena not periodical enough. We also tried the Variable-Interval Time Average (VITA) method to detect flapping. It is commonly used to detect burst structures in turbulent flows. However the results revealed were too sensitive for the detection criteria to give general conclusions. Finally we used the Proper Orthogonal Decomposition (POD) method to characterise the spatial patterns of pressure variations, in order to decompose complex pressure evolutions into simpler modes. These pressure modes could help to describe a global temporal behaviour in a better way than analysing each pressure sensor signal. They can also be correlated with other recorded data.

4.2 Modal analysis on pressure fluctuations

4.2.1 Proper Orthogonal Decomposition (POD) method

The Proper Orthogonal Decomposition (POD) is based on the Karhunen-Loeve expansion and is also called Principal Component Analysis, PCA. It was first introduced in the context of Fluid Mechanics

by [Lumley, 1967] and is widely used in Wind Engineering ([Bienkiewicz et al., 1995, Tamura et al., 1997, Gilliam et al., 2004]). The input data (in our case $\Delta C_P(x, t)$) can be expanded into orthogonal basis functions $\varphi_i(x)$ with time coefficient $a_n(t)$:

$$U(x, t) = \sum_n a_n(t) \varphi_n(x).$$

As proper modes are derived from the data itself (data driven decomposition), there is no need for a-priori knowledge or an education scheme. Moreover, each basis function has its own amount of fluctuation energy different from each other. These functions are statistically optimal in the least mean-square sense. As a result, fluctuation energy drops quickly which means a low number of modes is needed in the expansion to reproduce the main variations of the field. The POD method is a powerful tool for generating lower dimensional models of dynamical systems.

Most of the time, POD is used on the fluctuations of the input data only. After subtracting the average component (seen as the zeroth mode) from the data, a matrix \mathbf{U} is created as a set of N observations (commonly called snapshots) of M records. Each column contains all fluctuating input data (M values) from a specific snapshot and each row contains all snapshots (N snapshots) from a specific measurement point.

$$\mathbf{U} = \begin{bmatrix} u_{11} & u_{12} & \cdots & u_{1N} \\ u_{21} & u_{22} & \cdots & u_{2N} \\ \vdots & \ddots & \ddots & \vdots \\ u_{M1} & u_{M2} & \cdots & u_{MN} \end{bmatrix}$$

In fluid mechanics, it is common to have $N \gg M$ when using PIV or CFD results for example. For those cases the so-called ‘‘Snapshot POD’’ introduced first by [Sirovich, 1987] is used. We have $M = 44$ measurement points and $N \approx 20000$ ($M \ll N$). Thus for our experiments, the ‘‘Direct POD’’ was applied. The auto covariance matrix \mathbf{C} ($M \times M$) is calculated as:

$$\mathbf{C} = \mathbf{U} \times \mathbf{U}^T$$

The corresponding eigenvalue problem of the auto covariance matrix is solved:

$$\mathbf{C} \times \varphi = \lambda \varphi$$

The eigenvectors $\varphi(i)$ are the POD modes. POD modes are sorted out in descending order according to their corresponding eigenvalue $\lambda(i)$ which represents their energy. The POD mode with the highest corresponding eigenvalue is mode 1. The expansion coefficient (or mode time coefficient) is calculated as follows:

$$\mathbf{a} = \mathbf{U}^T \times \varphi$$

4.2.2 Main POD results

The following results are based on stable periods where AWA and AWS are considered constant and the spinnaker trim fixed.

Figure 4.4 shows the energy distribution for each POD mode at different AWA. Spatial modes are independent of the AWA. Each mode has a similar pattern of pressure distribution for different AWA. The first mode contains almost 45% of the fluctuation energy. Mode 2 varies mainly between 15% and 20%, while mode 3 represents only about 10%. Other modes have less than 5% of the fluctuation energy. It is clear that the first mode is dominant compared to the others.

The evolution of pressure distribution can be simplified by taking only the first terms of the expansion. The reconstruction using the first modes makes it possible to only keep the most energetic part of the signal and remove insignificant variations and noises.

The precision of the reconstruction was calculated by the Frobenius norm of the approximation error between the reconstruction with a certain number of modes and the full data sequence. With mode 0 (the average) and mode 1, 85% of the signal is already reconstructed. With modes 0, 1, 2 and 3, 90% of the signal is reconstructed. About 10 modes are required to achieve a reconstruction with less than 5% of difference.

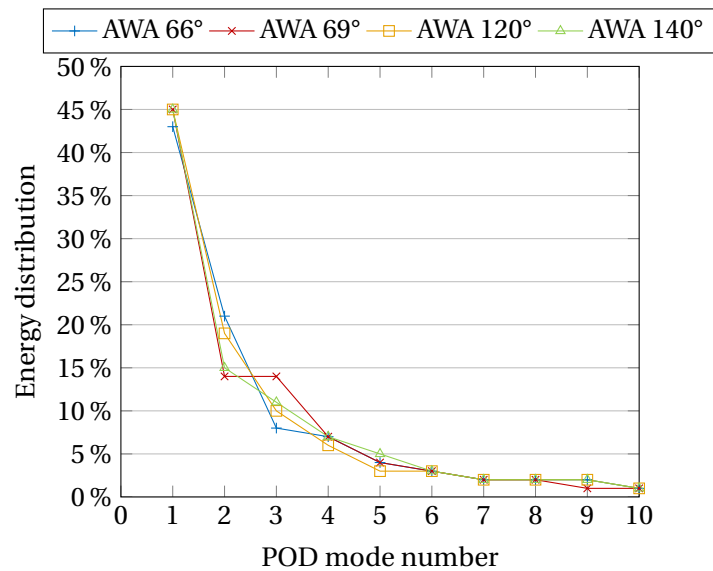


Figure 4.4 – Energy distribution of the pressure fluctuations for the first 10 modes for different AWAs.

Figure 4.5 presents the first 3 modes for a stable period where the average AWA is 69° and which is representative to what we have observed for other periods at different AWA. Like in section 3.3, the shapes used to display the modes are those presented in section 3.1. To display the pressure distribution on the whole sail from discrete measurement points (displayed by crosses in figure 4.5), a linear Radial Basis Function interpolation was used. The unique colour scale in figure 4.5 is arbitrary. To represent a fluctuation of ΔC_P , the spatial mode amplitude must be multiplied by the corresponding mode time coefficient - which can be positive or negative - presented in figure 4.6. Mode 1 has a bulb of pressure on the top half of the spinnaker at the leading edge and a smaller bulb of pressure of opposite sign on the bottom half of the spinnaker. Mode 2 is similar to the standard deviation pattern presented in Figure 3.28b. Mode 3 and further modes display less coherent patterns and may change with the decomposed period.

To make the pressure distribution vary, a time coefficient $a_n(t)$ is applied to the fixed spatial mode.

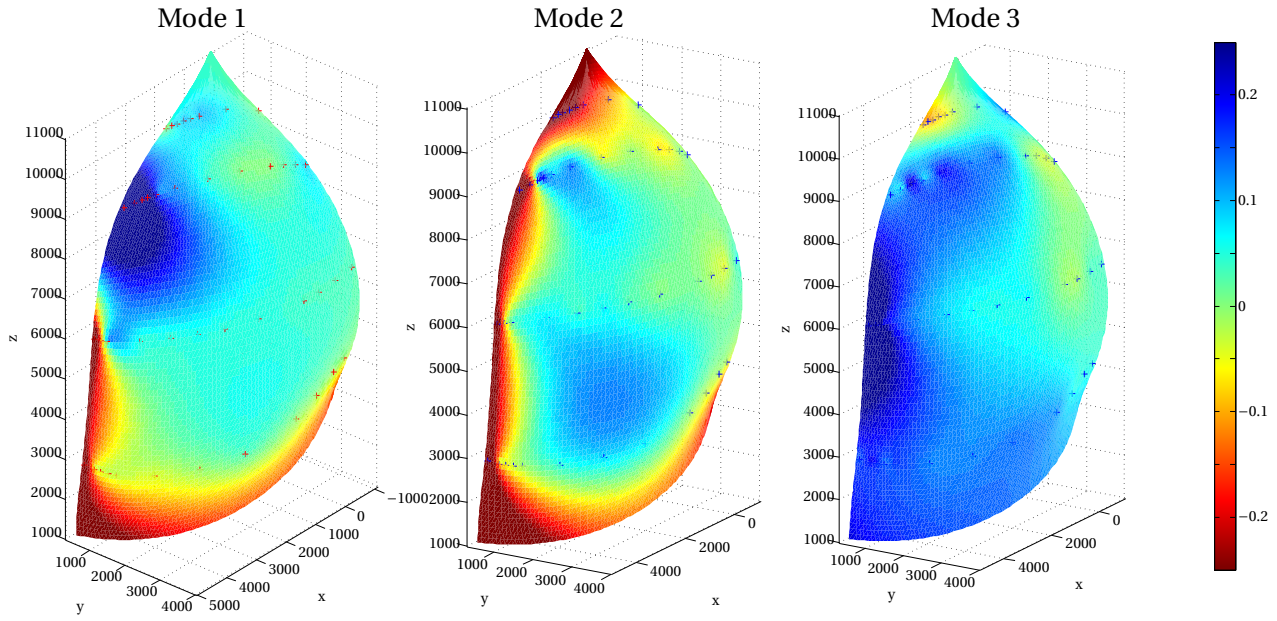


Figure 4.5 – First 3 spatial orthogonal modes $\varphi_n(x)$ deduced from the pressure measurements from POD method for a stable period at AWA 69°. Mode 1 is the most energetic mode.

When the time coefficient of a corresponding mode is at an extremum, the corresponding mode is then preponderant. Figure 4.6 shows the evolution of the time coefficient for the first 3 modes. Amplitudes of mode 1 are greater than the other modes as expected due to its larger energy. Analysing time coefficients would give a simple access to a global characterisation of the dynamic behaviour and then help to link pressure variations with other recorded data.

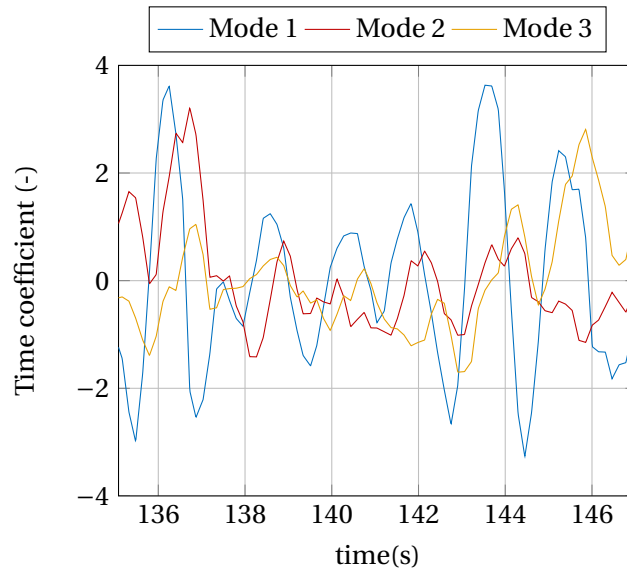


Figure 4.6 – Time coefficient $a_n(t)$ for the first three modes for a stable period at AWA 69°.

4.2.3 Application of the POD method on the specific period of flappings

The run used to describe the dynamics of flapping in section 4.1 is analysed with the POD method. Figure 4.7, similar to Figure 4.3, describes the time coefficients of the first two POD modes (see Figure 4.7c). Those two spatial modes clearly describe the dynamics of the flapping at 3/4 and 1/2 height. When the luff is folded at its maximum (between instant A and B for 3/4 stripe and at instant C for 1/2 stripe), the time coefficients are at minima. When the peak of suction reaches the leading edge, the time coefficient of modes 1 and 2 are maxima. The intensity of the folding is also well represented by the time coefficients. If the peak of suction is large (for example at 69 s for 1/2 stripe), the local maximum of the time coefficient is larger than for the weaker peak of suction (for example at 72 s for 1/2 stripe).

Mode 1 and mode 2 are correlated. When mode 1 is at an extremum, mode 2 is null. This delay between mode 1 and mode 2 makes it possible to represent the propagation of the pressure patterns. Figure 4.8 highlights that the combination of mode 1 and mode 2 enables the representation of the propagation and the expansion of the high suction area in space and time. It is difficult to extract a precise phase shift since it varies during the pseudo-period. At the maxima of mode 1, there is a shift of about 1/6-1/5 of a pseudo period; and at the minima, 1/3-1/2 of a pseudo period. Figure 4.7 also shows there is a strong correlation between the time coefficient of mode 1 (the most energetic mode) and the load coefficients on the corners of the sail.

To confirm the correlations shown in Figure 4.7, the cross-correlations of all data measured for this specific period are presented in Table 4.3. The normalized cross-correlation is calculated with the time coefficients of the first three modes. Cross correlation between two signals X and Y is defined as follows:

$$C_{xy}(\tau) = \mathcal{E} [(X(t_2) - \mu_X) - (Y(t_1) - \mu_Y)]$$

where $\mathcal{E}[\cdot]$ is the expected value operator, $\tau = t_2 - t_1$ is the shift applied between two signals. μ_X and μ_Y are the mean values. The cross correlation matrix is calculated to determine the correlations of every signal with each other. The values are between 0 when not correlated at all -in blue in the table- and 1 when signals have the same dynamics -in red in the table-. Colours in Table 4.3 highlight the correlations between experimental data. The diagonal represents the auto-correlation of every signal. The time shift between signals corresponds to the τ for the maximum cross-correlation.

Since all data were simultaneously measured, table 4.3 presents the cross-correlations between each measured signal. But we now only discuss the correlations between the time coefficients of the pressure modes and the loads. A very strong correlation is present between the loads except with the forestay and the shroud D1 on the leeward side as they are not loaded and slack. The time coefficient of mode 1 of the POD is well correlated with the loads (around 0.9). There is no delay between mode 1 and the spinnaker aerodynamic loads. Spinnaker aerodynamic loads are 0.1 s earlier than the standing rigging loads. In this case the pressure evolution is instantaneously transmitted to the corners of the spinnaker which then transmit this increase of loads to the shrouds and backstay. Here mode 2 is reasonably correlated with mode 1 with a coefficient of 0.72. The shift between the two modes is 0.4 s. Here the pseudo-period is around 1.5 s. The average shift between the two time coefficients is therefore about a quarter of a pseudo-period ($0.4/1.5 = 0.27$). The average shift calculated is indeed between the phase shift measured at the maxima of the modes (1/6-1/5 of a pseudo period) and at the phase shift found at their minima (1/3-1/2 of a pseudo period).

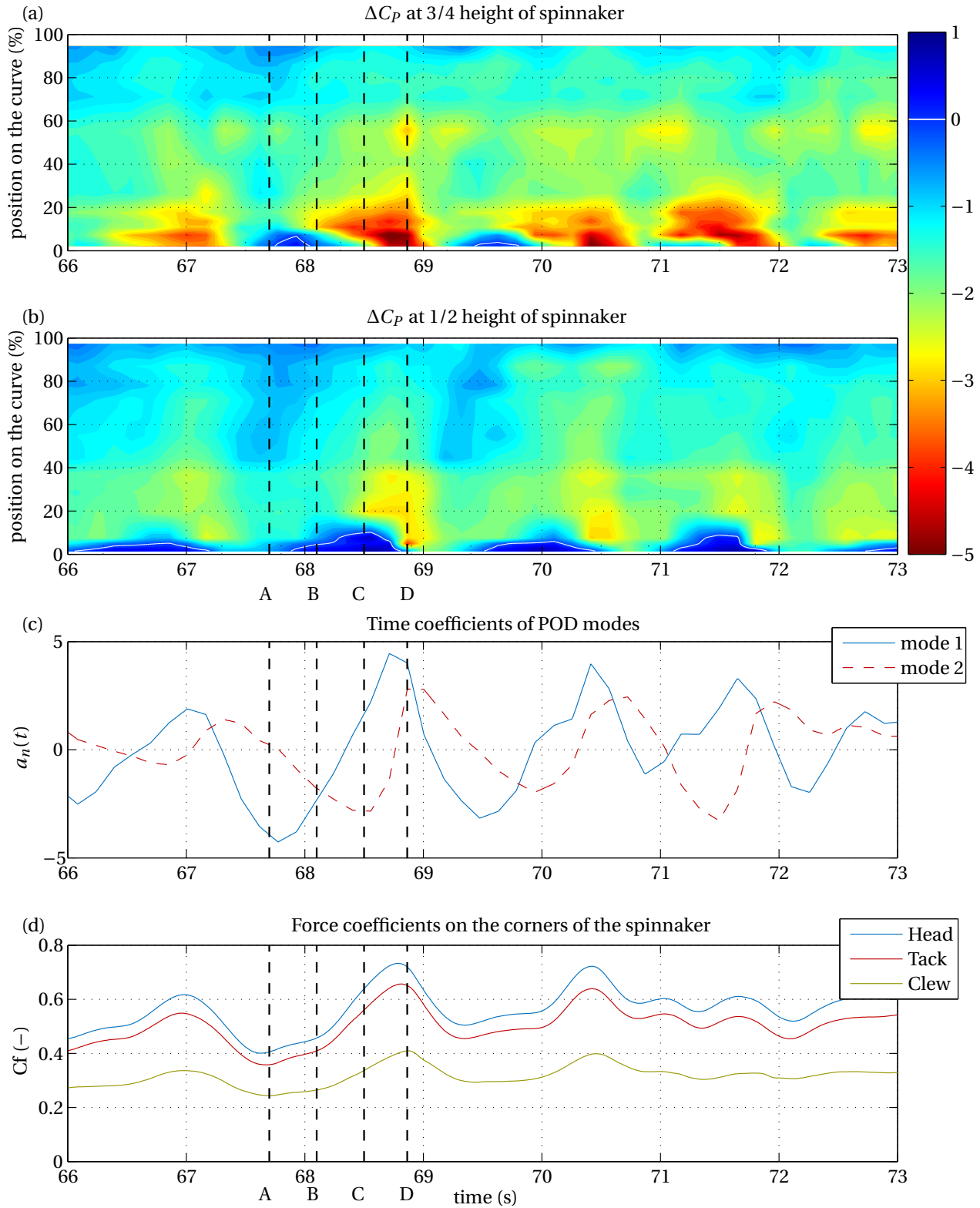


Figure 4.7 – Same as Figure 4.3 except at (c) where the time coefficients of the first two POD modes are represented.

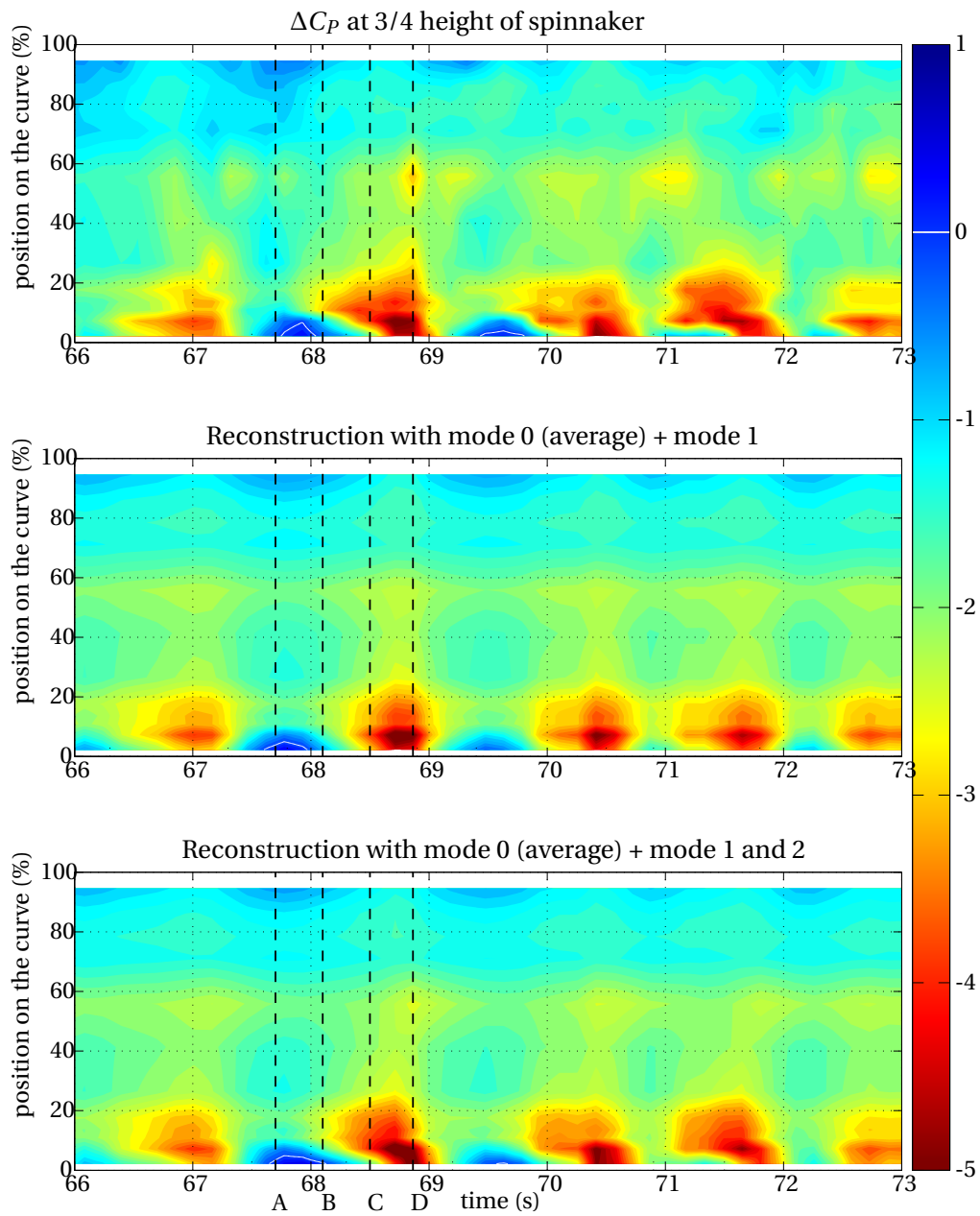


Figure 4.8 – Reconstruction of the space-time diagram of the 3/4 stripe (presented at the top), by the mode 0 (the time-averaged pressure distribution) + mode 1 (middle) -78% of the signal reconstructed, and by the mode 0 + mode 1 + mode 2 (bottom) -86% of the signal reconstructed-.

In conclusion, mode 1 -the most energetic mode- describes well the flapping of the luff. The addition of mode 2 is necessary to describe the propagation of this flapping at a different height of the sail and describes the expansion of the high suction towards the leading edge (cf. figure 4.8). It confirms that flapping prevails in the fluctuations of the corner loads.

In subsection 3.3.2, we have observed that the standard deviation of pressures is high at the leading edge

	forestay	backstay	V1 windw'd	D1 windw'd	D1 leew'd	Head	Tack	Clew	mode 1	mode 2	mode 3	roll	pitch	yaw	AWA	AWS	BS
forestay	1.00	0.58	0.62	0.63	0.78	0.59	0.59	0.59	0.65	0.62	0.59	0.60	0.69	0.51	0.73	0.59	0.40
backstay	0.58	1.00	0.88	0.92	0.62	0.96	0.95	0.93	0.91	0.66	0.45	0.58	0.61	0.75	0.58	0.49	0.57
V1 windw'd	0.62	0.88	1.00	0.99	0.79	0.94	0.94	0.94	0.85	0.66	0.41	0.48	0.61	0.68	0.63	0.50	0.44
D1 windw'd	0.63	0.92	0.99	1.00	0.79	0.95	0.95	0.95	0.88	0.68	0.41	0.54	0.61	0.71	0.63	0.54	0.46
D1 leew'd	0.78	0.62	0.79	0.79	1.00	0.69	0.70	0.76	0.66	0.53	0.52	0.49	0.52	0.65	0.60	0.54	0.44
Head	0.59	0.96	0.94	0.95	0.69	1.00	1.00	0.98	0.90	0.63	0.47	0.58	0.57	0.71	0.63	0.53	0.57
Tack	0.59	0.95	0.94	0.95	0.70	1.00	1.00	0.98	0.88	0.61	0.45	0.54	0.55	0.71	0.62	0.51	0.58
Clew	0.59	0.93	0.94	0.95	0.76	0.98	0.98	1.00	0.85	0.65	0.44	0.63	0.58	0.70	0.67	0.61	0.60
mode 1	0.65	0.91	0.85	0.88	0.66	0.90	0.88	0.85	1.00	0.72	0.43	0.52	0.63	0.74	0.54	0.47	0.38
mode 2	0.62	0.66	0.66	0.68	0.53	0.63	0.61	0.65	0.72	1.00	0.46	0.64	0.84	0.60	0.68	0.48	0.29
mode 3	0.59	0.45	0.41	0.41	0.52	0.47	0.45	0.44	0.43	0.46	1.00	0.66	0.41	0.45	0.56	0.75	0.51
roll	0.60	0.58	0.48	0.54	0.49	0.58	0.54	0.63	0.52	0.64	0.66	1.00	0.83	0.83	0.77	0.88	0.47
pitch	0.69	0.61	0.61	0.61	0.52	0.57	0.55	0.58	0.63	0.84	0.41	0.83	1.00	0.76	0.85	0.68	0.28
yaw	0.51	0.75	0.68	0.71	0.65	0.71	0.71	0.70	0.74	0.60	0.45	0.83	0.76	1.00	0.66	0.56	0.46
AWA	0.73	0.58	0.63	0.63	0.60	0.63	0.62	0.67	0.54	0.68	0.56	0.77	0.85	0.66	1.00	0.58	0.52
AWS	0.59	0.49	0.50	0.54	0.54	0.53	0.51	0.61	0.47	0.48	0.75	0.88	0.68	0.56	0.58	1.00	0.50
BS	0.40	0.57	0.44	0.46	0.44	0.57	0.58	0.60	0.38	0.29	0.51	0.47	0.28	0.46	0.52	0.50	1.00

Table 4.3 – Cross-correlation between different signals recorded during experiments, and the first 3 POD modes. Correlation values (and their corresponding colors) vary between 0 (in blue) meaning no correlation and 1 (in red), strong correlation.

for all AWA. Flappings are spotted in all the measurements carried out at different AWA, however their dynamics change too. Therefore, it would be interesting to analyse the spatial mode $\varphi_1(x)$ and the time coefficient $a_1(t)$ of mode 1 for different AWA from stable periods with a fixed spinnaker trim.

4.2.4 Mode 1, the flapping mode

4.2.4.1 Spatial mode

To compare spatial modes -that have normalised values-, the maximum value of time coefficient is taken to be multiplied by the spatial mode: $\max(a_1(t)) \varphi_1(x)$. Maximum value of time coefficient is used since we want to analyse and compare dominant variations. Maximum values of mode 1 for different AWA are presented in Figure 4.9 at 4 different stripes where the pressures are measured (1/4, 1/2, 3/4, 7/8 height of the spinnaker). Differential pressure coefficients have comparable distributions for each AWA, except that $|\Delta C_P|$ on the bottom half is slightly smaller for deeper AWA. The bulb of suction at the leading edge at 7/8 and 3/4 of the spinnaker height is always present and a smaller bulb of positive ΔC_P at 1/2 and 1/4 height is also spotted at the leading edge. For all stripes, for $x/\text{curve} > 30\%$ the spatial modes are around zero.

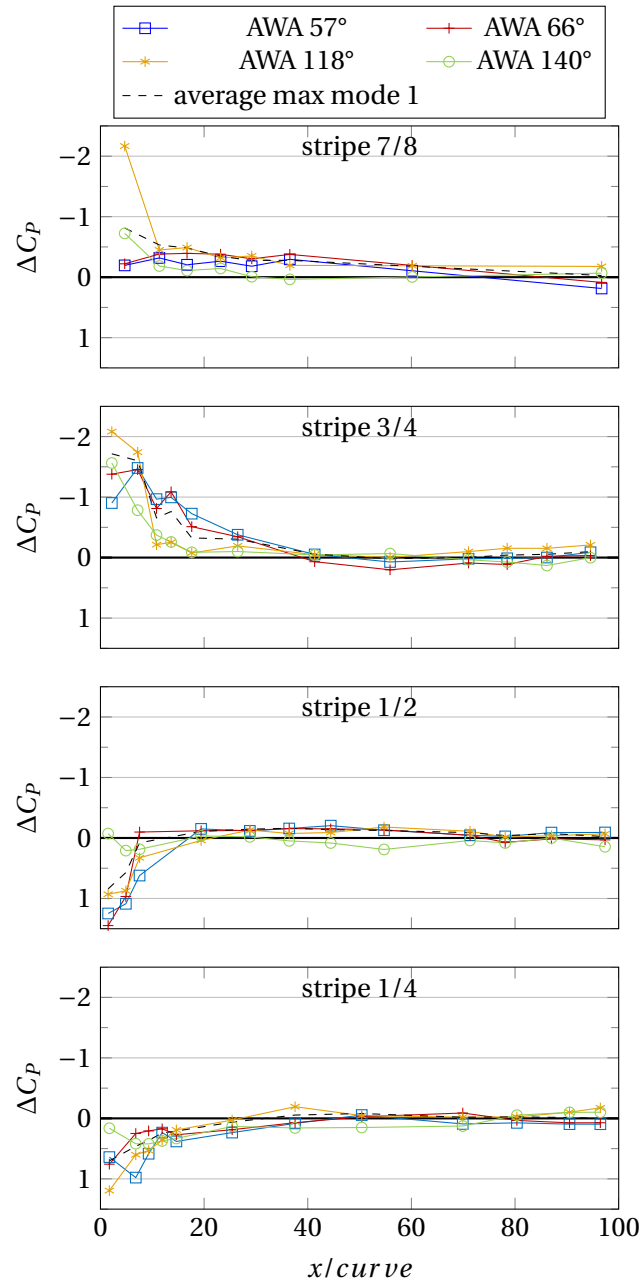


Figure 4.9 – Differential pressure coefficient of mode 1 of the POD for maximum time coefficient $\max(a_1(t)) \varphi_1(x)$ at different heights of the spinnaker for different AWAs.

Figure 4.10 confirms this observation. The overall pressure pattern is similar to two pressure areas of opposite signs at the leading edge, with one in the bottom half and the other in the top half. For AWA 140° the bottom pressure area might be less clear. But for large AWA, the variations of the apparent wind are larger and the average pressure coefficient is smaller and therefore more sensitive to noise variations. Due to noisier signals, it is more difficult to spot less energetic flapping patterns.

Even if the POD method is a data driven decomposition (i.e. modes are derived from the data itself),

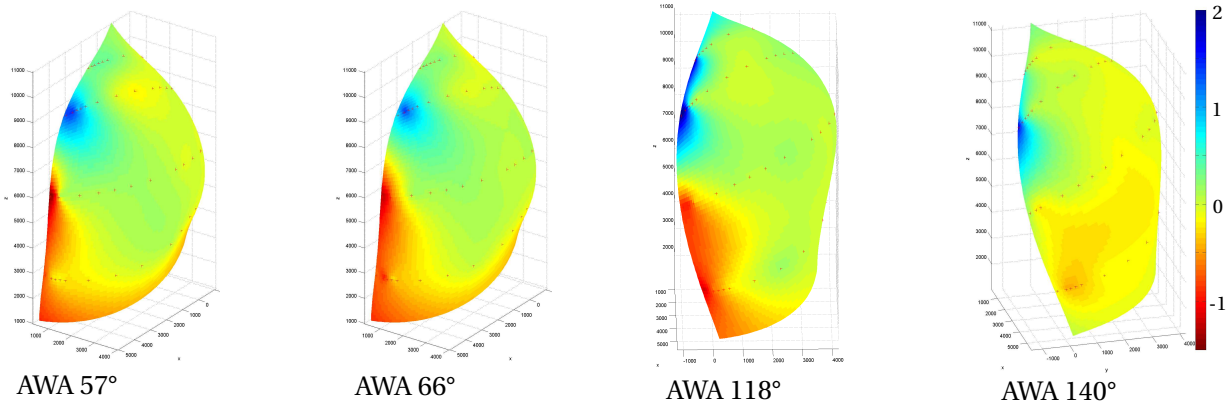


Figure 4.10 – Pressure distribution projected on flying shapes for different AWAs of mode 1 for the maximum time coefficient $\max(a_1(t)) \varphi_1(x)$.

there is a good repeatability of the POD spatial modes for “stable” periods when the spinnaker has a fixed trim. Mode 1, which defines the flapping of the luff, could be defined as a unique spatial mode whatever the AWA.

4.2.4.2 Time coefficient

From Figure 4.6 (displaying the evolution of the time coefficient for the first 3 modes at an average AWA of 69°) and Figure 4.7, typical pseudo-periods for mode 1 emerge for these AWA. Furthermore, for different “stable” periods, at different AWA -not displayed here-, similar variations of the temporal coefficient of mode 1 are detected. The dynamics vary with the AWA. A pseudo-period is determined, and the corresponding pseudo-frequency f_s is displayed in Figure 4.11 (left) according to the corresponding average AWS of the “stable” period. The reduced frequency f_r shown in Figure 4.11 (right) is calculated as follows:

$$f_r = \frac{f_s \sqrt{S}}{\text{AWS}}$$

with S the sail area, thus $\sqrt{S} = 8.3 \text{ m}$.

When the AWA is increased, the typical pseudo frequency of the time coefficient of mode 1 is reduced proportionally. A linear interpolation passing by the origin can be plotted, hence there is a constant interpolated reduced frequency. There is a linear dependence of the pseudo-frequencies with the AWS. It demonstrates that mode 1 is mostly driven by aerodynamic phenomena, which confirms what has been described in section 4.3, and not by mechanical resonance of the rigging or of the membrane of the sail.

In conclusion, the POD method makes it possible to describe a global temporal behaviour in a better way than analysing each pressure sensor signal. Mode 1 which represents almost half of the fluctuation energy describes well the flapping of the luff. The spatial pattern of mode 1 of the differential pressure coefficients does not change with the AWA. It can be represented as a unique spatial pattern for all AWA.

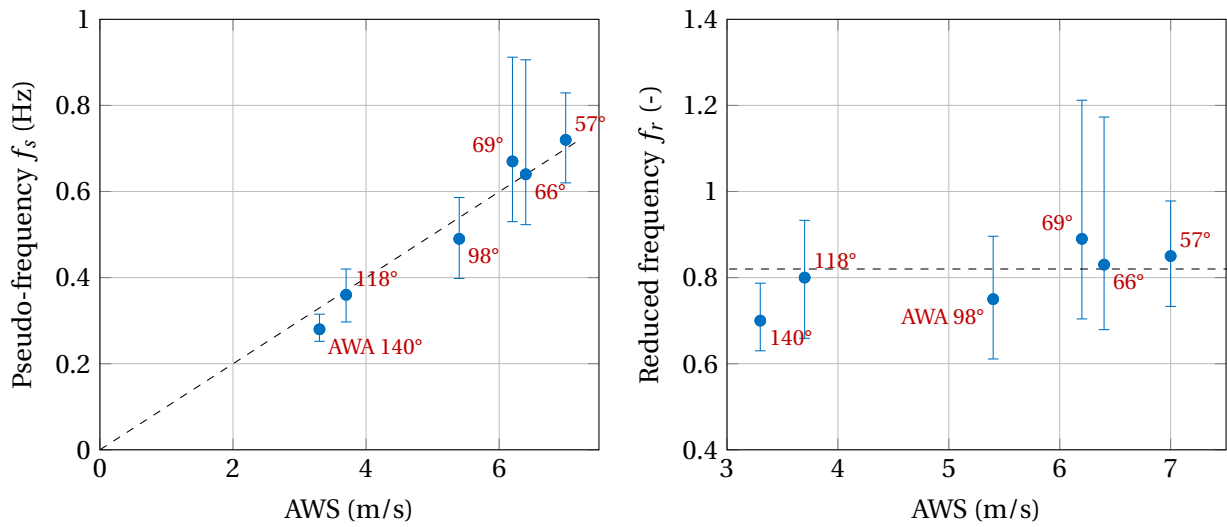


Figure 4.11 – Pseudo-frequency (left) and reduced frequency (right) of the time coefficient of the first POD mode (blue dots) for different AWA as a function of the AWS. A linear interpolations fit the experimental data.

The variations of pressures due to the flapping are therefore proportional to the square of the AWS. The dynamics of POD mode 1 evolves with the AWA. For each AWA, a typical pseudo-period is noticed. It increases linearly with the AWS. It proves the flapping phenomenon is not a random fluctuation but is an almost periodical behaviour, an intrinsic instability of the spinnaker in certain conditions. This conclusion is also confirmed by on-going wind tunnel experiments at the Yacht Research Unit of Auckland carried out by Nicolas Aubin from IRENav. With a fixed trim, and a steady wind, the luff of the spinnaker can stay in a dynamic instability.

4.3 Physical interpretation of flapping and discussions

From these observations, a physical interpretation is proposed. To describe the phenomenon of flapping, we based our arguments using different theoretical models described in the following subsections. This physical interpretation is only a speculation and would need further developments and validations. The main assumption as explained previously is flapping is a dynamic instability which can be a self-maintained system in steady conditions.

4.3.1 Two-string membrane model

The flapping of the spinnaker can be modelled as a 1D membrane (a string) in the streamwise direction, where the flapping occurs, coupled with another string in the spanwise direction representing the luff (cf. figure 4.12). This interpretation is based on the membrane theory. For a better comprehension the equation 1.13 presented in subsection 1.5.4 is presented as a reminder:

$$\rho \frac{\partial^2 w}{\partial t^2} = \underline{\underline{\chi \kappa}} + \Delta P \quad (4.1)$$

with:

w : normal displacement from plane $(\underline{u}, \underline{v})$

ρ : surface density of membrane

ΔP : difference of pressure

$\underline{\underline{\chi}}$: tension tensor

$\underline{\underline{\kappa}}$: curvature tensor: $-\frac{\partial^2 w}{\partial u \partial v} = -\nabla^2 w$

The curvature tensor can be estimated, as a first approach, by the mean curvature: $\nabla^2 w \approx \kappa_u + \kappa_v$. Near the leading edge, let us assume κ_u the principal curvature set streamwise, from the luff to the leech, and κ_v , the principal curvature set spanwise, from the tack to the head. On each string the equation 4.1 can be reduced to one dimension, with either u or v used depending on which string we deal with:

$$\rho \frac{\partial^2 w}{\partial t^2} = T \frac{\partial^2 w}{\partial u^2} + F_{aero} \quad (4.2)$$

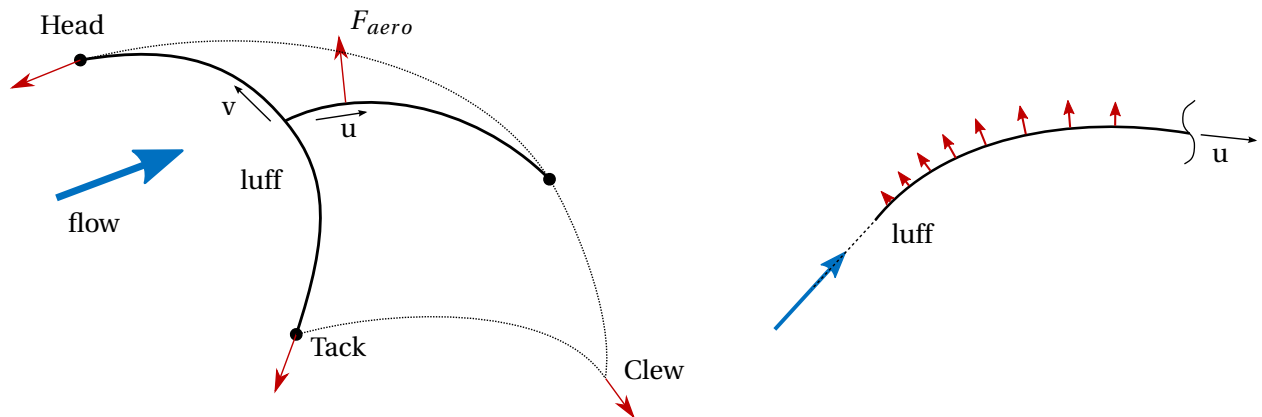
where F_{aero} is the integration of ΔP along the curve. This equation explains that an increase of pressure is counteracted by an increase of tension in the sail or an increase of curvature. For the same pressure distribution, a sail with more curvature should have less tension in the sailcloth. Furthermore, the curvature creates a bending stiffness.

Figures 4.12 and 4.13 describe the main stages of the flapping. To compare with the observations described in section 4.1, the instants A, C and D are used. In the next part, to simplify the discussion, when the suction increases, the pressure ΔP increases.

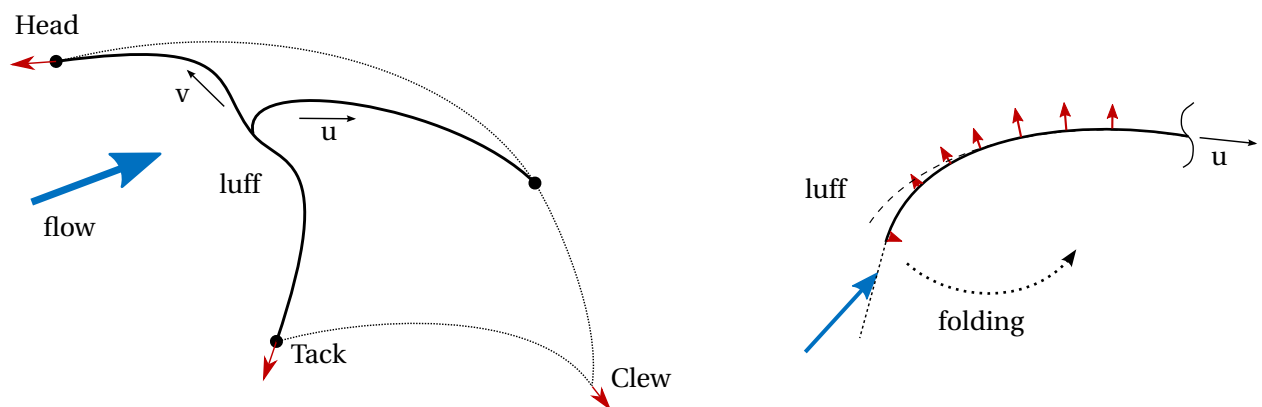
4.3.1.1 Beginning of flapping

First it is interesting to note that the spinnaker always folds towards the windward side (concave side) and not towards the leeward side (convex side). If the luff of the sail was folded itself towards the leeward side, there would be a local change of the curvature and an increase of the angle of attack. Streamwise, the curvature κ_u would change sign, and therefore $\underline{\underline{\kappa}}$ would reduce. The increase of the angle of attack would increase the pressure ΔP at the leading edge. Therefore according to equation 4.1, an increase of the pressure ΔP and a decrease of the curvature $\underline{\underline{\kappa}}$ would cause an increase of the tension $\underline{\underline{\chi}}$ to stay at an equilibrium. However an increase of the tension in the spanwise string would prevent the spinnaker from folding towards the leeward side. It would improve the shape stability of the sail.

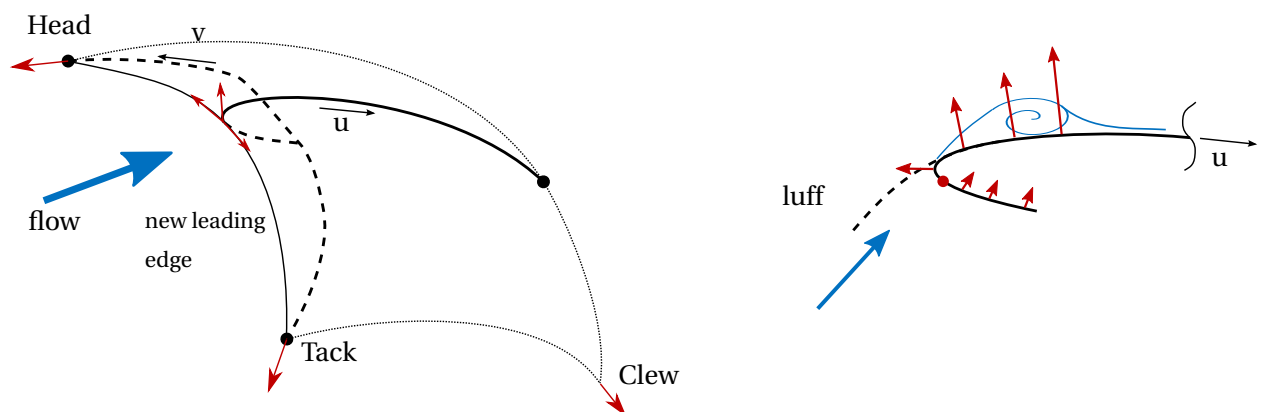
A simple experiment can be run to understand this: With a squared thin and flexible sheet of paper -without any bending stiffness- held at two opposite summits, one curves it by approaching these two summits. Then one applies pressure (by blowing for example) on a freed quarter of the sheet of paper from the concave side. One can notice even if there is only one curvature ($\kappa_u = 0$ and $\kappa_v > 0$), it is almost impossible to fold the paper. If one reduces the curvature κ_v (by moving the extremities away from each



(a) Just before flapping (*instant A*). Low pressure on the streamwise string u .

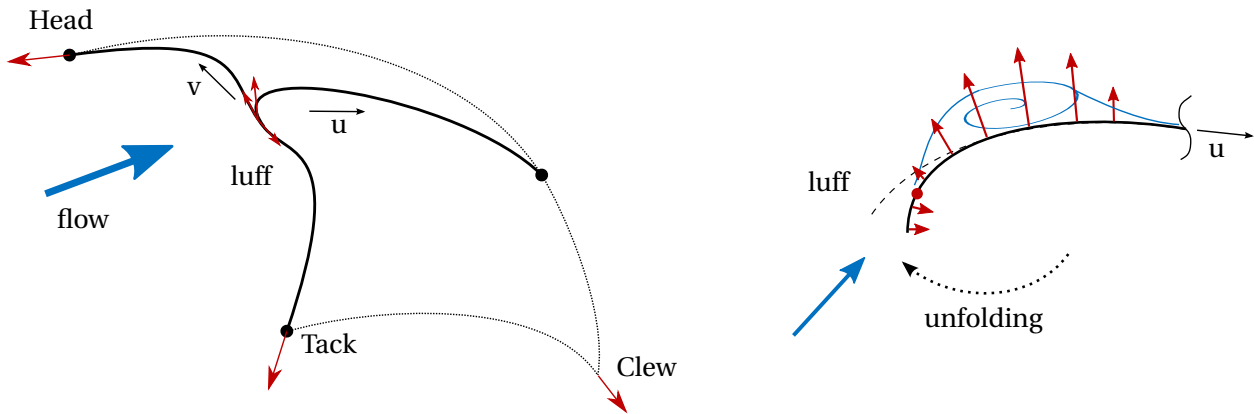


(b) During folding (*from instant A to C*). Spanwise string v not loaded, decrease of the angle of attack, decrease of pressure on streamwise string u .

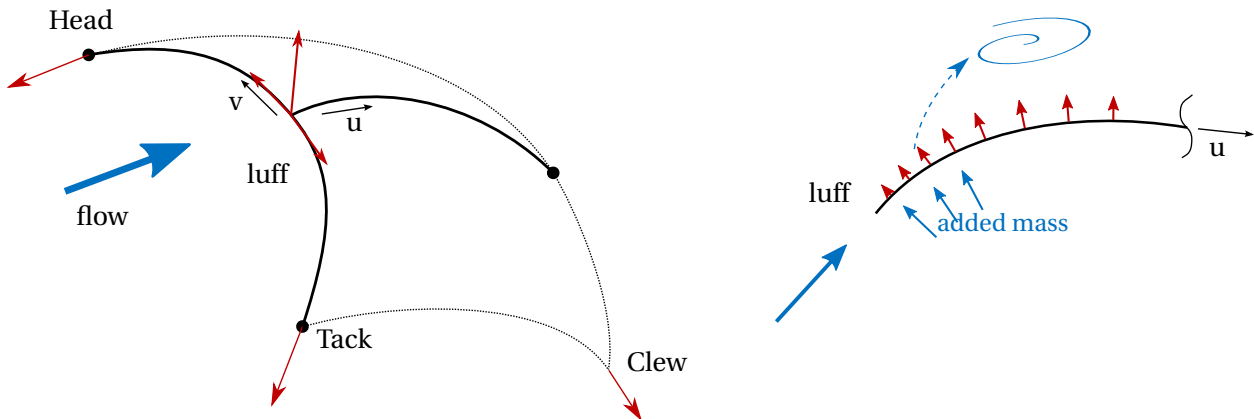


(c) Maximum of folding (*instant C*). Streamwise string folded enough to create a new aerodynamic profile with a high angle of attack. Creation of a leading edge separation bubble.

Figure 4.12 – *Folding stage*. Simplified representation of the spinnaker to model the flapping of the luff with one spanwise string v modelling the luff and one streamwise string u .



(a) During unfolding (*from instant C to D*). Due to high gradient of pressure at the luff, streamwise string unfolds. Leading edge separation bubble expands.



(b) Full flying shape again (*instant D*). Spanwise string suddenly tensioned, stopping brutally the unfolding of the streamwise string. Peak of load due to displaced air around the luff. Leading edge separation bubble detaches, low pressure back on the streamwise string. First situation appears again.

Figure 4.13 – *Unfolding stage*. Simplified representation of the spinnaker to model the flapping of the luff with one spanwise string v modelling the luff and one streamwise string u .

other for example), it is easier to fold the spinnaker with the same pressure applied on the freed quarter. However if one blows on the other side (convex side), the sheet is easily folded.

Whereas if the luff folds itself towards the windward side (concave side) as seen on water, the angle of attack becomes negative, the streamwise curvature κ_u increases locally and the spanwise curvature κ_v decreases (cf. figure 4.12b). The negative angle of attack decreases the differential pressure ΔP at the leading edge. According to equation 4.2, if ΔP decreases and κ_u increases, the tension which is already low must decrease. When the tension is almost null, the sail collapses and folds. This description is still possible if there is a positive angle of attack at the beginning and the angle of attack is decreasing and not necessarily negative.

4.3.1.2 Folding stage

Figure 4.12 describes the physical interpretation during the folding stage. At instant A, the luff of the spinnaker stands still, hence $\frac{\partial^2 w}{\partial t^2} = 0$. ΔP as well as T are at a minimum. The sail is at a weak static equilibrium. [Thwaites, 1961, Newman, 1987] demonstrated that a loss of shape stability occurs for two-dimensional sails held at both extremities, for a certain ratio between the camber, angle of attack and tension in the sail. Unlike upwind sails, the leading edge of a spinnaker is mainly maintained spanwise by the tensions applied at the head and tack which set the sail (cf. figure 4.12a) and might be even more subject to collapse. For a tension and a pressure small enough, the spinnaker starts folding towards the windward side as explained previously.

During the folding stage, from instant A to C, the spinnaker keeps folding, κ_u increases, and ΔP decreases because of a negative angle of attack. While the luff is still folding, the shape of the profile changes and the leading edge shifts from the luff to a new leading edge further downstream. At instant C, the angle of attack of this "new" profile is larger (cf. figure 4.12c). When a flow encounters a thin profile with an angle of attack large enough, a leading edge separation bubble can be created since the flow cannot follow the profile but reattaches further downstream. It creates a high suction area just after the folded area.

4.3.1.3 Unfolding stage

In the folded area, the tension is low because the sail has more curvature and less pressure. Downstream the new leading edge, the high suction yields a high tension in the sail. There is therefore a difference of tension at the frontier of the folded area (see red arrows on the 2-string models in Figure 4.13a). The tension is spread spanwise and towards the high suction area -towards the trailing edge-. This difference of tension tends to pull the folded area and therefore to unfold the luff². Moreover the stagnation point (represented by a red point in Figure 4.12c) is upstream the limit of the folded area. At this point, the pressure is null. Therefore a small part of the folded area -the most curved part- has a high suction which tends to unfold the sail too.

During the unfolding stage (from instant C to D), the leading edge separation bubble expands (cf. figure 4.13a). The tension at the limit of the folded area increases and contributes even more to unfold the luff up to the full recovery of the flying shape (instant D) (cf. figure 4.13b).

At instant D, the spinnaker is unfolded. Just before that instant, a strong deceleration brutally stops the unfolding motion. The spanwise tension and curvature prevent the spinnaker from being folded streamwise in the other direction (towards the leeward side) as explained previously. During the folding, the spanwise tension and curvature is null because the string is slack. But as soon as the spinnaker recovers its full flying shape, the high suction at the leading edge suddenly tensions the luff (cf. figure 4.13b). During this brutal deceleration, the inertia of the air displaced on the windward side by the movement of the luff (the added mass) adds an extra tension in the luff. The air displaced on the leeward side has also some inertia (added mass) and tears the leading edge suction bubble off the luff.

Then, the pressure is low again, and after this high peak of tension, the situation described at instant A is

²While sailing, when the luff stays folded, it is common to sharply and briefly trim-in the clew sheet in order to unfold the luff. Similarly to the above interpretation, the trimmer applies a tension in the sail which unfolds the spinnaker.

found again. Therefore without any change in the trim of the spinnaker and without any modifications of the wind, the sail would be able to flap again.

4.3.1.4 3D aspects

The previous interpretation describes the flapping at one height only and the reality is of course a more complex 3D phenomenon. For example, in section 4.1, the luff at the top part of the spinnaker flaps before the middle part. The leading edge separation bubble stays attached in the top part of the spinnaker where the full shape is recovered, "locked" by the expansion of the leading edge separation bubble in the folded middle part. When the flapping finishes, the high suction disappears on the whole span of the sail.

During the SAILING FLUIDS project, Dario Motta and I carried out experiments for his PhD in Auckland on a larger spinnaker (89 m^2 instead of 68 m^2 for the J/80). The sail has a higher definition of the pressure distribution with 72 pressure taps (instead of 44 on the J/80) distributed on 6 stripes (instead of 4). These experiments jointly carried out by the Yacht Research Unit of the University of Auckland and the French Naval Academy Research Institute (IRENav) are described in detail in [Motta et al., 2015] and in the PhD thesis of Dario Motta [Motta, 2015]. Even with a larger spinnaker with less luff curve, the overall dynamics is similar on this larger spinnaker: the flapping "travels down" from the top part to the bottom part. The conclusions are similar as stated in [Motta, 2015]: *"If the spinnaker is trimmed on the verge of luffing, the recovery from the folding of the luff leads to the development of high suctions near the leading edge at the higher stripes, which are responsible for the temporary increase of the force coefficients that would not be otherwise achieved"*.

Figure 4.14 presents some measurements as space-time diagrams of the 6 pressure stripes on this larger spinnaker and confirms the high suction at the leading edge in the top part of the sail which stays after the flapping. With this higher resolution in pressure distribution, a spatial and temporal evolution of the suction is measured in 4/5 and 15/16 height stripes. Dashed lines in Figure 4.14 highlights a possible shedding velocity of 20% of the AWS of the leading edge separation bubble. It supports the idea that the leading edge separation bubble is detached after the flapping.

As explained in subsection 1.4.3, [Viola et al., 2014] demonstrates with a Detached Eddy Simulation, the presence of a Leading-Edge Vortex (LEV) for a rigid spinnaker *"which increases in diameter from the foot to the head, where it becomes the tip vortex and convects downstream in the direction of the far field velocity"*. This stable numerical LEV might be similar to the one described previously created during the flapping of the luff, but which is not as stable. Finally the flapping of the spinnaker might be compared with the LEV commonly found in insects and birds flights during the downstroke of a flapping of wing. Nonetheless the Reynolds numbers are quite different (10^3 for insects, and 10^6 for a spinnaker).

4.3.2 Wave propagation model

During the unfolding stage, the frontier of the folded area is almost the stagnation point. At the stagnation point there is zero pressure. It is the limit where the pressure changes sign from positive pressure in the

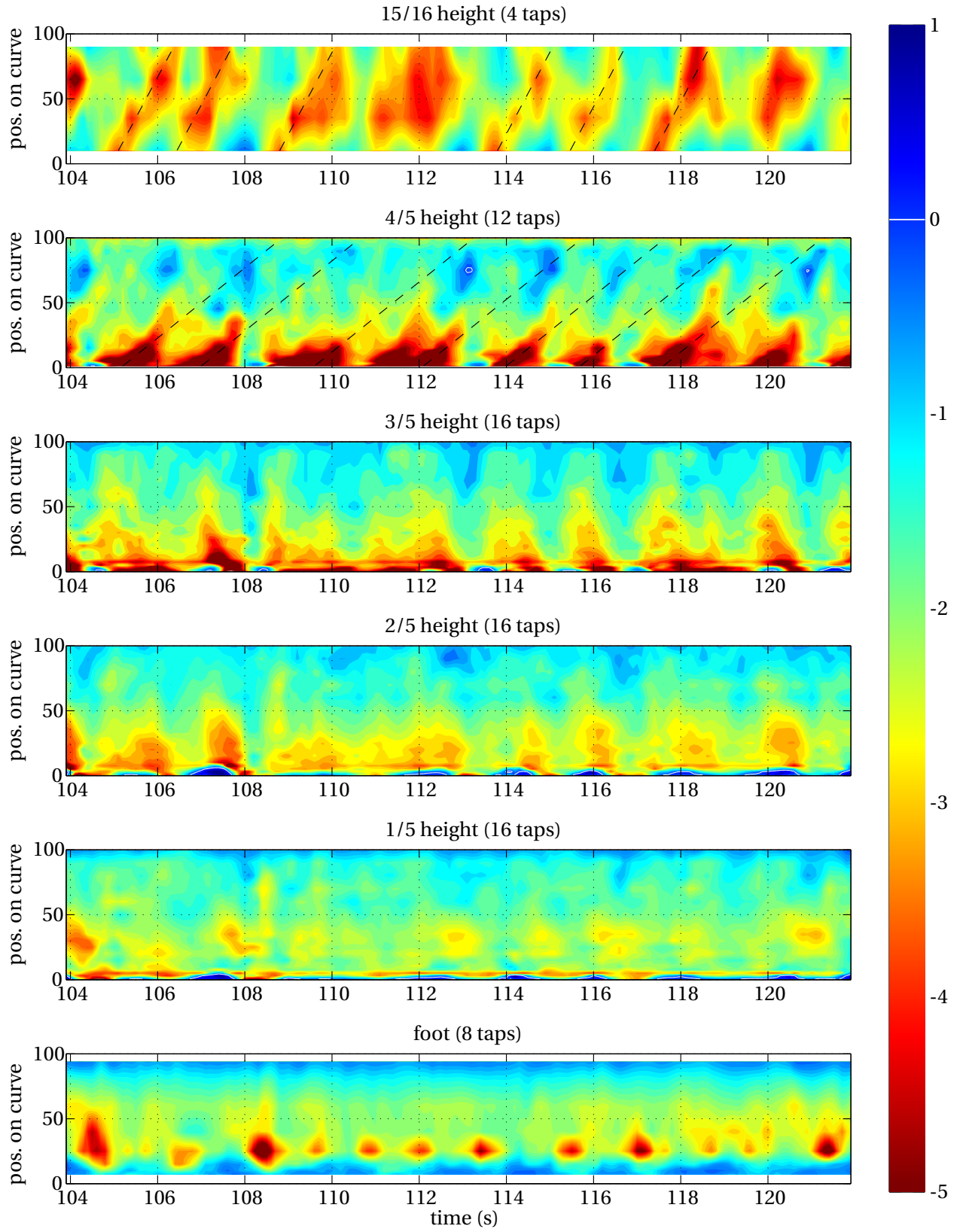


Figure 4.14 – Space-time diagrams of $\Delta C_p(x, t)$ at different heights of the sail. Dashed lines on the 15/16 and 4/5 height stripes correspond to a convection speed of $0.2\langle AWS(t) \rangle$. These measurements come from experiments carried out in Auckland and more explained in [Motta et al., 2015, Motta, 2015].

folded area to suction downstream. Thus at the frontier of this folded area, the external pressure F_{aero} is null. Therefore if we model the flapping as a string, the equation is simplified:

$$\rho \frac{\partial^2 w}{\partial t^2} = T \frac{\partial^2 w}{\partial u^2}$$

which can be rewritten as a wave equation:

$$\frac{\partial^2 w}{\partial u^2} - \frac{1}{c^2} \frac{\partial^2 w}{\partial t^2} = 0 \quad (4.3)$$

with $c = \sqrt{\frac{T}{\rho}}$, the celerity of the wave. The unfolding can indeed be seen as a pulse wave with a celerity c . The tension in the sail T can be estimated by integrating the pressure created by the leading edge separation bubble. On a unit width section, the pressure coefficient is about -3 over 10% of the curve of a length of 7.37 m. With an AWS of 7 m/s, the pressure is therefore: $P = |\Delta C_p| \frac{1}{2} \rho_f \text{AWS}^2 = 90 \text{ Pa}$. Hence $T \approx 70 \text{ N}$. The theoretical velocity of the wave with no air resistance is calculated at $\sqrt{\frac{T}{\rho_s}} = 37 \text{ m/s}$ with $\rho_s = 0.05 \text{ kg/m}$.

From Figure 4.7, we deduce the time ($\Delta t = 0.37 \text{ s}$) to unfold about 10% of the curve ($d_f = 0.1 \times 7.37 \text{ m} = 0.74 \text{ m}$). The celerity of the unfolding wave is therefore $c = 2 \text{ m/s}$, which is about 20 times smaller than the theoretical velocity.

To match the measured velocity with the theoretical velocity, the density $\rho^* = \sqrt{\frac{T}{c^2}}$ should be 350 times larger than the density of the sail. As explained in the previous subsection 4.3.1, the membrane also displaces the surrounded air which has an inertia. Assuming the mass of the sail to be small compared to the added mass of the fluid, it would mean the added mass of air would be 350 times larger than the mass of the luffing part of the spinnaker. It is of the order of magnitude of what was found in subsection 1.5.3.

4.3.3 Mechanical model

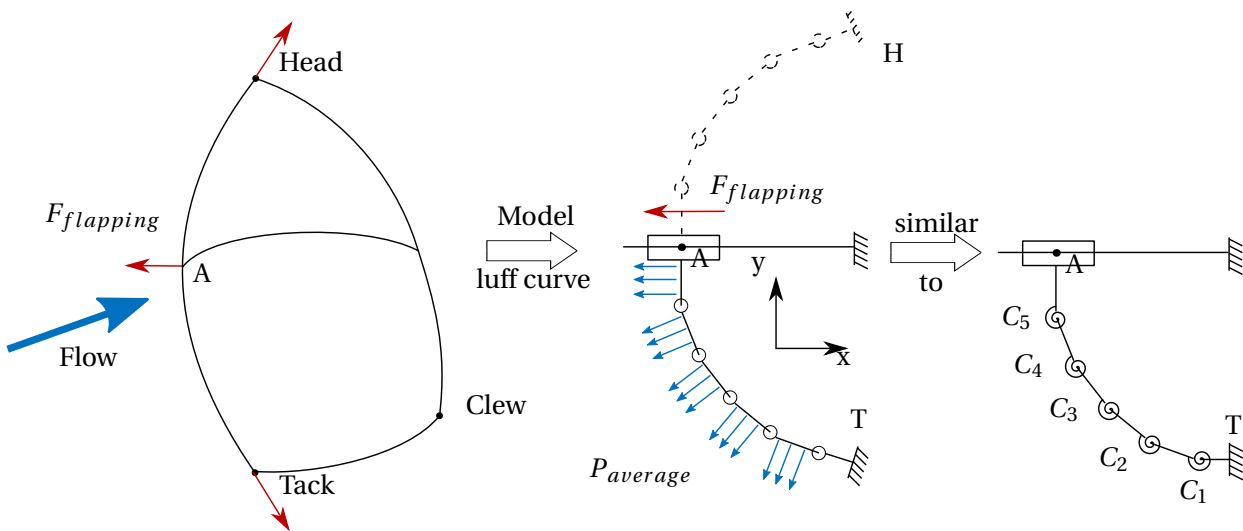


Figure 4.15 – Simplified model of the spinnaker luff while absorbing the force created by the flapping.

The unfolding stage finishes by a peak of tension with the brutal deceleration of the luff (instant D). This phenomenon can be modelled as a mass-spring problem. The energy of the unfolding described previously as a pulse wave is transmitted to the luff curve as seen in Figure 4.13b. The tension in the luff curve can be imagined as a stiffness. To better understand the phenomenon, let us simplify it to a 2D problem as presented in Figure 4.15. Using a mechanical representation, the camber of the luff curve is represented by a succession of pivots spaced by undeformable weightless straight segments of sail. Like a membrane, no bending stiffness is taken into account. On each segment, an average pressure is applied. Let us assume the force created by the flapping is applied in the middle of the luff curve, at A. The problem is therefore symmetrical and can be reduced by half, with the slope of the shape necessarily null. At an equilibrium state, the system finds a stable position thanks to the external pressure applied. A disturbance created by the brutal deceleration of the flapping of the luff (at instant D for half curve) displaces the luff curve (in -x direction in Figure 4.15). This disturbance can be found by calculating the energy of the pulse wave of the flapping which is transmitted to the luff curve at the point A. The system wants to recover an equilibrium state. For each segment, the linear pressure creates a moment for the previous segment at their common pivot point, acting like a spiral spring $C_i\theta_i$, with θ_i the angle between two segments i and $i + 1$, and C_i the stiffness (cf. figure 4.15). These spiral springs in series create an overall stiffness C_l .

If the fluid-structure phenomenon of the flapping is modelled as a mass-spring problem with no damping terms, the period of flapping should therefore be:

$$T = \frac{1}{2\pi} \sqrt{\frac{k}{m}}$$

In subsection 4.2.4.2 we demonstrated that the period of flapping was proportional to the speed of the flow. [Wakaba and Balachandar, 2007] shows that the added mass is independent of the flow and of the viscosity of the fluid. Thus m might be constant. However as seen in the subsection 4.2.4, the differential pressure coefficient of flapping is similar for all AWA, thus proportional to the square of the AWS. The stiffness is highly dependent on the pressure which evolves with the square of the flow speed. Thus if k is proportional to $AW S^2$ then T is proportional to AWS . However, Figure 4.11 demonstrates the linear regression of the pseudo-frequency is not null when the AWS is null. This is why there is a slight increase of the reduced frequency with the AWS. This simple model cannot represent this offset. At this stage, we do not know if this offset is due to the incertitude of full-scale measurements or due to high non-linearities present in this FSI system.

4.3.4 Discussions

The question from sailors: "Is letting the luff flap more efficient, more propulsive than an overtrimmed spinnaker?" could be transposed in terms of energy: if the work of loads created during a flapping period is positive. Using a single mode approximation, let us consider the dynamics of the sail while flapping described by a unique time function $q(t)$ with a modal shape $\psi(x)$, the displacement of the luff during the flapping is $\xi(x, t) = \psi(x)q(t)$. The work of loads created during a flapping period is then:

$$W_{flapping} = \int_T F_{flapping} \frac{\partial q(t)}{\partial t} dt > 0 \quad (4.4)$$

Calculating the energy from the wave equation or from the differential equation of a spring-mass system could help to answer this question. However, there are several other issues. The time averaged pressure distribution for an overtrimmed spinnaker and for a spinnaker "on the verge of luffing" is not necessarily identical. Moreover due to the importance of the flapping, it is difficult to extract from measurements the time averaged pressure distribution without any flappings. And it is not necessarily the time averaged pressure distribution measured in the POD method. Therefore even if the work of loads created during a flapping period is positive, the time averaged aerodynamic force might be lower than the averaged force with an overtrimmed sail.

Nevertheless, we have demonstrated that flapping of the luff yields a high suction zone especially in the top part of the sail. This increase of suction is in the forward part of the sail which is oriented towards the bow of the boat. This high suction would therefore lead to an increase of the propulsive force. This assumption is confirmed by wind tunnel experiments carried out during the writing of this thesis. These experiments developed and carried out by Nicolas Aubin (IRENav) at the wind tunnel of the Yacht Research Unit in Auckland demonstrate that the propulsive force finds a maximum when the trim of the spinnaker is on the verge of luffing.

4.4 Conclusions

In this last chapter, a specific dynamic behaviour of a downwind sail has been analysed. From observations, we realised that this flapping phenomenon is a complex three dimensional fluid-structure interaction problem producing high variations of loads. It can be self-maintained and does not necessarily need an external action to keep the luff flapping. It is a dynamic instability of the sail. When the suction decreases and changes sign, the sail folds. At the maximum of folding, a high suction area appears. Then the spinnaker unfolds and recovers a full flying shape. At that instant the loads measured are at a maximum.

An interpretation of this phenomenon has been proposed. When the sail is folded, the modified aerodynamic shape creates a leading edge separation bubble producing a high suction. This leading edge separation bubble expands during the unfolding. It accumulates energy that is transmitted to the luff curve when the spinnaker has recovered its full shape. The luff curve takes this extra tension which is reflected into the head and tack lines. To my knowledge, this dynamic instability has not been described before. This physical interpretation is a proposition and would need further developments and validations, such as experiments in a wind tunnel for example where the environment is more controlled. During full-scale experiments at a constant TWS, the apparent wind angle and speed are intrinsically linked. Experiments in laboratory could be conducted with the wind speed and angle independent in order to analyse if the dynamics is mostly linked by the speed of the flow or by the shape of the structure due to different wind angles.

Using the POD method, we were able to characterise a global behaviour of the flapping. This dynamics is predominant in the pressure and loads fluctuations. Its period is proportional to the AWS. The POD method also helps to reduce the problem to a few modes. The first modes allow the reconstruction a signal with the main variations and remove noises. This therefore can facilitate future comparisons

between unsteady numerical simulations and experiments.

In addition to geometrical non-linearities (high displacements and curvatures, no bending stiffness and compression taken by the sail), the problem is highly three dimensional, with the flapping of the luff propagating downwards and the leading edge suction bubbles growing along the span of a three dimensional shape.

Many other unsteady dynamics of the spinnaker exist such as the easing of the clew sheet, a dynamic trimming of the clew (pumping), the sudden inflation of the spinnaker after a general collapse of the sail giving the highest peak of loads. A periodic pitching or rolling of the boat in waves also affects the shape, pressure distribution and loads on the spinnaker. Each of these examples are complex to study and analyse from full-scale experiments because many dynamic phenomena can be present at the same time. Numerical simulations could help to model these different dynamics, but first need validations. At the time of writing of this thesis, a comparison between unsteady numerical simulation and full-scale experiments is ongoing with an easing of the clew sheet followed by a flapping of the luff.

Conclusion

This PhD is part of the IRENav's VOILENAV project, gathering research studies of fluid-structure interaction on sailing boats. This PhD project enabled the development of a full-scale instrumented sailing yacht dedicated to time-resolved measurements of the aero-elasticity of the sails and rigging in downwind navigations. The evolutions of the flying shapes, loads and pressures on the spinnaker were analysed according to the apparent wind angle. Not only has the global averaged behaviour been analysed but also the unsteady behaviour of the flying sail. The flapping of the luff -which is the most efficient trim according to sailors- has been investigated.

A J/80 class sailing boat is instrumented to measure the flying shape of the spinnaker, the aerodynamic loads transmitted to the rigging, the pressures on the asymmetric spinnaker and the boat and wind data, with the constraints of still being able to sail like in regatta conditions and of acquiring time-resolved data. Particular attention has been paid to the precision and the dynamics of the measurements.

The main improvement has been on a system dynamically measuring the flying shape of the spinnaker. It is synchronised with the other data. The photogrammetry flying shape acquisition system measures the shape of the spinnaker with an average accuracy better than 1.5% (0.15 m for 10 m) at a frequency rate of 25Hz. This accuracy achieved is fine to measure the typical dynamic behaviours of a spinnaker having a time scale of 1 s with displacements around 1 m.

To measure the aerodynamic loading generated by the spinnaker, load sensors are placed on the three corners of the sail (head, tack and clew). Two types of load sensors have been used. First, instrumented shackles, developed during the PhD project of [Augier, 2012], are upgraded to wireless sensors. The precision is better than 1% of the measurement range (0 N to 5000 N) which is sufficient for the loads we measured. Then for a second experimental campaign, Directional Load Cells (DLCs) measure the magnitude and the direction of the loads, which is of importance on flying sails such as a spinnaker. It is developed by the Yacht Research Unit in the University of Auckland. During this PhD project, the dynamics and the calibration of these load cells are analysed and upgraded. A time shift of about 0.1 s is still present. The precision of the strain gauge is better than 2% of the measurement range thus about 100 N. The uncertainty in directions lead to an uncertainty of 100 N of the projected forces. It is reasonable to analyse the main evolutions of the load directions according to the apparent wind angle.

The pressure acquisition system was developed and also used during the PhD project of [Motta, 2015] which, with my PhD, was part of SAILING FLUIDS, a UK-France-NZ collaboration project funded by the European Union's Seventh Programme and by the Royal Society of New Zealand. The sampling rate of 7 Hz is just sufficient for analysing the evolution in time of the pressure distribution on the spinnaker. The

precision of 4 Pa is good for most of the tests, but is of the same order of magnitude as pressures measured at large apparent wind angles. Boat and wind data have sampling rates varying from 1 Hz to 20 Hz and are thus only used to analyse the time averaged performance of the sailing boat.

Two campaigns were carried out in France (in 2013 and 2014), and another in New-Zealand mostly conducted by Dario Motta. Several in-situ measurements in upwind and downwind navigations were acquired. These time-resolved data create a database for numerical-experimental comparisons in different steady and unsteady conditions. Downwind numerical-experimental comparisons remain to be made. The global behaviour of a spinnaker has been assessed according to the apparent wind angle. For tight apparent wind angles (about 60°-90°), it seems the spinnaker is bridled in the top half of the sail. The average differential pressure coefficient is larger than for other apparent wind angles. Since the apparent wind speed is also higher, the loads on the corners are the largest, with the head and tack loads almost twice as large as the clew load (respectively 1000 N and 600 N). The propulsive and side forces are within the same order of magnitude.

The spinnaker shape changes less between 90° and 150° than between 70° and 90°. At AWA 90°-120° the sail is more twisted in the top half. The pressure distribution pattern is similar to lower apparent wind angles (existence of a bulb of suction at the leading edge) with globally the same average differential pressure coefficient. However the apparent wind speed is reduced resulting in a lower aerodynamic force produced by the spinnaker. Nonetheless, the sail is eased and more rotated towards the bow. The maximum of propulsive load coefficient is found for this range of apparent wind angles with the side force half of the propulsive force. This spinnaker is optimised for this range of apparent wind angle.

For larger apparent wind angles (about 120°-150°), the shape is globally the same but the average pressure coefficient is decreased. With an apparent wind speed almost divided by 2 relative to tight angles, the loads at head and tack corners are almost divided by 5.

For all apparent wind angles, most of the temporal variations of loads and of pressures appear near the leading edge mainly due to the flapping of the sail.

Flying shapes of a spinnaker are measured by the photogrammetry flying shape acquisition system. Unlike upwind sails, a spinnaker has a 3D shape which changes a lot with the apparent wind angle. Sail designers generally use classical parameters of aerodynamic stripes to design a spinnaker. Although this is convenient for a shape close to a 2D extruded shape and for upwind sail for which horizontal profiles have a moderate variation along height, it is much less appropriate to describe a spinnaker shape. During this PhD, new representations are developed to analyse the shape of the spinnaker as a 3D surface. The 3D camber representation is used to easily compare the shapes and highlight where the main camber of the sail is. A triangular Bézier surface is also developed to represent the shapes of sails. This has the big advantage of defining the spinnaker with only a few control points. Moreover for sail designers, these control points can characterise different types of sails for all apparent wind angles so they can be easily stored in a database. Using control points instead of a whole surface would indeed lead to a reduction and simplification of the data storage.

Finally, the flapping of the luff, a typical unsteady behaviour of the spinnaker, is analysed. It is well-known by the sailors to be at the best trim, when the spinnaker is "on the verge of luffing", i.e. when the luff of the sail is slightly flapping. From measurements, we realised that this flapping phenomenon is a complex three dimensional fluid-structure interaction problem producing high variations of loads. The

sail folds when the suction at the leading edge decreases. At the maximum of folding, a high suction area occurs again. Then the spinnaker unfolds and recovers a full flying shape. At that instant the measured loads are at a maximum.

The pressure evolution is investigated with a modal analysis using the Proper Orthogonal Decomposition method. It is used to describe a global temporal behaviour in a better way than analysing each pressure sensor signal. Two specific modes represent the flapping. While its spatial mode is similar for every apparent wind angle, its temporal behaviour varies. The apparent wind speed (associated with the apparent wind angle in real sailing conditions) determine the characteristic time scale.

From these observations, a physical interpretation of the flapping is proposed. When the sail is folded, the modified aerodynamic shape creates a leading edge separation bubble producing a high suction. This leading edge separation bubble expands during the unfolding stage. It accumulates energy that is transmitted to the luff curve when the spinnaker has recovered its full shape. It is then reflected into the head and tack lines by load peaks.

Flapping of a spinnaker leads to the development of high suction near the leading edge which is mostly oriented towards the bow. It permits a temporary increase of the force coefficients that would not be possible if the spinnaker was not trimmed "on the verge of luffing".

Perspectives

The inboard instrumentation setup was greatly enhanced between the end of the PhD project of [Augier, 2012], and the current setup at the end of my PhD, thanks to financial investments, new technologies, useful feedback and a lot of effort to upgrade sensors and acquisition systems. However many sensors could still be upgraded. A new spinnaker dedicated to measurements has been purchased and has not been used yet. The positions of circular target points were marked during the conception and are precisely known. Furthermore new cameras have been purchased with a better resolution, a bigger optical sensor and a global shutter that would provide a better synchronisation and more precise measurements. Not only could the shape acquisition system be improved but also the load and pressure acquisition systems. New Directional Load Cells dedicated to dynamic measurements could be developed. A separate reference voltage from the supply voltage, as well as an optimised embedded algorithm would lead to a higher sampling rate and better precision of load measurement. Thorough calibration tests and a clear procedure to correctly place the *Base Unit* inside the boat would improve the precision of direction load measurement.

The pressure measurement system was fragile and several pressure taps were broken during the measurements. A more robust system with more pressure taps on the sail for a finer pressure distribution would allow a deeper analysis in the pressure measurements.

Finally experiments should be carried out with the photogrammetry flying shape acquisition system and the pressure measurement system at the same time. This would then open up new possibilities of research studies.

Other researchers carry out full-scale experiments. Combining our efforts and sharing our knowledge with them, like the LECCO dynamometer sailing boat at the Politecnico di Milano, would bring new perspectives.

Several measurements at different apparent wind angles were conducted. However the true wind speed we had during the experiments was sufficient but in a narrow range. Time-resolved data in stronger winds would make it possible to analyse the evolution of the loads and flying shapes according to the wind speed for similar apparent wind angles. The difference of dynamics of shape and loads between a boat in a displacement or a planning navigation would then be possible. Offshore racing yachts mostly sail downwind and can easily surf on waves. This dynamic and extreme navigation is still complex to model with numerical tools. Full-scale experiments would give actual forces at work and useful data. Other unsteady measurements where the highest peaks of loads are achieved could be conducted. The hoist of the spinnaker in strong winds, or when the whole sail collapses and inflates suddenly are good critical situations prevailing in sail and rig design.

Further improvements on the instrumented sailing yachts and other experiments could be conducted. But some analyses and comparisons presented in this thesis could be further developed as well. Different designs of downwind sails could be measured in-situ to create a large database of flying shapes. The Bézier control points might be able to sort them out. A gennaker used for beam reaching courses has a different shape from a large spinnaker used for running courses. The proposed Bézier description would magnify these differences. To characterise the most efficient sails, specific control point clouds could be extracted.

Class rules limit the design of sails such as the lengths of the luff, leech, foot and curve at mid height. With other restrictions such as the tangential plane at the clew point which must contain the spinnaker sheet block on the deck, an optimisation process could be developed numerically since the sail is defined by a polynomial formula. It would restrict the allowable shift of the different control points. A boundary around each control point would then help the sail designer to respect the class rule.

Numerical models could also help sail designers. But downwind sails are difficult to model with numerical tools due to the strong coupling between the highly detached and turbulent flow and the thin and flexible membrane. Strong coupling schemes are required with automatic remeshing. Some numerical simulations resolved in time were achieved [Durand, 2012, Durand et al., 2014] and still need validations. At the time of the writing of this thesis, a numerical/experimental comparison is ongoing with an easing of the clew sheet followed by a flapping of the luff. The measured wind and boat data are the input of the numerical simulation with the known spinnaker sheet length. The measured dynamic flying shape as well as the loads on the corners and in the rigging will be compared with the numerical results.

Time-resolved measurements permit a comparison with time-resolved numerical simulations, but also mean the dynamics of a spinnaker can be analysed in greater detail. The physical interpretation proposed to explain the flapping needs further investigations to refute or confirm this. Experimental studies in a controlled environment on a simpler shape should therefore be conducted with PIV measurements to detect the leading edge separation bubble if present. It would also be possible to decouple the speed and the angle of the flow affecting the shape of the membrane, which is not possible in full-scale experiments with a fixed true wind speed. Their influence could therefore be analysed separately.

Other modal analyses could be used, like the Bi-orthogonal decomposition [Hémon and Santi, 2003] or the Dynamic Mode Decomposition [Schmid, 2010]. These methods are also suitable to analyse temporal evolutions, hence might help to better understand the phenomenon.

On-going research studies are also conducted in the wind tunnel of the University of Auckland by Nicolas

Aubin, a IRENav's PhD student. For different apparent wind angles, the spinnaker clew sheet is adjusted around the optimal trim "on the verge of luffing", and the propulsive and side forces are measured thanks to a force balance. These experiments now carried out in a wind tunnel seem to confirm that it is the best trim for spinnakers, with the most propulsive force. However one should still be aware of the non-respect of rules of similitude in the wind tunnel. A combination of numerical studies, wind tunnel tests and full-scale experiments remains necessary to explore in more detail these complex phenomena.

Appendices

A

Photogrammetry measurements, calibration and precision

A.1 Photogrammetry principles

This appendix section describes the basics and the main theory of photogrammetry. For further information, the reader can find many books on photogrammetry and especially [Kraus and Waldhäusl, 1997] translated into many languages.

Photogrammetry consists of obtaining reliable geometric measurements by means of photographs. Historically, soon after the creation of photography, in the 1850s, stereophotogrammetry appeared. Based on the human eye principle, two planar images of a 3D object taken at different known positions make it possible to extract the third dimension, the depth.

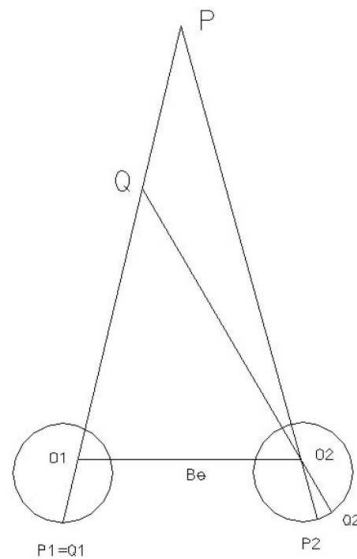


Figure A.1 – Principle of binocular vision. From [Kraus and Waldhäusl, 1997].

Figure A.1 shows that object-points P and Q in the space are at different distances from the observation points. For O1, the image points P1 and Q1 are the same, whereas for O2, the image points P2 and Q2 are distinct. By knowing precisely the distance B_e , and using optical theory, we can therefore calculate the distance between P and Q.

Nowadays, with digital cameras, a photograph can be seen as a matrix of values, and some image correlation can be processed to detect patterns in photographs and automatically recreate the 3D geometry of the object. However for a white featureless sail, this method is not appropriate.

The aerotriangulation is another photogrammetric process. For aerial cartography using tacheometry or GPS data of the plane to obtain altitude from a reference, speed, etc. and using only one orthophotograph, it is possible to determine the geometry of the landscape.

Finally the triangulation method using several object points seen by several photographs means the 3D shape of the object can be recomputed. This is the method used to acquire the flying shape of spinnakers. The perspective lines of one object-point from different photographs intersect each other at one location (cf. figure A.2). These intersecting lines are used to compute the location of an object-point in three dimensions. In order to triangulate these object-points, the camera positions and aiming angles (also called orientations) must be known. To determine the positions and orientations of photographs at least 3 object-points must be seen by 3 photographs. Once the photographs are positioned and oriented, every point seen in at least two photographs can be calculated in all three dimensions. Figure A.2 shows the principles of photogrammetry triangulation.

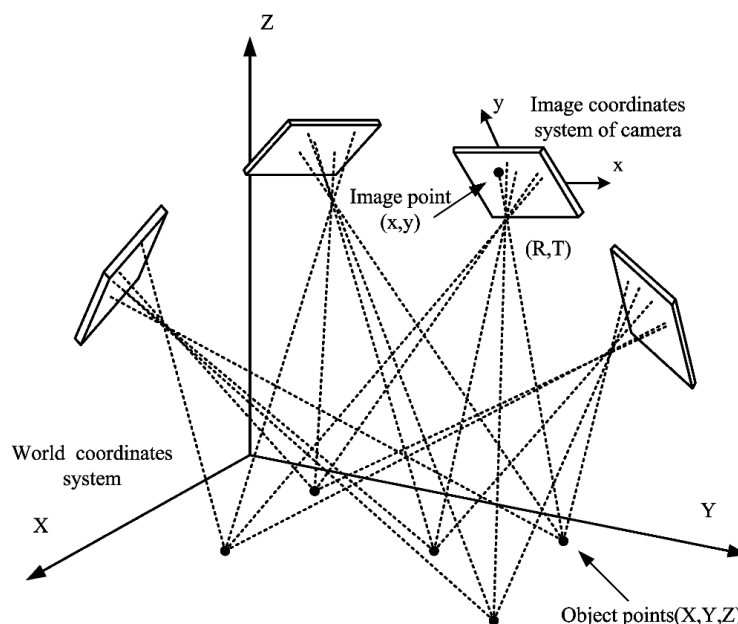


Figure A.2 – Principle of photogrammetry using triangulation. Several object-points are projected onto different image planes (photographs).

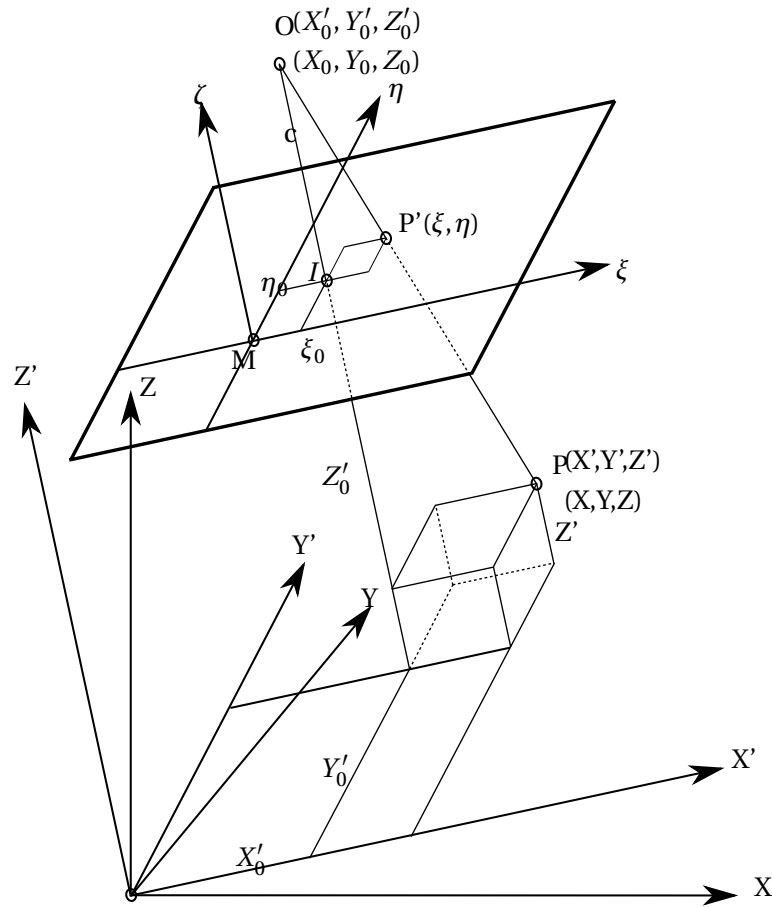


Figure A.3 – Characteristic parameters used in photogrammetry. When, camera is calibrated, a straight line (perspective ray) links the point of view O, the image point P', and the object-point P (collinearity relation). c is the focal length. The plane $(M; \{\xi, \eta\})$ is the image plane. The point (ξ_0, η_0) is the principal point of the photograph.

Figure A.3 presents the projection of an object-point P to the image plane $(M; \{\xi, \eta\})$. O is the point where the camera is located. The orthogonal axes $\{\xi, \eta, \zeta\}$ belongs to the camera. It is the image coordinate axes. $\zeta = 0$ for all the image-points and $\zeta = c$ for the centre of projection. c is the focal length. (X', Y', Z') defines the object coordinates. It belongs to the measured object. (X, Y, Z) defines the reference coordinate axes. The straight line linking the point of view O, the image-point P' and object-point P is the perspective ray. Collinearity equations can be expressed:

$$\frac{\xi - \xi_0}{c} = \frac{X' - X'_0}{Z' - Z'_0} \quad (\text{A.1})$$

$$\frac{\eta - \eta_0}{c} = \frac{Y' - Y'_0}{Z' - Z'_0} \quad (\text{A.2})$$

Equations A.1 and A.2 are expressed in the system (X', Y', Z') parallel to the system $(\{\xi, \eta, \zeta\})$. A matrix of rotation $R(\omega, \varphi, \kappa)$ is needed to express this equation in the reference system (X, Y, Z) . By writing the

matrix of rotation R :

$$R(\omega, \varphi, \kappa) = \begin{pmatrix} r_{11} & r_{12} & r_{13} \\ r_{21} & r_{22} & r_{23} \\ r_{31} & r_{32} & r_{33} \end{pmatrix} \quad (\text{A.3})$$

we have:

$$\begin{pmatrix} X - X_0 \\ Y - Y_0 \\ Z - Z_0 \end{pmatrix} = \begin{pmatrix} r_{11} & r_{12} & r_{13} \\ r_{21} & r_{22} & r_{23} \\ r_{31} & r_{32} & r_{33} \end{pmatrix} \begin{pmatrix} X' - X'_0 \\ Y' - Y'_0 \\ Z' - Z'_0 \end{pmatrix} \quad (\text{A.4})$$

With Equations A.1, A.2 and A.4, we can obtain the relation between the images points in the reference frame:

$$\xi = \xi_0 - c \frac{r_{11}(X - X_0) + r_{21}(Y - Y_0) + r_{31}(Z - Z_0)}{r_{13}(X - X_0) + r_{23}(Y - Y_0) + r_{33}(Z - Z_0)} = \xi_0 - c \frac{Z_x}{D} \quad (\text{A.5})$$

$$\eta = \eta_0 - c \frac{r_{12}(X - X_0) + r_{22}(Y - Y_0) + r_{32}(Z - Z_0)}{r_{13}(X - X_0) + r_{23}(Y - Y_0) + r_{33}(Z - Z_0)} = \eta_0 - c \frac{Z_y}{D} \quad (\text{A.6})$$

with Z_x , Z_y and D are here to simplify the equations.

A.2 Calibration

A.2.1 Main principles

Equations A.5 and A.6 are not linear. Therefore a computational method is required to determine the unknown variables.

- ξ_0, η_0 : the image-coordinates of the principal point
- c : focal length

These parameters are known thanks to camera calibration. Moreover calibration process evaluates the defects of the cameras.

Nonetheless there are six parameters that cannot be determined before the measurements.

- X_0, Y_0, Z_0 : coordinates of the position of the point of view (position of the camera)
- ω, φ, κ : rotations of the image (orientation of the camera)

To obtain those 6 parameters, several object-points must be seen by many photos. Using an optimisation algorithm, on each photo, the 3 rotations ω, φ, κ and the 3 translations X_0, Y_0, Z_0 are optimised

until the perspective rays (OP') of each object-point are intersected at a unique location as well as possible.

Figure A.3 shows the principal parameters used for photogrammetry. If the camera is calibrated the perspective ray linking O, the image-point P' and the object-point P is a straight line. The lens distortions cause an image-point on the image surface to be shifted from its true position. Therefore an important assumption is that the image surface $\{M; (\xi, \eta)\}$ is a perfectly flat plane. A compensation formula is used. For any point (x,y) on the image surface, the compensated point (xc,yc) is given by:

$$\begin{cases} xc = x + x \times dr + dp_x \\ yc = y + y \times dr + dp_y \end{cases}$$

The principal point $(\xi_0, \eta_0) = (0,0)$. dr is the radial lens distortion correction, and dp_x and dp_y the respectively x and y component of the decentering lens distortion correction.

It is assumed the radial lens distortion is radially symmetric about the principal point. The point (x,y) is at a radial distance $r = \sqrt{x^2 + y^2}$ from the principal point. It has to be compensated by a factor $dr = r \times dr$.

$$\begin{cases} xc = x(1 + dr) \\ yc = y(1 + dr) \end{cases}$$

where $dr = K1.r^2 + K2.r^4 + K3.r^6$. The software Photomodeler uses this formula called the "unbalanced form", which takes into account the "calibrated" focal length.

The decentering distortion compensation is not always used because of its much smaller contribution to the global compensation. The formulas used by Photomodeler are:

$$\begin{cases} dp_x = P1(r^2 + 2x^2) + 2.P2.x.y \\ dp_y = P2(r^2 + 2y^2) + 2.P1.x.y \end{cases}$$

To assume a flat imaging plane, these parameters (K1,K2,K3,P1,P2) but also the focal length and the position of the principal point need to be defined.

A.2.2 Calibration parameters of cameras used for measurements

Table A.1 describes the calibration parameters needed to undistort the images before applying the photogrammetric process.

	Focal length (mm)	Format size		Principal point		Lens distortion parameters				
		W	H	X	Y	K1	K2	K3	P1	P2
GP2G	3.1793	6.2994	3.5140	3.1396	1.8544	$5.426e-2$	$-3.212e-3$	$5.664e-4$	$3.018e-4$	$1.289e-4$
GP2W	3.1495	6.2922	3.5140	3.0905	1.8345	$5.156e-2$	$-2.509e-3$	$4.921e-4$	$-4.097e-4$	$-2.205e-4$
GP2Y	3.1654	6.3166	3.5248	3.1951	1.7392	$4.985e-2$	$-2.190e-3$	$4.892e-4$	$8.899e-5$	$-2.064e-4$
GP3G	2.7897	6.2486	4.6860	3.1604	2.2462	$5.523e-2$	$-1.154e-3$	$2.350e-4$	0	0
GP3W	2.7247	6.3840	3.5140	3.2738	1.7205	$5.622e-2$	$-1.148e-3$	$2.192e-4$	$-1.363e-4$	$1.860e-4$
GP3Y	2.7996	6.2482	4.6860	3.0592	2.3536	$5.553e-2$	$-1.298e-3$	$2.380e-4$	0	0

Table A.1 – Calibration parameters for each camera.

A.3 Precision of photogrammetric measurements

PhotoModeler shows several parameters to analyse the precision of the measurements. The three most important parameters are presented.

Figure A.4 displays the tightness. The tightness of a point relates to how well its defining perspective rays intersect. The better and closer they intersect in 3D space, the smaller the tightness value. For the four measurements presented the tightness is on average better than 7 mm. 75% of the points (about a 75 out of a hundred points) have a tightness better than 10 mm. Some points have higher tightness of about 32 mm. The points having high tightness values are not necessarily at the top of the mast nor really close to the camera. I think the biggest values are due to points in motion. The precision of the synchronisation is 0.04 s (1/25fps). If the synchronisation was better, there would be less difference of position between cameras of the moving points, thus a better tightness.

Figure A.5 displays the residual error. When the point has its 3D position calculated, PhotoModeler can project it back onto the photograph (using the perspective ray). The distance between this projection and its actual marked position on the photograph is calculated and gives the residual error. The RMS residual of one point is the Root-Mean-Squared of the residual of this point on all photographs where it is marked. Due to the sub-pixel coded targets used on the sail, the residual error can be less than one pixel. If all points were below 1, the project would be characterised as an "highest accuracy" project.

Figure A.6 displays the precision of all points for 4 different AWA. The precision is defined as one standard deviation based on the post-processing covariance matrix of the 3D object points. It means if the Photomodeler algorithm converges well, the confidence region on a position is small. 75% of the points have a precision better than 30 mm, while a few points have precision values 10 times larger. Still only 3% of the points have a precision value less than 100 mm.

Figure A.7 presents the precision of every point projected onto the boat frame. One can notice the few points with the worst precision are above 11 m high (near the top of the mast). The Z precision is the most affected. The angles between the perspective rays are reduced and the resolution of the furthest

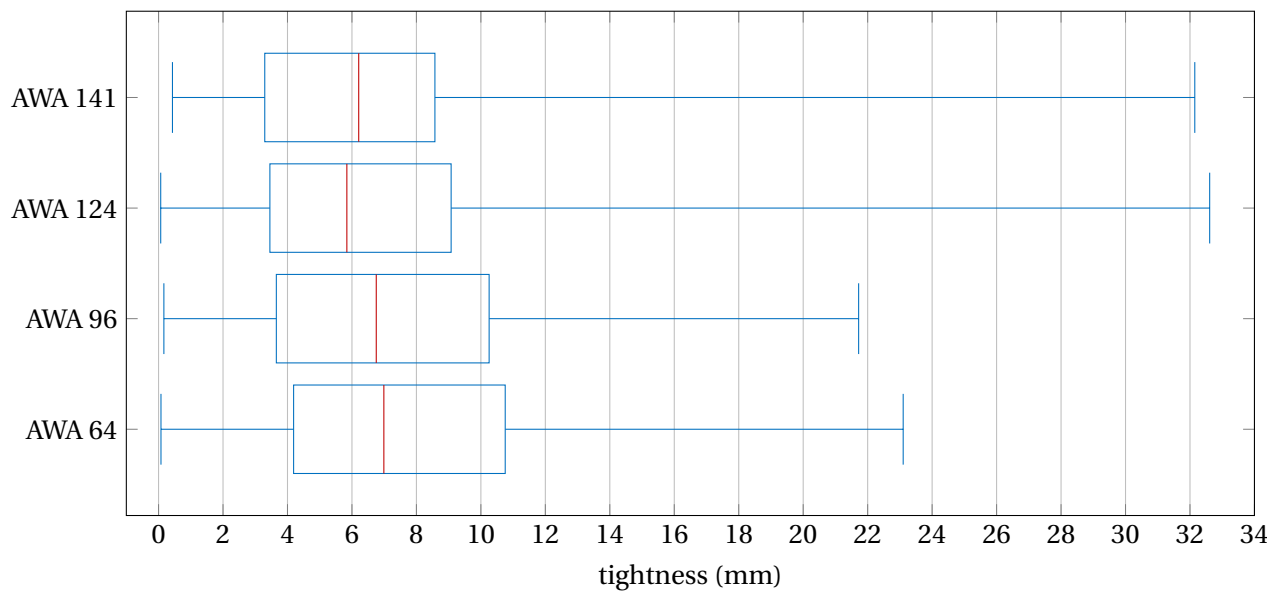


Figure A.4 – Tightness values for 4 different AWA. The lower and upper whisker indicate respectively the minimum and maximum value. The red mark represents the median, and the bottom and top of the box the first and third quartile.

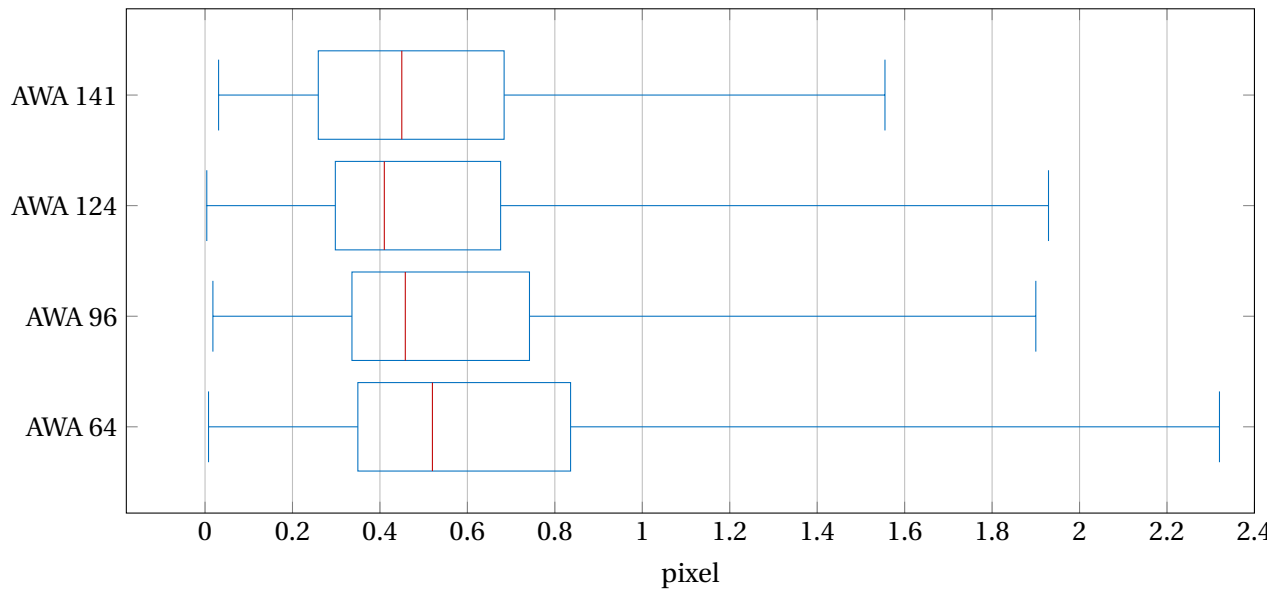


Figure A.5 – RMS values for 4 different AWA. The lower and upper whisker indicate respectively the minimum and maximum value. The red mark represents the median, and the bottom and top of the box the first and third quartile.

points is lower. A camera with a small field of view and with a specific focus could be dedicated to improve the accuracy for the highest points.

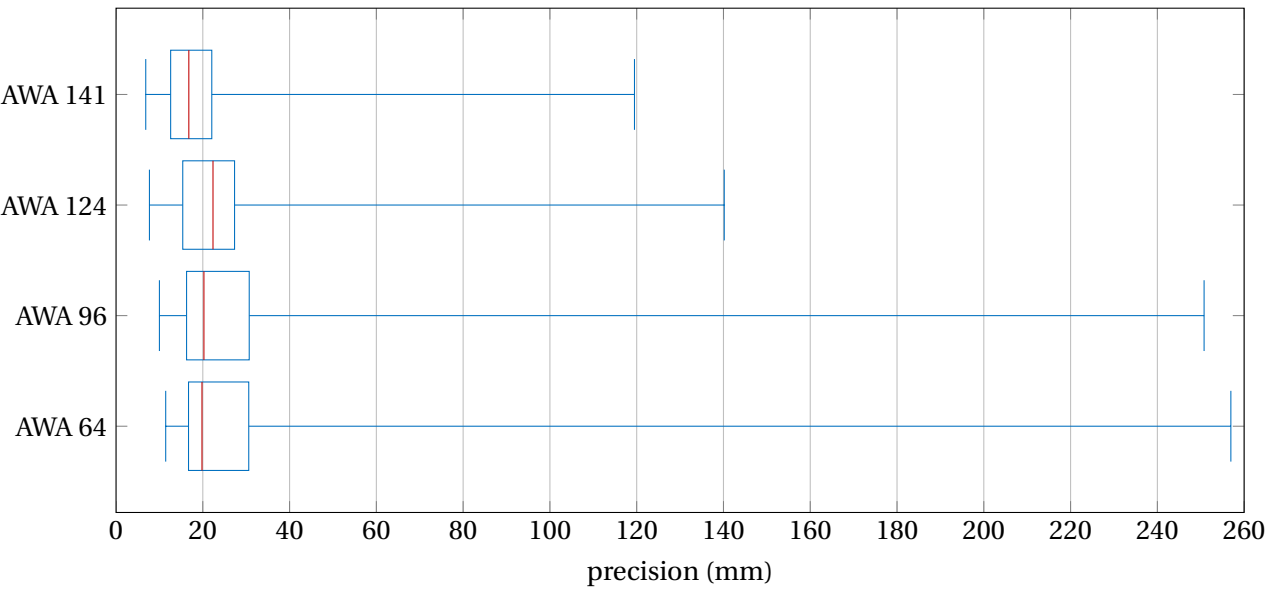


Figure A.6 – precision values for 4 different AWA. The lower and upper whisker indicate respectively the minimum and maximum value. The red mark represents the median, and the bottom and top of the box the first and third quartile.

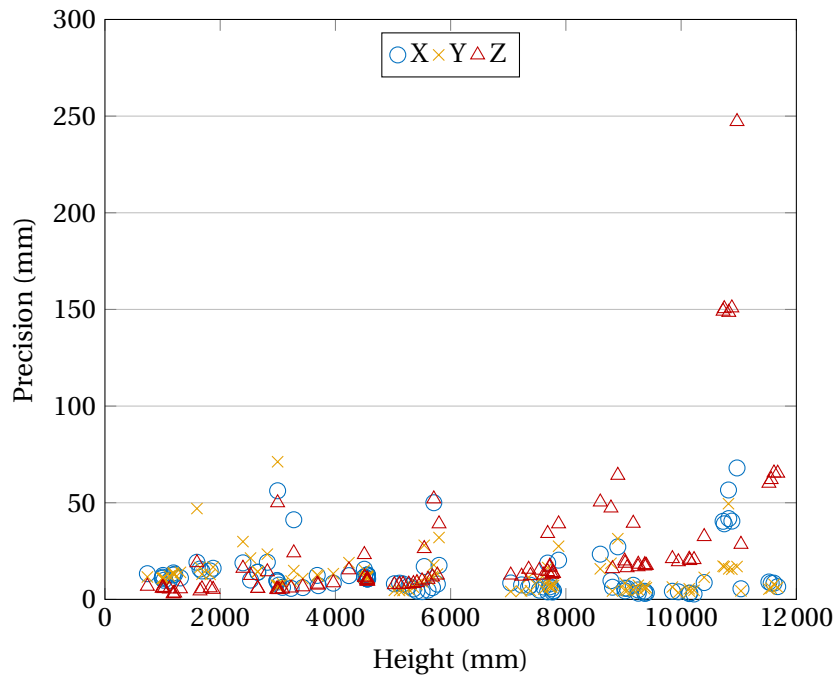


Figure A.7 – Distribution of the precision of the points according to their height for a flying shape measured at AWA 64°. The precisions are projected onto the boat frame: X means the precision in the forward direction, Y in the lateral direction and Z upwards.

B

Calibration of all load sensors

This appendix describes the accuracy obtained on the load sensors. They are presented in Table B.1 with their sensitivity and offset. Each error is briefly explained.

Sensitivity and accuracy of all load sensors

Sensitivity Se and offset S_0

The variation of load is measured by the variation of the voltage signal of the strain gauges.

$$Se = \frac{\delta u}{\delta f}$$

With u the output voltage of the strain gauge in mV/V et f the measurand which is here the load in N. The variations of both signals are proportional. Thus for each sensor, the sensitivity is measured by least mean square linear regression, the best linear regression fitting the measurement points. And the offset is measured as the the voltage signal of the strain gauge when no load is applied:

$$Se = \frac{\sum u_i \cdot f_i - n \bar{u} \bar{f}}{\sum x_i^2}$$

$$S_0 = \bar{u} - Se \bar{f}$$

Hysteresis error E_{hy}

During the calibration, the sensor is loaded increasingly then decreasingly. There is a possible shift of the output voltage between the ascending and descending stages. After determining the linear regression for both stages, the maximum difference on the measuring range MR is calculated:

$$E_{hy} = \frac{\delta u_{max}}{MR}$$

		Sensitivity mV/V/kg	Offset mV/V	Errors in % on Measuring Range			
				hysteresis	trueness	precision	Accuracy
Shackle 1	Backstay	1.564	3.6818	0.12	0.34	0.97	1.03
Shackle 2	Jib clew	1.532	0.3375	0.05	0.15	0.52	0.55
Shackle 3	Jib head	1.480	3.2355	0.08	0.14	0.53	0.56
Shackle 5	Boom vang	1.495	-2.3755	0.11	0.49	1.61	1.69
Shackle 6	mainsail head	1.622	5.3046	0.13	0.34	0.59	0.70
Shackle 7	outhaul	1.656	0.6670	0.08	0.11	0.17	0.22
Shackle 8	mainsail sheet	0.921	1.5766	0.27	0.39	0.49	0.68
Shackle 9	jib tack	1.746	8.0572	0.31	0.40	1.03	1.15
Shackle 9	spinnaker tack	1.391	204.46	0.13	0.24	0.27	0.46
Shackle 10	spinnaker clew	1.392	206.09	0.20	0.29	1.03	1.09
Shackle 11	spinnaker head	1.416	198.61	0.19	0.37	0.50	0.73
Turnbuckle 1	V1 SB	1.739	-0.7688	0.08	0.19	0.17	0.31
Turnbuckle 2	D1 SB	1.771	-0.6797	0.00	0.08	0.14	0.16
Turnbuckle 3	forestay	1.788	-0.0284	0.05	0.11	0.19	0.22
Turnbuckle 4	D1 PS	1.763	0.4052	0.05	0.10	0.10	0.19
Turnbuckle 5	V1 PS	1.848	0.3691	0.07	0.13	0.09	0.26
Turnbuckle 6	V2 PS	1.739	0.1292	0.05	0.11	0.44	0.46
Turnbuckle 7	V2 SB	1.670	0.1719	0.05	0.10	0.09	0.18
DLC 6	Head	36.94	9477.8	0.04	0.23	0.34	0.40
DLC 7	Tack	36.87	10365.9	0.05	0.24	1.60	1.62
DLC 8	Clew	34.47	10583.2	0.12	0.20	1.47	1.49

Table B.1 – Calibration errors for load sensors. Shackle 9, 10 and 11 are used wirelessly on the spinnaker. The measuring range for the shackles and the DLCs is 0-5000 N and 0-10 000 N for the turnbuckles and the shackle 8.

Precision error E_{pr}

The precision is the ability of the sensor to give measures without too much dispersion for similar measurand, the quantity intended to be measured. A bad precision might come from a noisy signal, or weak connections. To measure the precision error, a sufficient number of measured values is required, respecting the following equation:

$$E_{fi} > \frac{\sigma_{max}}{\sqrt{N_{ech}}}$$

with σ_{max} the maximum standard deviation on all measures and N_{ech} the amount of measurement points.

If this assumption is true, the fidelity error is taken as the value of two standard deviations. For a normal distribution, 96% of the values are taken in $[-2\sigma_{max}; 2\sigma_{max}]$.

$$E_{pr} = \pm \frac{2\sigma_{max}}{MR}$$

The precision error is calculated separately for the values of the ascending and descending stage. The hysteresis error takes already into account the difference of value between the ascending and descending stage. Measuring the precision error on all values would mix both errors. The maximum value is used to define the precision error.

Linearity error E_{lr}

The trueness or linearity error is defined as the difference δu between the output voltage and the theoretical linear regression given by the sensitivity. If a sensor has a good trueness, the output values given by the sensor are close to the theoretical one. The linearity of the sensor is well respected.

$$E_{li} = \pm \frac{\delta u}{MR}$$

For the same reasons as for the precision error, the linearity error is calculated separately for the ascending and descending stage. The maximum value is used to define the linearity error.

Accuracy

Finally a good accuracy of a sensor is the combination of a good linearity and precision associated with a low hysteresis effect. If we suppose these 3 errors independent to each other, then the accuracy error is the square root of the sum of the squared errors:

$$E_{acc_Ind} = \sqrt{E_{li}^2 + E_{hy}^2 + E_{fi}^2}$$

If the errors are dependent on each other, the accuracy error is estimated by two times the maximum standard deviation calculated for all measurands.

$$E_{acc_De} = \pm \frac{2\sigma_{maxAll}}{MR}$$

The accuracy error is the maximum of both values:

$$E_{accuracy} = \max(E_{acc_Ind}, E_{acc_De})$$

C

Quaternions and projection of loads onto boat frame

In this appendix, the main principles of the quaternion representation are explained. For further details, there are many lectures and books on this topic, mostly in robotics [Craig, 1989, Kuipers, 1999, Leroyer, 2004, Shankar and Harmon, 2005, Diebel, 2006].

In this PhD, quaternions are used to represent the boat attitude and to project the loads measured by the DLCs onto the boat frame. The quaternion representation permit easier calculations without any special cases like the gimbal lock. With the Euler angle representation, an orientation pointing upwards for example can be defined by only 2 Euler angles, thus losing a degree of freedom. Mathematically, a singularity is reached which needs a specific case in the algorithm. The quaternion representation also prevents typical errors in the calculation of the projection of a vector onto another frame.

C.1 Main principles of quaternion representation

C.1.1 Definition

Similar to complex numbers to represent a vector in a plane, quaternions can represent a vector in space over reals. However while complex numbers need only 2 real elements, quaternions need 4. They can be used to represent the orientation of a rigid body or a coordinate frame in a three-dimensional space. A quaternion \mathbf{q} can be written in different forms:

$$\mathbf{q} = q_0 + q_1 i + q_2 j + q_3 k$$

$$\mathbf{q} = [q_0, q_1, q_2, q_3]^T$$

$$\mathbf{q} = \begin{bmatrix} q_0 \\ q_{1:3} \end{bmatrix}$$

$$\mathbf{q} = q_0 + \hat{q}$$

where q_0 is the *scalar part* and \mathbf{q} is the *vector part*, and with $\mathbf{q} \in \mathbb{H}$ and $(q_0, q_1, q_2, q_3) \in \mathbb{R}$. There are six important axioms:

$$\begin{aligned} i^2 &= j^2 = k^2 = -1 \\ ij &= k \\ jk &= i \\ ki &= j \end{aligned}$$

C.1.2 Quaternion product

We can write a quaternion product in several ways:

$$\begin{aligned} \mathbf{pq} &= (p_0 + \hat{p})(q_0 + \hat{q}) \\ &= (p_0 q_0 + p_0 \hat{q} + q_0 \hat{p} + \hat{p} \hat{q}) \\ \mathbf{pq} &= (p_0 + p_1 i + p_2 j + p_3 k)(q_0 + q_1 i + q_2 j + q_3 k) \\ &= (p_0 q_0 - p_1 q_1 - p_2 q_2 - p_3 q_3) + \dots i + \dots j + \dots k \end{aligned}$$

C.1.3 Quaternion conjugate

The quaternion conjugate is defined as:

$$\mathbf{q}^* = q_0 - q_1 i - q_2 j - q_3 k$$

One can remark that:

$$\mathbf{qq}^* = q_0^2 + q_1^2 + q_2^2 + q_3^2$$

Therefore the norm of the quaternion is:

$$|\mathbf{q}| = \sqrt{\mathbf{qq}^*} = \sqrt{q_0^2 + q_1^2 + q_2^2 + q_3^2}$$

C.1.4 Quaternion inverse

Every quaternion other than the additive identity 0 has an inverse:

$$\mathbf{q}^{-1} = \frac{\mathbf{q}^*}{|\mathbf{q}|^2}$$

From a mathematical point of view, that means quaternions are a linear algebra and a field.

C.1.5 Rotation using unit quaternions

The motion of the boat relative to different frames can be expressed by rotations. Let \mathbf{q} be a unit quaternion, i.e. $|\mathbf{q}| = 1$. It can be expressed as

$$\mathbf{q} = \cos \frac{\theta}{2} + \sin \frac{\theta}{2} \hat{n}$$

If \hat{x}' is the vector \hat{x} rotated by an angle θ , then let define \mathbf{x} as a quaternion:

$$\mathbf{x} = 0 + \hat{x}$$

Therefore $\mathbf{x}' = \mathbf{q}\mathbf{x}\mathbf{q}^*$, and $\hat{x}' = \text{rot}(\theta, \hat{n})\hat{x}$.

Similarly, multiple successive rotations can easily be applied. For example with two rotations defined by p and q .

$$\mathbf{q}(\mathbf{p}\mathbf{x}\mathbf{p}^*)\mathbf{q}^* = (\mathbf{q}\mathbf{p})\mathbf{x}(\mathbf{q}\mathbf{p})^*$$

Unit quaternions have 4 interesting properties:

- Unit quaternions live on the unit sphere in \mathbb{R}^4 .
- Quaternions \mathbf{q} and $-\mathbf{q}$ represent the same rotation.
- Inverse of rotation \mathbf{q} is the conjugate \mathbf{q}^* .
- Null rotation, the identity, is the quaternion $\mathbf{1}$.

C.2 Conversion of quaternions to other representations

C.2.1 From axis-angle to quaternion

$$\mathbf{q} = \cos \frac{\theta}{2} + \sin \frac{\theta}{2} \hat{n}$$

C.2.2 From quaternion to axis-angle

$$\theta = 2 \tan^{-1}(|\hat{q}|, q_0)$$

$$\hat{n} = \hat{q}/|\hat{q}|$$

assuming θ is nonzero.

C.2.3 From quaternion to rotation matrix

$$\begin{aligned} \mathbf{q}\mathbf{x}\mathbf{q}^* &= \begin{pmatrix} q_0^2 + q_1^2 - q_2^2 - q_3^2 & 2(q_1 q_2 - q_0 q_3) & 2(q_1 q_3 + q_0 q_2) \\ 2(q_1 q_2 + q_0 q_3) & q_0^2 - q_1^2 + q_2^2 - q_3^2 & 2(q_2 q_3 - q_0 q_1) \\ 2(q_1 q_3 - q_0 q_2) & 2(q_2 q_3 + q_0 q_1) & q_0^2 - q_1^2 - q_2^2 + q_3^2 \end{pmatrix} \hat{x} \\ &= R\hat{x} = (r_{ij})\hat{x} \end{aligned}$$

C.2.4 From rotation matrix to quaternion

$$q_0^2 = \frac{1}{4}(1 + r_{11} + r_{22} + r_{33})$$

$$q_1^2 = \frac{1}{4}(1 + r_{11} - r_{22} - r_{33})$$

$$q_2^2 = \frac{1}{4}(1 - r_{11} + r_{22} - r_{33})$$

$$q_3^2 = \frac{1}{4}(1 - r_{11} - r_{22} + r_{33})$$

or also:

$$q_0 q_1 = \frac{1}{4}(r_{32} - r_{23})$$

$$q_0 q_2 = \frac{1}{4}(r_{13} - r_{31})$$

$$q_0 q_3 = \frac{1}{4}(r_{21} - r_{12})$$

$$q_1 q_2 = \frac{1}{4}(r_{12} + r_{21})$$

$$q_1 q_3 = \frac{1}{4}(r_{13} + r_{31})$$

$$q_2 q_3 = \frac{1}{4}(r_{23} + r_{32})$$

C.2.5 From Euler angles to quaternion and vice versa

There are many ways to define Euler angles. 12 combinations of three rotations of Euler angles lead to the same 3D rotation. [Diebel, 2006] presents and summarises all the conversions between Euler angles, rotation matrix, axis-angle and quaternion.

C.3 Use of quaternions to represent the load vector onto the boat frame

C.3.1 Quaternion representation for the representation of one frame to another

Figure C.1 presents 2 frames A and B with their respective orthogonal unit vectors $\hat{x}_A, \hat{y}_A, \hat{z}_A$ and $\hat{x}_B, \hat{y}_B, \hat{z}_B$. The quaternion ${}^A_B\mathbf{q}$ describes the orientation of frame B relative to frame A. This notation is adopted from [Craig, 1989] to indicate the relative frames of orientations and vectors.

The arbitrary orientation of frame B relative to frame A can be also achieved through a rotation of angle θ around an axis ${}^A\hat{r}$ defined in frame A by the components of the unit vector r_x, r_y and r_z .

Therefore from the previous section, the unit quaternion ${}^A_B\mathbf{q}$ is also defined as:

$${}^A_B\mathbf{q} = [q_0, q_1, q_2, q_3]^T = [\cos \frac{\theta}{2}, r_x \sin \frac{\theta}{2}, r_y \sin \frac{\theta}{2}, r_z \sin \frac{\theta}{2}]^T$$

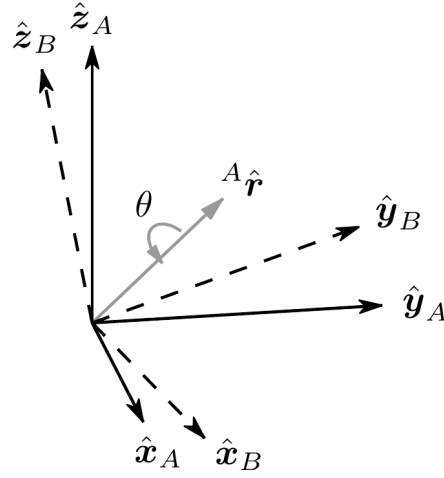


Figure C.1 – Figure 1: The orientation of frame B relative to frame A can be defined as a rotation of angle θ around the axis ${}^A\hat{r}$. From [Madgwick et al., 2011].

The conjugate of this quaternion is therefore the quaternion describing the orientation of frame A relative to frame B:

$${}^A_B\mathbf{q}^* = {}^B_A\mathbf{q} = [q_0, -q_1, -q_2, -q_3]^T$$

The quaternion product of ${}^A_B\mathbf{q}$ and ${}^B_C\mathbf{q}$ is then the quaternion describing the orientation of frame C relative to frame A:

$${}^A_C\mathbf{q} = {}^B_C\mathbf{q} \otimes {}^A_B\mathbf{q}$$

C.3.2 Projection of the load vector onto the boat frame

An IMU measures the gravity and the magnetic field -defining the Earth frame- in the sensor frame. Thus an IMU measures the earth frame E relative to the load frame L for a DLC or the boat frame B for the *Base Unit*. The corresponding quaternion for the DLC is defined as follows:

$${}^L_E\mathbf{q}$$

and for the *Base Unit*:

$${}^B_E\mathbf{q}$$

And we want the load frame relative to the boat frame:

$$\begin{aligned} {}^B_L\mathbf{q} &= {}^E_L\mathbf{q} \otimes {}^B_E\mathbf{q} \\ &= {}^L_E\mathbf{q}^* \otimes {}^B_E\mathbf{q} \end{aligned} \tag{C.1}$$

The force direction is along the X axis of the load frame:

$${}^D\mathbf{v} = \begin{bmatrix} 0 \\ 1 \\ 0 \\ 0 \end{bmatrix}$$

The force projected onto the boat frame ${}^B\mathbf{v}$ is finally:

$${}^B\mathbf{v} = {}^L_E\mathbf{q}^* \otimes {}^D\mathbf{v} \otimes {}^L_E\mathbf{q}$$

D

Resampling for dynamic studies

D.1 Context and reasons for resampling

In this PhD, sensors communicate "on the flow" and not on a "slave-master" configuration. It means as soon as a sensor acquires a new measure, the value is transmitted to the data acquisition system. The data acquisition system instantaneously timestamps the received value. This type of communication permits a precise timestamp when using various sensors because no buffer, a memory which stores temporarily the data, can delay the timestamping. Therefore as soon as a value is measured, it is timestamped and stored. The sensors have different sampling rates varying from 1 Hz to 100 Hz. To study closely the dynamic effects on a sail boat, a resample is therefore required in order to have a unique time vector for all sensors. But before resampling, every sensor must be interpolated. Since the sensors communicate "on the flow", the values are not necessarily uniformly distributed over time. The given sampling rate is only an average rate. The difference between the delta time between two measured values and the theoretical delta time -from the average sampling rate- is calculated. For sensors having an averaged sampling rate between 10 Hz ($\Delta t = 0.1$ s) and 25 Hz ($\Delta t = 0.04$ s), we calculate the standard deviation of this difference. It is found between 0.005 s and 0.01 s. Due to this non-neglected deviation, some dynamics of the system might be missed with the resampling process even if the Nyquist-Shannon condition is respected.

D.2 Study on a simple case

D.2.1 Presentation of the simple case

A simple case is presented to better assess the importance of the resampling for non uniform samples. The theoretical signal studied is a sinusoidal signal composed of two frequencies (2 Hz and 10 Hz) with amplitudes respectively of 0.7 and 1:

$$s(t) = 0.7 \sin(2\pi 2 t) + \sin(2\pi 10 t)$$

To be closer to reality, some noise is added to the recorded signal. A fictitious recorded signal is then created with an average sampling rate of 25 Hz. The Nyquist-Shannon condition is therefore respected.

This sample is nonetheless irregular with a Gaussian distribution with a standard deviation of 0.1 s as found for the sensors. Figure D.1 presents the theoretical signal and the fictitious recorded signal. One can notice the non-uniformity of the sample leads to the miss of some peaks of the signal.

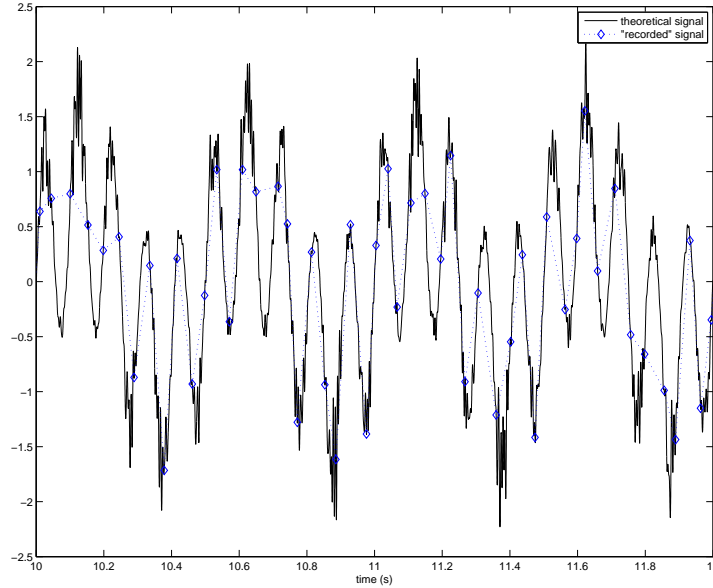


Figure D.1 – Theoretical signal (in black) with two frequencies (2 and 10 Hz) and the fictitious recorded signal (in blue).

D.2.2 Basic oversampling methods

This signal is now oversampled for example up to 100 Hz. Two classical over-sampling methods are used:

1. A *linear interpolation* is done between the measured values.
2. The *zero padding*. Adding zero frequencies at the ends of the sampled spectra creates an oversampled signal after a Fourier inversion. However the zeropadding method can only be applied on a uniform sample. So first a linear interpolation at the averaged frequency rate of the "sensor" (25 Hz) is applied. Then we apply the zeropadding method.

Figure D.2 shows that the linear interpolation lacks some extrema. The zeropadding method retrieves the amplitude of the real signal well, however a phase shift appears between the theoretical signal and the reconstructed signal. If we want to look closely into the dynamics of the sail boat using a fast-fourier transform (fft) or a power-spectral density (psd), or also analysing small phase shifts between signals, using these types of interpolation might lead to wrong interpretations.

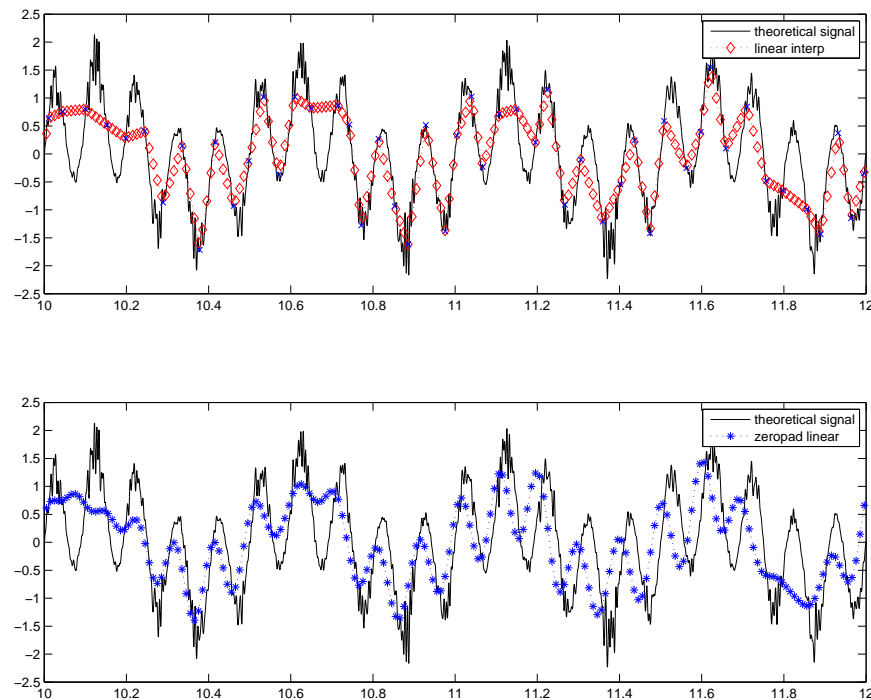


Figure D.2 – Linear interpolation from the "measured" signal (top), and using a zeropadding oversampling method (bottom).

D.2.3 Non-uniform oversampling methods

This poor interpolation is due to the non-uniformity of the sample. Certain methods exist that deal with non-uniform samples [Feichtinger et al., 1995, Chauvet et al., 2009]. Strohmer explains simply the main principles on his website¹. Figure D.3 shows a signal, and its Fourier transform. Below there is the irregular sampled version of this signal. Taking the unknown samples as zeroes, the Fourier transform of the sampled signal is calculated. It highlights that if a window is applied on this Fourier transform to recover the signal, it will not give a correct reconstruction of the first signal, unlike uniform sampled signals.

The idea is to use the difference between the original signal and the reconstructed signal. Knowing the positions of the sampled points, the reconstructed signal can be readjusted and by iteration, the algorithm converges to the original signal.

There are various approaches to reconstruct the signal between the known sampled points. Instead of taking the unknown samples as zeroes, a Voronoi-step function or an adaptive-weight function can be applied.

The tested irregular sampling methods using different approaches result in the same signal pre-

¹<https://www.math.ucdavis.edu/strohmer/research/sampling/irsampl.html>

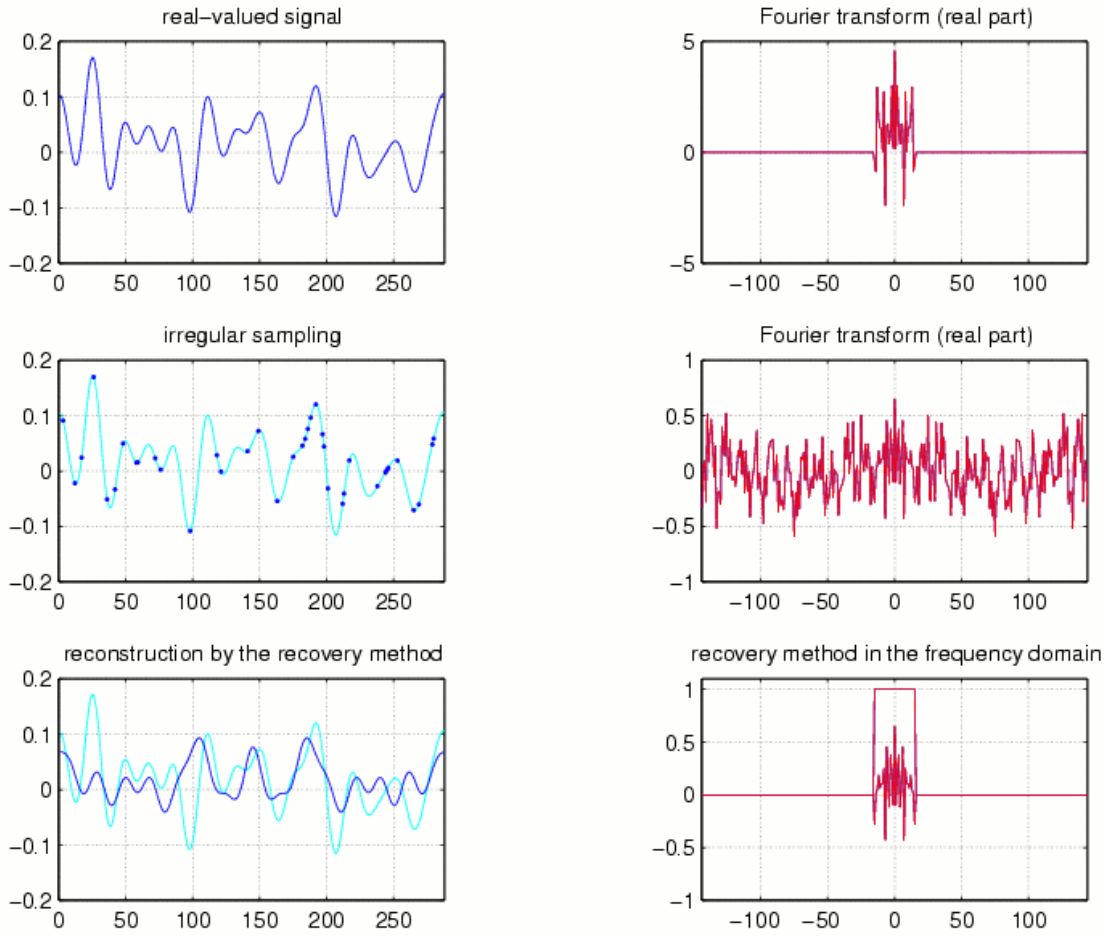


Figure D.3 – A signal with an irregular sampling and its corresponding Fourier transform. From <https://www.math.ucdavis.edu/~strohmer>.

sented in Figure D.4. The most simple (with the unknown values as zeroes) is presented in Figure D.4. It is called the Marvasti method. It clearly shows that both the amplitudes and the oscillations are correctly found despite the restrictive irregular samples. Between 10 s and 10.2 s, the amplitudes and the oscillations are not correct but the known samples miss all the extrema.

D.2.4 Conclusions

Finally these irregular sampling methods can retrieve most of the dynamics of a sensor, and are appropriate for precise dynamic analysis. However the computation time is much higher. For example for a 5 minute recording experiment, the linear interpolation is almost instantaneous while these more complex methods need between 10 and 20 minutes for each signal! Moreover it can happen that the algorithm fails to converge.

In this thesis, the dynamic phenomena presented were slow enough compared to the sample rates of the sensors. This simple case with this sinusoidal signal is too "extreme" compared with the data we analysed

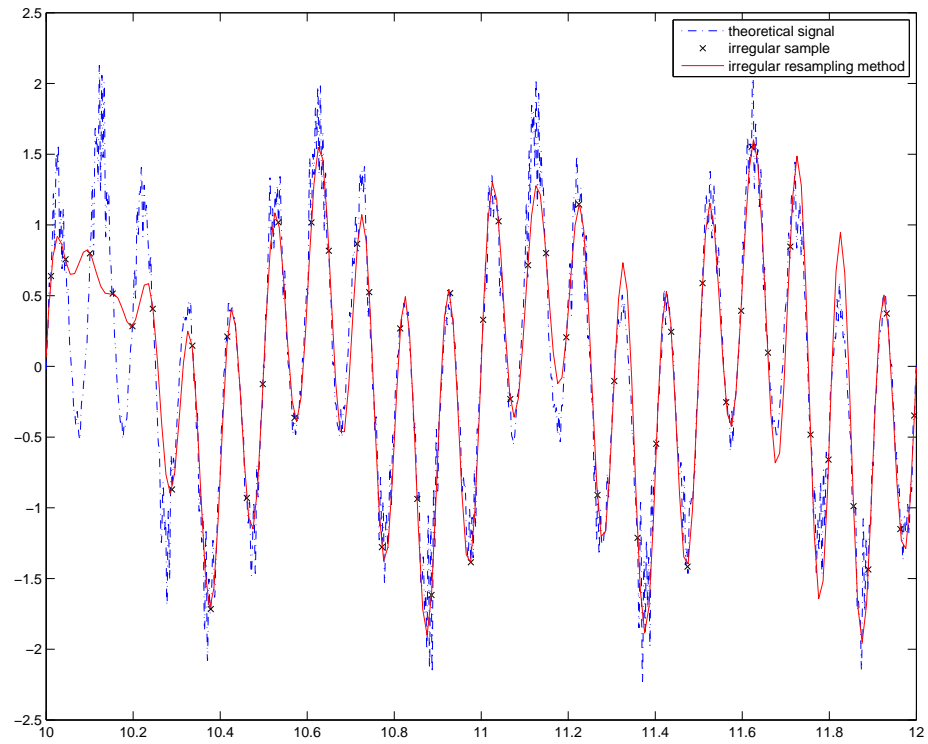


Figure D.4 – Oversampling of the simple signal using irregular sampling method.

and the dynamics we studied. In this thesis, all the data presented are set with a unique time vector from linear interpolations.

E.1 Introduction

Les performances obtenues par les voiliers de course récents démontrent que le design, les matériaux et les procédés de fabrication utilisés en architecture navale ont énormément évolué. Les architectes navals et maîtres voiliers utilisaient principalement leur expérience pour améliorer leurs designs. Ils utilisent maintenant des matériaux de haute technologie et des outils de recherche et développement avancés. Pour pouvoir réaliser des voiliers de course toujours aussi compétitifs, des études de plus en plus pointues permettent de réduire les marges de sécurité, rendant l'étude de la fiabilité des navires de plus en plus importante. La détermination des efforts dynamiques est donc maintenant un cas dimensionnant pour obtenir des voiliers encore plus puissants et légers.

Les voiliers de course au large (IMOCA Open 60, Mini 6.50 ou class 40) naviguent très souvent au portant et au travers où les vitesses maximales des bateaux sont atteintes. En régate, des voiles de portant efficaces permettent d'augmenter la différence de vitesse face aux autres compétiteurs. Pour les courses en solitaire, cette importance est accrue car les voiles de portant doivent être "stables" et ne pas être réglées en continu.

La plupart des sujets de recherche dans le domaine de la voile ont été effectués pour des navigations au près, et peu au portant. Les forces dynamiques réelles sur un voilier et les formes de voile de portant en navigation sont mal connues.

Pour mieux connaître les performances générales des voiles de portant, des essais en soufflerie sont souvent réalisés. Cependant, à cause de certaines règles de similitude non respectées, il est difficile d'étudier l'attitude dynamique de ces voiles en soufflerie. Ces données ont besoin d'être comparées avec des données *in situ* à taille réelle.

Pour des navigations au près, les voiles utilisées ont un angle d'incidence faible ainsi qu'une faible courbure. L'écoulement du vent sur les voiles de près est principalement attaché et peut être modélisé numériquement par un modèle de type "fluide parfait". Pour des résultats plus précis, les modèles numériques RANS sont de plus en plus utilisés par les concepteurs de voile et les équipes de course

pendant des phases de développement.

Les voiles de portant et de largue sont plus complexes à étudier. La forme de voile est une surface non développable avec des sections fortement cambrées. L'écoulement est largement détaché et tridimensionnel. Les modèles "fluide parfait" ne sont pas appropriés. L'écoulement du vent autour d'un gennaker ou d'un spinnaker est difficilement modélisé correctement par des simulations RANS. Des codes "LES" (Large Eddy Simulation) commencent à être utilisés mais demandent encore beaucoup de temps de calcul.

De plus les gennakers et spinnakers sont des structures fines, souples et légères. Une membrane souple avec un détachement important de l'écoulement turbulent implique une interaction fluide-structure fortement couplée et instationnaire.

Des modèles numériques instationnaires ont été développés par exemple par K-epsilon, une société spécialisée dans les calculs CFD aéro et hydrodynamiques, et l'École Centrale de Nantes. Pour analyser les performances aérodynamiques instationnaires d'un voilier, ces simulations numériques modélisent l'aéroélasticité des voiles et du gréement dans des conditions de navigation dynamiques. Un outil numérique, ARAVANTI, dédié plus particulièrement aux voiles de près, utilisant un modèle "fluide parfait" est maintenant intégré dans le logiciel de conception de voile SailPack développé par BSG Developments. Cependant pour les voiles de portant, le code ARA-ISIS couplant un code éléments finis ARA avec un solveur URANS ISIS-CFD a toujours besoin d'être validé.

L'Institut de Recherche de l'École Navale (IRENav) a les compétences académiques en Interaction Fluide-Structure et notamment sur surfaces souples comme les voiles de bateaux. De précédentes études et notamment la thèse de Benoît Augier [Augier, 2012] ont contribué au développement d'une instrumentation embarquée à bord d'un voilier dans le but de mesurer les efforts aérodynamiques instationnaires, les attitudes du voilier, la forme des voiles et les données de navigation au près. Avec le projet *Voil'ENav*, l'IRENav possède l'un des voiliers instrumentés les plus aboutis pour étudier les phénomènes physiques dynamiques appliqués aux voiles.

Le premier objectif de cette thèse est de développer ce voilier instrumenté pour des essais à taille réelle au portant. Nous voulons mesurer en conditions réelles et résolus dans le temps la forme du spinnaker en navigation, les efforts aérodynamiques des voiles et dans le gréement, les attitudes du voilier ainsi que les données du vent. Ce système d'instrumentation embarqué a été amélioré en partie grâce au projet SAILING FLUIDS, un projet entre les Universités d'Edimbourg et de Newcastle, l'École Navale et l'Université d'Auckland financé par le septième programme-cadre de la Communauté européenne pour des activités de recherche, de développement technologique et de démonstration. Des capteurs d'effort et un système d'acquisition de pression spécifiques pour le spinnaker ont ainsi pu être ajoutés. Des expériences *in situ* ont été menées conjointement à l'École Navale dans la rade de Brest et à l'Université d'Auckland dans le Golfe de Hauraki.

Le second objectif de cette thèse porte sur l'acquisition de mesures *in situ* au près et au portant. Ces données résolues en temps permettraient ainsi de mieux comprendre les phénomènes physiques sur les voiles et de construire une base de données pour des comparaisons numérique-expérimentales.

Le troisième objectif est d'acquérir puis d'analyser l'évolution de la forme du spinnaker en navigation, appelée *flying shape*, pour différents types de navigation au portant. Ces formes pourront être comparées avec la forme définie lors de la phase de conception, appelée *design shape*, et ainsi être capable de donner un retour aux concepteurs de voile.

Le quatrième objectif est d'analyser plus précisément le réglage optimal pour un spinnaker, qui est à la limite du faseyement lorsque le bord d'attaque commence à se replier. Il s'agit d'une instabilité dynamique connue par les marins mais peu étudiée et jamais analysée.

Le premier chapitre introduit les termes spécifiques utilisés dans cette thèse et les bases de la physique du voilier. L'aérodynamique sur les voiles est ensuite expliquée et je montre la complexité du problème fluide 3D présent pour les voiles de portant. L'interaction fluide-structure sur ces voiles est aussi expliquée. Enfin l'état de l'art des expériences dans la recherche liée à la voile sera décrit.

Le second chapitre présente le voilier instrumenté. Après avoir décrit le système d'instrumentation embarqué dans son ensemble, chaque système d'acquisition est alors détaillé avec une attention particulière sur la détermination de la précision et de la dynamique du capteur. L'acquisition en elle-même, le traitement des données et la sélection de périodes dites stables sont décrits à la fin de ce chapitre.

Le troisième chapitre présente l'évolution générale du spinnaker à partir de nos mesures *in situ*. La forme de voile en navigation est analysée et de nouvelles représentations de la forme sont présentées comme les surfaces de Bézier triangulaires. Les évolutions des efforts et des pressions sont décrites principalement en fonction de l'angle de vent apparent. Les grandes variations d'effort et de pression même lors des périodes stables sont également discutées.

Le quatrième et dernier chapitre décrit en détail le comportement dynamique propre aux voiles de portant. Des mesures *in situ*, le phénomène de faseyement est analysé à l'aide d'une décomposition modale. Enfin une interprétation physique de ce phénomène est proposé.

E.2 État de l'art

E.2.1 Vent apparent

Le vent rencontré par les voiles n'est pas le vent réel (TW) comme celui mesuré à une station météo mais la combinaison vectorielle entre ce vent et le vent créé par la vitesse du bateau (BS):

$$\overrightarrow{AW} = \overrightarrow{TW} - \overrightarrow{BS} \quad (E.1)$$

La figure E.1 montre ainsi le triangle de vent pour différents vents réels. Figure E.1-(a) présente le triangle de vent pour une navigation au près et figure E.1-(b) et (c) pour une navigation au portant. Le

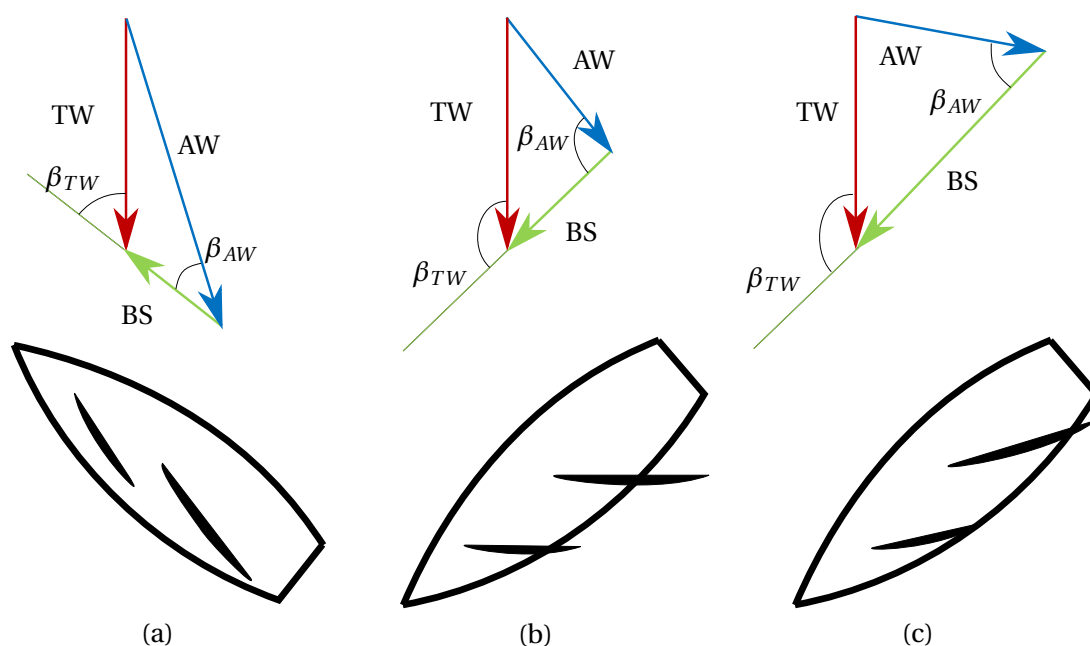


Figure E.1 – Triangles de vitesses pour différentes configurations. (a) au près (b) au portant (c) au portant avec un bateau plus rapide. TW: True wind, vent réel. AW: Apparent wind, vent apparent. BS: Boat Speed, vitesse du bateau.

bateau en situation (c) va plus vite qu'en situation (b) pour un même angle de vent réel. Le vent apparent résultant a ainsi un angle plus faible avec l'axe du bateau et est plus élevé en module.

Le vent apparent évolue en fonction de la hauteur de la voile, car le vent réel est gouverné par la couche limite atmosphérique créant un gradient de vitesse. Le vent apparent est donc vrillé en fonction de la hauteur (cf. figure E.2).

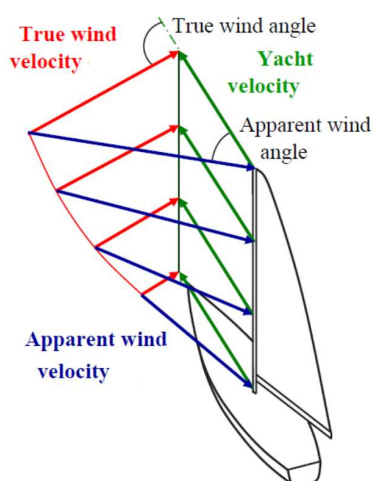


Figure E.2 – Gradient vertical de vitesse et vrillage du vent pour le vent apparent sur un voilier. [Hansen, 2006].

E.2.2 L'aérodynamique autour d'une voile de portant



(a) J/80s navigant au près pendant le GPEN 2015. Credit Pierrick Contin.



(b) J/80s navigant au portant pendant le GPEN.

Figure E.3 – Voiliers J/80 navigant au près avec un génois, et au portant avec un spinnaker asymétrique pendant le *Grand Prix de l'Ecole Navale (GPEN)*.

Pour obtenir la composante la plus propulsive, contrairement aux voiles de près cherchant à optimiser la finesse (le rapport entre la portance et la trainée), les voiles de portant, comme le spinnaker, ont une forme tri-dimensionnelle avec de fortes courbures et un grand guindant (cf. figure E.3b) et non 2D extrudée comme les voiles de près (cf. figure E.3a). Cette forme complexe indique que l'écoulement autour du spinnaker est fortement 3D et détaché.

[Viola et al., 2014] a modélisé à l'aide d'une simulation *Detached Eddy Simulation* un spinnaker asymétrique ayant la forme fixe et rigide mesurée en soufflerie. La figure E.4a extraite de son article décrit de manière schématique la répartition de pression sur un profil 2D qu'il y aurait sur un spinnaker. Un pic de dépression est ainsi repéré au bord d'attaque dû selon lui à un tourbillon de bord d'attaque créé par un détachement puis recollement de l'écoulement. Ce tourbillon de bord d'attaque stationnaire s'accroît de la bordure jusqu'en tête du spinnaker où il se transforme en vortex en bout de voile. Ce vortex est ainsi convecté dans le sens de l'écoulement comme le montre la figure E.4c.

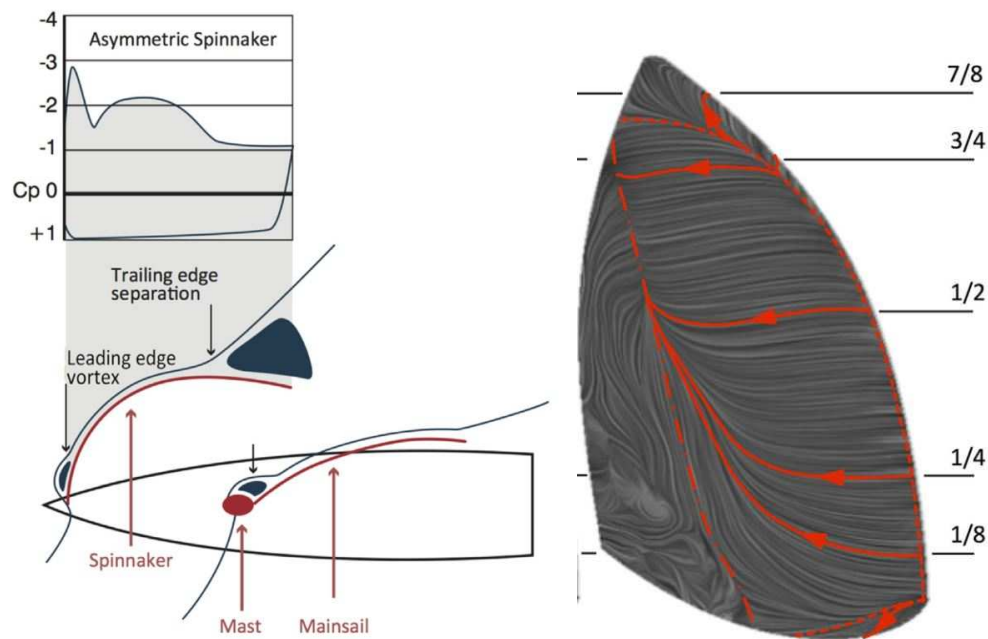
Après le recollement de l'écoulement, un deuxième pic de dépression apparaît dû à la forte courbure de la voile. Puis à 60% de la voile environ, l'écoulement est détaché (cf. figure E.4b).

Cette description est 2D, mais l'écoulement est tri-dimensionnel comme le montre les figures E.4b et E.4c, avec un décollement au bas de la voile, et un écoulement attaché remontant vers le haut de la voile.

E.2.3 L'interaction fluide-structure

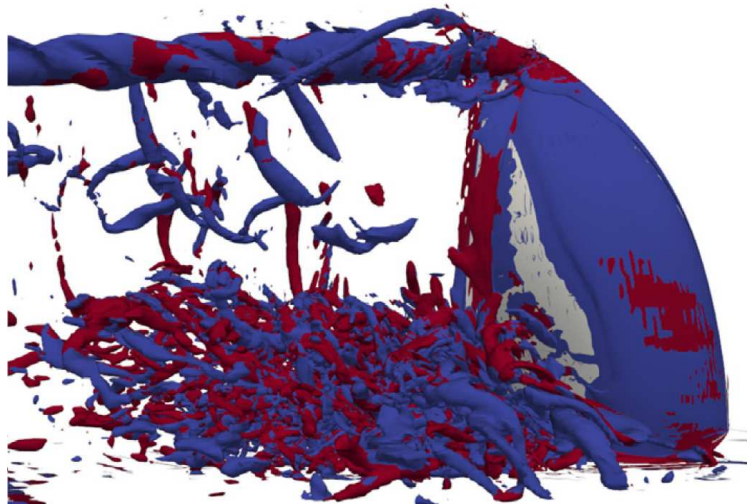
L'interaction fluide-structure a lieu lorsque l'écoulement (le vent pour un spinnaker) applique un effort aérodynamique qui déforme la structure. La déformation de la structure rétroagit sur l'écoulement. L'interaction entre le vent et la surface fine et souple qu'est un spinnaker est très fortement couplée.

Le tableau E.1 définit les principaux nombres adimensionnels définissant notre problème



(a) Schéma pour un écoulement type et la répartition de pression associée au portant.

(b) Écoulement sur la voile, sous le vent du spinnaker avec un modèle *DES* utilisant 32 millions de mailles. Les lignes rouges représentent l'écoulement moyenné dans le temps, les lignes en traits mixtes rouges représentent les lignes de séparation moyennes, et les lignes rouges en pointillés, les lignes de recollement.



(c) Les iso-surfaces du critère Q $500s^{-2}$ pour voir en couleur les vorticités simulées par le modèle *DES*. La couleur rouge représente une vorticité positive et bleue négative.

Figure E.4 – Résultats de [Viola et al., 2014] pour une simulation numérique utilisant une *Detached Eddy Simulation* sur un spinnaker asymétrique correspondant à une forme mesurée en soufflerie.

Vitesse réduite	$U_R = \frac{T_s}{T_f}$	0.6
Nombre de déplacement	$D = \frac{\xi_0}{L}$	0.125
Nombre de masse	$M = \frac{\rho_f}{\rho_s}$	1.2×10^{-3}
Nombre de Cauchy	$C_Y = \frac{\rho_f U_0^2}{E}$	1.9×10^{-8}
Nombre de Reynolds	$Re = \frac{\rho_f U_0 L}{\nu}$	2.7×10^6

Table E.1 – Principaux nombres adimensionnels décrivant l'étude d'interaction fluide-structure pour un spinnaker asymétrique d'un voilier de type J/80.

d'interaction fluide-structure. La vitesse réduite U_R et le nombre de déplacement D ont le même ordre de grandeur, empêchant toute hypothèse simplificatrice sur la vitesse et/ou l'accélération du fluide ou du solide à négliger.

Le nombre de Reynolds Re élevé indique que les forces visqueuses ne sont pas dominantes et que l'écoulement est principalement turbulent. Mais à cause de la forte courbure du spinnaker, un détachement massif de l'écoulement est attendu ce qui ne serait pas possible à obtenir avec une modélisation en fluide parfait.

Un faible nombre de Cauchy C_Y montre que le fluide provoque seulement de faible déformation sur la voile. Cependant une voile de spinnaker est modélisée par une membrane 3D où la raideur de flexion est nulle. Ainsi la courbure joue un rôle important, qui associée à la tension dans le tissu, s'oppose à la pression appliquée sur la voile ([Durand, 2012]):

$$\rho_{S.th} \frac{\partial^2 w}{\partial t^2} = \Delta p + \underline{\underline{\chi \kappa}} \quad (E.2)$$

avec:

w : le déplacement normal au plan $(\underline{u}, \underline{v})$ (cf. figure E.5)

$\rho_{S.th}$: la densité surfacique

Δp : la différence de pression

$\underline{\underline{\chi}}$: le tenseur tension

$\underline{\underline{\kappa}}$: le tenseur de courbure $-\frac{\partial^2 w}{\partial u \partial v} = -\nabla^2 w$

On obtient ainsi de larges déplacements de la voile mais de faibles déformations. Ces grands déplacements apportent de fortes instabilités dans les simulations numériques où un remaillage ou une déformation du maillage est nécessaire. De plus une membrane ne supporte pas la compression, des plis se créent ajoutant une non-linéarité au problème.

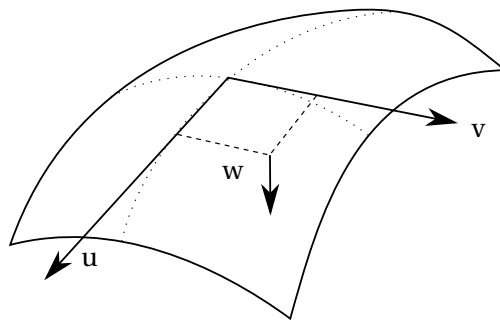


Figure E.5 – Le repère de référence pour une membrane 3D.

Pour finir, le nombre de masse n'est pas le terme le plus approprié pour définir le couplage avec la masse ajoutée pour une surface avec une faible épaisseur comme c'est le cas pour une voile de portant. [Durand, 2012] estime que la masse ajoutée du fluide due au déplacement de fluide est de l'ordre de 100 fois la masse du spinnaker. Cette masse ajoutée qui est un phénomène du premier ordre est une autre raison pour que ce phénomène d'interaction fluide-structure soit fortement couplé.

E.2.4 Sujets de recherche dans le domaine de la voile

De nombreuses recherches ont déjà été effectuées dans le domaine de la voile, que ce soit sur l'aérodynamique, sur l'hydrodynamique des voiliers ou sur la performance d'appendices dont les foils. Concernant les voiles de portant, le tableau E.2 présente l'état de l'Art en divisant les recherches en 3 catégories: les simulations numériques, les essais en soufflerie, et les essais in-situ. On distingue des projets de recherche avec une approche dite "statique" avec des résultats moyennés dans le temps, soit des projets de recherche avec une approche dite "dynamique" avec des résultats résolus dans le temps. Mesurer les pressions sur un spinnaker (flexible [Viola and Flay, 2009] ou rigide en soufflerie [Richards et al., 2006]) est un des sujets majeurs pour des voiles de portant. Ces résultats sont généralement comparés avec d'autres types d'essais: [Viola and Flay, 2011] [Hansen et al., 2002, Viola et al., 2014]. Mesurer la forme de voile fait également partie des sujets phares [Ranzenbach and Kleene, 2002, Graf and Müller, 2009, Mausolf et al., 2011, Renzsch and Graf, 2013]. Des simulations numériques modélisent de plus en plus l'Interaction Fluide-Structure [Renzsch and Graf, 2010, Trimarchi et al., 2013, Lombardi et al., 2012, Durand et al., 2014].

Avec une approche dynamique, due à la complexité du comportement du spinnaker, peu d'études ont été faites. Des simulations numériques ont été développées pouvant étudier les comportements instationnaires de la voile comme le fasyement du guindant lors d'un réglage dynamique [Durand et al., 2014]. En soufflerie, les forces lors d'un empannage ont été mesurées [Banks et al., 2010] et également l'évolution des pressions sur un spinnaker rigide [Bot et al., 2014]. Cependant aucun résultat n'a été publié pour des essais *in-situ* avant cette thèse. Le but de cette thèse est également de compléter ce "vide" comme le montrent les articles utilisant les résultats de ma thèse: [Deparday et al., 2014, Motta et al., 2015, Motta, 2015, Deparday et al., 2016].

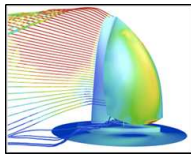
Downwind	Approche statique	Approche dynamique
In situ 	<ul style="list-style-type: none"> • [Viola and Flay, 2010], Pressions • [Mausolf et al., 2011], Formes de voile • [Motta et al., 2014], Pressions + formes • [Campbell, 2014b], Comparaison efforts taille réelle/soufflerie • ... 	<ul style="list-style-type: none"> • [Deparday et al., 2014] <i>Étude du fâseusement du guindant</i> • [Motta et al., 2015] <i>Évolution des pressions</i> • [Deparday et al., 2016] <i>Analyse modale sur les variations de pression</i>
Soufflerie 	<ul style="list-style-type: none"> • [Ranzenbach and Kleene, 2002], Forme de voile • [Hansen et al., 2002], Comparaison grandeur réelle/soufflerie • [Richards et al., 2006], Voiles rigides • [Graf and Müller, 2009], Forme de voile • [Viola and Flay, 2009], Efforts et pressions • [Renzsch and Graf, 2013], Efforts + formes de voile • [Campbell, 2014a], Comparaison d'essais en soufflerie • ... 	<ul style="list-style-type: none"> • [Banks et al., 2010], Efforts pendant l'empannage • [Bot et al., 2014], Évolution temporelle des pressions
Numerical 	<ul style="list-style-type: none"> • [Hedges et al., 1996] • [Lasher and Sonnenmeier, 2008] • [Renzsch and Graf, 2010] IFS • [Viola and Flay, 2011], Comparaison taille réelle, soufflerie, numérique • [Trimarchi et al., 2013] IFS avec coques • [Viola et al., 2014] DES • ... 	<ul style="list-style-type: none"> • [Lombardi et al., 2012] IFS dynamique • [Durand et al., 2014] réglage dynamique automatique

Table E.2 – État de l'art non-exhaustif pour les navigations au portant. Les références en *italiques* sont les articles présentant des résultats de cette thèse.

E.3 Voilier instrumenté

E.3.1 Essais

Deux grandes campagnes de mesures sur un voilier J/80 ont eu lieu lors de cette thèse: une en 2013 où la pression sur le spinnaker a été mesurée (cf. figure E.6) et une en 2014 où la forme en navigation du spinnaker a été mesurée utilisant la photogrammétrie avec 6 caméras à bord (cf. figure E.7). Pour les deux essais, les efforts sur le gréement, les attitudes du bateau et les données du vent ont été enregistrés. Toutes ces données ont été enregistrées avec un système d'acquisition qui datent les données des capteurs *à la volée*. Dès que le capteur a une donnée, il la transmet au système d'acquisition qui la date instantanément. Les enregistrements sont donc résolus précisément en temps, malgré les différents taux d'échantillonnage des capteurs (de 1 à 100 Hz).

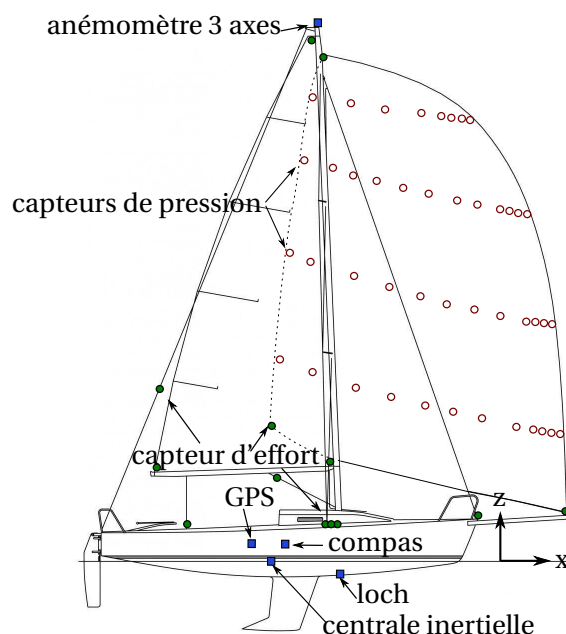


Figure E.6 – Présentation du montage expérimental sur le J/80 en 2013. 16 capteurs d'effort (disques verts), 44 capteurs de pression (cercles rouges) et capteurs de vent et du bateau (carrés bleus).

E.3.2 Système d'acquisition de forme de voile

Pour mesurer la forme du spinnaker en navigation, on a utilisé la photogrammétrie. A l'aide de différentes caméras qui filment un *point objet* dans l'espace, il est vu comme un *point image* sur la photographie (cf. figure E.8). La position du *point-image* sur le plan-image permet de savoir sur quelle ligne de perspective le *point objet* se trouve. Il faut donc déterminer la profondeur pour pouvoir placer dans l'espace le *point objet* à partir d'un *point image*. A l'aide de plusieurs caméras, l'intersection des lignes de perspective de chaque caméra permet de localiser dans l'espace la position du *point objet*.

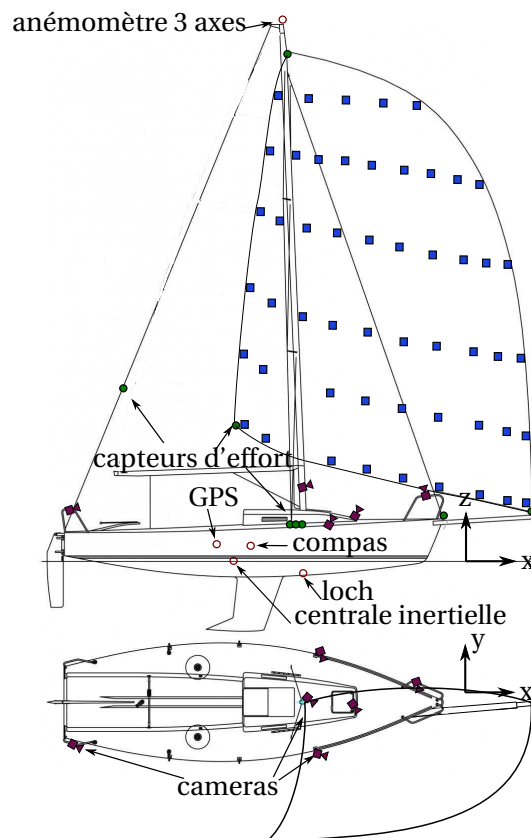


Figure E.7 – Présentation du montage expérimental sur le J/80 en 2014. 16 capteurs d'effort (disques verts) et capteurs de vent et du bateau (cercles rouges) comme pour la campagne d'essais en 2013. 54 cibles sur le spinnaker pour la mesure photogrammétrique (carrés bleus) sont ajoutées et les capteurs de pression ne sont pas installés.

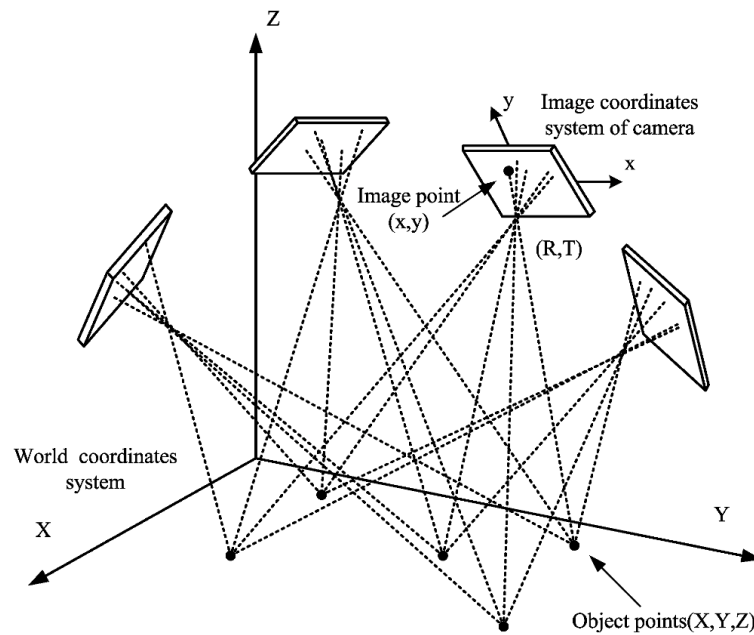
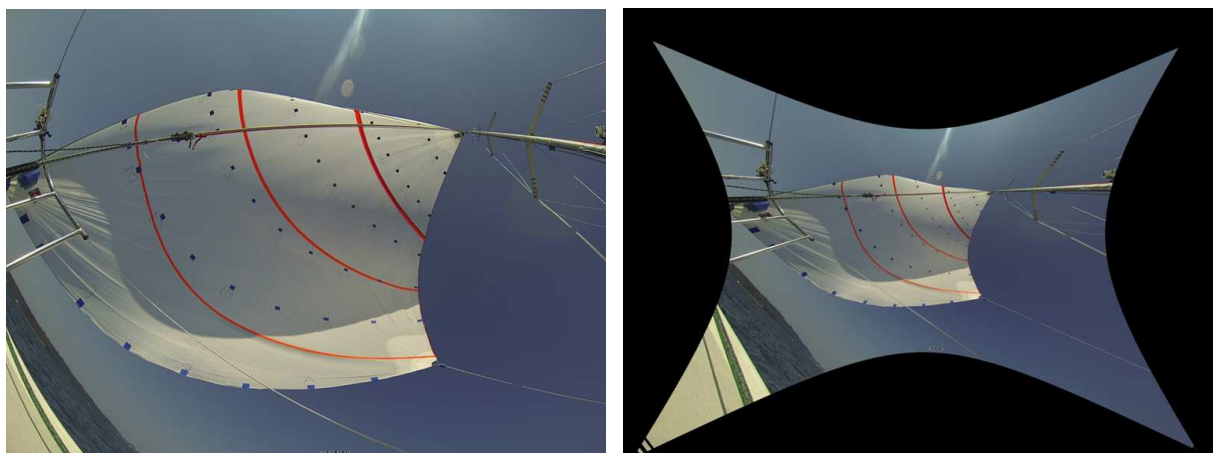


Figure E.8 – Principe de la photogrammétrie utilisant la triangulation. Plusieurs points-objets sont projetés sur différents plans images (photographies).



(a) Vue non calibrée du spinnaker d'une caméra GoPro placée sur le pont avant.

(b) Vue du spinnaker de la même caméra après redressement de l'image déterminé pendant l'étalonnage.

Figure E.9 – La même photographie avant et après le redressement de l'image déterminé pendant l'étalonnage qui retire l'effet barillet de la lentille grand-angle.

Ainsi une bonne résolution de la caméra apportera une bonne précision sur la position du *point image* sur le plan image, et un bon étalonnage de la caméra permettra de bien définir les lignes de perspective. Les angles entre les photos doivent être suffisants pour obtenir des intersections des lignes de perspective les plus nettes possibles. Augmenter le nombre de photos et de cibles permet d'augmenter la précision de la mesure également. 54 cibles *points-objets* sont ainsi collées sur le spinnaker (cf figures E.7 et E.9).

On a décidé de placer 6 caméras à bord du bateau, sur les balcons avant et arrière, sur le pont avant, à 1.5 m en hauteur sur le mât et sur les flancs bâbord et tribord. Ainsi elles restent fixes par rapport au repère du bateau et peuvent être plus facilement contrôlées. En contrepartie, elles auront un faible recul pour filmer le spinnaker de 68 m². Une lentille grand-angle est donc nécessaire. Pour prendre en compte la forte déformation de l'image due à l'effet barillet d'une lentille grand-angle, une calibration précise et minutieuse de chaque caméra a été nécessaire (cf. figure E.9).

Les caméras sont synchronisées avec les autres données à l'aide d'un signal laser déclenché par le système d'acquisition. La visualisation du point laser sur les images à des instants déterminés permettent de synchroniser les vidéos et donc la forme du spinnaker avec les autres mesures.

Pour déterminer la précision de ce système d'acquisition, certaines longueurs spécifiques de la voile (guindant, bordure, chute, ...) ont été comparées entre celles données par le maître-voilier et celles mesurées par le système de photogrammétrie. Une précision moyenne meilleure que 1.5% a été trouvée.

Ce nouveau système de mesure de forme de voile de portant a été développé pendant cette thèse. Il utilise la photogrammétrie à l'aide de 6 caméras placées à bord du voilier. Il permet de mesurer des formes de spinnaker évoluant dans le temps et synchronisées avec d'autres mesures.

E.3.3 Mesures des efforts

Les efforts ont été mesurés dans le gréement du voilier (haubans, étai, pataras) à l'aide de manilles et de ridoirs instrumentés qui ont été développés pendant la thèse de [Augier, 2012].

Les efforts ont également été mesurés aux 3 points du spinnaker (tête, amure, écoute). Cependant un spinnaker est une voile volante avec le point d'écoute mobile dans l'espace et qui a besoin d'être hissé et affalé rapidement. C'est pourquoi il a été décidé d'éviter toute connexion filaire entre le spinnaker et le système d'acquisition placé dans le bateau. Pendant la première campagne d'essais en 2013, les manilles instrumentées ont été connectées à des boîtes placées à l'amure et à la tête de la voile où s'effectuaient la numérisation, et l'émission des données sans fil à l'aide d'un protocole Zigbee.

Lors de la seconde campagne d'essais en 2014, ces manilles instrumentées ont été remplacées par des *Directional Load Cells (DLCs)*. Elles permettent de mesurer l'intensité de l'effort et sa direction à chacun des points du spinnaker. Puisque la voile n'est tenue qu'à ses 3 points, connaître la direction et la norme des efforts à chacun de ces points permet de calculer la force aérodynamique totale créée par la voile. Ces DLCs ont été développées au Yacht Research Unit de l'Université d'Auckland [Le Pelley et al., 2015].

Les manilles instrumentées ont une précision meilleure que 1% sur l'étendue de mesure (0-5000 N) et un taux d'échantillonnage de 25 Hz, suffisant pour nos essais.

Les DLCs ont une précision sur la norme des efforts inférieure à 2% sur la même étendue de mesure (donc environ 100 N en valeur absolue). Cependant il existe également une imprécision de l'ordre de 5° dans la direction des efforts. Pour des angles de vent élevés, les efforts projetés dans le repère bateau sont plutôt faibles (autour de 250 N), et cette incertitude en direction couplée avec une précision des efforts de 2% nous permet d'avoir une précision des efforts aérodynamiques projetés de l'ordre de 10% seulement. Les DLCs sont sans-fil et sur batterie. Or une faible tension de la batterie rend le signal plus bruité et diminue la précision sur la mesure de la norme des efforts. Une incertitude sur la datation des données a été mesurée et est de l'ordre de 0.1 s. Néanmoins les mouvements du spinnaker dynamiques mesurés et analysés sont de l'ordre de la seconde et donc ces capteurs sont suffisants pour analyser les déformations principales de la voile.

E.3.4 Système d'acquisition de pression sur le spinnaker

Lors de la première campagne d'essai en 2013, les pressions sur le spinnaker ont été mesurées à l'aide de capteurs mesurant la différence de pression entre l'intrados et l'extrados. 44 capteurs sont collés sur la voile, répartis en 4 lignes (à 1/4, 1/2, 3/4 et 7/8 de la hauteur). Plus de la moitié des capteurs se trouvent dans les premiers 50% de la voile, proche du guindant, là où les plus grandes variations de pression sont attendues (cf figure E.6).

Les pressions différentielles sont estimées dans une fourchette de 5 à 250 Pa environ pour des conditions normales de navigation (5 à 15 kn). Les capteurs peuvent mesurer jusqu'à 1 kPa, ce qui est suffisant pour qu'ils ne soient pas détériorés. Cependant l'incertitude de ces capteurs est de 5 Pa environ ce qui correspond à l'ordre de grandeur des pressions attendues à des angles de vent élevés. Ce système de

pression convient donc pour nos essais, et est juste limite pour des conditions extrêmes (un angle de vent apparent autour de 140° dans un vent réel de 8-10 kn).

De plus un compromis a dû être trouvé entre la fréquence d'échantillonnage et le bruitage des signaux. Une fréquence d'échantillonnage de 6.5 Hz en moyenne est certes assez faible mais permet d'obtenir des signaux bruts de pression pas trop bruités. Cette fréquence d'échantillonnage est suffisante pour analyser les phénomènes dynamiques du spinnaker de l'ordre de la seconde.

E.3.5 Mesures du vent et des données de navigation du bateau

Le vent est mesuré à environ 1.2 m au-dessus de la tête de mât à l'aide d'un anémomètre à ultrason 3 axes. On mesure donc la vitesse et l'angle du vent apparent. La vitesse du vent apparent (AWS en anglais) est utilisée pour calculer les coefficients d'effort et de pression et l'angle du vent apparent (AWA en anglais) pour classer et comparer les efforts, les distributions de pression et les formes de voile. La fréquence d'échantillonnage est de 10 Hz.

Les attitudes du voilier (gîte, cap, assiette) sont mesurées par une centrale inertielle située dans le bateau au plus proche du centre de rotation calculé pour des faibles angles de gîte. Ces angles d'Euler permettent de connaître la position du repère bateau par rapport au repère terrestre et ainsi projeter dans le repère bateau les efforts aérodynamiques du spinnaker mesurés aux 3 points par les DLCs. Un étalonnage précis a été réalisé sur toutes les centrales inertielles utilisées lors de ces essais.

Un compas et un loch roue à aubes standards sont également utilisés pour mesurer la vitesse surface et le cap surface du voilier.

E.3.6 Procédure et traitement des données

Après avoir récupéré toutes les données d'une campagne d'essais du système d'acquisition, une routine Matlab a été développée pour importer les données, les convertir, et resynchroniser tous les signaux à échantillonnage non-uniforme avec un unique vecteur temps. Différentes méthodes de rééchantillonnage ont été testées. Pour la plupart des cas, la méthode utilisée est d'interpoler linéairement chaque signal à sa fréquence d'échantillonnage moyenne pour obtenir un échantillonnage uniforme. Ensuite une seconde interpolation linéaire a été appliquée à une fréquence d'échantillonnage unique (en général 25 Hz) pour que toutes les données des capteurs aient un même vecteur temps pour faciliter l'analyse.

Pour analyser les phénomènes dynamiques intrinsèques au spinnaker, les "données d'entrée" doivent être fixes. La vitesse, la direction du vent apparent, les mouvements du bateau doivent être stationnaires. Or il est bien sûr impossible d'avoir des conditions fixes lors d'une navigation sur l'eau. C'est pourquoi des critères ont été définis pour extraire des périodes dites "stables". Les critères sont sur la vitesse et la direction du vent apparent mesurés. Le barreur doit naviguer à un angle de vent apparent constant et le réglage de la voile est à un réglage optimal. Aucun critère n'est établi sur les efforts ou les

pressions puisque l'on veut analyser des phénomènes dynamiques propres au spinnaker. Les critères sont:

- L'écart type du vent apparent pendant une période "stable" ne doit pas être supérieur à une certaine valeur: $\text{stdev(AWA)} < \text{thres}_{\text{AWA}}$, avec en général $\text{thres}_{\text{AWA}} = 4^\circ$.
- L'écart type du vent apparent pendant une période "stable" ne doit pas être supérieur à un certain pourcentage de la vitesse moyenne du vent apparent: $\text{stdev(AWS)} < \text{thres}_{\text{AWS}} \langle \text{AWS} \rangle$ avec en général $\text{thres}_{\text{AWS}} = 0.1$.
- La période "stable" doit durer au moins 10 secondes.

E.4 Évolution du comportement du spinnaker

Dans ce chapitre, l'évolution de la forme du spinnaker en navigation, ainsi que les efforts et la répartition de pression sont analysés en fonction de l'angle de vent apparent. Les données présentées ici sont donc des données moyennées dans le temps à partir des périodes stables décrites précédemment.

E.4.1 Formes du spinnaker en navigation

La figure E.10 présente 4 formes de voile mesurées par le système d'acquisition photogrammétrique pour 4 angles de vent apparent distincts (64° , 96° , 96° , 124°). A 64° , le point d'écoute est derrière le mât et le guindant est entièrement sous le vent. Le bord d'attaque est fortement courbé comme il est courant à cet angle de vent très serré pour ce type de voile. Le point d'écoute avance avec l'augmentation de l'angle du vent apparent. Le point d'écoute est donc plus proche des 2 autres points, tête et amure. Le spinnaker a donc plus de courbure et la chute s'ouvre plus dans la moitié supérieure de la voile. La figure E.10 indique également les données mesurées du vent et des efforts aux 3 points du spinnaker. Lorsque l'angle de vent augmente, la vitesse du vent apparent diminue et donc les efforts diminuent.

Les sections intrinsèques à la voile, souvent utilisées pour mesurer les voiles de près ou pour dessiner une voile, ne sont pas l'outil le plus approprié pour une forme fortement 3D et non développable. En effet la forme d'un spinnaker n'est pas une forme 2D extrudé comme peut l'être une voile utilisée pour des navigations au près et évolue beaucoup en fonction de l'angle de vent. Lors de cette thèse d'autres représentations ont été développées.

E.4.1.1 Cambrure 3D

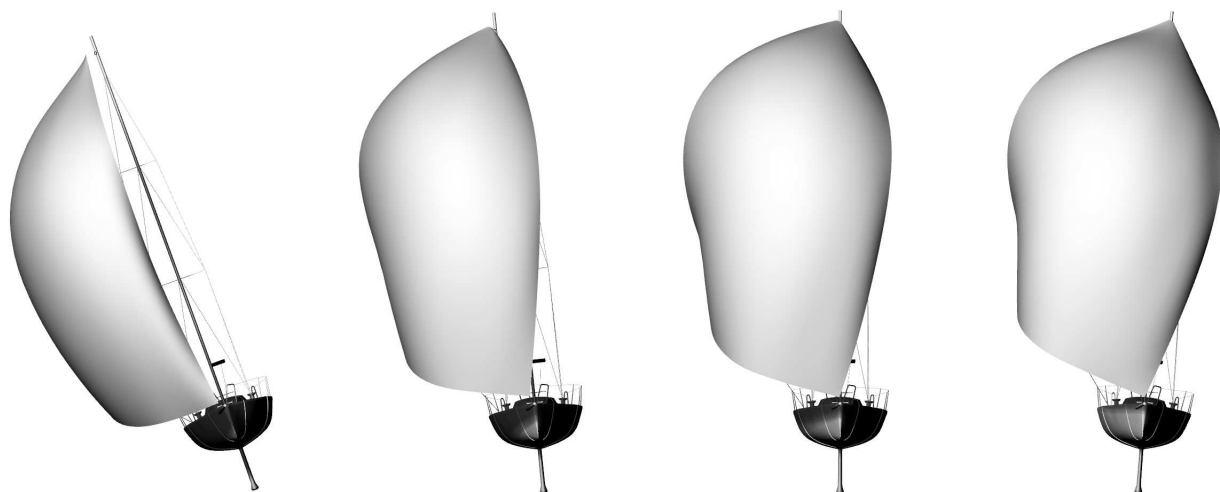
La forme du spinnaker évolue fortement dans le repère bateau en fonction de l'angle de vent, ce qui complexifie la comparaison des formes de la voile. La figure E.11 présente le spinnaker projeté dans le plan défini par les 3 points de la voile tête (H)-amure (T)-écoute(C). Quand l'angle de vent apparent augmente, la cambrure générale tend à avoir une forme plus allongée et en haricot, avec le maximum de profondeur

AWA: 64°
 AWS: 7.0 m/s
 Head: 897 N
 Tack: 730 N
 Clew: 407 N

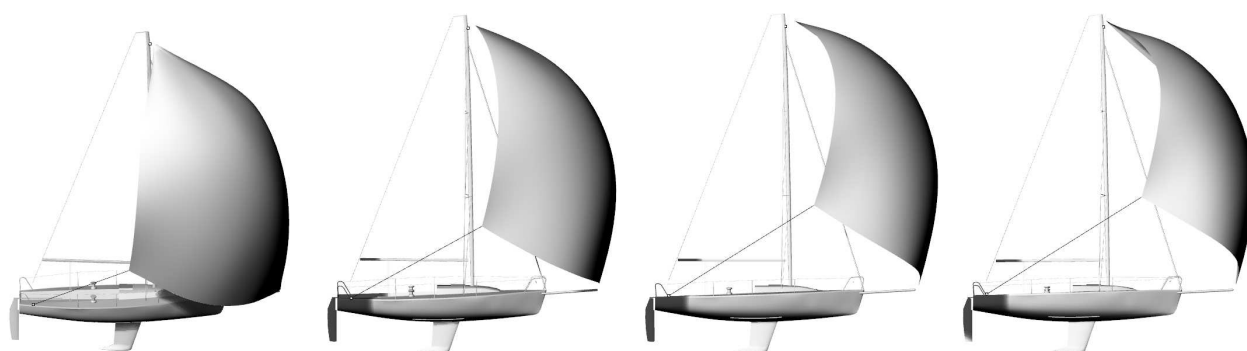
AWA: 96°
 AWS: 5.3 m/s
 Head: 803 N
 Tack: 608 N
 Clew: 325 N

AWA: 124°
 AWS: 4.4 m/s
 Head: 518 N
 Tack: 351 N
 Clew: 211 N

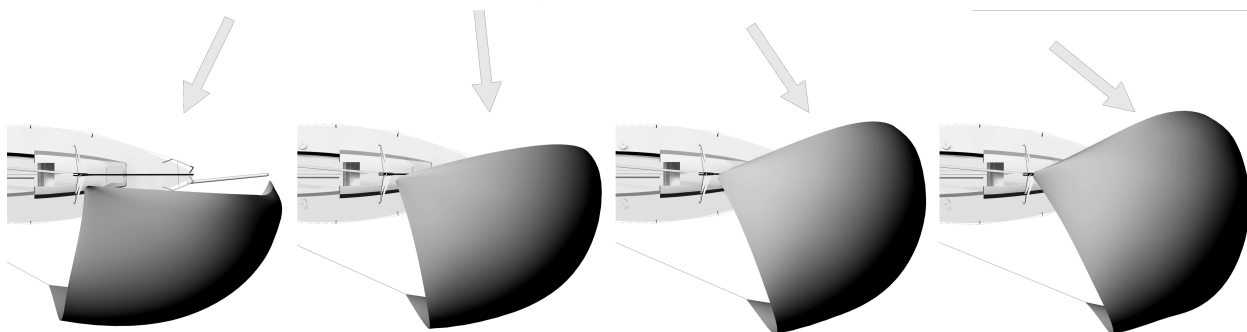
AWA: 141°
 AWS: 3.1 m/s
 Head: 259 N
 Tack: 90 N
 Clew: 86 N



(a) Vue de face



(b) Vue de tribord



(c) Vue d'au-dessus juste au-dessus de la tête de mât

Figure E.10 – Vues 3D de 4 formes du même spinnaker mesurées en navigation par photogrammétrie avec les efforts correspondants à la tête (Head), amure (Tack) et écoute (Clew). De gauche à droite, AWA: 64°, 96°, 124°, 141°.

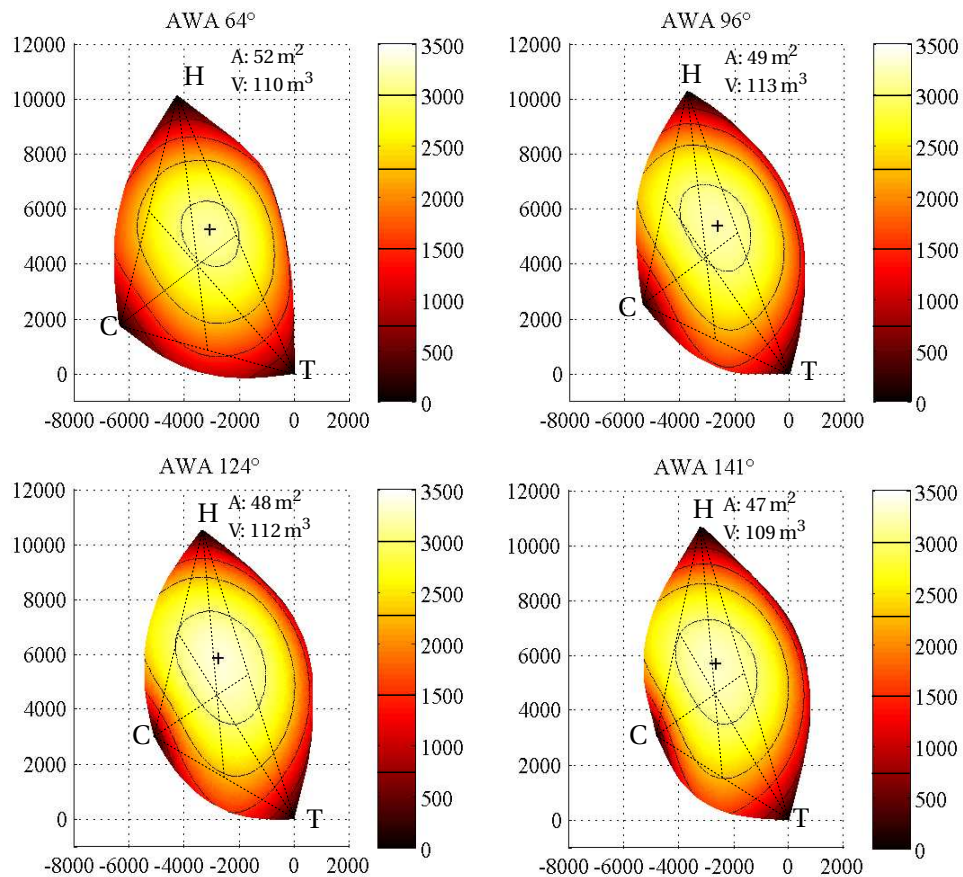


Figure E.11 – Profondeur du spinnaker en mm projetée dans le plan défini par les 3 points de la voile tête (H)-amure (T)-écoute(C) pour les mêmes angles de vent apparent présentés à la figure E.10. Les isoprofondeurs sont indiquées par les lignes noires. La croix rouge présente la position du maximum de profondeur. Les médianes du triangle HTC sont également représentées. Pour chaque angle de vent apparent, la surface projeté (A) du spinnaker sur le plan HTC et le volume entre le spinnaker et le plan sont donnés.

qui se rapproche de la moitié de la médiane issue de H. Alors que la surface projetée du spinnaker sur le plan HTC semble légèrement diminuer avec l'angle de vent, le volume (défini comme l'intégrale des profondeurs du spinnaker) reste à peu près constant. Les angles du triangle HTC permettent également d'analyser l'évolution de la forme.

Cette représentation permet donc de facilement visualiser et quantifier l'évolution générale de la forme de la voile pour différents angles de vent apparent.

E.4.1.2 Surface de Bézier

A l'aide de surfaces triangulaires de Bézier, il est possible de caractériser une forme de voile avec seulement quelques points de contrôle. La figure E.12 présente la reconstitution du spinnaker à l'aide d'une surface de Bézier de degré 4. Seulement 15 points de contrôle permettent de reconstruire la surface via une relation

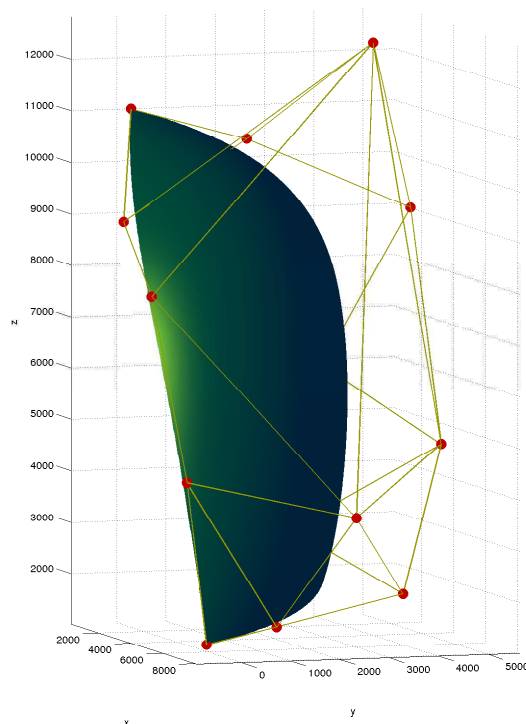


Figure E.12 – Surface de Bézier et ses points de contrôle (points rouges) représentant une forme de voile pour un angle de vent apparent de 96° utilisant un patch de Bézier triangulaire de degré 4.

polynomiale avec une précision de 50 mm. Le polyèdre rejoignant les différents points de contrôle suit la forme générale du spinnaker, accentue certaines caractéristiques (comme le creux), et les bords du polyèdre définissent également les bords du spinnaker par des courbes de Bézier.

Ainsi on peut quantifier à l'aide de polynômes une forme par seulement la position de quelques points de contrôle. Les surfaces de Bézier seraient donc un bon outil pour l'optimisation de forme en fonction de jauges de classe par exemple.

Ces points évoluent également en fonction de l'angle de vent apparent. A partir de l'interpolation de la trajectoire de ces points en fonction de l'angle de vent apparent, n'importe quelle forme de voile pour un angle de vent donné peut donc être interpolée.

De plus, la position de 15 points de contrôle permet de réduire significativement la quantité de donnée décrivant la forme d'une voile. Cet avantage est très intéressant pour créer une large base de donnée de formes de voile à la fois légère et accessible.

E.4.2 Évolution des efforts sur le spinnaker

La figure E.13 (à gauche) montre l'évolution des efforts projetés dans le repère du bateau grâce aux capteurs *Directional Load Cell (DLC)* placés aux 3 points de la voile en fonction de l'angle de vent apparent. Pour des angles serrés (environ 60°), l'effort propulsif est du même ordre de grandeur que l'effort latéral,

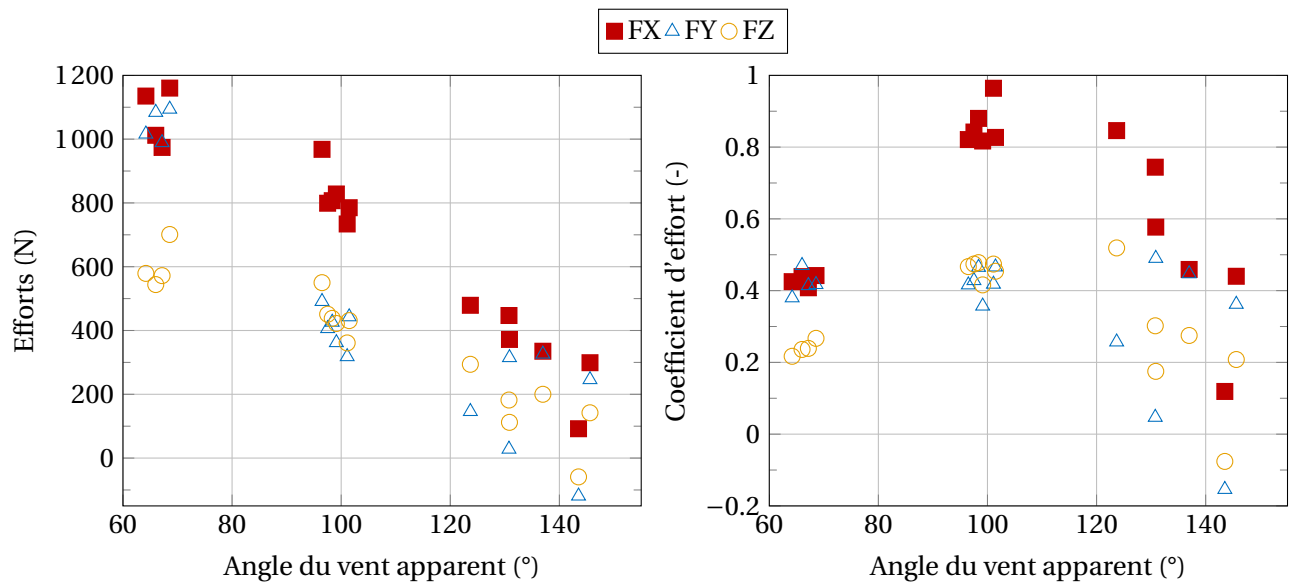


Figure E.13 – Décomposition de l'effort aérodynamique du spinnaker (avec la grand voile affalée) dans le repère bateau. FX est la force propulsive, FY la force latérale et FZ la force verticale.

autour de 1000 N. Pour des angles plus élevés, l'effort latéral est deux fois plus faible que l'effort propulsif. L'effort aérodynamique généré par le spinnaker a pour tendance globale de diminuer en fonction de l'angle de vent apparent. L'effort est 3 à 5 fois plus faible entre un angle de vent apparent de 60° et de 140°. La vitesse du vent apparent diminue quand l'angle du vent augmente. Une diminution de la vitesse du vent fait diminuer l'effort aérodynamique, comme présenté dans la figure E.10.

Pour s'affranchir de l'influence de la vitesse du vent apparent, le coefficient d'effort $C_f = \frac{\langle F \rangle}{\frac{1}{2} \rho S \langle AWS \rangle^2}$ est présenté sur la figure E.13 (à droite). On trouve un maximum de coefficient d'effort propulsif pour un angle de vent apparent de 100° environ, autour de 0.9; alors que l'effort latéral est de 0.4 environ. L'angle de vent optimal pour ce spinnaker serait autour de 100° car le coefficient d'effort propulsif est maximum et l'effort latéral (donnant de la gîte au bateau et donc plus de résistance hydrodynamique) est 2 fois plus faible que l'effort propulsif.

E.4.3 Évolution des pressions sur le spinnaker

Pour 3 angles de vent distincts (66°, 118°, 140°), la figure E.14a présente la répartition de pression moyenne en utilisant le coefficient de pression différentielle ΔC_p , défini comme la différence entre la pression sous le vent (intrados) et la pression au vent (extrados) divisée par la pression dynamique: $\Delta C_p = \frac{P_{leeward} - P_{windward}}{\frac{1}{2} \rho AWS^2}$. Les pressions différentielles sont mesurées sur un nombre discret de positions indiquées par des croix bleues. Les pressions sont interpolées et extrapolées en utilisant une *Radial Basis Function* linéaire.

Pour des angles serrés (représenté ici par un cas à 66°), le maximum de dépression $\Delta C_p \approx -3$ se trouve principalement sur le bord d'attaque dans la partie supérieure de la voile. Lorsque l'angle de vent

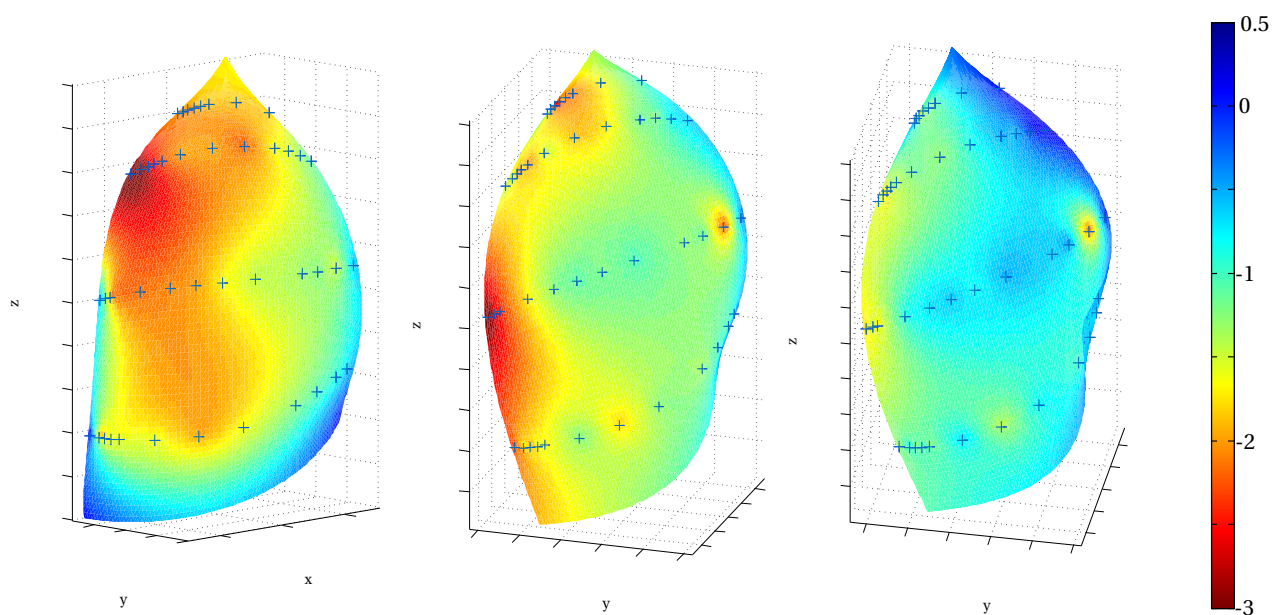
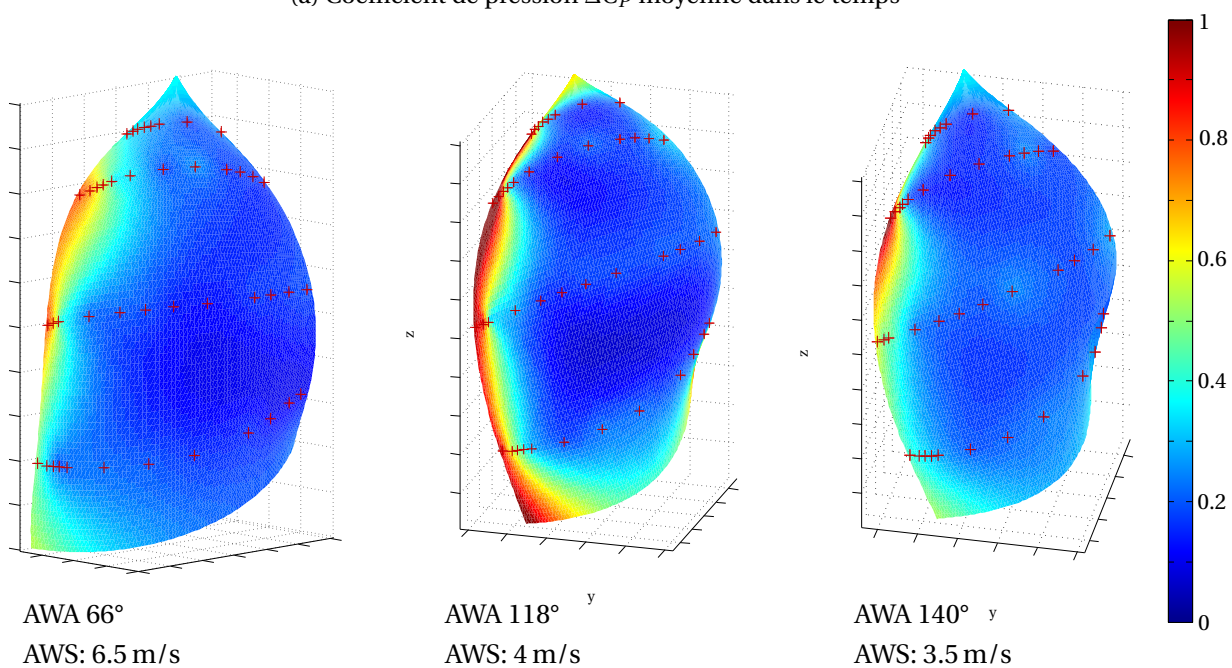
(a) Coefficient de pression ΔC_P moyenné dans le temps(b) Ecart type du coefficient de pression ΔC_P

Figure E.14 – Distributions de pression interpolés et extrapolés sur des formes de voile types pour 3 angles de vent apparent différents: (66°, 118°, 140°). Les croix (en bleu en (a) et en rouge en (b)) indiquent les positions des capteurs de pression.

augmente (comme pour le cas 118° dans la figure E.14a) le maximum de dépression se trouve toujours sur le bord d'attaque mais plutôt dans la partie inférieure de la voile. Pour un angle de vent d'environ 65°, la voile est plutôt plate et complètement sous le vent et devient plus courbée et plus dans l'axe longitudinal

du bateau pour un angle d'environ 120° . L'effort propulsif principalement produit par la forte dépression au bord d'attaque est plus important que l'effort latéral pour un angle de vent d'environ 120° , ce qui corrobore avec les résultats présentés dans la sous-section précédente.

Pour des angles de vent apparent plus élevés, les coefficients de pression semblent plus faibles. Cependant les valeurs de pression mesurées ici sont de l'ordre de 5 Pa, l'ordre de grandeur de l'incertitude de mesure des capteurs de pression. Néanmoins le maximum de dépression, participant le plus à la création de la force aérodynamique, se trouve toujours au guindant.

La figure E.14b présente l'écart-type des coefficients de pression ce qui montre les variations de pression lors d'une période "stable". Le maximum de variation se trouve au niveau du bord d'attaque, là où le maximum de dépression a lieu. Dès que l'on s'éloigne du guindant, l'écart type est quasiment nul donc il y a très peu de variation. On conclut donc que la zone contribuant le plus à l'effort aérodynamique est également la zone où il y a le plus de variation de pression.

Or le réglage optimal d'un spinnaker est lorsque le guindant est à la limite du faseyement, donc une attitude dynamique qui pourrait provoquer cette forte variation de pression et également contribuer à la création de cette dépression au bord d'attaque. Le prochain chapitre étudie plus en détail ce phénomène du faseyement du guindant du spinnaker.

E.5 Le faseyement du guindant: un comportement instationnaire propre au spinnaker

Pour les marins, régler le spinnaker de manière optimale correspond à la limite du faseyement du guindant. Ce réglage est certes bien connu mais n'a jamais été scientifiquement étudié. Dans cette dernière partie, à partir des mesures de pressions et d'efforts, le repliement du guindant est étudié. Ce phénomène dynamique peut apparaître pour n'importe quel angle de vent et même avec un réglage fixe.

E.5.1 Description d'un faseyement du spinnaker

Le tableau E.3 décrit les étapes des évolutions de la forme, des pressions et des efforts lors d'un faseyement. La figure E.15 montre l'évolution de la forme du spinnaker pendant une phase de repliement-dépliage du guindant à 4 instants précis A,B,C et D et la figure E.16, l'évolution de la pression à la mi-hauteur et aux 3/4 de la hauteur du spinnaker à ces 4 mêmes instants. La figure E.17 présente quant à elle les diagrammes espace-temps de $\Delta C_p(x, t)$ aux deux mêmes sections (3/4 et 1/2 de la hauteur du spinnaker). L'évolution dans le temps de l'intégrale des pressions à chaque section et des efforts aux 3 points du spinnaker sont également présentés dans cette figure. Les accolades sous les diagrammes espace-temps indiquent quand le spinnaker est vu replié sur les vidéos.

Le tableau E.3 et la figure E.17 montrent qu'il existe une forte corrélation entre l'évolution des pressions, des efforts et le repliement de la voile. Une pression différentielle positive (i.e. une pression plus élevée à l'extrados qu'à l'intrados) apparaît au bord d'attaque en même temps que le repliement de la voile. Les maxima d'efforts ont lieu juste après les dépliements du guindant.

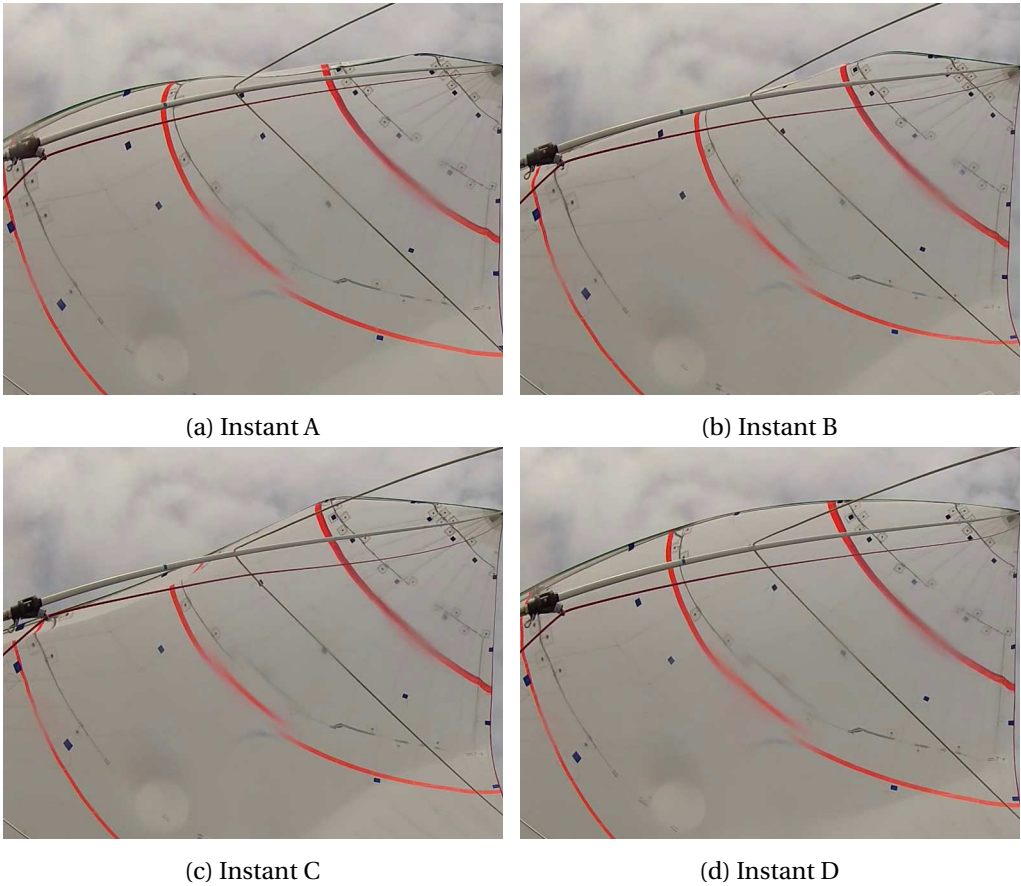


Figure E.15 – Instantanés de la voile lors d'un faseyement.

temps	section 3/4	section 1/2	efforts
67.6 s	minimum de dépression		minimum en tête
A 67.7 s			minimum à l'amure et l'écoute
67.8 s		minimum de dépression	
67.9 s	maximum de repliement		
B 68.1 s			
C 68.5 s			
68.6 s		maximum de repliement	
68.7 s	max. de dépression au guindant		
68.8 s			maximum à la tête et l'amure
D 68.9 s	maximum de dépression	maximum de dépression	maximum à l'écoute
69 s		max. de dépression au guindant	

Table E.3 – Évolutions des pressions et des efforts aux différents instants pendant un faseyement entre la 67ème seconde et la 69ème seconde.

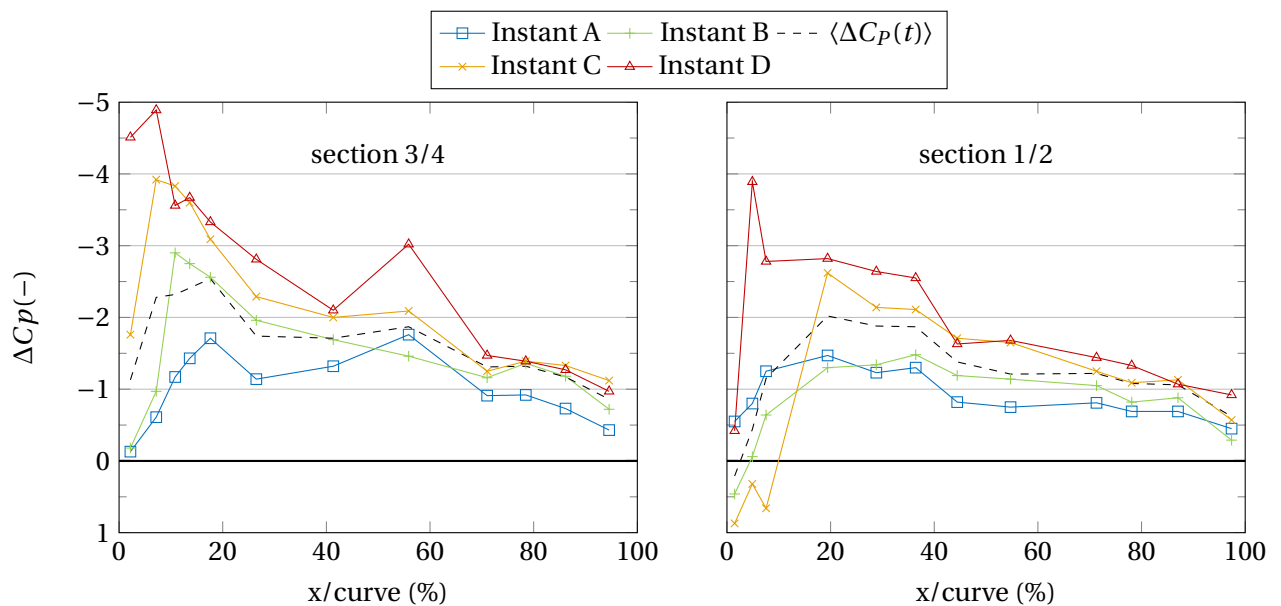


Figure E.16 – Mesures des pressions aux 4 instants choisis et la valeur moyenne dans le temps (trait pointillé).

Le faseyement aux 3/4 de la hauteur de la voile se produit plus rapidement et avant la faseyement à mi hauteur.

Sur la section 1/2, à l'instant A, la voile n'est pas encore pliée. La valeur absolue de la pression globale est minimale à cet instant. La figure E.16 montre également que la distribution de pression est plus faible que la distribution moyenne. Les efforts sont au minimum à cet instant également. Entre l'instant A et C, le guindant se replie. Une zone de pression faible voire positive s'agrandit au fur et à mesure que le guindant se replie. A l'instant C, le guindant est au maximum de son repliement. Une zone de dépression se crée derrière cette zone de pression positive (cf figures E.16 et E.17). Après l'instant C, le guindant se déplie, et la zone de dépression augmente en taille et "remplace" la zone de faible pression. Un pic de dépression remonte donc l'écoulement lors de la phase de dépliage. Ce pic de dépression atteint le bord d'attaque et est encore plus accentué au moment où le spinnaker retrouve sa forme dépliée. Ce pic de dépression s'accompagne d'un pic d'effort.

Cette description sur la section 1/2 peut être également faite sur la section 3/4 mais avec une dynamique différente. En effet le faseyement sur la section 3/4 commence avant la section 1/2. Et pendant le repliement de la section 1/2, la section 3/4 est déjà dans la phase de dépliage. Le faseyement peut être également vu comme une onde se propageant dans le sens du guindant vers le bas. Le pic de dépression sur la section 3/4 reste au bord d'attaque tant que le dépliage du spinnaker sur la section 1/2 n'est pas finie. Ce n'est que quand le dépliage du spinnaker sur la section 1/2 est terminée que la zone de dépression disparaît sur toute la hauteur du spinnaker en même temps. Le faseyement du spinnaker est donc un problème tri-dimensionnel.

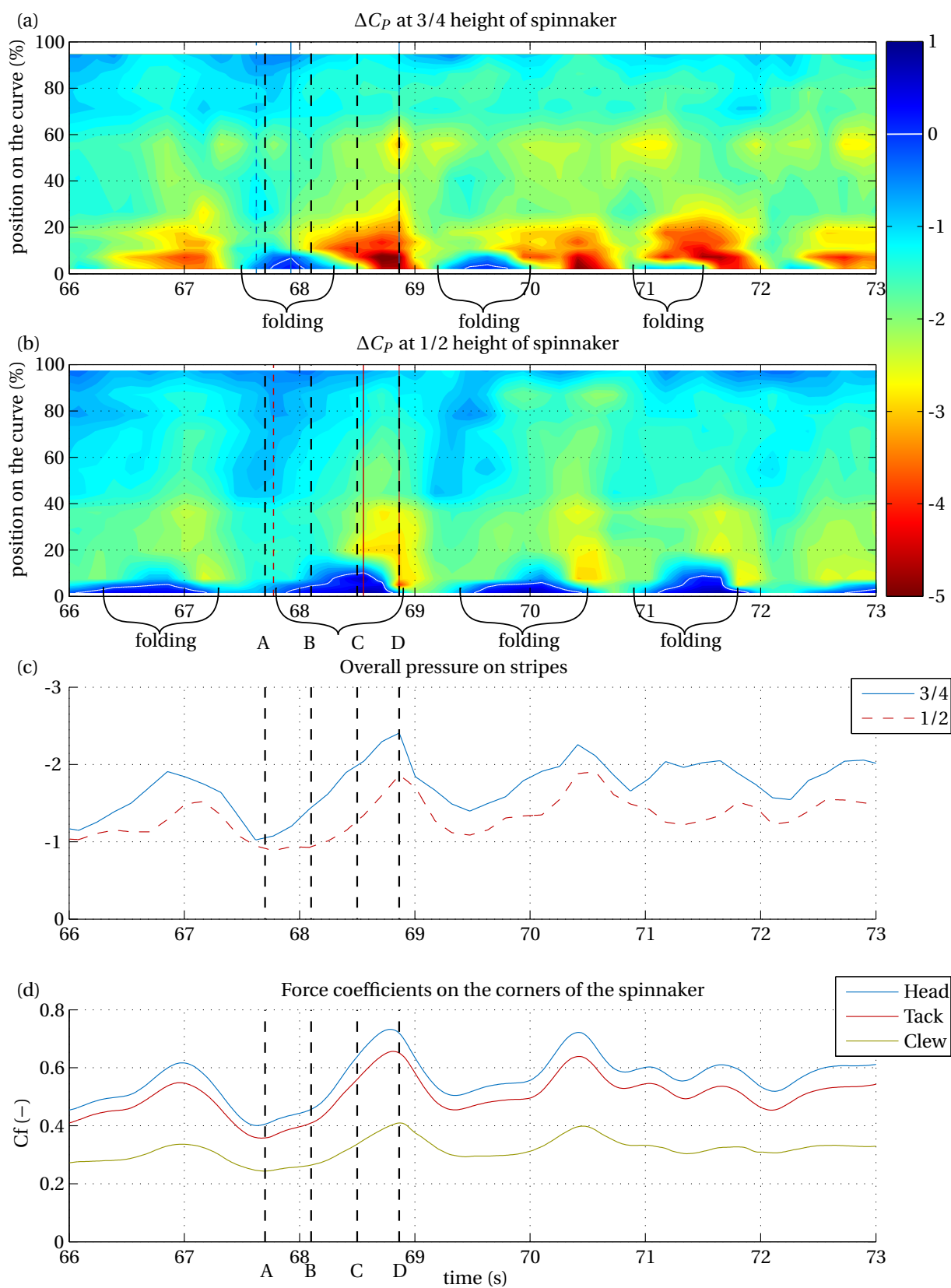


Figure E.17 – Évolution dans le temps des distributions de pression et des efforts sur le spinnaker. Diagramme espace-temps de $\Delta C_p(x, t)$ à la section 3/4 de la hauteur (a), et à la section 1/2 de la hauteur (b); l'intégration de la pression sur toute l'abscisse curviligne c de la section de pression $\frac{1}{c} \int_0^c \Delta C_p dx$ (c); coefficients d'effort mesurés aux 3 points de la voile (d).

E.5.2 Analyse modale des fluctuations de pression

Les faseyements présentés sur la figure E.17 se reproduisent de manière assez périodique. Une pseudo-période (et donc pseudo-fréquence) peut être quantifiée. Ce phénomène de faseyement a lieu pour n'importe quel angle de vent apparent. A l'aide d'outils comme la décomposition en modes propres orthogonaux (Proper Orthogonal Decomposition, POD), il est possible de détecter automatiquement les faseyements du spinnaker à l'aide des mesures de pressions.

La POD décompose les signaux de pressions en modes propres contenant chacun un mode spatial $\varphi_n(x)$ (fixe dans le temps) et un coefficient temporel $a_n(t)$, qui fait évoluer ce mode spatial dans le temps. La somme de tous ces produits reconstruit le signal des variations de pression $U(x, t)$:

$$U(x, t) = \sum_n a_n(t) \varphi_n(x).$$

Les modes sont triés selon leur énergie. Le premier mode est le plus énergétique. Les deux premiers modes permettent de décrire la propagation des pressions lors du faseyement du guindant.

En analysant l'évolution temporelle de ces deux premiers modes propres, une pseudo-période peut être extraite du coefficient temporel $a_1(t)$ qui correspond à la pseudo-période du faseyement décrite précédemment. La figure E.18 trace les pseudo-fréquences f_s , mesurées à l'aide du coefficient temporel du premier mode de la POD, en fonction de la vitesse du vent apparent (AWS) qui est associée à un unique angle de vent apparent (AWA) lors de nos essais *in-situ* (le vent réel est considéré constant). La fréquence réduite f_r est calculée ainsi

$$f_r = \frac{f_s \sqrt{S}}{AWS}$$

avec S la surface du spinnaker, donc $\sqrt{S} = 8.3\text{m}$. Une relation linéaire est visible entre les pseudo-fréquences. La fréquence réduite est donc considérée comme constante pour n'importe quel angle de vent. On peut donc conclure que le faseyement du guindant est guidé par un phénomène aérodynamique.

E.5.3 Interprétation physique du faseyement

A partir de l'idée que le faseyement est gouverné par un phénomène aérodynamique, je propose un modèle simple pour essayer d'expliquer pourquoi un spinnaker peut faseyer périodiquement même avec un angle de vent, une vitesse de vent et un réglage fixes. Cette interprétation physique n'est qu'une proposition et aurait besoin d'être validée.

Les figures E.19 et E.20 montrent le faseyement (repliement-dépliement du guindant) à l'aide de deux cordes. Une corde représentant un profil aérodynamique à mi-envergure environ u et une autre représentant le guindant v . Les images de droite représentent le bord d'attaque de la corde u et sa répartition de pression.

A l'instant A, (cf figure E.19a) le spinnaker est non replié. L'angle d'attaque du vent sur la corde "écoulement" u est faible voire nul. La pression est faible également comme mesurée et présentée sur la

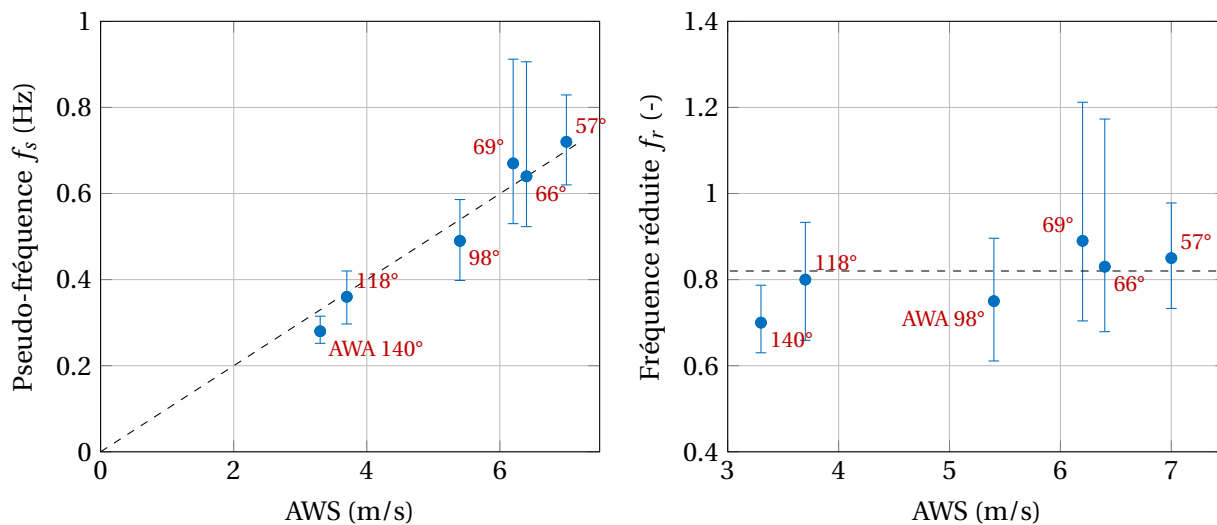
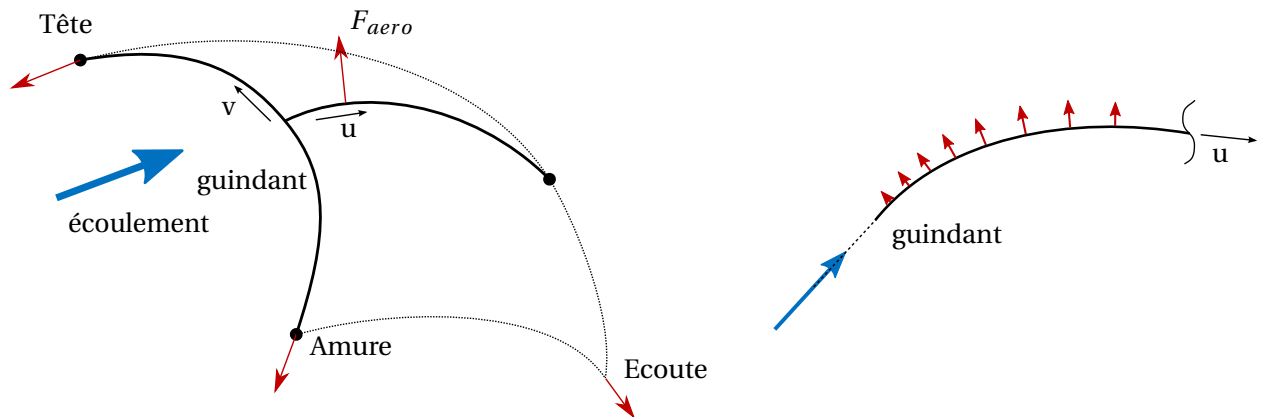


Figure E.18 – Pseudo-fréquence f_s (gauche) et fréquence réduite f_r (droite) du fasyement du spinnaker pour différent angles de vent apparents (AWA) en fonction de la vitesse du vent apparent (AWS). Une interpolation linéaire passe par les points expérimentaux.

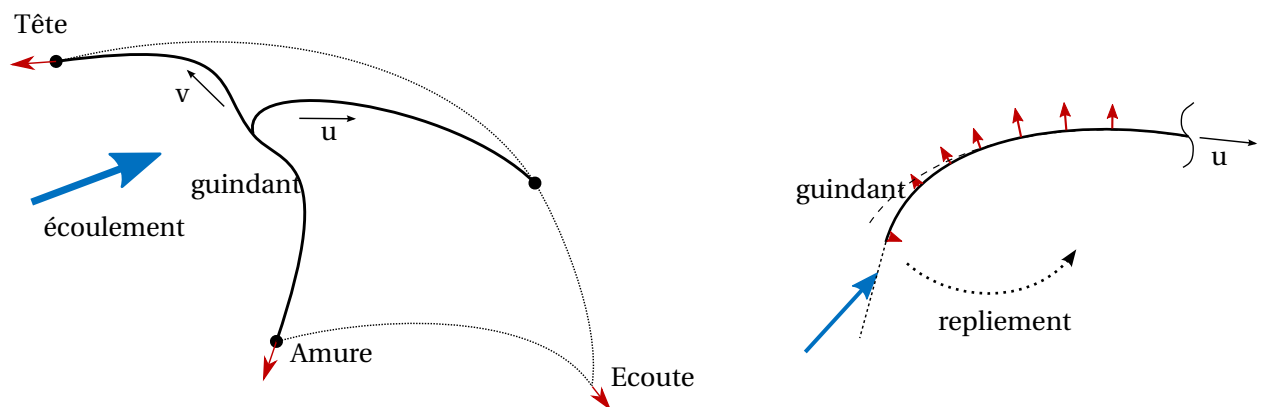
figure E.17. Le bord d'attaque aura tendance à se replier, déchargeant la corde "envergure" v . L'angle d'attaque devient donc négatif, ce qui tend à faire replier encore plus le bord d'attaque (cf figure E.19b). A l'instant C, le profil aérodynamique de la corde u aura changé. Le guindant est suffisamment replié pour que le point d'arrêt ne soit plus au guindant mais plus reculé (indiqué par le point rouge sur la figure E.19c). L'angle d'attaque ne sera donc plus négatif mais largement positif. Ce grand angle d'attaque crée une bulle de séparation au bord d'attaque créant une zone de dépression. Due à la forte courbure du spinnaker, l'écoulement se rattache au profil.

Cette grande zone de dépression proche de la zone de pression positive en amont du point d'arrêt crée un fort gradient de pression qui tend à faire se déplier le spinnaker (cf figure E.20a). La bulle de séparation suit le dépliement et augmente donc en taille. La zone de dépression accroît augmentant ainsi l'effort aérodynamique.

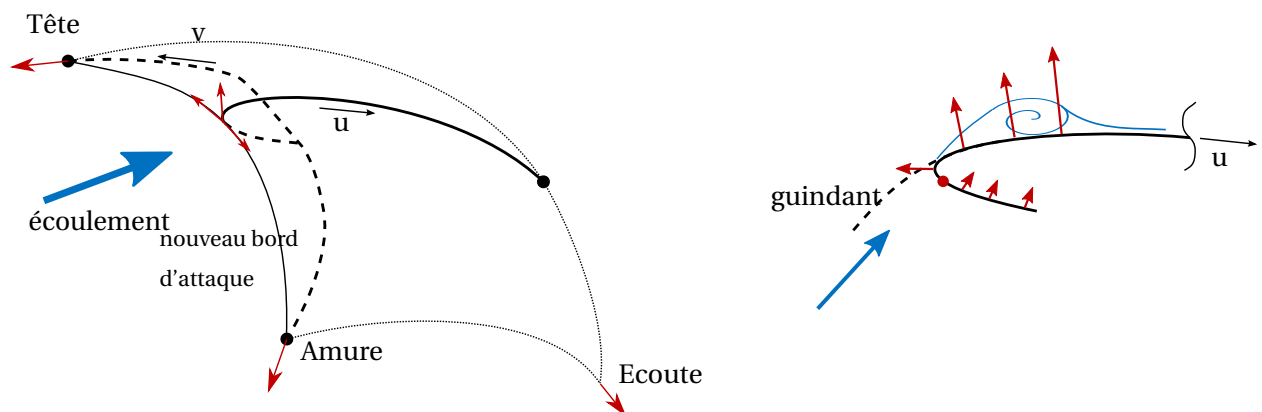
Lorsque le bord d'attaque est déplié, la corde "envergure" v se retend soudainement. Une forte décélération du bord d'attaque a donc lieu. Cette forte accélération négative génère un effort de masse ajoutée qui fait décrocher la bulle de séparation au bord d'attaque et augmente l'effort dans la corde "envergure" v . La corde "écoulement" se retrouve à nouveau dépliée et avec une faible pression au bord d'attaque. On est de nouveau à l'instant A. Un nouveau cycle repliement-dépliement peut recommencer.



(a) Juste avant le repliement (*instant A*). Faible pression sur la corde "écoulement" u .

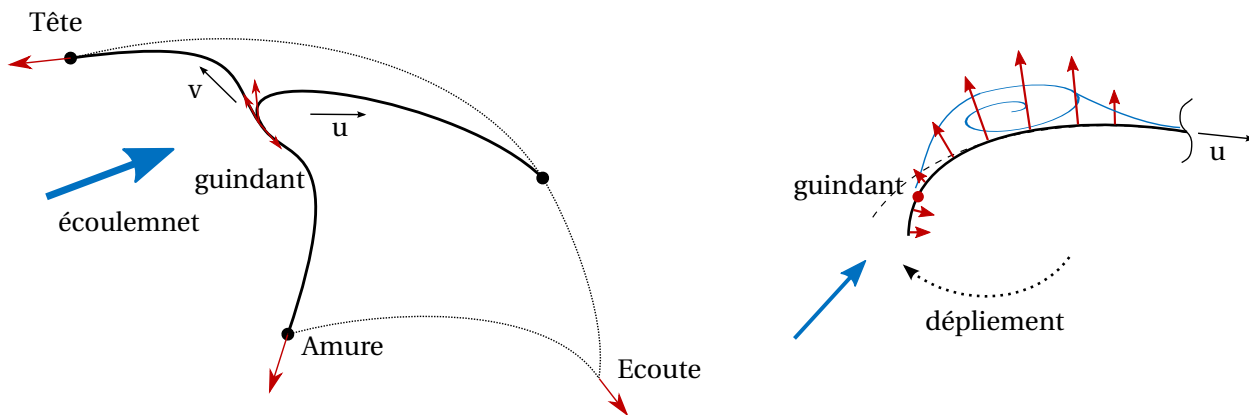


(b) Pendant le repliement (*entre les instants A et C*). Corde "envergure" v non chargée, diminution de l'angle d'attaque, diminution de la pression sur la corde "écoulement" u .

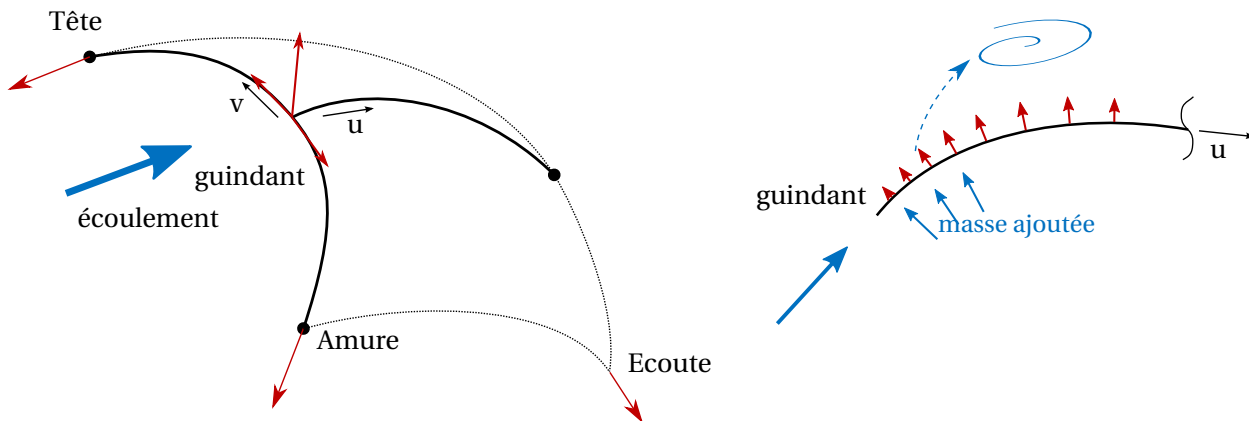


(c) Au maximum du repliement (*instant C*). Corde "écoulement" suffisamment repliée pour créer un nouveau profil aérodynamique avec un angle d'attaque élevé. Création d'une bulle de séparation au bord d'attaque.

Figure E.19 – *Pendant le repliement*. Représentation simplifiée du spinnaker pour modéliser le faseyement du guindant avec une corde sur l'envergure v modélisant le guindant et une corde le long de l'écoulement u .



(a) Pendant le dépliement (entre les instants C et D). Du fait d'un important gradient de pression au guindant, la corde "écoulement" u se déplie. La taille de la bulle de séparation au bord d'attaque augmente.



(b) Forme de la voile complètement dépliée retrouvée (instant D). La corde "envergure" v est sous tension soudainement, arrêtant brutalement le dépliement de la corde "écoulement" u . Un pic d'effort apparaît dû à l'air déplacé autour du guindant. La bulle de séparation du bord d'attaque se détache, une faible pression est de nouveau présente sur la corde "écoulement" u . La première situation est de nouveau présente. Le cycle peut recommencer.

Figure E.20 – Pendant le dépliement. Représentation simplifiée du spinnaker pour modéliser le fasyement du guindant avec une corde sur l'envergure v modélisant le guindant et une corde le long de l'écoulement u .

E.6 Conclusion

Cette thèse fait partie du projet VOIL'ENav du laboratoire de l'IRENav sur les interactions fluide-structure sur les voiliers. Elle a permis de développer un voilier instrumenté pour des mesures *in situ*, résolues en temps sur l'aéro-élasticité des voiles et du gréement pour des navigations au portant. Les évolutions des formes de voile en navigation, ainsi que les efforts et les pressions sur le spinnaker ont été analysées en fonction de l'angle de vent apparent. Non seulement le comportement général de la voile a été analysé mais aussi son comportement instationnaire. Le fasyement du guindant, qui est le réglage optimal selon les marins, a été étudié.

Un voilier J/80 est instrumenté pour mesurer la forme du spinnaker, les efforts aérodynamiques

transmis au gréement, les pressions sur le spinnaker asymétrique et les données du voilier et du vent. Toutes ces données peuvent être mesurées en condition de régate et sont résolues en temps. Un effort important a été mis sur l'étude de la précision et la dynamique des mesures.

La principale amélioration a été sur le système d'acquisition de mesure dynamique de la forme en navigation du spinnaker. Ce système est synchronisé avec les autres données. Le système d'acquisition photogrammétrique mesure la forme du spinnaker avec une précision moyenne meilleure que 1.5% (0.15 m pour 10 m) à une fréquence d'échantillonnage de 25 Hz. Cette précision est suffisante pour mesurer les comportements dynamiques du spinnaker qui ont une échelle de temps de l'ordre de la seconde et des déplacements de l'ordre d'un mètre.

Pour mesurer l'effort aérodynamique généré par le spinnaker, des capteurs d'effort sont placés aux 3 points de la voile (tête, amure et écoute). Deux types de capteur ont été utilisés. D'abord, les manilles instrumentées, développées pendant la thèse de [Augier, 2012], ont été améliorées en capteurs sans fil. Le second type de capteur est le *Directional Load Cell (DLC)*. Il mesure l'intensité et la direction des efforts. Pendant ma thèse, la dynamique et l'étalonnage de ces capteurs ont été optimisés pour nos essais. La précision de ces jauges de contrainte est inférieure à 2% de l'étendue de mesure. Une incertitude dans la direction des efforts apporte une incertitude de 100 N dans les efforts projetés dans le repère bateau. On peut néanmoins analyser l'évolution générale de la direction des efforts aérodynamiques en fonction de l'angle du vent.

Le système d'acquisition de pression a été développé et utilisé pendant la thèse de [Motta, 2015] qui fait partie comme ma thèse du projet SAILING FLUIDS. La faible fréquence d'échantillonnage de 7 Hz est juste suffisant pour analyser l'évolution dans le temps des distributions de pression sur le spinnaker. La précision de 4 Pa est correcte pour la plupart des cas, mais est du même ordre de grandeur que les mesures pour des angles de vent apparent élevés (environ 140°).

Les données de navigation du bateau et du vent ont des fréquences d'échantillonnage variant entre 1 Hz et 20 Hz et sont seulement utilisées pour analyser les performances globales du voilier.

Deux campagnes d'essais ont eu lieu en France (en 2013 et en 2014), ainsi qu'une autre en Nouvelle-Zélande principalement dirigée par Dario Motta. Plusieurs expériences *in situ* ont été effectuées au près et au portant. Ces données résolues dans le temps ont créé une base de données pour des comparaisons numérique-expérimental pour différentes conditions, stationnaires ou non. Des comparaisons numérique-expérimental ont toujours besoin d'être effectuées pour des navigations au portant.

L'évolution générale du spinnaker a été étudiée en fonction de l'angle de vent apparent. Pour des angles de vent serrés (autour de 60°-90°), le spinnaker est comme bridé dans sa partie supérieure. Le coefficient moyen de pression différentielle est plus élevé que pour les autres angles de vent apparent. Puisque la vitesse du vent apparent est aussi plus élevée, les efforts aux 3 points sont à un maximum. Les efforts à la tête et à l'amure sont presque 2 fois plus importants qu'à l'écoute. Les efforts propulsifs et latéraux sont du même ordre de grandeur.

La forme du spinnaker évolue moins entre 90° et 150° qu'entre 70° et 90°. Pour un angle de vent apparent entre 90° et 120°, la voile est plus vrillée dans la partie haute. La distribution de pression est similaire à celle pour des angles de vent plus faibles (présence d'un bulbe de dépression au bord d'attaque) avec un coefficient moyen de pression différentielle globalement équivalent. Cependant la vitesse du

vent apparent diminue produisant un effort aérodynamique plus faible. Mais puisque la voile est plus ouverte, la force est plus tournée dans l'axe longitudinal du bateau. Le maximum du coefficient d'effort propulsif est trouvé pour cette gamme d'angles. L'effort latéral est 2 fois plus faible que l'effort propulsif. Le spinnaker est le plus efficace dans cette gamme de vent apparent.

Pour des angles de vent plus élevés (120° - 150°), la forme est globalement la même mais la valeur absolue du coefficient de pression diminue. Les efforts aux 3 points sont à peu près divisés par 5.

Pour n'importe quel angle de vent apparent, la plupart des variations temporelles des efforts et des pressions ont lieu au niveau du bord d'attaque.

Les formes en navigation du spinnaker sont mesurées par le système d'acquisition photogramétrique. Contrairement aux voiles de près, un spinnaker a une forme 3D qui évolue avec l'angle du vent apparent. Les maîtres voiliers utilisent généralement des sections pour dessiner un spinnaker. C'est la méthode la plus appropriée pour des surfaces proches d'une forme 2D extrudée comme les voiles de près où les profils horizontaux ont peu de variation en fonction de la hauteur. Elle est sans doute moins à propos pour décrire un spinnaker. Lors de cette thèse, de nouvelles représentations ont été développées pour analyser la forme d'un spinnaker comme une surface 3D. La représentation "cambrure 3D" permet une visualisation 3D simple et ainsi de facilement comparer les formes et la répartition de cambrure. Une surface de Bézier triangulaire a aussi été développée pour représenter les formes de voiles. Cette représentation a l'avantage de définir un spinnaker avec seulement quelques points de contrôle. De plus, ces points de contrôle peuvent caractériser distinctement différents types de voile pour tous types d'angles de vent et permettent également de stocker plus facilement des surfaces dans une large base de données. Utiliser la position de quelques points de contrôle plutôt que toute une surface réduirait et simplifierait considérablement le stockage de ces données.

Pour finir, le fasyement du guindant, un comportement instationnaire propre au spinnaker, a été analysé. Ce phénomène est connu des marins. Être à la limite du fasyement serait en effet le réglage optimal. A partir des mesures de pressions et d'efforts, nous avons pu conclure que c'est un phénomène tri-dimensionnel d'interaction fluide-structure qui entraîne de fortes variations de l'effort aérodynamique. La voile se replie au niveau du guindant quand la dépression au bord d'attaque diminue. Au maximum du repliement, une zone de forte dépression apparaît derrière le repliement qui fait déplier le spinnaker. A cet instant les efforts mesurés sont maximaux, ce qui peut expliquer l'intérêt de ce réglage. L'évolution des pressions a été étudiée par analyse modale en utilisant la décomposition en modes propres orthogonaux (POD). Cette décomposition a été utilisée pour décrire plus facilement l'évolution générale dans le temps de ce comportement plutôt que d'analyser les signaux de pression un par un. Deux modes spécifiques de cette décomposition décrivent le fasyement du guindant. Alors que les modes spatiaux sont similaires pour n'importe quel angle de vent, leur comportement temporel diffère. La vitesse du vent (associé à un unique angle de vent pour des expériences *in situ*) détermine l'échelle de temps du fasyement.

De ces observations, une interprétation physique a été proposée. Quand le guindant est replié, un nouveau profil aérodynamique se forme amenant une bulle de séparation au bord d'attaque produisant une zone de dépression. Cette bulle de séparation s'accroît lors du dépliement augmentant la zone de

dépression. Cette énergie accumulée est transmise au guindant lorsque la voile a retrouvé sa forme dépliée, qui est ressentie par un pic d'efforts dans la drisse et l'amure.

Le faseyement du spinnaker provoque le développement d'une zone de dépression proche du guindant qui est principalement orientée dans l'axe longitudinal du bateau. Cette augmentation temporaire des efforts n'a donc lieu que si le spinnaker est réglé pour faseyer ou à la limite du faseyement.

Perspectives

L'instrumentation embarquée a été particulièrement améliorée entre la fin de la thèse de [Augier, 2012] et la configuration actuelle à la fin de ma thèse grâce à un soutien financier, de nouvelles techniques plus facilement disponibles, et un retour d'expérience très utile. Cependant certains capteurs peuvent encore être améliorés. Un nouveau spinnaker dédié aux essais a été acheté mais n'a pas encore été utilisé. Les positions de cibles circulaires ont été marquées pendant la fabrication de la voile et sont donc connues précisément. De nouvelles caméras ont aussi été achetées. Elles ont une meilleure résolution, un capteur optique plus grand, un obturateur global et peuvent être parfaitement synchronisées avec les autres données.

Non seulement le système d'acquisition des formes de voile pourrait être encore amélioré mais également les systèmes d'acquisition d'effort et de pression. De nouvelles *Directional Load Cells* dédiées à des mesures dynamiques pourraient être développées. Une tension de référence séparée de la tension d'alimentation, ainsi qu'un algorithme embarqué optimisé amélioreraient considérablement la fréquence d'échantillonnage et la précision de la mesure des efforts. Un étalonnage précis et une procédure claire pour positionner correctement la centrale inertielle dans le bateau permettrait d'améliorer la précision dans la mesure de la direction des efforts.

Le système d'acquisition de pression était fragile et plusieurs capteurs se sont débranchés pendant les essais. Un système plus robuste avec plus de capteurs de pression sur la voile pour une distribution plus fine améliorerait la précision dans les mesures de pression.

Enfin ces expériences devraient être effectuées avec en même temps le système d'acquisition photogramétrique de forme de voile et le système d'acquisition de pression. Des résultats synchronisés avec la forme et la distribution de pression permettraient d'explorer de nouvelles pistes.

D'autres scientifiques effectuent des essais *in situ* comme au Politecnico di Milano avec le bateau dynamomètre LECCO. Travailler avec eux et partager nos connaissances et notre savoir-faire ouvrirait sans doute de nouvelles perspectives.

Plusieurs essais ont été effectués pour différents angles de vent apparent. Cependant la vitesse du vent réel n'a que peu varié lors de nos essais. Des données dans du vent plus fort permettraient d'analyser l'évolution des efforts et des pressions avec la vitesse du vent pour des angles de vent similaires. On pourrait ainsi voir s'il y a une différence de comportement dynamique sur la forme et les efforts entre un bateau en mode archimédien et un bateau au planing. Les voiliers de course au large naviguent en effet la plupart du temps au portant en planant et surfant sur les vagues. Ces navigations instables et extrêmes sont complexes à modéliser et à étudier numériquement. Des essais *in situ* mesurant les vrais efforts

apporteraient des données intéressantes.

D'autres mesures instationnaires où des pics d'efforts extrêmes peuvent être enregistrés pourraient être effectuées également. Le hissage d'un spinnaker dans du vent fort ou lorsque le spinnaker décroche complètement et se regonfle brutalement sont des situations critiques à prendre en compte lors de la conception de la voile et du gréement du bateau.

D'autres améliorations sur l'instrumentation et sur les expériences pourraient donc être effectuées. Mais des analyses et des comparaisons présentées dans cette thèse pourraient être plus approfondies également. Différents designs de voile de portant pourraient être mesurés pour créer une large base de données. Les points de contrôle de Bézier pourrait aider à trier ces formes. Un gennaker utilisé pour du travers ou du petit largue a une forme différente par rapport à un spinnaker large utilisé pour du grand largue ou vent arrière.

Les règles de classe déterminent la conception des voiles en délimitant certaines longueurs et la surface de la voile. En utilisant d'autres limites comme le plan tangent au point d'écoute qui doit contenir la poulie de renvoi sur le bateau, un processus d'optimisation pourrait être développé numériquement puisque la voile est définie par une formule polynomiale à l'aide des points de contrôle. On pourrait ainsi contraindre le déplacement des points de contrôle pour aider le maître voilier à rester dans la jauge.

Des modèles numériques peuvent aussi aider les maîtres voiliers. Mais les voiles de portant sont difficiles à modéliser. Il y a en effet un fort couplage entre un écoulement turbulent et fortement détaché et une membrane mince et souple. Des schémas avec un couplage fort, et un remaillage automatique sont donc nécessaires. Des simulations numériques résolues en temps ont été créées [Durand, 2012, Durand et al., 2014], mais ont toujours besoin de validations. Au moment de l'écriture de cette thèse, une comparaison numérique/expérimentale est en cours sur le choqué puis le faseyement d'un spinnaker. Le vent, les attitudes du bateau et la longueur de l'écoute mesurés sont les données d'entrée. La forme du spinnaker ainsi que les efforts aux 3 points et dans le gréement sont les données qui sont comparées.

Des mesures dynamiques peuvent donc être comparées à des simulations numériques, mais peuvent aussi permettre de mieux comprendre les phénomènes dynamiques du spinnaker. L'interprétation physique proposée pour expliquer le faseyement devrait être confirmée ou infirmée. Des études expérimentales dans un environnement contrôlé sur une forme plus simple devraient donc être effectuées avec des mesures PIV pour détecter la possible présence d'une bulle de séparation au bord d'attaque. Ces essais permettraient aussi de découpler la vitesse et l'angle de l'écoulement sur la membrane.

D'autres analyses modales pourraient être utilisées, comme la décomposition bi-orthogonale (BOD) [Hémon and Santi, 2003] ou la décomposition en modes dynamiques (DMD) [Schmid, 2010]. Ces méthodes sont pratiques pour analyser les évolutions temporelles, et donc aideraient sans doute à mieux comprendre le phénomène du faseyement.

D'autres études expérimentales sont en cours en soufflerie à l'Université d'Auckland par Nicolas Aubin, doctorant à l'IRENav. Pour différents angles de vent, l'écoute du spinnaker est ajusté autour du réglage optimal, à la limite du faseyement, et les efforts propulsifs et latéraux sont mesurés grâce à une balance.

Ces expériences semblent confirmer qu'il s'agit bien du réglage optimal pour les spinnakers, où la force propulsive est maximale. Cependant il ne faut pas oublier que les similitudes ne sont pas respectées en soufflerie pour un voilier. L'association et la combinaison des simulations numériques, des essais en soufflerie et *in situ* en grandeur réelle restent nécessaires pour pouvoir explorer en détail ces phénomènes complexes.

Bibliography

- [Astolfi et al., 2015] Astolfi, J. A., Lelong, A., and Bot, P. (2015). Experimental Analysis of Hydroelastic Response of Flexible Hydrofoils. In *The 5th High Performance Yacht Design Conference*, pages 200–207, Auckland. 27, 35
- [Aubin et al., 2016] Aubin, N., Augier, B., Bot, P., Hauville, F., Sacher, M., and Flay, R. G. (2016). Wind tunnel investigation of dynamic trimming on upwind sail aerodynamics. In *The 22nd Chesapeake Sailing Yacht Symposium*, pages 111–121, Annapolis. 36, 37
- [Augier, 2012] Augier, B. (2012). *Etudes expérimentales de l'interaction fluide-structure sur surface souple : application aux voiles de bateaux*. PhD thesis, Université de Bretagne Occidentale/IRENav. 2, 30, 34, 64, 65, 66, 88, 159, 161, 192, 203, 219, 221
- [Augier et al., 2012] Augier, B., Bot, P., Hauville, F., and Durand, M. (2012). Experimental validation of unsteady models for fluid structure interaction: Application to yacht sails and rigs. *Journal of Wind Engineering and Industrial Aerodynamics*, 101:53–66. 36, 37, 40
- [Augier et al., 2013] Augier, B., Bot, P., Hauville, F., and Durand, M. (2013). Dynamic behaviour of a flexible yacht sail plan. *Ocean Engineering*, 66:32–43. 37, 40
- [Augier et al., 2014] Augier, B., Hauville, F., Bot, P., Aubin, N., and Durand, M. (2014). Numerical study of a flexible sail plan submitted to pitching: Hysteresis phenomenon and effect of rig adjustments. *Ocean Engineering*, 90:119–128. 36, 37
- [Banks et al., 2010] Banks, J., Webb, A., Spenkuch, T., and Turnock, S. R. (2010). Measurement of dynamic forces experienced by an asymmetric yacht during a gybe, for use within sail simulation software. *Procedia Engineering*, 2(2):2511–2516. 36, 38, 198, 199
- [Belloli et al., 2014] Belloli, M., Rosa, L., and Zasso, A. (2014). Wind loads on a high slender tower: Numerical and experimental comparison. *Engineering Structures*, 68:24–32. 27
- [Belouaer et al., 2015] Belouaer, L., Boussard, M., and Bot, P. (2015). Strategic Decision Making in Yacht Match Racing : Stochastic Game Approach. In *The 5th High Performance Yacht Design Conference*, pages 150–159, Auckland. 35
- [Bergsma et al., 2012] Bergsma, F., Motta, D., Le Pelley, D. J., Richards, P., and Flay, R. G. (2012). Investigation of shroud tension on sailing yacht aerodynamics using full-scale real-time pressure and sail shape

- measurements. In *The 22nd HISWA Symposium on Yacht Design and Yacht Construction*, Amsterdam. 37, 40
- [Bertram, 2012] Bertram, V. (2012). *Practical Ship Hydrodynamics*. Elsevier, butterwort edition. 27
- [Bethwaite, 2010] Bethwaite, F. (2010). *High Performance Sailing: Faster Racing Techniques*. Adlard Coles Nautical. 7
- [Bézier, 1968] Bézier, P. E. (1968). How Renault Uses Numerical Control for Car Body Design and Tooling. In *SAE Technical Paper 680010*. 102
- [Bienkiewicz et al., 1995] Bienkiewicz, B., Tamura, Y., Ham, H., Ueda, H., and Hibi, K. (1995). Proper orthogonal decomposition and reconstruction of multi-channel roof pressure. *Journal of Wind Engineering and Industrial Aerodynamics*, 54-55(C):369–381. 138
- [Billah, 1991] Billah, K. Y. (1991). Resonance, Tacoma Narrows bridge failure, and undergraduate physics textbooks. *American Journal of Physics*, 59(2):118. 27
- [Birch and Dickinson, 2001] Birch, J. M. and Dickinson, M. H. (2001). Spanwise flow and the attachment of the leading-edge vortex on insect wings. *Nature*, 412(6848):729–733. 24
- [Black et al., 2010] Black, J. T., Pitcher, N. a., Reeder, M. F., and Maple, R. C. (2010). Videogrammetry Dynamics Measurements of a Lightweight Flexible Wing in a Wind Tunnel. In *Journal of Aircraft*, volume 47, pages 172–180, Palm Springs, California. American Institute of Aeronautics and Astronautics. 41
- [Blakeley et al., 2015] Blakeley, A. W., Flay, R. G., Furukawa, H., and Richards, P. J. (2015). Evaluation of multi-element wing sail aerodynamics from two-dimensional wind tunnel investigations. In *The 5th High Performance Yacht Design Conference*, pages 37–47, Auckland. 35
- [Bles et al., 2009] Bles, G., Nowacki, W. K., and Tourabi, A. (2009). Experimental study of the cyclic visco-elasto-plastic behaviour of a polyamide fibre strap. *International Journal of Solids and Structures*, 46(13):2693–2705. 34
- [Blevins, 1995] Blevins, R. (1995). *Formulas for Natural Frequency and Mode Shapes*. Kreifer Pub Co. 32
- [Bot et al., 2014] Bot, P., Viola, I. M., Flay, R. G., and Brett, J. S. (2014). Wind-tunnel pressure measurements on model-scale rigid downwind sails. *Ocean Engineering*, 90:84–92. 36, 38, 198, 199
- [Bradski and Kaehler, 2008] Bradski, G. and Kaehler, A. (2008). *Learning OpenCV: Computer Vision with the OpenCV Library*. O'Reilly Media, Inc. 41
- [Braun and Imas, 2008] Braun, J. B. and Imas, L. (2008). High fidelity CFD simulations in racing yacht aerodynamic analysis. In *The 3rd High Performance Yacht Design Conference*, pages 168–175, Auckland. 37
- [Brennen, 1982] Brennen, C. E. (1982). A review of added mass and fluid inertial forces. Technical Report January, Naval Civil Engineering Laboratory, Port Hueneme, California. 32

- [Campbell, 2014a] Campbell, I. M. C. (2014a). A comparison of downwind sail coefficients from tests in different wind tunnels. *Ocean Engineering*, 90:62–71. 36, 38, 118, 120, 199
- [Campbell, 2014b] Campbell, I. M. C. (2014b). Comparison of downwind sailing performance predicted from wind tunnel tests with full-scale trials from America's Cup class yachts. In *The 23rd HISWA Symposium on Yacht Design and Yacht Construction*, pages 104–123. 38, 199
- [Camps et al., 2009] Camps, F., Harasse, S., and Monin, A. (2009). Numerical calibration for 3-AXIS accelerometers and magnetometers. *Proceedings of 2009 IEEE International Conference on Electro/Information Technology, EIT 2009*, pages 217–221. 81
- [Chae, 2015] Chae, E. J. (2015). *Dynamic response and stability of flexible hydrofoils in incompressible and viscous flow*. PhD thesis, University of Michigan. 27
- [Chapin et al., 2015] Chapin, V., Gourdain, N., Verdin, N., Fiumara, A., and Senter, J. (2015). Aerodynamic Study of a Two-Elements Wingsail for High Performance Multihull Yachts. In *The 5th High Performance Yacht Design Conference*, pages 25–36, Auckland. 35
- [Chapin et al., 2011] Chapin, V. G., de Carlan, N., and Heppel, P. (2011). A Multidisciplinary Computational Framework for Sailing Yacht Rig Design & Optimization through Viscous FSI. In *The 20th Chesapeake Sailing Yacht Symposium*, pages 1–18, Annapolis. 32, 37
- [Chauvet et al., 2009] Chauvet, W., Chabert, M., and Lacaze, B. (2009). Influence d'un échantillonnage irrégulier sur les performances de la reconstruction. In *GRETSI, Groupe d'Etudes du Traitement du Signal et des Images*, Toulouse. Université de Toulouse. 87, 187
- [Chéret, 1997] Chéret, B. (1997). *Les voiles: comprendre, régler, optimiser*. Voiles/Gallimard, ffv edition. 7
- [Claughton and Campbell, 1994] Claughton, A. R. and Campbell, I. M. C. (1994). Wind Tunnel Testing of Sailing Rigs. In *The 13th HISWA International Symposium on Yacht Design and Yacht Construction*, pages 86–106, Amsterdam. 36, 37
- [Clauss and Heisen, 2005] Clauss, G. F. and Heisen, W. (2005). CFD analysis on the flying shape of modern yacht sails. In *The 12th International Congress of the International Maritime Association of the Mediterranean*, pages 87–94, Lisbon. 36, 37, 39, 41
- [Cobelli et al., 2009] Cobelli, P. J., Maurel, A., Pagneux, V., and Petitjeans, P. (2009). Global measurement of water waves by Fourier transform profilometry. *Experiments in Fluids*, 46(6):1037–1047. 41
- [Craig, 1989] Craig, J. J. (1989). *Introduction to Robotics: Mechanics and Control*. Pearson Education International/Prentice Hall. 179, 182
- [Curry, 1928] Curry, M. (1928). *Yacht Racing The Aerodynamics of Sails and Racing Tactics*. Etienne Chiron, french edition. 22
- [de Langre, 2002] de Langre, E. (2002). *Fluides et solides*. ellipses diffusion, Palaiseau. 28, 29

- [Deparday et al., 2016] Deparday, J., Bot, P., Augier, B., Rabaud, M., Motta, D., and Le Pelley, D. (2016). Modal Analysis of Pressures on a Full-Scale Spinnaker. In *The 22nd Chesapeake Sailing Yacht Symposium*, pages 98–110, Annapolis. 38, 198, 199
- [Deparday et al., 2014] Deparday, J., Bot, P., Hauville, F., Motta, D., Le Pelley, D. J., and Flay, R. G. (2014). Dynamic measurements of pressures, sail shape and forces on a full-scale spinnaker. In *The 23rd HISWA Symposium on Yacht Design and Yacht Construction*, pages 61–73, Amsterdam. 38, 198, 199
- [Diebel, 2006] Diebel, J. (2006). Representing Attitude: Euler Angles, Unit Quaternions, and Rotation Vectors. Technical report. 179, 182
- [Digne, 2013] Digne, F. (2013). *Caractérisation et identification des sources électromagnétiques radar en contexte de guerre électronique navale*. PhD thesis, UBO. 102
- [Douguet et al., 2013] Douguet, R., Diguët, J.-P., Laurent, J., and Riou, Y. (2013). A New Real-time Method for Sailboat Performance estimation based on Leeway Modeling. In *The 21st Chesapeake Sailing Yacht Symposium*, pages 37–49, Annapolis. 9
- [Doyle et al., 2016] Doyle, T., Knight, B., and Swain, D. (2016). A Comparison of a RANS Based VPP to on the Water Sailing Performance. In *The 22nd Chesapeake Sailing Yacht Symposium*, pages 16–35, Annapolis. 35, 41
- [Durand, 2012] Durand, M. (2012). *Interaction fluide-structure souple et légère, applications aux voiliers*. PhD thesis, Ecole Centrale Nantes. 30, 32, 33, 34, 35, 43, 100, 162, 197, 198, 222
- [Durand et al., 2014] Durand, M., Leroyer, A., Lothodé, C., Hauville, F., Visonneau, M., Floch, R., and Guillaume, L. (2014). FSI investigation on stability of downwind sails with an automatic dynamic trimming. *Ocean Engineering*, 90(2013):129–139. 32, 35, 36, 38, 43, 162, 198, 199, 222
- [Eos Systems Inc., 2015] Eos Systems Inc. (2015). *Photomodeler 2015 User Guide*. 51
- [Farin, 1986] Farin, G. (1986). Triangular Bernstein-Bézier patches. *Computer Aided Geometric Design*, 3(2):83–127. 101
- [Feichtinger et al., 1995] Feichtinger, H. G., Grochenig, K., and Strohmer, T. (1995). Efficient numerical methods in non-uniform sampling theory. *Numerische Mathematik*, 440:423–441. 87, 187
- [Flay, 1996] Flay, R. G. (1996). A twisted flow wind tunnel for testing yacht sails. *Journal of Wind Engineering and Industrial Aerodynamics*, 63(1-3):171–182. 23, 36, 37
- [Flay and Millar, 2006] Flay, R. G. and Millar, S. (2006). Experimental considerations concerning pressure measurement on sail. In *The 2nd High Performance Yacht Design Conference*, pages 123–130, Auckland. 37, 40
- [Floch et al., 2012] Floch, F., Phoemsapthawee, S., Laurens, J. M., and Leroux, J. B. (2012). Porpoising foil as a propulsion system. *Ocean Engineering*, 39:53–61. 27
- [Fossati, 2009] Fossati, F. (2009). *Aero-Hydrodynamics and the Performance of Sailing Yachts: The Science Behind Sailing Yachts and Their Design*. International Marine / Mc Graw Hill. 8, 10, 22, 23, 42, 73, 116

- [Fossati et al., 2016] Fossati, F., Bayati, I., Muggiasca, S., Vandone, A., Campanardi, G., Burch, T., and Malandra, M. (2016). Pressure Measurements on Yacht Sails: Development of a New System for Wind Tunnel and Full Scale Testing. In *The 22nd Chesapeake Sailing Yacht Symposium*, pages 84–97, Annapolis. SNAME. 39
- [Fossati et al., 2015a] Fossati, F., Bayati, I., Orlandini, F., Muggiasca, S., Vandone, A., Mainetti, G., Sala, R., Bertorello, C., and Begovic, E. (2015a). A novel full scale laboratory for yacht engineering research. *Ocean Engineering*, 104:219–237. 39, 114
- [Fossati et al., 2015b] Fossati, F., Mainetti, G., Malandra, M., Sala, R., Schito, P., and Vandone, A. (2015b). Offwind sail flying shapes detection. In *The 5th High Performance Yacht Design Conference*, pages 48–59, Auckland. 39, 41, 42, 101
- [Fossati and Muggiasca, 2010] Fossati, F. and Muggiasca, S. (2010). Numerical modelling of sail aerodynamic behaviour in dynamic conditions. In *The 2nd International Conference On Innovation in High Performance Sailing Yachts*, Lorient. 37
- [Fossati and Muggiasca, 2011] Fossati, F. and Muggiasca, S. (2011). Experimental investigation of sail aerodynamic behavior in dynamic conditions. *Journal of Sailboat Technology*, 2(03):1–42. 36, 37
- [Fossati et al., 2006] Fossati, F., Muggiasca, S., Viola, I. M., and Zasso, A. (2006). Wind Tunnel Techniques for Investigation and Optimization of Sailing Yachts Aerodynamics. In *The 2nd High Performance Yacht Design Conference*, pages 105–113, Auckland. 36, 37
- [Garrett, 1987] Garrett, R. (1987). *The symmetry of Sailing*. Adlard Coles, London. 8, 20, 21
- [Gentry, 1971] Gentry, A. (1971). The Aerodynamics of Sail Interaction. In *The Third AIAA Symposium of Aero/Hydronautics of Sailing*, pages 1–12, Redondo Beach, California. 37, 39
- [Gerhardt et al., 2011] Gerhardt, F. C., Flay, R. G., and Richards, P. J. (2011). Unsteady aerodynamics of two interacting yacht sails in two-dimensional potential flow. *Journal of Fluid Mechanics*, 668:551–581. 36, 37
- [Gerhardt et al., 2009] Gerhardt, F. C., Le Pelley, D. J., Flay, R. G., and Richards, P. J. (2009). Tacking in the Wind Tunnel. In *The 19th Chesapeake Sailing Yacht Symposium*, pages 161–175, Annapolis. 36, 37
- [Gilliam et al., 2004] Gilliam, X., Dunyak, J. P., Smith, D. A., and Wu, F. (2004). Using projection pursuit and proper orthogonal decomposition to identify independent flow mechanisms. *Journal of Wind Engineering and Industrial Aerodynamics*, 92(1):53–69. 138
- [Giovannetti et al., 2015] Giovannetti, L. M., Banks, J., Boyd, S. W., and Turnock, S. R. (2015). Fluid structure interaction in high performance catamaran C-foils under load. In *The 5th High Performance Yacht Design Conference*, pages 171–179, Auckland. 41
- [Graf and Müller, 2009] Graf, K. and Müller, O. (2009). Photogrammetric Investigation of the Flying Shape of Spinnakers in a Twisted Flow Wind Tunnel. In *The 19th Chesapeake Sailing Yacht Symposium*, Annapolis. 36, 38, 198, 199

- [Graf et al., 2016] Graf, K., Renzsch, H., and Meyer, J. (2016). Prediction and optimization of aerodynamic and hydrodynamic forces and boat speed of foiling catamarans with a wing sail and a jib. In *The 22nd Chesapeake Sailing Yacht Symposium*, pages 1–15, Annapolis. 35
- [Graves et al., 2008] Graves, W., Barbera, T., and Braun, J. B. (2008). Measurement and simulation of pressure distribution on full size sails. In *The 3rd High Performance Yacht Design Conference*, pages 239–246, Auckland. 40
- [Green and Unruh, 2006] Green, D. and Unruh, W. G. (2006). The failure of the Tacoma Bridge: A physical model. *American Journal of Physics*, 74(8):706–716. 27
- [Gregory and Païdoussis, 1966] Gregory, R. W. and Païdoussis, M. (1966). Unstable oscillation of tubular cantilevers conveying fluid I. Theory. *Proceedings of the Royal Society A: Mathematical, Physical and Engineering Sciences*, 293(1435):512–527. 27
- [Hansen, 2006] Hansen, H. (2006). *Enhanced wind tunnel techniques and aerodynamic force models for yacht sails*. PhD thesis, University of Auckland. 16, 194
- [Hansen et al., 2002] Hansen, H., Jackson, P., and Hochkirch, K. (2002). Comparison of wind tunnel and full-scale aerodynamic sail force measurements. In *The High Performance Yacht Design Conference*, Auckland. 36, 38, 39, 198, 199
- [Hedges et al., 1996] Hedges, K., Richards, P., and Mallinson, G. (1996). Computer modelling of downwind sails. *Journal of Wind Engineering and Industrial Aerodynamics*, 63(1-3):95–110. 38, 199
- [Hémon, 2006] Hémon, P. (2006). *Vibrations des structures couplées avec le vent*. Ecole Polytechnique. 15
- [Hémon and Santi, 2003] Hémon, P. and Santi, F. (2003). Applications of biorthogonal decompositions in fluid–structure interactions. *Journal of Fluids and Structures*, 17(8):1123–1143. 162, 222
- [Heppel, 2015] Heppel, P. (2015). Flight dynamics of sailing foilers. In *The 5th High Performance Yacht Design Conference*, pages 180–189, Auckland. 35
- [Herman, 1989] Herman, J. S. (1989). *A sail force dynamometer: design, implementation and data handling*. PhD thesis, Massachusetts Institute of Technology. 37, 39
- [Hochkirch and Brandt, 1999] Hochkirch, K. and Brandt, H. (1999). Fullscale hydrodynamic force measurement on the Berlin sailing dynamometer. In *The 14th Chesapeake Sailing Yacht Symposium*, pages 33–44, Annapolis. 37, 39
- [Huetz and Guillerm, 2014] Huetz, L. and Guillerm, P. E. (2014). Database building and statistical methods to predict sailing yacht hydrodynamics. *Ocean Engineering*, 90:21–33. 35
- [Kerwin and Newman, 1979] Kerwin, J. and Newman, J. (1979). A Summary of the H. Irving Pratt Ocean Race Handicapping Project. In *The 4th Chesapeake Sailing Yacht Symposium*, Annapolis. 37
- [Keuning and Katgert, 2008] Keuning, J. A. and Katgert, M. (2008). A bare hull resistance prediction method derived from the results of the Delft systematic yacht hull series extended to higher speeds. In *The International Conference on Innovation in High Performance Sailing Yachts*, Lorient. 35

- [Kraus and Waldhäusl, 1997] Kraus, K. and Waldhäusl, P. (1997). *Manuel de photogrammétrie, principes et procédés fondamentaux*. Hermès. 167
- [Kuipers, 1999] Kuipers, J. B. (1999). *Quaternions and Rotations: a Primer with Applications to Orbits, Aerospace, and Virtual Reality*. Princeton University Press. 179
- [Larsson et al., 1994] Larsson, L., Eliasson, R., and Orych, M. (1994). *Principles of Yacht Design*. International Marine / Mc Graw Hill, third edition. 8, 73
- [Lasher and Sonnenmeier, 2008] Lasher, W. C. and Sonnenmeier, J. R. (2008). An analysis of practical RANS simulations for spinnaker aerodynamics. *Journal of Wind Engineering and Industrial Aerodynamics*, 96(2):143–165. 38, 199
- [Lautrup, 2010] Lautrup, B. (2010). Surface tension. *Physics of continuous Matter*, pages 69–94. 33
- [Le Pelley and Modral, 2008] Le Pelley, D. J. and Modral, O. (2008). VSPARS: A combined sail and rig recognition system using imaging techniques. In *The 3rd High Performance Yacht Design Conference*, pages 57–66, Auckland. 40, 41
- [Le Pelley et al., 2012] Le Pelley, D. J., Morris, D., and Richards, P. J. (2012). Aerodynamic force deduction on yacht sails using pressure and shape measurements in real time. In *The 4th High Performance Yacht Design Conference*, pages 28–37, Auckland. 40, 73
- [Le Pelley and Richards, 2011] Le Pelley, D. J. and Richards, P. (2011). Effective Wind Tunnel Testing of Yacht Sails Using a Real-Time Velocity Prediction Program. In *The 20th Chesapeake Sailing Yacht Symposium*, Annapolis. 35
- [Le Pelley et al., 2015] Le Pelley, D. J., Richards, P. J., and Berthier, A. (2015). Development of a directional load cell to measure flying sail aerodynamic loads. In *The 5th High Performance Yacht Design Conference*, pages 66–75, Auckland. 40, 68, 203
- [Lelong and Astolfi, 2015] Lelong, A. and Astolfi, J. A. (2015). Hydroelastic Response Experimental setup. In *Fourth International Symposium on Marine Propulsors*, pages 521–528. 27
- [Leon, 2010] Leon, S. J. (2010). *Linear algebra with applications*. Pearson Prentice Hall, 8th edition. 107
- [Leroyer, 2004] Leroyer, A. (2004). *Etude du couplage écoulement/mouvement pour des corps solides ou à déformation imposée par résolution des équations de Navier-Stokes. Contribution à la modélisation numérique de la cavitation*. PhD thesis, Ecole Centrale de Nantes et Université de Nantes. 179
- [Lombardi et al., 2012] Lombardi, M., Cremonesi, M., Giampieri, A., Parolini, N., and Quarteroni, A. (2012). A strongly coupled fluid-structure interaction model for wind-sail simulation. In *4th High Performance Yacht Design*, pages 212–221, Auckland. 32, 36, 38, 198, 199
- [Lozej et al., 2012] Lozej, M., Golob, D., and Bokal, D. (2012). Pressure distribution on sail surfaces in real sailing conditions. In *The 4th High Performance Yacht Design Conference*, pages 242–251, Auckland. 37, 40

- [Lumley, 1967] Lumley, J. (1967). The structure of inhomogeneous turbulence. In Yaglom, A. and Tatarski, V., editors, *Atmospheric Turbulence and Wave Propagation*, pages 166–178. Nauka, Moscow. 138
- [Madgwick et al., 2011] Madgwick, S. O. H., Harrison, A. J. L., and Vaidyanathan, R. (2011). Estimation of IMU and MARG orientation using a gradient descent algorithm. In *IEEE International Conference on Rehabilitation Robotics*, pages 1–7. IEEE. 72, 81, 183
- [Marchaj, 1962] Marchaj, C. A. (1962). *Sailing Theory and Practice*. Adlard Coles. 8, 22
- [Masuyama, 2014] Masuyama, Y. (2014). The work achieved with the sail dynamometer boat "fujin", and the role of full scale tests as the bridge between model tests and CFD. *Ocean Engineering*, 90:72–83. 37, 39, 41, 78
- [Masuyama and Fukasawa, 2011] Masuyama, Y. and Fukasawa, T. (2011). Tacking Simulation of Sailing Yachts with New Model of Aerodynamic Force Variation During Tacking Maneuver. *Journal of Sailing Technology*, 01:1–34. 36, 37
- [Mausolf et al., 2011] Mausolf, J., Deparday, J., Graf, K., Renzsch, H., and Böhm, C. (2011). Photogrammetry Based Flying Shape Investigation of Downwind Sails in the Wind Tunnel and at Full Scale on a Sailing Yacht. In *The 20th Chesapeake Sailing Yacht Symposium*, pages 33–43, Annapolis. 36, 38, 42, 198, 199
- [Michalski et al., 2011] Michalski, A., Kermel, P. D., Haug, E., Löhner, R., Wüchner, R., and Bletzinger, K. U. (2011). Validation of the computational fluid-structure interaction simulation at real-scale tests of a flexible 29m umbrella in natural wind flow. *Journal of Wind Engineering and Industrial Aerodynamics*, 99(4):400–413. 27
- [Milgram et al., 1993] Milgram, J. H., Peters, D. B., and Eckhouse, D. N. (1993). Modeling IACC sail forces by combining measurements with CFD. In *The 11th Chesapeake Sailing Yacht Symposium*, pages 65–73, Annapolis. 37
- [Moireau et al., 2012] Moireau, P., Xiao, N., Astorino, M., Figueroa, C. A., Chapelle, D., Taylor, C. A., and Gerbeau, J. F. (2012). External tissue support and fluid-structure simulation in blood flows. *Biomechanics and Modeling in Mechanobiology*, 11(1-2):1–18. 27
- [Motta, 2015] Motta, D. (2015). *An experimental investigation of full-scale sail aerodynamics using pressures, shapes and forces*. PhD thesis, University of Auckland. 38, 39, 40, 75, 89, 121, 152, 153, 159, 198, 219
- [Motta et al., 2015] Motta, D., Flay, R. G., Richards, P. J., Le Pelley, D., Bot, P., and Deparday, J. (2015). An investigation of the dynamic behaviour of asymmetric spinnakers at full-scale. In *The 5th High Performance Yacht Design Conference*, pages 76–85, Auckland. 38, 40, 74, 137, 152, 153, 198, 199
- [Motta et al., 2014] Motta, D., Flay, R. G., Richards, P. J., Le Pelley, D. J., Deparday, J., and Bot, P. (2014). Experimental investigation of asymmetric spinnaker aerodynamics using pressure and sail shape measurements. *Ocean Engineering*, 90:104–118. 38, 40, 76, 199

- [Nava et al., 2016] Nava, S., Cater, J., and Norris, S. (2016). A Comparison of RANS and LES for Upwind Sailing Aerodynamics. In *The 22nd Chesapeake Sailing Yacht Symposium*, pages 73–83, Annapolis. 36, 37
- [Newman, 1987] Newman, B. G. (1987). Aerodynamic theory for membranes and sails. *Progress in Aerospace Sciences*, 24(1):1–27. 19, 32, 151
- [Nguyen et al., 2016] Nguyen, T., Shyam Sundar, D., Yeo, K. S., and Lim, T. T. (2016). Modeling and analysis of insect-like flexible wings at low Reynolds number. *Journal of Fluids and Structures*, 62:294–317. 27
- [Offshore Racing Congress, 2015] Offshore Racing Congress (2015). ORC VPP Documentation 2015. Technical report. 118, 120
- [Pappa et al., 2003] Pappa, R. S., Black, J. T., Blandino, J. R., Jones, T. W., Danehy, P. M., and Dorrington, A. A. (2003). Dot-Projection Photogrammetry and Videogrammetry of Gossamer Space Structures. *Journal of Spacecraft and Rockets*, 40(6):858–867. 41
- [Pastva, 1998] Pastva, T. A. (1998). *Bezier curve fitting*. Master's thesis, Naval Postgraduate School, Monterey, California. 101
- [Patrick, 2007] Patrick, D. A. (2007). *Bezier Surface Generation of the Patella*. Master's thesis, Wright State University. 101, 106
- [Polhamus, 1966] Polhamus, E. C. (1966). a Concept of the Vortex Lift of Sharp-Edge Delta Wings Based on a Leading-Edge-Suction Analogy. *National Aeronautics and Space Administration*, Nasa Techn. 24
- [Prautzsch et al., 2002] Prautzsch, H., Boehm, W., and Paluszny, M. (2002). *Bézier and B-Spline Techniques*. 101
- [Prince and Claughton, 2016] Prince, M. and Claughton, A. R. (2016). The SYRF Wide Light Project. In *The 22nd Chesapeake Sailing Yacht Symposium*, pages 135–150. 35
- [Puddu et al., 2006] Puddu, P., Erriu, N., Nurzia, F., Pistidda, A., and Mura, A. (2006). Full scale investigation of one-design class catamaran sails. In *The 2nd High Performance Yacht Design Conference*, Auckland. 37, 40
- [Rafiee et al., 2016] Rafiee, R., Tahani, M., and Moradi, M. (2016). Simulation of aeroelastic behavior in a composite wind turbine blade. *Journal of Wind Engineering and Industrial Aerodynamics*, 151:60–69. 27
- [Ranzenbach et al., 2013] Ranzenbach, R., Armitage, D., and Carrau, A. (2013). Mainsail Planform Optimization for IRC 52 Using Fluid Structure Interaction. In *The 21st Chesapeake Sailing Yacht Symposium*, pages 50–58, Annapolis. 36, 37
- [Ranzenbach and Kleene, 2002] Ranzenbach, R. and Kleene, J. (2002). Utility of flying shapes in the development of offwind sail design database. In *The High Performance Yacht Design Conference*, Auckland. 36, 38, 40, 42, 101, 114, 198, 199

- [Ratto, 2016] Ratto, N. (2016). Surface modelisation with Bézier surfaces. Application to spinnaker sails. Technical report, IRENav, Lanvéoc. 106, 107
- [Renzsch and Graf, 2010] Renzsch, H. and Graf, K. (2010). Fluid Structure Interaction Simulation of Spinnakers – Towards Simulation Driven Sail Design. In *The 21st HISWA International Symposium on Yacht Design and Yacht Construction*, Amsterdam. 32, 36, 38, 198, 199
- [Renzsch and Graf, 2013] Renzsch, H. and Graf, K. (2013). An experimental validation case for fluid-structure-interaction simulations of downwind sails. In *The 21st Chesapeake Sailing Yacht Symposium*, page 8, Annapolis. 36, 38, 42, 119, 120, 198, 199
- [Richards et al., 2006] Richards, P., Le Pelley, D., Cazala, A., Mccarty, M., Hansen, H., and Moore, W. (2006). The use of independent supports and semi-rigid sails in wind tunnel studies. In *The 2nd High Performance Yacht Design Conference*, pages 114–122, Auckland. 36, 38, 198, 199
- [Richards, 1997] Richards, P. J. (1997). The effect of wind profile and twist on downwind sail performance. *Journal of Wind Engineering and Industrial Aerodynamics*, 67-68:313–321. 22
- [Roux et al., 2008] Roux, Y., Durand, M., Leroyer, A., Queutey, P., Visonneau, M., Raymond, J., Finot, J. M., Hauville, F., and Purwanto, A. (2008). Strongly Coupled VPP and CFD RANSE Code for Sailing Yacht Performance Prediction. In *The 3rd High Performance Yacht Design Conference*, pages 215–226, Auckland. 35
- [Salzmann and Fua, 2011] Salzmann, M. and Fua, P. (2011). Linear local models for monocular reconstruction of deformable surfaces. *IEEE Transactions on Pattern Analysis and Machine Intelligence*, 33(5):931–944. 42
- [Sarpkaya, 2004] Sarpkaya, T. (2004). A critical review of the intrinsic nature of vortex-induced vibrations. *Journal of Fluids and Structures*, 19(4):389–447. 29
- [Sawada and Hisada, 2007] Sawada, T. and Hisada, T. (2007). Fluid-structure interaction analysis of the two-dimensional flag-in-wind problem by an interface-tracking ALE finite element method. *Computers and Fluids*, 36(1):136–146. 27
- [Schmid, 2010] Schmid, P. J. (2010). Dynamic mode decomposition of numerical and experimental data. *Journal of Fluid Mechanics*, 656(July 2010):5–28. 137, 162, 222
- [Schoop and Bessert, 2001] Schoop, H. and Bessert, N. (2001). Instationary aeroelastic computation of yacht sails. *International Journal for Numerical Methods in Engineering*, 52(8):787–803. 37
- [Schutt and Williamson, 2016] Schutt, R. R. and Williamson, C. (2016). Unsteady Sail Dynamics Due To Bodyweight Motions. In *The 22nd Chesapeake Sailing Yacht Symposium*, pages 58–72, Annapolis. SNAME. 36, 37, 41
- [Shankar and Harmon, 2005] Shankar, K. S. and Harmon, T. L. (2005). *Introduction to Robotics*. Pearson Education International/Prentice Hall, third edition. 179
- [Sirovich, 1987] Sirovich, L. (1987). Turbulence and the dynamics of coherent structures part i: coherent structures. *Quarterly of Applied Mathematics*, XLV(3):561–571. 138

- [Song et al., 2008] Song, a., Tian, X., Israeli, E., Galvao, R., Bishop, K., Swartz, S., and Breuer, K. (2008). Aeromechanics of Membrane Wings with Implications for Animal Flight. *AIAA Journal*, 46(8):2096–2106. 27
- [Souilliez et al., 2006] Souilliez, C., Schouveiler, L., and Eloy, L. (2006). Flutter modes of a flexible plate in an air flow. *Journal of Visualization*, 9(3):242–242. 27
- [Tagliaferri and Viola, 2016] Tagliaferri, F. and Viola, I. M. (2016). Development of a routing software for inshore match race. In *The 22nd Chesapeake Sailing Yacht Symposium*, pages 200–209, Annapolis. 35
- [Tamura et al., 1997] Tamura, Y., Ueda, H., Kikuchi, H., Hibi, K., Suganuma, S., and Bienkiewicz, B. (1997). Proper orthogonal decomposition study of approach wind-building pressure correlation. *Journal of Wind Engineering and Industrial Aerodynamics*, 72:421–431. 138
- [Thomas, 2011] Thomas, O. (2011). *Dynamique linéaire et non linéaire de structures élastiques et piezoélectriques. Instruments de musique, micro/nano systèmes électromécaniques, contrôle de vibration*. Habilitation à diriger des recherches, Ecole Normale Supérieure de Cachan. 34, 35
- [Thwaites, 1961] Thwaites, B. (1961). The Aerodynamic Theory of Sails. I. Two-Dimensional Sails. *Proceedings of the Royal Society A: Mathematical, Physical and Engineering Sciences*, 261(1306):402–422. 19, 32, 151
- [Tregidgo et al., 2013] Tregidgo, L., Wang, Z., and Gursul, I. (2013). Unsteady fluid-structure interactions of a pitching membrane wing. *Aerospace Science and Technology*, 28(1):79–90. 27
- [Trimarchi et al., 2013] Trimarchi, D., Vidrascu, M., Taunton, D., Turnock, S. R., and Chapelle, D. (2013). Wrinkle development analysis in thin sail-like structures using MITC shell finite elements. *Finite Elements in Analysis and Design*, 64:48–64. 32, 36, 38, 198, 199
- [Van den Berg and Ellington, 1997] Van den Berg, C. and Ellington, C. P. (1997). The vortex wake of a ‘hovering’ model hawkmoth. *Philosophical Transactions of the Royal Society of London Series B-Biological Sciences*, 352(1351):317–328. 24
- [Van Hemmen, 1986] Van Hemmen, R. F. (1986). Twelve meter design: state of the art in 1986. *Marine Technology*, 23(4):320–337. 37, 40
- [Videler, 2004] Videler, J. J. (2004). Leading-Edge Vortex Lifts Swifts. *Science*, 306(5703):1960–1962. 24
- [Viola et al., 2014] Viola, I. M., Bartesaghi, S., Van-Renterghem, T., and Ponzini, R. (2014). Detached Eddy Simulation of a sailing yacht. *Ocean Engineering*, 90(November 2014):93–103. 23, 24, 25, 36, 38, 152, 195, 196, 198, 199
- [Viola et al., 2015] Viola, I. M., Biancolini, M. E., Sacher, M., and Cella, U. (2015). A CFD-based wing sail optimisation method coupled to a VPP. In *5th High Performance Yacht Design Conference*, pages 1–7, Auckland. 35
- [Viola et al., 2013] Viola, I. M., Bot, P., and Riotte, M. (2013). Upwind sail aerodynamics: A RANS numerical investigation validated with wind tunnel pressure measurements. *International Journal of Heat and Fluid Flow*, 39:90–101. 36, 37

- [Viola and Flay, 2009] Viola, I. M. and Flay, R. G. (2009). Force and pressure investigation of modern asymmetric spinnakers. *Transactions of the Royal Institution of Naval Architects Part B: International Journal of Small Craft Technology*, 151(2):31–40. 36, 38, 73, 198, 199
- [Viola and Flay, 2010] Viola, I. M. and Flay, R. G. (2010). On-water pressure measurements on a modern asymmetric spinnaker. In *21st HISWA Symposium on Yacht Design and Yacht Construction*, Amsterdam. 19, 38, 40, 199
- [Viola and Flay, 2011] Viola, I. M. and Flay, R. G. (2011). Sail pressures from full-scale, wind-tunnel and numerical investigations. *Ocean Engineering*, 38(16):1733–1743. 36, 38, 198, 199
- [Virot et al., 2013] Virot, E., Amandolese, X., and Hémon, P. (2013). Fluttering flags: An experimental study of fluid forces. *Journal of Fluids and Structures*, 43(November 2013):385–401. 27
- [Wakaba and Balachandar, 2007] Wakaba, L. and Balachandar, S. (2007). On the added mass force at finite Reynolds and acceleration numbers. *Theoretical and Computational Fluid Dynamics*, 21(2):147–153. 155
- [Yan et al., 2015] Yan, J., Augier, B., Korobenko, A., Czarnowski, J., Kettermann, G., and Bazilevs, Y. (2015). FSI modeling of a propulsion system based on compliant hydrofoils in a tandem configuration. *Computers & Fluids*, (July 2015). 27